

Czech Technical University in Prague

Faculty of Electrical Engineering

Department of Physics



**Engineering of diamond synthesis
towards bioapplications**

Habilitation Thesis

Štěpán Potocký

October 2022

Acknowledgements

Těm, kteří mi dali možnost,
těm, kteří mi dali schopnost,
a těm, kteří mi dali čas.

Děkuji

Abstract

Diamond excels in combining intrinsic and surface properties, controlling its application in various life science fields. Understanding the complex interaction with living organisms is highly desirable but limited by the technological possibilities of diamond synthesis. They are displayed to some extent. Yet, the fabrication over large areas and substrate temperature limitation remain open. At the same time, high throughput methods of optically active diamond fabrication are missing. We conducted targeted experiments to understand how high-quality diamond can be grown at low substrate temperatures and how the deposition area can be extended with control of diamond film morphology. We extend the traditional diamond deposition area in C-H-O ternary diagram at the expense of the non-growth area and presented plasma chemistry leading to the direct growth of porous diamond morphology. At the same time, we assess key parameters that determine the optical activity of prepared color centers in a diamond matrix. Finally, in collaboration with biologists and doctors, we conducted targeted experiments to understand how diamond morphology and surface influence interaction with bone cells. These *in vitro* experimental findings were transferred to *in vivo* and resulted in increased body implant osteointegration in the early stage of bone formation.

Contents

Chapter 1	Introduction.....	1
1.1	Structure of the thesis.....	2
1.2	Objectives.....	3
Chapter 2	Diamond Synthesis and Challenges.....	5
2.1	HPHT synthesized diamonds.....	5
2.2	Detonation nanodiamonds	6
2.3	Chemical vapor deposited diamonds.....	6
Chapter 3	Low-temperature diamond growth and kinetics in focused MW plasma ellipsoidal cavity resonator	9
Chapter 4	Plasma chemistry and growth kinetics at low pressure in MW plasma with linear antenna setup	13
Chapter 5	The controllable activity of silicon-vacancy color centers in diamond films via plasma chemistry.....	19
Chapter 6	Engineered diamond surface for life sciences – from nanoparticles to three- dimensional diamond coatings.....	23
Chapter 7	Conclusion and future outlooks.....	29
Chapter 8	References.....	31
Appendix A	Included author's publications	35
A.1	Growth of nanocrystalline diamond films deposited by microwave plasma CVD system at low substrate temperatures	35
A.2	Investigation of nanocrystalline diamond films grown on silicon and glass at substrate temperature below 400 °C.....	41
A.3	Linear antenna microwave plasma CVD diamond deposition at the edge of no- growth region of C-H-O ternary diagram	46
A.4	Influence of surface wave plasma deposition conditions on diamond growth regime.....	51
A.5	Perspectives of linear antenna microwave system for growth of various carbon nano-forms and its plasma study	58

A.6	Great Variety of Man-Made Porous Diamond Structures: Pulsed Microwave Cold Plasma System with a Linear Antenna Arrangement.....	63
A.7	Influence of the growth temperature on the Si-V photoluminescence in diamond thin films.....	74
A.8	Si-related color centers in nanocrystalline diamond thin films	80
A.9	Influence of gas chemistry on Si-V color centers in diamond films.....	85
A.10	Nucleation of diamond micro-patterns with photoluminescent SiV centers controlled by amorphous silicon thin films	91
A.11	Uptake and intracellular accumulation of diamond nanoparticles – a metabolic and cytotoxic study.....	98
A.12	Alterations to the adhesion, growth and osteogenic differentiation of human osteoblast-like cells on nanofibrous polylactide scaffolds with diamond nanoparticles	108
A.13	Coating Ti6Al4V implants with nanocrystalline diamond functionalized with BMP-7 promotes extracellular matrix mineralization in vitro and faster osseointegration in vivo.....	121

Chapter 1

Introduction

Diamond, as a standard of beauty, wealth, destruction, and cruelty in its pure essence, represents a unique configuration of physical and chemical properties. In modern science and technology, the synthetic diamond represents a novel semiconductor material with the same unique set of physical and chemical properties but higher flexibility in adjusting such properties for intended applications ranging from electronics and power devices to quantum technologies and medicine. For the biomedical entreaties determined by human society, we cannot forget that carbon is the second or third if we use atomic concentration instead of mass one, the most abundant element in the human body. An example of an open question in bone replacements is a postoperative complication, while an ideal bone replacement requires high mechanical resistance, chemical resistance, and biocompatibility.

Suppose we accept as a fact that the natural occurrence of diamonds on Earth is insufficient for the growing demands or simply its size. In that case, it is necessary to look for ways of synthetic diamond fabrication. The specific properties of the diamond predetermine the specifically difficult conditions of its fabrication, which have been gradually overcome step by step since the 1950s.

Despite significant progress in diamond synthesis, the questions of its fabrication over large areas and substrate temperature limitations remain open. At the same time, the ability of a diamond to host lattice defects leading to optical properties enabling the sensing of weak fields even at room temperatures down to the level of a single nuclear level is being intensively developed and studied. This work contributes to answering them, while we can point out other remaining open questions related to nanoparticles, thin layers, and bulk objects. Challenges such as the controlled preparation of diamond nanoparticles of defined dimensions with the simultaneous incorporation of defined impurities without the need for further activation, a configuration of microwave reactors for large-area thin-film deposition of diamond with growth rates of focused systems, and preparation of diamond porous structures with controlled pore size are still waiting to be answered and solved.

1.1 Structure of the thesis

This thesis is a collection of published works linked by supplementary texts that explain the relationships between the author's individual articles, see Fig. 1.1. Introductory chapter is followed by a chapter summarizing the primary diamond synthesis routes and challenges. Chapter three discusses the initial contribution to the technology of low-temperature diamond growth and hence the origin of the research strand for bioapplications of a diamond. Chapter four discusses the contribution to one of the latest advances in the diamond fabrication technology of microwave plasma-enhanced chemical vapor deposition using linear antenna plasma generation, which facilitates the deposition of a diamond at low temperatures over large areas and three-dimensional substrates. Chapter five acquaints us with a contribution to directly grown silicon-vacancy optical centers in diamond. Using chapter six findings summarizing our contribution to the bioapplication of diamond, we reach the final chapter seven summarizing the benefits of the presented work and the vision for further research. The thesis's Appendix includes 13 peer-reviewed published articles relevant to the thesis topic.

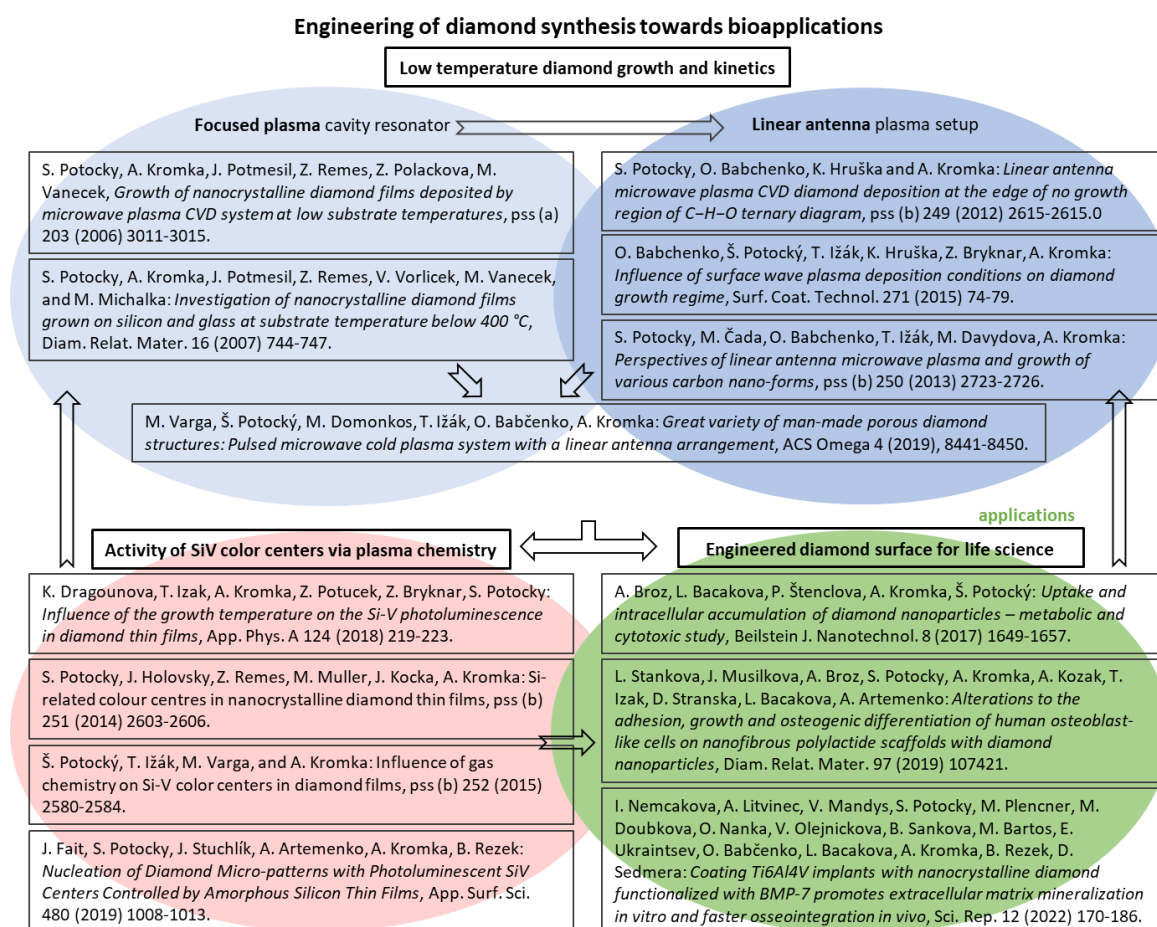


Fig. 1.1 Schematic visualization of the thesis composition grouped accordingly to common themes.

1.2 Objectives

The subject of this thesis is pushing the boundaries and related knowledge contribution in diamond microwave plasma-enhanced chemical vapor deposition (MW PECVD) technology which emerged from the needs of biomedical applications (low substrate temperature, large area, controlled contamination, and optical center fabrication). Still, we must keep in mind that diamond's dominance as the key element for functions is more due to its enabling capability than to its cost-effectiveness. The work followed the line of tailor-made diamond-based hybrid multifunctional nanomaterial research with the state of the art and technological readiness at the given time. The objectives were based on concepts of MW PECVD of diamond thin films for large-area biocompatible substrates having limited temperature resistance, diamond-based delivery systems, and optical imaging and sensing. The main objectives can be summarized as follows.

- Fabrication of nanocrystalline diamond films at low temperatures in sufficient quality.
- Understand the growth kinetics for low-temperature growth and the relation of process parameters with diamond film quality.
- New technological attainment for large and temperature-sensitive substrates during diamond deposition.
- Understanding the correlation between plasma conditions, process parameters, and diamond film characteristics in the linear antenna coaxial discharge chemical vapor deposition system.
- Expand the knowledge of direct optical centers fabrication in diamond grown by chemical vapor deposition, focusing on silicon-vacancy centers. Characterize such prepared optical centers and correlate their characteristic with deposition parameters.
- Prepare diamond structures and discuss crucial factors controlling cells' interaction with them.

Chapter 2

Diamond Synthesis and Challenges

Diamond exhibits unique mechanical, chemical, optical, and electrical properties that offer a wide range of use in physical and chemical science and opens up new possibilities in material science and in interdisciplinary cooperation where we allude to biomedicine and pharmacology [1,2]. If we start from the carbon phase diagram [3], the first and, in this case, the natural way of diamond formation is the phase transformation from liquid carbon under conditions of sufficiently high pressure. Such conditions occur in the Earth's mantle and are consequently the source of natural diamonds in many known areas [4]. If we were not limited to the occurrence of diamonds on Earth, the sources would be much richer [5] and more surprising – planets made of diamond [6].

We cannot face this competition, and therefore we will limit ourselves to man-made diamond. From the point of view of synthetic diamond production, there are three basic methods that we will conceive. Remembering the carbon phase diagram, the main challenge in the synthesis of diamond is its metastability.

2.1 HPHT synthesized diamonds

The oldest synthetic diamond production method dates back to the 1950s [7] and is based on imitating the natural process under high pressure and high temperature (HPHT) conditions. It uses existing diamond seeds on which liquid carbon recrystallizes due to the presence of a metal catalyst and HPHT conditions. Recent developments show the possibilities of preparing diamonds without catalysts, enabling the preparation of optically active centers in diamonds [8] and increasing crystal size. In February 2022, the International Gemological Institute reported the analysis of a 30 g (150.42 ct) diamond single crystal measuring $28.55 \times 28.25 \times 22.53$ mm³. Nevertheless, the fundamental limitations of this method still include the crystal size typically reaching units of mm, the presence of impurities, especially metallic inclusions and nitrogen from the surrounding atmosphere, high surface roughness, and the impossibility of preparing a diamond on foreign substrates or surface geometries. From the point of view of

biological applications, HPHT preparation of nanodiamonds has the advantage of reduced toxicity [9].

2.2 Detonation nanodiamonds

Detonation nanodiamonds (DND) prepared by the method discovered in the sixties during the development of explosive technologies in the synthesis of superhard materials [10] are of great interest. In this process, a diamond is created with a typical grain size of ≈ 5 nm, resulting in subsequent uses and limitations. The driving force behind the research is mainly biomedical use [11] despite unceasing discussions regarding the consequences of the accumulation of such nanoparticles in the body. The limitations of high-purity synthesis with optical centers are gradually being overcome [12] when the incorporation of color centers other than nitrogen-vacancies into DND is currently desired for cutting-edge bioimaging techniques. An example is the discovery of the direct synthesis of DND with silicon-vacancy centers [13]. Diamonds prepared in this way have apparent limitations in the area (grain size), substrate overcoating, purity, and the presence of non-diamond phases on the surface. For biological applications, morphological differences with other methods producing single-digit nanodiamonds are shown [9].

2.3 Chemical vapor deposited diamonds

The breakthrough in diamond synthesis limitations was overcome by the invention of the chemical vapor deposition (CVD) technique, in which a diamond is deposited on a substrate from a hydrocarbon gas at reduced pressure and temperature, in contrast to the HPHT process. The method was developed in the seventies and eighties of the twentieth century. It is based on the crucial role of atomic hydrogen as a driving force for the decomposition of hydrocarbons (also preventing polymerization), creating active radical sites on the substrate surfaces, much faster etching of non-diamond bonded carbons than sp^3 bonded carbon, and last but not least terminating the diamond surface for surface passivation [14]. The requirement for the presence of hydrogen as a growth factor was later revised by the discovery of the possibility of diamond growth from C_2 dimers [15].

From the point of view of the aforementioned limitations, the CVD of diamond brought the possibility of preparing thin layers at a typical process temperature below 1000 °C on a diamond, but especially on non-diamond substrates. Another advantage is the

controllable purity when we can prepare diamonds of the highest purity (type IIa) due to the vacuum tightness of the system and free of contamination from used gases. This results in subsequent possibilities of controlled doping of the prepared diamonds.

The process procedure can be classified by reactant gases, energy supply for activation, and temperature and density distribution. The most prominent carbon source is methane, while hydrogen, oxygen, and argon are critical components in gas phase chemistry. According to the production of diamond growth species, CVD processes can be classified into two major groups. The first consists of systems based on thermal-induced gas activation, most abundantly represented by hot filament CVD. The second group consists of systems based on electromagnetic excitation where microwave (MW) plasma-enhanced CVD plays the most important role. A more detailed classification, including details of individual implementations, can be found in the publication [16].

The hot filament CVD can be modified from the deposition of planar to complex geometry substrates, while the filament assembly is capable of upscaling. The major drawbacks are the incorporation of the filament material into the films during deposition, limited usage of oxygen-containing gases, narrow range of growth temperatures, and filament instability during the CVD.

The second group of diamond preparation technology, MW PECVD, is based on electromagnetic wave absorption, where we will focus on the most common variant of MW cavity reactors [17]. The resonator chamber and the absorption conditions result in a stable plasma that can produce a wide variety of diamond film morphologies.

Even though MW PECVD is popular and considered the only reliable method of preparing electronic grade quality diamond films, the deposition area and temperature of the substrate were still limiting factors. The solution was a modification of the surface wave sustained discharges in the coaxial structure [18] capable of a greater plasma volume [19]. For the deposition processes, it is moreover necessary to know the chemical composition, plasma state, molecule fraction, and temperature above the substrate. However, these parameters are unknown in many cases due to the highly technical requirements and the dependency on the layout.

Chapter 3

Low-temperature diamond growth and kinetics in focused MW plasma ellipsoidal cavity resonator

This chapter addresses a closely related topic of low-temperature diamond growth in a MW cavity reactor system represented by an ellipsoid cavity developed at the Fraunhofer Institute [20]. This chapter is based on the author's works [21–24], two of which are included in the thesis Appendices A.1 [24] and A.2 [23]. As part of my research, I had to solve the problem of the relationship between deposition temperature, pressure, MW power, and the design of the sample holder for controlled heat removal in relation to the properties of the prepared diamond layers. In this regard, it was possible to cover a standard microscope glass with a thin layer of diamond without subsequent damage to the layer due to internal stress.

Standard MW PECVD of polycrystalline and/or nanocrystalline diamond thin films and membranes takes place at substrate temperatures 700–900 °C [16]. Such a high temperature limits a family of suitable substrates. The deposition of diamond on temperature-sensitive substrates like glass, metals, piezo crystals, or microelectronic devices requires a decrease of the substrate temperature to 400 °C or less while keeping the excellent material properties of diamond. Why glass substrate was of concern is due to its usage in biomedicine but also in electronic devices where various types of glass are used, which differ by their bulk properties. Diamond surface is used either as a passive functional material for immobilizing various biomolecules or as an electrically active part of the biosensing element [25]. In the case of diamond deposition, particularly thermal expansion coefficient, softening point, annealing point, and strain point are important [21].

Generally, the diamond growth from $\text{CH}_4\text{-H}_2$ gas mixture is based on methyl radicals [16]. At low-temperature processes, the unwished development of non-diamond phases can be minimalized either via lowering the concentration of carbon source and hence lowering deposition rate or by using substituted chemistry based on partial replacing of hydrogen gas by oxygen (or halogen). Furthermore, the growth of nanocrystalline

diamond (NCD) film mostly requires the addition of other gases like nitrogen or argon [26]. Argon-based growth seemed to be a promising technique, where C₂ dimers play a dominant role in the sufficient re-nucleation process at low activation energy. Changes in chemistry result in the growth of ultra-nanocrystalline diamond (UNCD) films at low temperatures (400 °C). However, the final optical quality of these films is degraded due to the incorporation of a relatively high amount of non-diamond phases [26].

We studied NCD thin film deposition in MW PECVD on silicon and glass substrates from hydrogen/methane gas mixture in the wide temperature range from 1100 to 370 °C. Process parameters were correlated by the kinetic of the process, and resulting film chemical and optical quality, and morphology.

The diamond character of samples was confirmed by Raman spectra [23] corroborated by the calculated refractive index independent of the substrate temperature. The surface morphology of NCD films on glass showed homogenous surface morphology with surface roughness less than 10 nm and crystal size of up to 60 nm at the lowest substrate temperature (370 °C). Fully closed NCD films of very low thickness is possible due to high nucleation densities as long-term time-optimized research strand [27]. Figure 3.1 shows typical transparency/reflectance spectra from the NCD layer deposited on glass. The surface scattering decreases with decreasing film thickness, and the optical roughness is reduced below 10 nm for thin films grown typically at temperatures below 400 °C, confirmed by AFM measurements. Based on Jacob and Unger [28], we concluded from the Fourier-transform infrared measurements that the total content of bounded hydrogen over our films is below 10²¹ cm⁻³, i.e. less than 1 at. % as observed for the whole studied temperature range. The quantitative percentage of the sp³ hybridized carbon atoms was above 90 % in the analyzed volume of the NCD films evaluated by XPS [21].

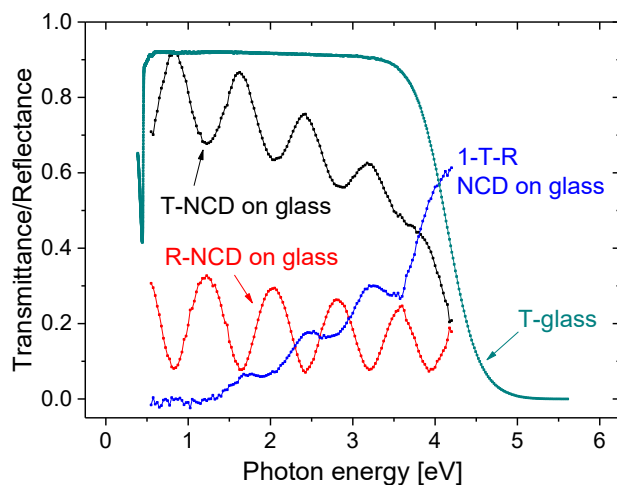


Fig. 3.1 Transmittance and reflectance spectra of a 320 nm thick NCD film deposited on a glass substrate [24].

To expand the knowledge about low-temperature process in the ellipsoidal resonator system, the chemical kinetic of NCD growth was evaluated by the activation energy of the process, E_a . Nearly a linear relationship is observed in the investigated temperature range. The growth rate monotonically decreased from 620 to 10 nm/h with substrate temperature decrease from 1100 to 370 °C.

The success of high-quality NCD layers opened a new research strand of low-temperature NCD depositions on temperature-sensitive substrates like least resistant soda-lime glass slides used in biology and medicine.

Though the growth of smooth and very thin fully closed NCD films was enabled on temperature-sensitive substrates, we had to admit technological limitation by the ellipsoid resonator system, respectively plasma ball size. The typical homogenous limit of 2" diameter substrates was pushed by process parameter optimization to its limit. Moreover, no more than one substrate per deposition is possible to be overcoated. Under these conditions, instead of studying the possibility of further optimization of the process by changing the gas mixture composition (addition of oxygen), we decided to adopt [29] a large-area deposition system, however, designed for the deposition of nitride layers for solar cells.

Chapter 4

Plasma chemistry and growth kinetics at low pressure in MW plasma with linear antenna setup

This chapter continues the story of large-area and low-temperature diamond growth in a MW coaxial discharge reactor system represented by a linear antenna MW PECVD system. We addressed the point of gas and plasma conditions for successful deposition not only of diamond films but other carbon allotropes. This chapter is based on the author's works [19,30–34], four of which are included in the thesis Appendices A.3 [34], A.4 [30], A.5 [33], and A.6 [19]. As part of my input, I had to solve the problem of the growth kinetics in a working gas mixture with a high oxygen concentration for diamond. It paved the road to diamond film's controlled morphology, resulting in the direct growth of porous structures without a template.

Based on the promising results of Japanese research groups, it was experimentally showed the ability to grow thin diamond films over an area of $200 \times 300 \text{ mm}^2$ by the modified commercial linear antenna pulsed MW PECVD process from the $\text{CH}_4\text{-H}_2\text{-CO}_2$ gas mixture [35]. Nevertheless, it has been pointed out that the conditions for diamond growth are different in each type of depositional system, from which we focused on the influence of working gas composition and pressure on plasma characteristics and growth kinetics.

The role of oxygen in the precursor gases is generally accepted to increase growth rate and/or to improve the diamond film quality. However, the use of oxygen is very limited and summarized by the narrow area in the C/H/O-gas-phase compositional diagram [16]. We experimentally proved the enlargement of deposition area thought to be limited alongside $\text{C}/(\text{C}+\text{O}) = 0.5$ tie-line to the value of 0.385 as seen in Fig 4.1 [34]. Contrary to typical growth parameters, diamond coatings were grown from a gas mixture of methane in hydrogen (up to 20 % in H_2) and carbon dioxide (up to 80 % in H_2), moreover at reduced substrate temperatures (550 °C).

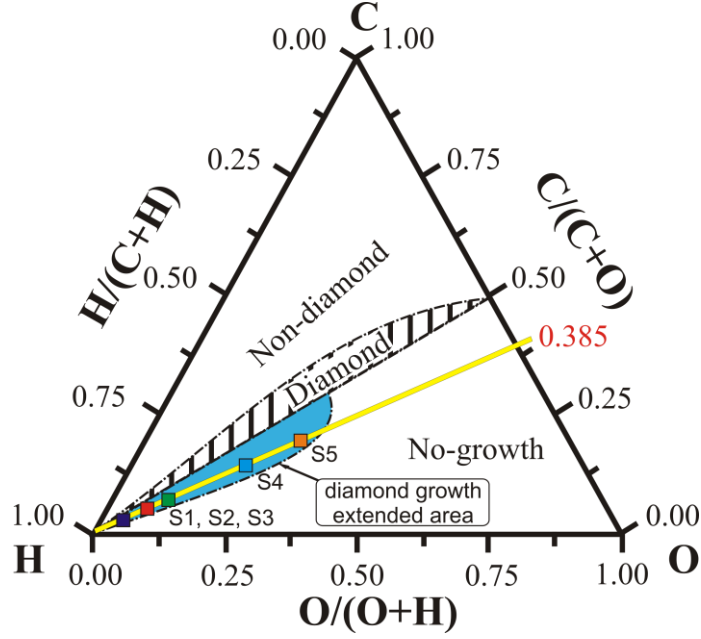


Fig. 4.1 The modified C/H/O feed gas compositional ternary diagram with an enlarged diamond region (hatched and blue area) alongside 0.385 C/(C+O) line [34].

Raman spectra confirmed the diamond character of all deposited layers. Not only the ability to deposit the diamond films but the changes in the morphology are of importance. We are able to tune it by plasmochemistry changes to obtain the diamond grains in sizes from 20 nm to 150 nm. With the extreme CH_4 and CO_2 concentrations (20 %, resp. 80 % in H_2), a drastic morphology change dominated by diamond nanorods, as confirmed by Raman measurement. Moreover, the nanoporosity of such film was confirmed [19].

Another growth transition effect was observed for fixed gas mixture composition. The transition between large grain lateral-like growth regime to a small crystal size growth regime was observed in the pressure range of 6–100 Pa [33]. In addition, the influence of distance from antennas to the substrate (close \equiv 40 mm, far \equiv 70 mm) was also studied [30]. Depending on the process pressure, we identify two main diamond growth regimes. The so-called re-nucleation regime (>50 Pa) led to the growth of diamond crystals (<50 nm). On the other hand, the larger diamond crystals (grains up to 400 nm) were formed at low-pressure processes (below 10 Pa) and are attributed to the dominance of lateral growth. To understand the transition between growth regimes, we analyzed plasma parameters by Langmuir probe (Fig. 4.2) and hydrogen concentration by optical emission spectroscopy (Fig. 4.3).

Figure 4.2 shows plasma density N_e and effective electron temperature T_{eff} (i.e. mean electron energy in a unit of $k_B \times T$) as a function of total gas pressure and distance from the antenna during diamond depositions. It is evident that with increasing pressure, the

N_e decreases. For the substrate localized at 70 mm, it means a drop of N_e by three orders of magnitude within the range of 10–150 Pa. Approaching the plasma source (antenna), the drop of N_e is decreased (one or two orders of magnitude for 10–150 Pa pressure drop with respect to the 16 and 33 mm distance from the antenna). In the close vicinity to the antenna and for the lowest pressure, the T_{eff} reaches the value of 4.5 eV and exponentially drops with increasing pressure. For higher distances, the value of T_{eff} drops by 2 eV and saturates at the value of $T_{\text{eff}} \approx 1.2$ eV for pressures >50 Pa.

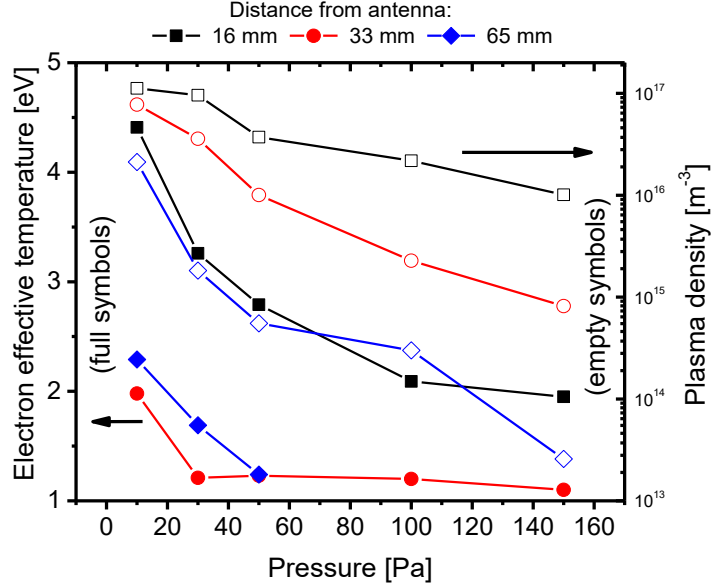


Fig. 4.2 Plasma density and electron effective temperatures as a function of total gas pressure p and distance from the antenna [33].

The Langmuir probe measurements were also used to evaluate plasma and floating potentials with the studied pressure range confirming that $(U_{\text{pl}} - U_{\text{fl}})$ is smaller for larger distances from antennas. Thus, enabling control of substrate power loading by ion bombardment. Observed U_{pl} drop at 50 Pa indicates higher ion energy at lower pressures supporting higher crystallinity and grain size of grown diamond films.

The actinometry measurement supported the recombination model for hydrogen in CVD at high pressures, i.e. the recombination rate of atomic hydrogen increases, thus its concentration decreases. On the other hand, at low pressures, the plasma density and thus species concentration is low. The maxima of $\text{H}_\alpha/\text{Ar}$ line intensity were found together with its shift to lower pressures for farther distances from the plasma source (Fig. 4.3). The results were corroborated by growth rate dependence. It seems that further approaching of the samples towards the antennas will approximate the process conditions to focused plasma systems, and its advantages will be lost.

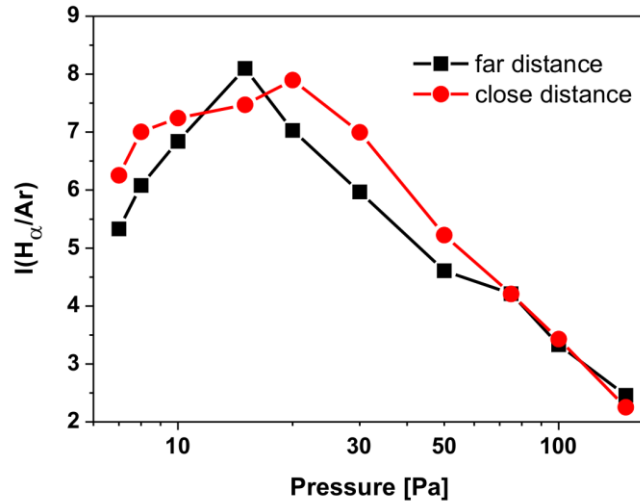


Fig. 4.3 The evaluation of hydrogen amount in the chamber as calculated from emission spectra ratio of H_α line (656.3 nm) intensity to Ar line (750 nm) intensity as the function of pressure [30].

These results show that the linear antenna MW PECVD system enables low power loading of the substrates during the CVD growth. Further process parameters tuning enables diamond growth at temperatures <250 °C [31].

By combining achieved results, knowledge of advanced nucleation and seeding methods [32], many hours of additional experiments and their analysis, we explored the potential of the linear antenna MW PECVD system for the deposition of a great variety of man-made porous diamond structures [19].

Plasmochemically driven growth of porous diamond at the substrate temperature of 350–650 °C was successfully shown. The evidence of the plasmochemical effect for the growth is clearly demonstrated in the cross-sectional view of the diamond sandwich structures (UNCD/dendrite-like/NCD), especially in a two-layer compartment of the dendrite-like diamond film on a rough microcrystalline diamond film (Fig. 4.4). It is evident from the cross-sectional SEM images that the dendrite-like growth is not disturbed (influenced) by the base microcrystalline diamond layer.

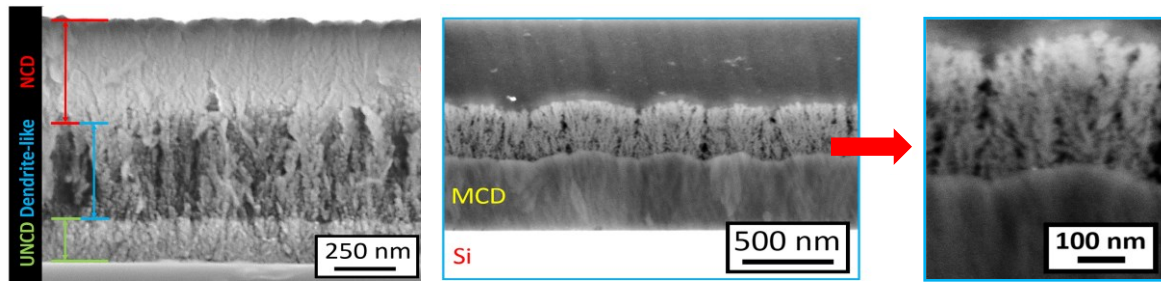


Fig. 4.4 Cross-sectional view of the diamond sandwich UNCD/dendrite-like/nanocrystalline structure (left), and the microcrystalline (MCD)/dendrite-like diamond structure with the detailed zoom (right) [19].

With the diamond bio-imaging potential [36] and the ability to grow diamond over large areas, we were attracted to the idea of combining periodic structures, such as two-dimensional photonic crystals, with the diamond as a source of light.

Chapter 5

The controllable activity of silicon-vacancy color centers in diamond films via plasma chemistry

Within this chapter, we present our contribution to the capability of monitoring the molecular machinery in living systems and sensing and quantum light sources. In this regard, the negatively charged silicon-vacancy (SiV) color centers are produced directly during diamond growth. To the other common SiV center fabrication technique by ion implantation, we address the technological challenges of introducing color centers during diamond growth. Specifically, the cases of the ellipsoidal cavity and linear antenna deposition systems correlated with process parameters and the outlook to nanoscale dimensions. This chapter is based on the author's works [37–41], four of which are included in the thesis Appendices A.7 [37], A.8 [41], A.9 [40], and A.10 [39]. As part of my activities, I had to solve the problem of the Si doping source in a quartz bell jar reactor concerning the process parameters, mainly gas pressure and electromagnetic field distribution. In this regard, it was possible to use robust doping from a solid source, and by proper tuning of gas composition control the activity of fabricated color centers in diamond.

The long-dreamed-of capability of monitoring the molecular events in cells has not been realized yet, mainly due to the technical limitations of current sensing technologies. Emerging photostable quantum sensors like nitrogen-vacancy optical centers in diamond are showing great promise for molecular detection and imaging [42]. Atomic-sized quantum emitters can quantitatively measure nanoscale electromagnetic fields via optical means at ambient conditions. In contrast to nitrogen-vacancy centers, SiV centers concentrate their photoluminescence (PL) into a narrow, 100 nm redshifted intense zero phonon line (ZPL), even at room temperature. Though biological tissue has the first optical window in the range of 650–950 nm, the usage of SiV centers having ZPL at 738 nm decreases autofluorescence as well as absorption due to typical tissues [43]. The PL properties of color centers near the surface are sensitive to surface termination because their electron levels are affected by the position of the Fermi level. Due to the

carbon-carbon bonds, diamond can be easily modified with a wide range of functional groups [44]. The combination of such properties and the existence of SiV PL in diamond particles <10 nm make them attractive candidates for photostable fluorescent biomarkers in life sciences [27,45]. In simplicity, we can claim that due to the carbon compatibility with living organisms, the problem of ensuring biocompatibility and low cytotoxicity, elaborated in more detail in Chapter 6, is eliminated [46].

The paper [41] represents the first insight into a controllable method for preparing SiV centers in NCD for both MW PECVD systems discussed in Chapter 3 and Chapter 4. We focused on the source of Si doping in the case of an ellipsoidal resonator where the bell jar wall was identified as the source due to the local maxima of the electrical field strength and process parameters during diamond deposition. We have to admit that such a "contamination" was detected previously [47], but it was not understood as a feature of the system that created optically active centers in diamond. Nevertheless, later on we utilize a similar approach when clean Si substrates are introduced as a source of Si atoms [27]. On the other hand, the linear antenna deposition system allows the preparation of diamond layers with no detectable SiV PL and hence opens the way for sandwich or diamond microstructures with and without SiV PL areas. The question regarding the in situ deposition of diamond layers with and without SiV PL was the subject of research following work [40]. The SiV ZPL intensity was studied in nano- and micro-crystalline diamond films deposited by MW PECVD ellipsoidal cavity resonator system as a function of substrate temperature and gas composition. The gas composition was studied with respect to CO₂ and N₂ concentrations by which, as discussed in Chapter 3, quality and morphology in diamond film can be induced and controlled. The PL spectra of the ZPL SiV was studied in a broad substrate deposition temperature range of 450–1100 °C [37]. Increased intensity, observed for the deposition temperatures within 650–800 °C, is attributed to increased diamond phase content and the vacancy motion through the NCD film. Figure 5.1 shows the strong sensitivity of SiV PL to gas composition. With a small addition of CO₂ or N₂ into the gas mixture, the SiV ZPL intensity gradually decreased. It vanished for admixtures of more than 1% and 2.5% of CO₂ and N₂, respectively. Moreover, the morphology of the diamond films with active SiV centers was insensitive to the CO₂ admixture. In the case of nitrogen addition, the diamond film morphology changed from micro- to nanocrystalline structure still revealing active SiV centers. In all cases, no shift of the ZPL was observed.

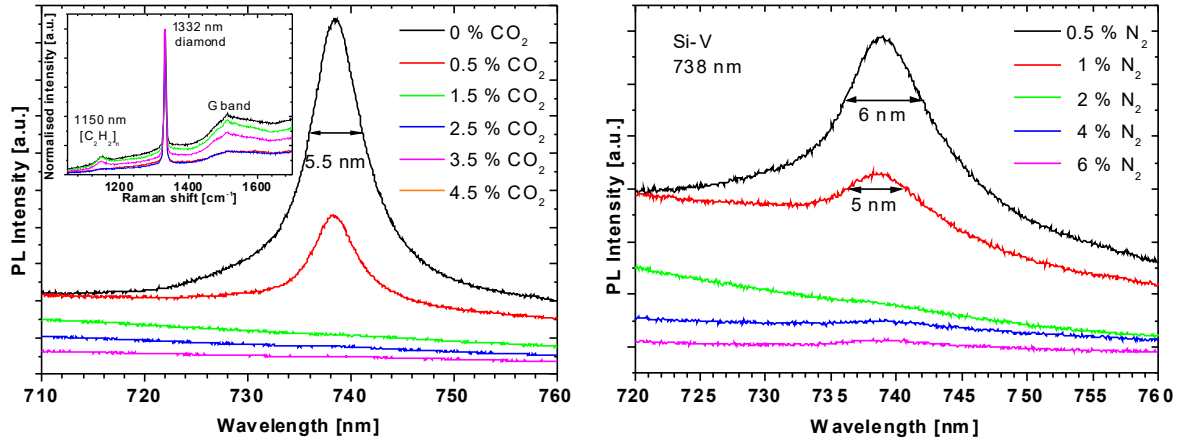


Fig. 5.1 Photoluminescence emission spectra and Raman spectra (inset) of the diamond films as a function of (left) CO₂ addition and (right) N₂ addition to the H₂/CH₄ gas mixture [40].

These experiments indicate that a gradient intensity of SiV color centers within the diamond film can be prepared by precise control of the gas mixture and still keeping good enough film quality and morphology. Using this strategy, sandwich-like structures consisting of optically active and not active SiV centers can be fabricated. Moreover, micro- or nanocrystalline diamond character can be tailored by the gas admixture while keeping the optical activity of the SiV centers.

The correlation between the integral intensity of ZPL of the SiV center PL and the quality of the diamond film reveals the key role of the diamond carbon phase [37]. The detailed temperature development of the PL emission spectra for the selected deposition temperature (800 °C) is shown in Fig. 5.2. The ZPL narrowing from FWHM = 123 cm⁻¹ (~6 nm) to FWHM = 40 cm⁻¹ (~2 nm) was observed for a temperature decrease from 300 to 11 K, respectively as a result of the T^3 dependence expressing the homogenous broadening determined by vibrations of the perturbed host lattice. Additionally, the blue shift by 29 cm⁻¹ (~1.5 nm) in the ZPL position from room temperature to 11 K follows the $T^2 + T^4$ polynomial dependence and is explained as effects of lattice contraction and weakening of the strength of electron-phonon coupling.

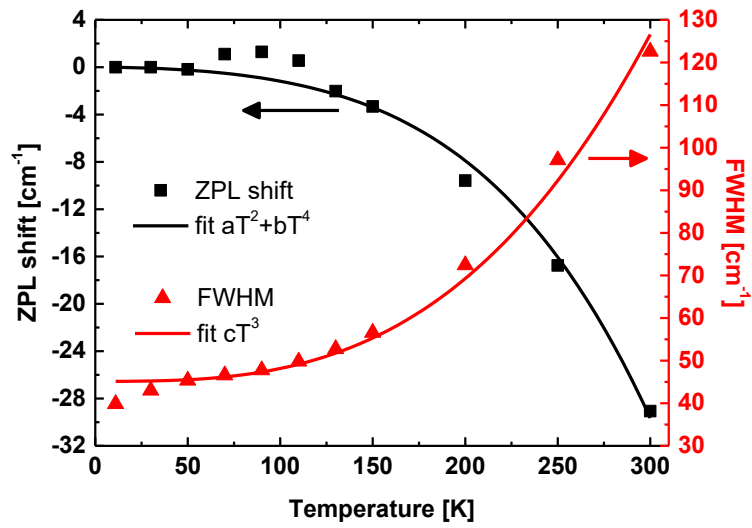


Fig. 5.2 The SiV ZPL peak position (full symbols) and FWHM (empty symbols) as a function of temperature obtained under excitation by 442 nm line of He-Cd laser for NCD film deposited at 800 °C. The ZPL shift is referred to the ZPL position at 11 K that is 736.6 nm [37].

To support the biomimetic behavior of fabricated material specific topography effects on cellular behavior are known and must be taken into account. In our contribution [39], we advantageously used the minimization of spontaneous parasitic nucleation by structured amorphous silicon film. By patterning the amorphous silicon layer with photolithography, highly selective growth of nanocrystalline diamond with optically active SiV centers was achieved even at relatively low substrate temperatures (430 °C). The suppression of diamond nucleation attributed to surface disorder on an atomic scale does not depend on the substrate materials below the hydrogenated amorphous silicon studied (Si, SiO₂, Pt, Ni) and can be used for commercial materials in biomedicine.

Chapter 6

Engineered diamond surface for life sciences – from nanoparticles to three-dimensional diamond coatings

The last piece in the puzzle of this thesis is the intersecting line of bioapplications of diamond structures. Diamond thin films or (nano-)particles have become very attractive and promising materials. Constantly evolving disciplines such as nanotechnology and biomimetics are making significant advances, and in materials science and biology could contribute significantly. The chemical properties of diamond enable surface tailoring for specific biological purposes, such as electrical stimulation of neurons, regenerative medicine, and also for tissue engineering, which is used as an example of diamond bioapplication in the presented thesis. This chapter provides insight into three cases representing nano- to micro-scale unique structural, physiochemical, and functional features and their interaction with living matter. This chapter is based on the author's works [46,48–51], three of which are included in the thesis Appendices A.11 [48], A.12 [51], and A.13 [50]. As part of my contribution, I had to solve the issue of diamond nanoparticle aggregation and distribution in a polymer matrix. Similarly, for nonwoven samples, I had to prepare disaggregated nanodiamond polymeric solution of certain viscosity suitable for needleless electrospinning with variable weight concentration of diamond. In the *in vivo* study, I was responsible for diamond coating over three-dimensional cortical metal screws and the diamond layer adhesion. Initial adhesion problems were eliminated by optimizing deposition process conditions.

According to publication outputs and volume production, nanodiamonds (NDs) are diamonds' most studied structural form for bioapplications. Nanodiamonds refers to diamond particles with sizes from a few to nearly 100 nanometers. Among bulk properties, they incorporate distinct nanomaterials properties, like the nano-size, quantum-size, quantum tunneling, and surface/interface effects [52]. Nanodiamonds are generally accepted as the most biocompatible nanoparticle in the carbon family. Studies on the cell cytotoxicity of NDs in the cellular model [11] paved the way for the

bio/medical applications of NDs, where we contributed by a metabolic and cytotoxic study of NDs origin (HPHT and detonation), crystal size, and surface treatment [48]. The mitochondrial activity and the cell nuclei count of the human osteoblastic cell line were used as an indicator of the material cytotoxicity. The most pronounced toxicity effect is attributed to particle surface modification, as shown in Fig. 6.1.

Detonation NDs have a positive zeta potential, characteristic of hydrogenated NDs. In their as-received state, they reduced the viability of the cells by >80 % after 3 days of cultivation. However, when such NDs were oxidized (annealed in the air), their toxicity was reduced by 30 %. This effect could still be observed after 7 days of cultivation. On the other hand, no significant toxicity of oxidized samples was measured. This positive effect can be attributed to the fact that the mechanism of the NDs uptake was clathrin-mediated endocytosis, a physiological cellular mechanism for the internalization of various bioactive substances from the extracellular environment. Different oxidized NDs types revealed no apparent difference evaluated by Fourier-transform infrared spectra corroborated by the negative zeta potential measurements, typically in the range of -20 to -40 mV.

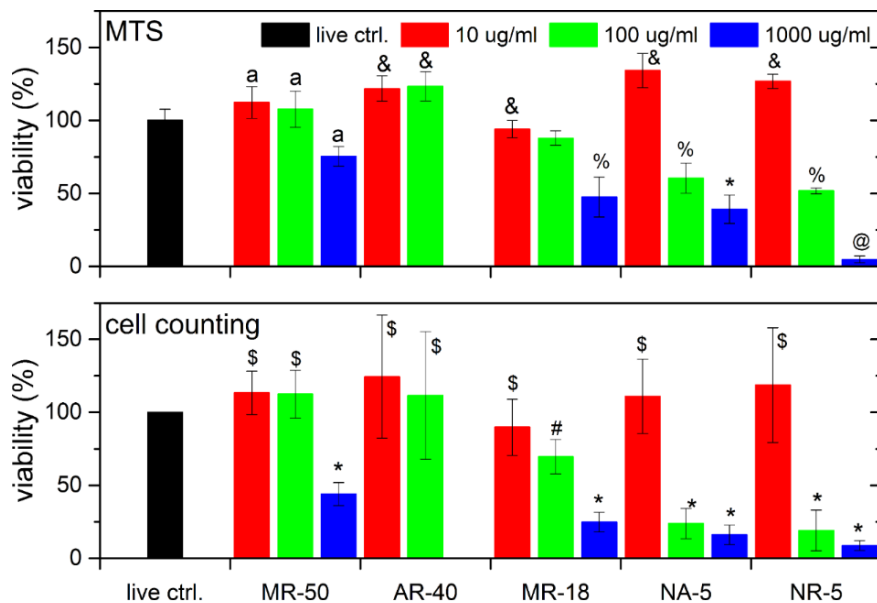


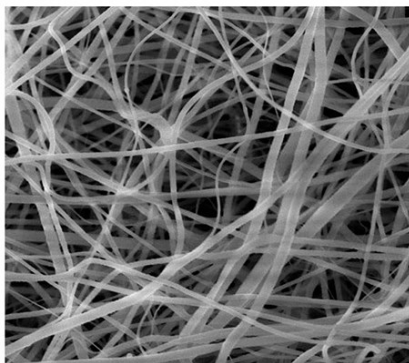
Fig. 6.1 Viability of SAOS-2 cells incubated with nanodiamonds for three concentrations as a function of nanodiamond type and surface treatment after 7 days. (upper row) results of the mitochondrial metabolic activity test assay; (lower row) results of cell counting after nuclei staining [48].

Live-cell imaging showed DND aggregation, accumulation on cell surfaces and their endocytoses. The accumulation and the cytotoxicity of the DNDs in the cell depend on their surface termination. Cells with as-received hydrogenated DNDs reveal rapid uptake of NDs by the cells. The cells are soon congested by the nanoparticles causing rapid

viability drop, and before the end of the experiment, more than half of the cells are dead. An expelled cytoplasm can be seen exiting the cell membrane in at least one or two cases of cell death. This indicates uncontrolled cell death and rupture. The remaining living cells have an elongated shape due to the accumulated NDs, which mechanically restrain their spreading and migration. In the case of the air-annealed DND, i.e. oxygen terminated, formed aggregates are not taken up by the cells as rapidly as their non-annealed counterparts. Most of the cells survive the whole experiment.

Another potential of NDs is as a filler of polymer matrix in cell growth scaffolds for tissue engineering. NDs are introduced into fibers to harness their chemical and mechanical properties [53,54]. The incorporation of NDs into the matrix of poly(vinyl) alcohol suppressed the polymer dynamics and improved the mechanical properties of the composite [55]. Composite nanofibrous membranes of the copolymer of L-lactide and glycolide (PLGA) with NDs showed higher mechanical resistance and promising substrate properties for bone tissue engineering [56]. In the study [51], poly(l-lactide) (PLLA) nanofibrous membranes reinforced with DNDs were prepared by a needle-less electrospinning process and tested *in vitro* using two human lines of osteoblast-like cells, MG-63 and Saos-2 (see Fig. 6.2).

**(PS) Control, (1) 0 wt.%,
 (2) 0.44 wt.%, (3) 0.87wt.%,
 (4)1.72 wt.%, (5), 3.38wt.%,
 (6)6.54 wt.%, (7) 12.28 wt.%**



Cell
 growth
 →

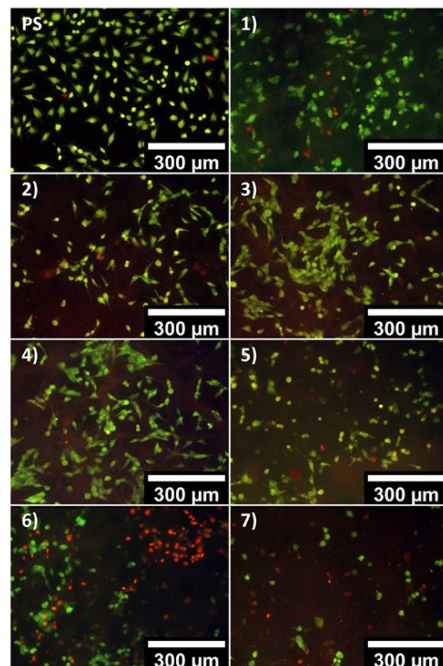


Fig. 6.2 Filling rate of NDs and an illustrative morphology of nanofibrous PLLA scaffolds (left), and morphology and viability of human osteoblast-like cells MG-63 (right) on day 3 after seeding in standard cell culture polystyrene wells (PS) and on PLLA nanofibrous scaffolds with increasing concentrations of NDs [51]. Live cells are stained in green, and dead or dying cells are stained in red.

In general, we can see a decrease in the mRNA expression of all studied markers of osteogenic cell differentiation at the highest NDs concentration (12.28 wt %). Similarly to NDs study [48], we conclude that the usage of as-received DND in the PLLA nanofibrous scaffolds has a damaging effect on the viability, proliferation, and mitochondrial activity of human osteoblast-like MG-63 and Saos-2 cells used in this study. Apart from the discussed gene expression and specific cell markers regulation, adhesion, and differentiation at the mRNA level, we supported the results by evaluating PLLA-ND scaffolds hydrophobicity which increased with increasing NDs concentration. The water drop contact angle ranged from 45° to 139°. In contrast, in PLGA scaffolds in an earlier study, the maximum angle of water drop contact was 70°, which can be considered a moderate level of hydrophilicity, optimal for cell adhesion and growth [56]. In accordance with current trends, biomaterials used as innovative coatings are being studied to increase the biocompatibility of substrates or implants. New types of materials such as polymer composites with diamond nanoparticles, soft polymeric substrates, self-standing diamond structures, diamond-like composites, carbides, and metal oxides seem to be promising candidates for new biomaterials for further enhancement of functionality and an increase in biocompatibility [57]. Optimization of hierarchically organized micro and nanostructures, as well as their chemical properties and wettability of surfaces, is essential in biomaterials [58]. In order to improve their interaction with the cells, these biomaterials can be further functionalized with atoms, molecules or large biomolecules (proteins, DNA, etc.). Tissue engineering can benefit from diamond's high mechanical resistance, chemical inertness, and biocompatibility, especially for designing bone implants, which tend to be heavily mechanically stressed. However, there is a significant risk of releasing small parts of the material into other patient tissues, causing severe inflammatory reactions and other adverse effects [12,49]. These postoperative complications could be significantly reduced or eliminated using an adequately designed diamond-coated bone replacement.

We investigated the effect of an oxidized NCD coating functionalized with bone morphogenetic protein 7 (BMP-7) on human osteoblast maturation and extracellular matrix mineralization *in vitro* and on new bone formation *in vivo* [50]. The Ti₆Al₄V plates and cortical screws were coated with a thin NCD film in linear antenna MW PECVD at the substrate temperature of 450 °C. To fully encapsulate the substrate, deposition was repeated twice for the top and the bottom part of the screws. A part of the samples coated with oxidized NCD was further functionalized with BMP-7 lying on the diamond surface, forming a uniform coating of only 2 nm. Typical material and morphological characteristics of the NCD-coated cortical screws Fig. 6.3(a) is shown in

Fig. 6.3(b)-(f). Raman spectroscopy and surface mapping show a uniform coating by NCD and corrugated morphology conforms to the screw surface finish. SEM confirmed fine nanostructures related to the NCD grains in both critical areas along the thread and the screw tip. The effect of oxygen NCD coating and further functionalization with BMP-7 on the maturation of human osteoblasts was first studied *in vitro*, later also by *in vivo* showing no adverse effect of an oxidized NCD with good long-term stability and tolerance, and the possibility of functionalizing this oxygen NCD coating with BMP-7 protein, resulting in a considerable increase in mineralization of the matrix *in vitro* and significantly faster osseointegration *in vivo*.

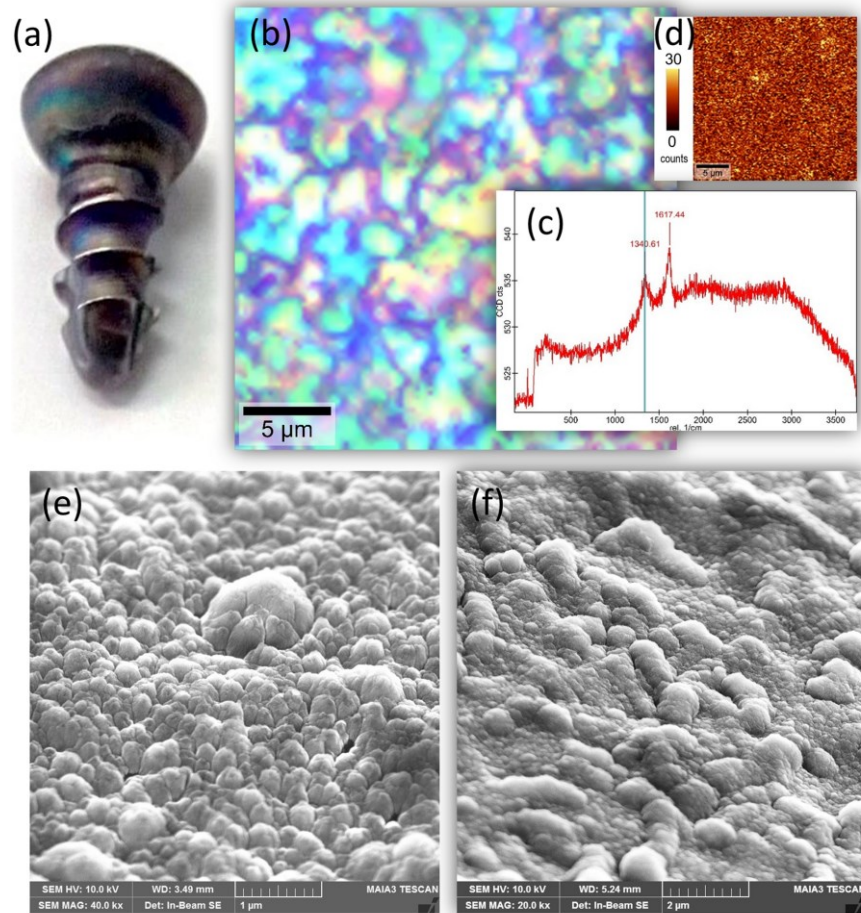


Fig. 6.3 Material and morphological characteristics of the nanocrystalline diamond-coated cortical screws: (a) a photograph of a coated screw, (b) bright-field optical microscope image, (c) Raman spectrum showing characteristic nanocrystalline diamond features, (d) a Raman diamond peak intensity map, (e) SEM image of the coated screw surface along the thread and (f) in the screw tip area [50].

Implants coated by nanocrystalline diamond, especially with further functionalization with bioactive molecules, can provide significant added value and medical benefits in clinical applications.

Chapter 7

Conclusion and future outlooks

Nowadays, constantly evolving disciplines such as nanotechnology and biomimetics are making significant advances in many scientific fields. The application of these disciplines in materials science and biology and in interdisciplinary cooperation among scientists could contribute significantly to the evolution of several medical disciplines, including orthopedics. Bone replacements are one of the most common reasons for surgery worldwide. The need for these surgeries is mainly associated with an aging society, lifestyle diseases, traffic, sport, and work accidents. Based on the above, in this thesis are summarized some of the activities in which I have participated with my colleagues and students, contributing to solving technological challenges and understanding events in the field of material engineering.

These are the main results that we have achieved:

- We have extended experimental studies of low-temperature diamond growth and kinetics in an ellipsoidal cavity resonator chemical vapor deposition system. With these optimized process parameters, high optical and chemical quality diamond films can be grown on temperature-sensitive substrates but still limited for potential applications by substrate area.
- We have revealed the correlation between plasma conditions, process parameters, and diamond film characteristics in the linear antenna coaxial discharge chemical vapor deposition system. With these optimized parameters, high-quality diamond films can be grown over large substrate areas.
- New plasma chemistry and growth kinetics at low temperatures resulted in the proposal of an updated diamond growth process area in the ternary C/H/O gas phase diagram based on experimentally observed phenomena resulting in direct porous growth of nanocrystalline diamond films.
- We have extended the knowledge of the influence of gas composition on SiV optical centers' controlled activity during diamond CVD. With this knowledge,

we have identified a mechanism that enables the chemically controlled fabrication of complex optical center photoluminescence diamond-based devices.

- We supported the understanding of the diamond surface role in the interaction with cells. This interface was found as a crucial factor for bone cell proliferation and osteointegration. These conclusions were based on the successful fabrication of three-dimensional diamond implants and composite scaffolds.

Most of our interactions with the physical world happen through various interfaces packed with sensors, receptors, transporters, and other components. Progress in biomedical research has highlighted the need for developing tailor-made bio-functional materials and interfaces with enhanced functionalities capable of sensitive and reliable operations over a broad range of living organisms-based conditions. I consider the following as my future perspectives for continued work with my colleagues and students on emerging topics:

- The development of tailor-made hybrid multifunctional nanomaterials using diamond-based and metallic materials.
- Combination of CVD with gas aggregation by cluster source magnetron sputtering for in situ nanoparticle fabrication.
- Biomedical-oriented diamond-based optical sensors not limited only to localized physiological species and action potentials.
- Diverse imaging methods and drug delivery systems which will employ nanoparticles with optimized structures and specific defects.
- Design a three-dimensional porous diamond-based scaffold to study interaction with cell cultures under various field stimulations.
- The development of advanced microfluidic systems for lab-on-chip devices.

Chapter 8

References

- [1] C.E. Nebel, D. Shin, B. Rezek, N. Tokuda, H. Uetsuka, H. Watanabe, *Journal of The Royal Society Interface* **4**, 14 (2007).
- [2] P.A. Nistor, P.W. May, *Journal of The Royal Society Interface* **14**, 134 (2017).
- [3] F.P. Bundy, *J. Geophys. Res.* **85**, B12 (1980).
- [4] F. Nestola, J.R. Smyth, *International Geology Review* **58**, 3 (2016).
- [5] T.L. Daulton, in: *Ultrananocrystalline Diamond*, Elsevier, 2006, pp. 23–78.
- [6] M. Bailes, S.D. Bates, V. Bhalerao, N.D.R. Bhat, M. Burgay, S. Burke-Spolaor, N. D’Amico, S. Johnston, M.J. Keith, M. Kramer, S.R. Kulkarni, L. Levin, A.G. Lyne, S. Milia, A. Possenti, L. Spitler, B. Stappers, W. van Straten, *Science* **333**, 6050 (2011).
- [7] F.P. Bundy, H.T. Hall, H.M. Strong, R.H. Wentorf, *Nature* **176**, 4471 (1955).
- [8] V.A. Davydov, A.V. Rakhmanina, S.G. Lyapin, I.D. Ilichev, K.N. Boldyrev, A.A. Shiryaev, V.N. Agafonov, *Jetp Lett.* **99**, 10 (2014).
- [9] Z. Chu, S. Zhang, B. Zhang, C. Zhang, C.-Y. Fang, I. Rehor, P. Cigler, H.-C. Chang, G. Lin, R. Liu, Q. Li, *Sci Rep* **4**, 1 (2015).
- [10] V.V. Danilenko, *Physics of the Solid State* **46**, 4 (2004).
- [11] E. Perevedentseva, Y.-C. Lin, C.-L. Cheng, *Expert Opinion on Drug Delivery* **18**, 3 (2021).
- [12] O.A. Shenderova, G.E. McGuire, *Biointerphases* **10**, 3 (2015).
- [13] Y. Makino, T. Mahiko, M. Liu, A. Tsurui, T. Yoshikawa, S. Nagamachi, S. Tanaka, K. Hokamoto, M. Ashida, M. Fujiwara, N. Mizuochi, M. Nishikawa, *Diamond and Related Materials* **112**, (2021).
- [14] P.W. May, *Phil. Trans. R. Soc. Lond. A* **358**, 1766 (2000).
- [15] O. Auciello, A.V. Sumant, *Diamond and Related Materials* **19**, 7–9 (2010).
- [16] M. Schwander, K. Partes, *Diamond and Related Materials* **20**, 9 (2011).
- [17] F. Silva, K. Hassouni, X. Bonnin, A. Gicquel, *Journal of Physics: Condensed Matter* **21**, 36 (2009).
- [18] S. Letout, L.L. Alves, C. Boisse-Laporte, P. Leprince, *J. Optoelectron. Adv. Mater.* **7**, 5 (2005).
- [19] M. Varga, Š. Potocký, M. Domonkos, T. Ižák, O. Babčenko, A. Kromka, *ACS Omega* **4**, 5 (2019).
- [20] M. Fünér, C. Wild, P. Koidl, *Applied Physics Letters* **72**, 10 (1998).

- [21] T. Izak, O. Babchenko, S. Potocky, Z. Remes, H. Kozak, E. Verveniots, B. Rezek, A. Kromka, in: O.A. Williams (Ed.), RSC Nanoscience & Nanotechnology, Royal Society of Chemistry, Cambridge, 2014, pp. 290–342.
- [22] A. Kromka, Š. Potocký, J. Čermák, B. Rezek, J. Potměšil, J. Zemek, M. Vaněček, *Diamond and Related Materials* **17**, 7–10 (2008).
- [23] S. Potocky, A. Kromka, J. Potmesil, Z. Remes, V. Vorlicek, M. Vanecek, M. Michalka, *Diamond and Related Materials* **16**, 4–7 (2007).
- [24] S. Potocky, A. Kromka, J. Potmesil, Z. Remes, Z. Polackova, M. Vanecek, *Physica Status Solidi (a)* **203**, 12 (2006).
- [25] J.M. Lackner, W. Waldhauser, *Journal of Adhesion Science and Technology* **24**, 5 (2010).
- [26] D. Das, R. Raj, J. Jana, S. Chatterjee, K.L. Ganapathi, M. Chandran, M.S. Ramachandra Rao, *J. Phys. D: Appl. Phys.* **55**, 33 (2022).
- [27] S. Stehlik, M. Varga, P. Stenclova, L. Ondic, M. Ledinsky, J. Pangrac, O. Vanek, J. Lipov, A. Kromka, B. Rezek, *ACS Appl. Mater. Interfaces* **9**, 44 (2017).
- [28] W. Jacob, M. Unger, *Applied Physics Letters* **68**, 4 (1996).
- [29] K. Tsugawa, M. Ishihara, J. Kim, M. Hasegawa, Y. Koga, *New Diam. Front. Carbon Technol.* **16**, 6 (2006).
- [30] O. Babchenko, Š. Potocký, T. Ižák, K. Hruška, Z. Bryknar, A. Kromka, *Surface and Coatings Technology* **271**, (2015).
- [31] T. Izak, O. Babchenko, M. Varga, S. Potocky, A. Kromka, *Physica Status Solidi (b)* **249**, 12 (2012).
- [32] A. Kromka, O. Babchenko, S. Potocky, B. Rezek, A. Sveshnikov, P. Demo, T. Izak, M. Varga, in: *Diamond-Based Materials for Biomedical Applications*, Elsevier, 2013, pp. 206–255.
- [33] Š. Potocký, M. Čada, O. Babchenko, T. Ižák, M. Davydova, A. Kromka, *Physica Status Solidi (b)* **250**, 12 (2013).
- [34] Š. Potocký, O. Babchenko, K. Hruška, A. Kromka, *Physica Status Solidi (b)* **249**, 12 (2012).
- [35] A. Kromka, O. Babchenko, T. Izak, K. Hruska, B. Rezek, *Vacuum* **86**, 6 (2012).
- [36] Y. Xing, L. Dai, *Nanomedicine* **4**, 2 (2009).
- [37] K. Dragounová, T. Ižák, A. Kromka, Z. Potůček, Z. Bryknar, Š. Potocký, *Appl. Phys. A* **124**, 3 (2018).
- [38] K. Dragounová, Z. Potůček, Š. Potocký, Z. Bryknar, A. Kromka, *Journal of Electrical Engineering* **68**, 1 (2017).
- [39] J. Fait, Š. Potocký, Š. Stehlík, J. Stuchlík, A. Artemenko, A. Kromka, B. Rezek, *Applied Surface Science* **480**, (2019).
- [40] Š. Potocký, T. Ižák, M. Varga, A. Kromka, *Physica Status Solidi (b)* **252**, 11 (2015).
- [41] Š. Potocký, J. Holovský, Z. Remeš, M. Müller, J. Kočka, A. Kromka, *Physica Status Solidi (b)* **251**, 12 (2014).

- [42] T. Zhang, G. Pramanik, K. Zhang, M. Gulka, L. Wang, J. Jing, F. Xu, Z. Li, Q. Wei, P. Cigler, Z. Chu, *ACS Sens.* (2021).
- [43] M. Monici, in: *Biotechnology Annual Review*, Elsevier, 2005, pp. 227–256.
- [44] D.H. Jariwala, D. Patel, S. Wairkar, *Materials Science and Engineering: C* **113**, (2020).
- [45] T.D. Merson, S. Castelletto, I. Aharonovich, A. Turbic, T.J. Kilpatrick, A.M. Turnley, *Optics Letters* **38**, 20 (2013).
- [46] L. Bacakova, A. Broz, J. Liskova, L. Stankova, S. Potocky, A. Kromka, *Diamond and Carbon Composites and Nanocomposites*, InTech, 2016.
- [47] A. Kromka, R. Kravetz, A. Poruba, J. Zemek, V. Perina, J. Rosa, M. Vanecek, *Phys. Stat. Sol. (a)* **199**, 1 (2003).
- [48] A. Brož, L. Bačáková, P. Štenclová, A. Kromka, Š. Potocký, *Beilstein Journal of Nanotechnology* **8**, (2017).
- [49] L. Grausova, A. Kromka, L. Bacakova, S. Potocky, M. Vanecek, V. Lisa, *Diamond and Related Materials* **17**, 7–10 (2008).
- [50] I. Nemcakova, A. Litvinec, V. Mandys, S. Potocky, M. Plencner, M. Doubkova, O. Nanka, V. Olejnickova, B. Sankova, M. Bartos, E. Ukraintsev, O. Babčenko, L. Bacakova, A. Kromka, B. Rezek, D. Sedmera, *Sci Rep* **12**, 1 (2022).
- [51] L. Stankova, J. Musilkova, A. Broz, S. Potocky, A. Kromka, H. Kozak, T. Izak, A. Artemenko, D. Stranska, L. Bacakova, *Diamond and Related Materials* **97**, (2019).
- [52] M. Bilal, H. Cheng, R.B. González-González, R. Parra-Saldívar, H.M.N. Iqbal, *Journal of Materials Research and Technology* **15**, (2021).
- [53] K.D. Behler, A. Stravato, V. Mochalin, G. Korneva, G. Yushin, Y. Gogotsi, *ACS Nano* **3**, 2 (2009).
- [54] Q. Zhang, V.N. Mochalin, I. Neitzel, I.Y. Knoke, J. Han, C.A. Klug, J.G. Zhou, P.I. Lelkes, Y. Gogotsi, *Biomaterials* **32**, 1 (2011).
- [55] S. Morimune, M. Kotera, T. Nishino, K. Goto, K. Hata, *Macromolecules* **44**, 11 (2011).
- [56] M. Parizek, T.E. Douglas, K. Novotna, A. Kromka, M.A. Brady, A. Renzing, E. Voss, M. Jarosova, L. Palatinus, P. Tesarek, P. Ryparova, V. Lisa, A.M. dos Santos, L. Bacakova, *International Journal of Nanomedicine* (2012).
- [57] S.K. Bhatia, ed., *Engineering Biomaterials for Regenerative Medicine: Novel Technologies for Clinical Applications*, Springer, New York, NY, 2012.
- [58] E.S. Place, N.D. Evans, M.M. Stevens, *Nat Mater* **8**, 6 (2009).

Appendix A

Included author's publications

Below is the list of selected thirteen author's publications related to the thesis.

A.1

Growth of nanocrystalline diamond films deposited by microwave plasma CVD system at low substrate temperatures

Growth of nanocrystalline diamond films deposited by microwave plasma CVD system at low substrate temperatures

S. Potocky¹, A. Kromka^{*,1,2}, J. Potmesil¹, Z. Remes¹, Z. Polackova¹, and M. Vanecek¹

¹ Institute of Physics, Academy of Sciences of Czech Republic, Cukrovarnicka 10, CZ-16253 Prague 6, Czech Republic

² Department of Microelectronics, Slovak University of Technology, Ilkovicova 3, 81219 Bratislava, Slovak Republic

Received 2 March 2006, revised 28 June 2006, accepted 29 June 2006

Published online 13 September 2006

PACS 81.05.Uw, 81.15.Gh

Nanocrystalline diamond (NCD) films were grown by microwave plasma CVD in hydrogen-based gas mixture. Deposition experiments were performed at different temperatures varying from 370 to 1100 °C. Before growth step, silicon (100) oriented substrates were nucleated by bias enhanced nucleation procedure and glass substrates were pretreated in ultrasonic bath. Optical, structural and morphological properties of NCD films were systematically studied by using an optical spectroscopy, scanning electron microscopy and Raman spectroscopy. NCD films were optically transparent in wide range and had high refractive index of 2.34. All deposited samples exhibited diamond characteristic line in the Raman spectrum. The growth kinetic was attributed to the hydrogen abstraction model.

© 2006 WILEY-VCH Verlag GmbH & Co. KGaA, Weinheim

1 Introduction

Standard microwave plasma enhanced chemical vapor deposition of polycrystalline and/or nanocrystalline diamond thin films and membranes takes place at substrate temperatures 700–900 °C [1]. Such a high temperature process limits a family of suitable substrates. The deposition of diamond on glass or on CMOS electronic devices requires decrease of the substrate temperature to 400 °C or less, while keeping the excellent material properties of diamond.

CVD diamond growth at a low temperature is not a technologically solved task yet. Generally, the diamond growth from CH₄–H₂ gas mixture is believed to be based on methyl radicals (CH₃) [1]. At low temperature processes, the unwished developing of non-diamond phases can be minimalized either via lowering the concentration of carbon source (which substantially slow the growth) or by using substituted chemistry based on partial replacing of hydrogen gas source by oxygen [2–4] or halogen [5, 6]. Furthermore, growth of nanocrystalline diamond film mostly requires an addition of other gases like nitrogen [7, 8] or argon [9]. Argon-based growth seems to be a promising technique, where C₂ dimers play a dominant role in sufficient re-nucleation process at a low activation energy (5.8 kcal/mol). Change in chemistry results in a growth of ultra-nano-crystalline diamond films also at low temperatures (400 °C) [9]. However, a final optical quality of these films is degraded due to an incorporation of relatively high amount of non-diamond phases.

In this paper, we present the growth of nanocrystalline diamond films from hydrogen-based gas mixture by microwave CVD process. Films grown at high (800 °C) and low (400 °C) temperature range reveal nearly identical optical properties, confirming an excellent quality of grown material. Nanocrystal-

* Corresponding author: e-mail: kromka@fzu.cz

line diamond films exhibit the diamond characteristic line centered at $\sim 1332.5 \text{ cm}^{-1}$ in the Raman spectrum. The growth kinetic seems to be controlled via hydrogen abstraction model as dedicated from the Arrhenius plot.

2 Experimental

Nanocrystalline diamond films were grown on (100) oriented silicon and glass slides (1×3 inches, Schott AF45) by microwave plasma CVD technique [10]. Prior to deposition process, all silicon substrates were pretreated under identical conditions in the bias enhanced nucleation step at a negative substrate bias of -180 V for 8 minutes, 5% of methane in hydrogen and at $850 \text{ }^\circ\text{C}$. The nucleation procedure of glass substrates was realized ultrasonically using 5 nm diamond powder for 40 minutes. The diamond growth step was provided at a constant methane concentration (1% CH_4 in H_2), the total gas pressure was 30 mbar. Substrate temperatures varied between 370 and $1100 \text{ }^\circ\text{C}$. High temperature range (above $600 \text{ }^\circ\text{C}$) was measured by the two-color pyrometer working at the wavelengths of 1.35 and $1.55 \text{ }\mu\text{m}$ (CHINO type) and low temperature range (below $600 \text{ }^\circ\text{C}$) was measured by the two-color pyrometer working at the wavelengths of 2.13 and $2.35 \text{ }\mu\text{m}$ (Williamson type). Both pyrometers were found to be insensitive to the quartz bell jar. Raman spectra of grown films were measured by using a 514.5 nm excitation wavelength laser. Diamond film morphology was investigated by scanning electron microscopy (SEM). Film thickness and refractive index were calculated from optical measurements. Thickness of NCD films deposited at low temperatures ($\leq 400 \text{ }^\circ\text{C}$) was in the range 50–300 nm.

3 Results and discussions

Raman spectra of samples deposited at the high temperature range ($>600 \text{ }^\circ\text{C}$) exhibited one sharp peak centred at 1332.5 cm^{-1} , identified as the diamond characteristic line [11]. In addition, two broad bands centred at 1350 and 1590 cm^{-1} (known as D and G band [12]) were observed over some samples. No specific correlation between intensity of these bands and the high temperature growth range was observed. Raman spectra of NCD film deposited at the low temperature range are shown in Fig. 1. We observed that the variation and intensity of non-diamond phases increased with decreasing substrate temperature. In addition, non-diamond phases were more dominant over silicon substrate (Fig. 1). The origin of this behaviour is not clear yet. We assume that during the early growth stage a change in a gas chemistry can take place due to an oxygen coming from the glass substrate. Further plasma characterization is required to understand the differences between the NCD growth on silicon and glass. Figure 2

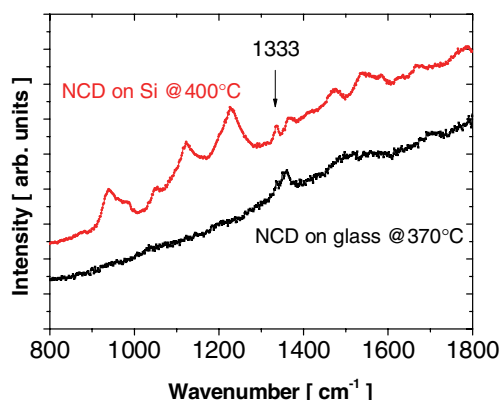


Fig. 1 (online colour at: www.pss-a.com) Raman spectra of NCD films deposited on glass ($370 \text{ }^\circ\text{C}$) and on silicon ($400 \text{ }^\circ\text{C}$).

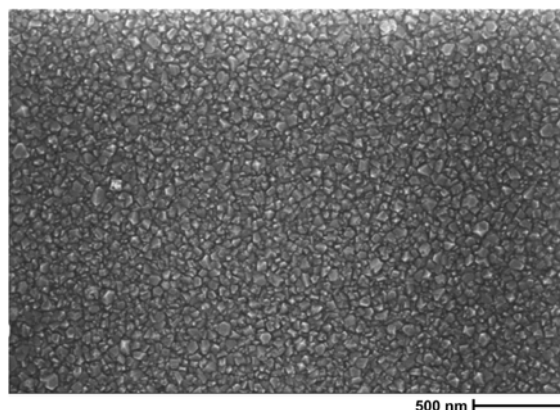


Fig. 2 (online colour at: www.pss-a.com) Surface morphology of a NCD film grown on glass substrate at the temperature of $400 \text{ }^\circ\text{C}$.

shows a surface morphology of the NCD film grown on glass at low substrate temperature of 400 °C. The film consisted of randomly oriented nano-crystals up to 40 nm in size. The surface roughness was less than 10 nm (as measured by atomic force microscopy). Adhesion of NCD to silicon substrates was very good and independent on the growth temperature and/or the film thickness. Adhesion of NCD films deposited on glass was limited to a certain film thickness (400–600 nm). Thick nanocrystalline diamond films (>600 nm) have tendency to delaminate spontaneously from the glass substrates due to different thermal expansion coefficient of the diamond and the glass substrate.

The influence of the substrate temperature on optical properties of NCD films was investigated by the transmittance/reflectance measurements. In this case, all investigated NCD films were deposited on optically transparent glass substrate. The film thickness d , index of refraction n , and root mean square roughness σ were calculated from the transmittance spectra using the interference fringes [13–15].

Figure 3 shows a typical transmittance/reflectance spectrum of a NCD layer deposited on a glass substrate. To avoid the suppression of the interference fringes due to the inhomogeneous thickness [16], the size of the light spot was reduced to diameter 1 mm. The deposited NCD film is optically transparent in broad spectral range from infrared to ultraviolet light. The transparency in IR region below 0.5 eV (above 2500 nm) and in UV region above 3.5 eV (below 350 nm) is suppressed due to the glass substrate. In our previous work it was shown that self-standing NCD membranes are fully transparent from far IR to deep UV [17]. The calculated refractive index of the NCD film is 2.34. It is interesting to note that this calculated value is not influenced by the substrate temperature. The surface scattering from NCD layers increased with an increasing film thickness.

An optical roughness of 500–1000 nm thick NCD films grown at the high temperature range (>600 °C) was $\sigma \approx 20$ –30 nm. This value reduced dropped down below 10 nm for ultra-thin NCD films typically grown at the low substrate temperature range (<400 °C). The calculated values of the optical surface roughness were confirmed also by AFM measurements.

Using the Clausius–Mossotti equation [18] we were able to calculate the mass density of $\rho = 3.45 \text{ g/cm}^3$ (for $n = 2.34$). A slight lowering of a mass density of NCD compared to single crystal diamond ($\rho = 3.52 \text{ g/cm}^3$) is probably due to a small non-diamond content (as observed also in Raman spectra) or voids between crystallites. Next, we used FTIR reflectance-absorbance measurements to estimate amount of hydrogen bonded to sp^3 carbon. Generally, no measurable absorption was observed in the sp^3 CH stretch region (2800–3100 cm^{-1} region) [19]. The absorption A related to hydrogen bounded to carbon was estimated to be less than 1% for 1 μm thick NCD film. Thus related absorption coefficient is lower than $\alpha \approx A/d < 100 \text{ cm}^{-1}$. According to Jacob and Unger [20], the total bounded hydrogen content in the diamond layer can be roughly estimated as $N_{\text{H}} \approx \alpha \times 10^{19} \text{ cm}^{-3}$. Based on these facts, we can conclude that the total content of bounded hydrogen over our films is below 10^{21} cm^{-3} (i.e. less than 1 at.%). Similar results were observed for the whole temperature range.

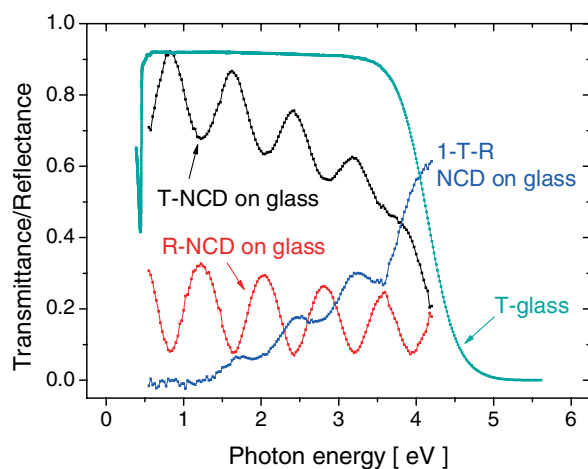


Fig. 3 (online colour at: www.pss-a.com) Transmittance and reflectance spectra of a 320 nm thick NCD film deposited on a glass substrate.

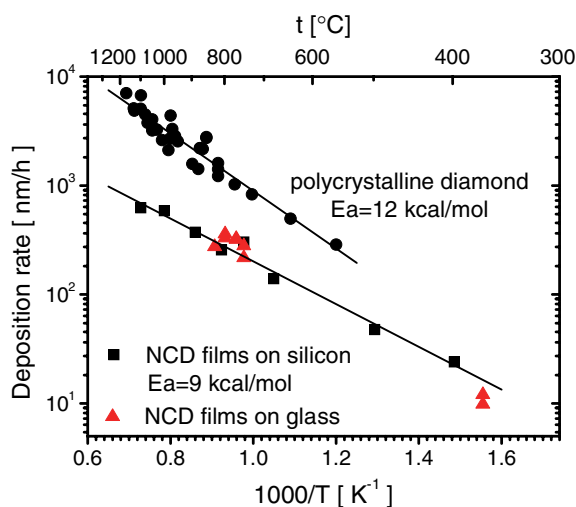


Fig. 4 (online colour at: www.pss-a.com) Growth rate of diamond films on Si as a function of a reciprocal temperature. *Rectangles* – growth of NCD films. *Circles* – growth of polycrystalline diamond films. *Triangle symbols* represent the growth rate of NCD film on glass substrate.

A significant parameter for chemical kinetic of nanodiamond growth is also activation energy of the process, E_a . The determination of the activation energy is not a simple task, while several surface reactions are sensitive to the actual temperature [21–23]. Therefore, first we provided the nucleation procedure at identical conditions for all the samples. Then the growth procedure was realized at different temperatures varying from 370 to 1100 °C. Figure 4 shows an Arrhenius plot of the growth rate versus a reciprocal substrate temperature. Nearly a linear relationship is observed in the investigated temperature range. The growth rate monotonically decreases from 620 to 10 nm/hr with the substrate temperature decrease from 1100 to 370 °C. No significant difference between the growth rate of NCD film on silicon or on glass is observed. The calculated activation energy of the NCD growth on silicon is 9 kcal/mol. For a comparison, there are added data of a polycrystalline diamond growth in Fig. 4. The growth of polycrystalline diamond films was provided in the same deposition apparatus and the process parameters were published in the previous work [24]. The activation energy for the polycrystalline diamond growth process is 12 kcal/mol. The main origin for the observed differences in the activation energies is not clear and further investigations are in progress. Our both activation energies indicate that the polycrystalline and/or nanocrystalline growth process is controlled via hydrogen abstraction model, as previously observed also for the $\text{CH}_4\text{--H}_2$ gas mixture [25]. It must be noted that our calculated activation energies do not include possible variation of the delay time for the diamond growth. We observed that the delay time is not a constant value and it has tendency to rapidly increase as the substrate temperature drops down. We believe that the optimization of the early growth stage can significantly lower this delay time and so indirectly enhances the nanocrystalline diamond growth at as low temperatures as 370 °C.

4 Conclusions

We presented a successful deposition of the nanocrystalline diamond films in the wide temperature range, varying from 370 to 1100 °C. The NCD films were grown on both substrate types, i.e. silicon and glass, respectively. All the films had low surface roughness in order of tens of nanometers. Very low surface roughness (<10 nm) was achieved for the ultra-thin NCD films deposited at the lowest temperature. Raman spectra exhibited a presence of non-diamond phases, most probably located at the grain boundaries. Optical measurements confirmed an excellent optical transparency of films from infrared to UV region. No significant degradation of the optical quality was observed for the NCD films deposited at the low substrate temperature range. The growth of the NCD films seems to be controlled via hydrogen abstraction model, as indirectly dedicated from the calculated activation energy.

Acknowledgement This work was supported by the Research Training Network of EC, contract MRTN-CT-2004-512224, by GACR contract 202/05/2233 and by project LC510.

References

- [1] K. E. Spear and J. P. Dismukes, *Synthetic Diamond: Emerging CVD Science and Technology*, The Electrochemical Society Series (John Wiley & Sons, NY, 1994).
- [2] Y. Muranaka, H. Yamashita, and H. Miyadera, *J. Appl. Phys.* **69**, 8145 (1991).
- [3] J. Wei, H. Kawarada, J. Suzuki, and A. Hiraki, *J. Cryst. Growth* **99**, 1201 (1990).
- [4] M. Yuasa, O. Arakaki, J. S. Ma, A. Hiraki, and H. Kawarada, *Diamond Relat. Mater.* **1**, 168 (1992).
- [5] I. Schmidt, F. Hentschel, and C. Benndorf, *Solid State Ionics* **101–103**, 97 (1997).
- [6] M. Asmann, J. Heberlein, and E. Pfender, *Diamond Relat. Mater.* **8**, 1 (1999).
- [7] D. Zhou, A. R. Krauss, L. C. Qin, T. G. McCauley, D. M. Gruen, T. D. Corrigan, R. P. H. Chang, and H. Gnaser, *J. Appl. Phys.* **82**, 4546 (1997).
- [8] S. G. Wang, Qing Zhang, S. F. Yoon, J. Ahn, Q. Zhou, Q. Wang, D. J. Yang, J. Q. Li, and Sam Zhang Shanyong, *Surf. Coat. Technol.* **167**, 143 (2003).
- [9] T. G. McCauley, D. M. Gruen, and A. R. Krauss, *Appl. Phys. Lett.* **73**, 1646 (1998).
- [10] M. Fünér, C. Wild, and P. Koidl, *Appl. Phys. Lett.* **72**, 1149 (1998).
- [11] S. Bühlmann, E. Blank, R. Haubner, and B. Lux, *Diamond Relat. Mater.* **8**, 194 (1999).
- [12] S. L. Heidger, *Mat. Res. Soc. Symp. Proc.* **383**, 319 (1995).
- [13] R. Swanepoel, *J. Phys. E: Sci. Instrum.* **16**, 1214 (1983).
- [14] Z. Yin, H. S. Tan, and F. W. Smith, *Diamond Relat. Mater.* **5**, 1490 (1996).
- [15] Z. Remes, Ph.D. Thesis, Prague, Charles University (1999).
- [16] R. Swanepoel, *J. Phys. E: Sci. Instrum.* **17**, 896 (1984).
- [17] V. Mortet, J. D'Haen, J. Potmesil, R. Kravets, I. Drbohlav, V. Vorliceck, J. Rosa, and M. Vanecek, *Diamond Relat. Mater.* **14**, 393 (2005).
- [18] L. Ward, *The Optical Constants of Bulk Materials and Films* (IPP, Bristol, 1994).
- [19] K. M. McNamara, K. K. Gleason, and C. J. Robinson, *J. Vac. Sci. Technol. A* **10**, 3143 (1992).
- [20] W. Jacob and M. Unger, *Appl. Phys. Lett.* **68**, 475 (1996).
- [21] S. Barrat, P. Pigeat, I. Dieguez, E. Bauer-Grosse, and B. Weber, *Thin Solid Films* **304**, 98 (1997).
- [22] F. Bénédic, M. Belmahi, T. Easwarakhanthan, and P. Alnot, *J. Phys. D: Appl. Phys.* **34**, 1048 (2001).
- [23] J. Lee, B. Hong, R. Messier, and R. W. Collins, *Appl. Phys. Lett.* **69**, 1716 (1996).
- [24] V. Mortet, A. Kromka, R. Kravets, J. Rosa, V. Vorliceck, J. Zemek, and M. Vanecek, *Diamond Relat. Mater.* **13**, 604 (2004).
- [25] E. J. Corat, R. C. Mendes de Barros, V. J. Trava-Airoldi, N. G. Ferreira, N. F. Leite, and K. Iha, *Braz. Phys. A* **27**, 138 (1997).

A.2

Investigation of nanocrystalline diamond films grown on silicon and glass at substrate temperature below 400 °C



Investigation of nanocrystalline diamond films grown on silicon and glass at substrate temperature below 400 °C

S. Potocky^{a,*}, A. Kromka^{a,b}, J. Potmesil^a, Z. Remes^a, V. Vorlicek^c, M. Vanecek^a, M. Michalka^d

^a Institute of Physics, Academy of Sciences of the Czech Republic, Cukrovarnicka 10, CZ 16253 Praha 6, Czech Republic

^b Department of Microelectronics, Slovak University of Technology, Ilkovicova 3, 81219 Bratislava, Slovak Republic

^c Institute of Physics, Academy of Sciences of the Czech Republic, Na Slovance 2, CZ 18221 Praha 8, Czech Republic

^d International Laser Centre, Ilkovicova 3, 812 19 Bratislava, Slovak Republic

Available online 18 December 2007

Abstract

We present investigation of nanocrystalline diamond films deposited in a wide temperature range. The nanocrystalline diamond films were grown on silicon and glass substrates from hydrogen based gas mixture (methane and hydrogen) by microwave plasma CVD process. Film composition, nano-grain size and surface morphology were investigated by Raman spectroscopy and scanning electron microscopy. All samples showed diamond characteristic line centred at 1332 cm^{-1} in the Raman spectrum. Nanocrystalline diamond layers revealed high surface flatness (under 10 nm) with crystal size below 60 nm. Surface morphology of grown films was well homogeneous over glass substrates due to used mechanical seeding procedure. Very thin films (40 nm) were successfully grown on glass slides (i.e. standard size $1 \times 3''$). An increase in delay time was observed when the substrate temperature was decreased. A possible origin for this behaviour was discussed.

© 2006 Elsevier B.V. All rights reserved.

Keywords: Nanocrystalline diamond; Low temperature growth; SEM

1. Introduction

The nanocrystalline diamond (NCD) has attracted many researchers because of advanced combination of intrinsic properties like smooth surface, excellent optical, mechanical and thermal properties, bio-compatibility and chemical inertness [1]. These films can be deposited over large area and become economically feasible for variety of industrial use. However, the conventional chemical vapour deposition (CVD) techniques for diamond growth use relatively high substrate temperature, i.e. above 700 °C [2]. The growth at lower temperatures is still not a trivial task resulting in a decrease of the growth rate and in an increased incorporation of non-diamond carbon phases in the film degrading the advanced properties [3–6]. The low temperature growth processes seem to be essential mainly for better establishing of NCD films in new fields like biochemistry and life science or for bio-encapsulation of electronic silicon devices. In these cases diamond surface is used either as a passive functional material for immobilization of various bio

molecules [7,8] or as an electrically active part of the bio-sensing element [9,10]. In addition, ability to overcoat glass slides (with standard size $1 \times 3''$) can substantially extend the life science topics. However, especially the soda-lime glass is not an optimal substrate material for the growth of NCD films. First, a soda-lime glass has low softening temperature $\sim 570\text{ °C}$. Second, the relatively high mismatch in the thermal expansion coefficient of a soda-lime glass ($9.2 \times 10^{-6}\text{ K}^{-1}$) and diamond ($0.8 \times 10^{-6}\text{ K}^{-1}$) results in development of high stress during cooling of the sample to room temperature [11,12].

In this study, the results of the growth of NCD films on silicon, low alkaline borosilicate glass and a soda-lime glass ($1 \times 3''$ slides) are presented. The films were deposited in the wide temperature range varying from 370 to 1100 °C. The growth was realized from hydrogen-based gas mixture. The soda-lime glass substrates have been successfully overcoated at temperatures as low as 400 °C.

2. Experimental

Nanocrystalline diamond films were grown on (100) oriented silicon and glass slides ($1 \times 3''$, a low alkaline borosilicate or

* Corresponding author. Tel.: +420 220 318 441; fax: +420 233 343 184.
E-mail address: potocky@fzu.cz (S. Potocky).

soda-lime glass) by microwave plasma enhanced CVD in the ellipsoidal cavity reactor [13]. Prior to deposition process, the substrates were either mechanically seeded in ultrasonic bath with a nanodiamond powder or they were pretreated in the bias enhanced nucleation step at a negative substrate bias of -180 V for 12 min, 5% of methane in hydrogen and at substrate temperature of 850 °C. The nucleation was followed by the growth step provided at a constant methane concentration (1% CH_4 in H_2) and at the total gas pressure of 30 mbar. Substrate temperature varied between 370 and 1100 °C. High temperature range (above 600 °C) was measured by the two-colour pyrometer working at the wavelengths of 1.35 and 1.55 μm (CHINO type) and low temperature range (below 600 °C) was measured by the two-colour pyrometer working at the wavelengths of 2.13 and 2.35 μm (Williamson type). Both pyrometers were found to be insensitive to the absorption of a quartz bell jar. Raman spectra of grown films were measured using a 514.5 nm excitation wavelength (Ar^+ laser). Diamond film morphology was investigated by scanning electron microscopy (SEM) and atomic force microscopy (AFM). Film thickness and refractive index were calculated from optical measurements [14,15].

3. Result and discussions

The high temperature growth of NCD films, i.e. substrate temperature $T_S \geq 600$ °C, was realized on silicon and on low alkaline borosilicate substrates (Schott AF45 glass). The soda-lime glass substrates were used only for a low temperature growth (≤ 400 °C). Raman spectra of nanocrystalline diamond films deposited at $T_S \geq 600$ °C displayed one dominant peak centred at 1333 cm^{-1} (optical phonon in diamond) that confirms presence of diamond [16]. In addition, two broad bands centred at 1350 and 1590 cm^{-1} (known as D and G band [17]) were observed for samples deposited on low alkaline borosilicate glass. It is observed that the variation and intensity of non-diamond phases increased with decreasing substrate temperature. Raman spectra of the NCD films deposited at the low temperature process ($T_S \leq 400$ °C) exhibit relatively high intensity of non-diamond carbon phases (Fig. 1). It seems that

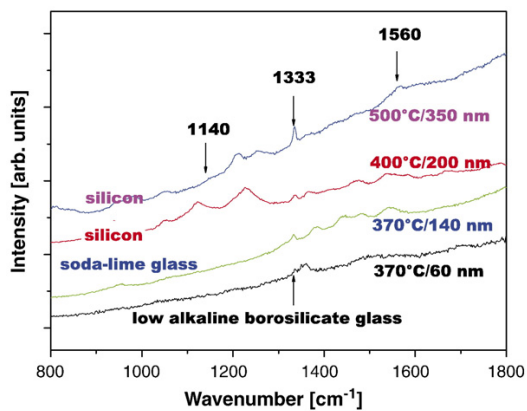


Fig. 1. Raman spectra of NCD films deposited on a silicon substrate (400 and 500 °C), on a low alkaline borosilicate glass and on a soda-lime glass (370 °C).

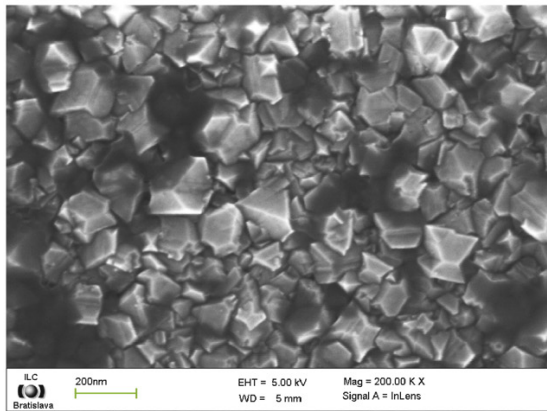
non-diamond phases are more dominant over silicon substrates. The origin of this behaviour is not clear yet. It is proposed that during the early growth stage a change in the gas chemistry can take place due to oxygen coming from the glass substrate. Consequently, oxygen addition to the hydrogen-methane gas mixture can result in improved film growth [18–20]. However, in our case the process should differ (for example due to other contamination coming from the glass substrate during the early stage of diamond growth) and further plasma characterization is required to understand the differences between the NCD growth on silicon and glass.

The quantitative percentage of the sp^3 hybridized carbon atoms in the analyzed volume of the NCD films were evaluated from the high resolution C 1s XPS spectra recorded at two emission angles, i.e. 0° and 60° with respect to the surface normal [21]. The resulting percentage of sp^3 hybridized carbon atoms was above 90%. Generally, this percentage was larger below the surface region (from 95.3 % to 98.5%) than at the surface region (from 92.7% to 95.2%). However, no remarkable differences between the NCD films prepared in the whole temperature range were observed by XPS measurements.

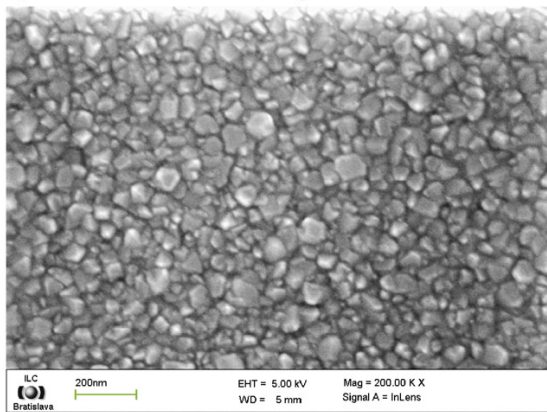
Fig. 2 shows surface morphology of the NCD films grown at low temperature on silicon and glass substrates. The nanocrystalline diamond film deposited over silicon exhibits a relatively rough surface. The crystal size varies from tens to hundreds nanometres with well visible crystal faceting. Next, the surface of NCD film exhibits some dark regions most probably related to non-diamond carbon phases, which is in good agreement with Raman measurements. On the other hand, nanocrystalline diamond films deposited on glass show more homogenous surface morphology in comparison to NCD growth on silicon. The deposition on glass results in the growth of randomly oriented nanocrystals, homogeneously distributed over the surface with crystal size up to approx. 60 nm. The surface roughness was less than 10 nm (as measured by AFM). The observed difference in the surface morphology of nanocrystalline diamond films deposited on silicon and on glass substrates seems to originate from a nucleation procedure. In the case of Si substrate, the bias enhanced nucleation procedure was used. However, the final film morphology was very sensitive to this procedure, mainly to the optimal process parameters and duration time [22]. In the case of glass substrates, the mechanical seeding procedure was used with the bath consisting of 5 nm diamond powder. Presently, this procedure was well optimized in our laboratory. The achieved nucleation density is very high, in order of 10^{12} cm^{-2} , as observed by AFM [23]. It is believed that the high nucleation density allows us to grow fully closed nanocrystalline diamond films of very low thickness (40 nm).

Another important parameter for the growth of a diamond thin film is its adhesion to the foreign substrate. In our case it was observed that the adhesion of NCD films to silicon substrates was very good and independent on the growth temperature or the film thickness. This was not the case for the deposition on glass substrates. It was observed that thick nanocrystalline diamond films (>600 nm) have tendency to delaminate spontaneously from the glass substrate due to the very different thermal expansion coefficient of the diamond and

a) silicon, 400 °C, 200 nm



b) low alkaline borosilicate glass, 370 °C, 60 nm



c) soda-lime glass, 370 °C, 42 nm

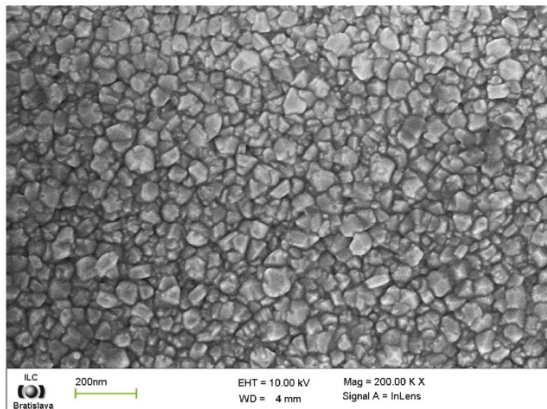


Fig. 2. Surface morphology of NCD films grown at low substrate temperatures on silicon (a) and on glass substrates (b, c).

glass substrate. In addition, the successful growth of NCD film on a soda-lime glass was possible only in the case of low temperature process, i.e. $T_S \leq 400$ °C. All NCD thin films successfully deposited on glass substrates exhibited excellent optical transparency in a broad spectral range from infrared to

ultraviolet light [24]. The measured transparency was suppressed due to the glass substrate. The calculated refractive index of the NCD films was 2.2–2.4, close to the single crystalline diamond (2.41).

The growth rate monotonically decreased from 620 to 10 nm/h with the substrate temperature decreasing from 1100 to 370 °C. No significant difference between the growth rate of NCD film on silicon or on glass substrate was observed. The calculated activation energy of the NCD growth on silicon, as calculated from an Arrhenius plot of the growth rate versus a reciprocal substrate temperature, was 9 kcal/mol [24]. That value indicates that such a growth process is limited by the temperature controlled chemical process, most probably by the removal of surface bonded hydrogen atoms from the carbon sites [25].

The delay time required to initialize the diamond growth for a certain substrate temperature was calculated from a linear fit of the dependence of film thickness on the deposition time for a constant substrate temperature. Table 1 summarizes the delay time values for various substrate temperatures. The value of delay time monotonically increases from approx. 2 min up to 2 h with a decreasing substrate temperature from 890 to 380 °C. It indicates that early stage of the growth is drastically hindered for the low temperature regime. Generally, the delay time was discussed and modelled as a function of several processes, like the type of the nucleation procedure, thermodynamic conditions, homogeneous and heterogeneous kinetics, implementation of a classical nucleation theory, adsorption–desorption kinetics and equilibrium conditions [26]. Some authors relate the delay time directly to the nucleation procedure in a steady-state regime [27–31]. However, due to nanocrystalline diamond seeding procedure used, it is not in our case. Our nucleation density is extremely high and the growth in the first assumption is similar to “homo-epitaxy”, which starts the growth on the nano-sized diamond crystallites remaining on the substrate surface after the nucleation procedure. In this case, the time needed for initializing the diamond growth can be prolonged i) due to possible reactions of carbon species with the substrate and ii) due to specific modification and stabilization of the nano-sized diamond nuclei (used in the mechanical seeding procedure). Both these processes need some favourable energy and can be strongly dependent on the temperature. Thus, a particular process or specific chemical reaction is strongly dependent on the temperature. When the nucleated surface is covered by nano-sized diamond crystallites, it is proposed that the less dominant role in the initialization of diamond growth seems to be a surface diffusion of carbon species to active sites.

The main origin for an increased initialization time for diamond growth (i.e. delay time) needs more detailed study and is under investigation. It is believed that the optimization of the early growth stage can significantly lower this delay time and so

Table 1
Calculated values of delay time for the NCD growth for various substrate temperatures

Substrate temperature [°C]	890	500	450	380
Delay time [min]	2	63	72	~120

shorten the total time for achieving fully closed nanocrystalline diamond film at temperatures as low as 370 °C.

4. Conclusions

Nanocrystalline diamond thin films were deposited in a wide temperature range, varying from 370 to 1100 °C. The NCD films were grown on silicon and glass substrates. The successful low temperature process allowed the deposition of NCD films over glass slides of standard size $1 \times 3''$. Decreasing the substrate temperature resulted in the increase of non-diamond carbon phases mainly in the case of silicon substrates. Surface morphology of NCD films grown on glass substrates was found to be more homogeneous and we were able to grow very thin (above 40 nm) and fully closed films. Finally, a drastic increase in the delay time for the nanocrystalline diamond growth was observed for the low substrate temperature range. The origin for this behaviour seems to be due to the temperature dependent process for preparing ready-active surface for the diamond growth during the early growth stage.

Acknowledgement

The research work at the Institute of Physics is supported by Institutional Research Plans No. AV0Z10100520 and AV0Z10100521. This work was supported by the DRIVE project of EC, contract MRTN-CT-2004-512224, by GACR contract 202/05/2233 and by LC510 Centrum for nanotechnology.

References

- [1] Olga A. Shenderova, Dieter M. Gruen, *Ultrananocrystalline Diamond: Synthesis, Properties, and Applications*, William Andrew Publishing, 2006 (ISBN: 0-8155-1524-1).
- [2] K.E. Spear, J.P. Dismukes, *The Electrochemical Society Series*, John Wiley & Sons, New York, 1994.
- [3] M. Yuasa, O. Arakaki, J.S. Ma, A. Hiraki, *Diamond Relat. Mater.* 1 (1992) 168.
- [4] M. Asmann, J. Heberlein, E. Pfender, *Diamond Relat. Mater.* 8 (1999) 1.
- [5] S.G. Wang, Qing Zhang, S.F. Yoon, J. Ahn, Q. Zhou, Q. Wang, D.J. Yang, J.Q. Li, Sam Zhang Shanyong, *Surf. Coat. Technol.* 167 (2003) 143.
- [6] T.G. McCauley, D.M. Gruen, A.R. Krauss, *Appl. Phys. Lett.* 73 (1998) 1646.
- [7] W. Yang, O. Auciello, J.E. Butler, W. Cai, J.A. Carlisle, J.E. Gerbi, D.M. Gruen, T. Knickerbocker, T.L. Lasseter, J.N. Russell Jr., L.M. Smith, R.J. Hamers, *Nat. Mater.* 1 (2002) 253.
- [8] S. Wenmackers, K. Haenen, M. Nesládek, P. Wagner, L. Michiels, M. van de Ven, M. Ameloot, *Phys. Status Solidi, A Appl. Res.* 199 (2003) 44.
- [9] A. Härtl, E. Schmich, J.A. Garrido, J. Hernando, S.C.R. Catharino, S. Walter, P. Faulner, A. Kromka, D. Steinmüller, M. Stutzmann, *Nat. Mater.* 3 (2004) 736.
- [10] J. Rubio-Retama, J. Hernando, B. López-Ruiz, A. Härtl, D. Steinmüller-Nethl, M. Stutzmann, E. López-Cabarcos, J.A. Garrido, *Langmuir* 22 (13) (2006) 5837.
- [11] M.J. Ulczynski, B. Wright, D.K. Reinhard, *Diamond Related Mater.* 7 (1998) 1639.
- [12] Z. Remes, Y. Avigal, R. Kalish, C. Uzan-Saguy, A. Chack, M. Nesládek, *Phys. Status Solidi, A Appl. Res.* 201 (2004) 2499.
- [13] M. Fünér, C. Wild, P. Koidl, *Appl. Phys. Lett.* 72 (1998) 1149.
- [14] R. Swanepoel, *J. Phys., E Sci. Instrum.* 17 (1984) 896.
- [15] A. Poruba, A. Fejfar, Z. Remes, J. Springer, M. Vanecek, J. Kocka, J. Meier, P. Torres, A. Shah, *J. Appl. Phys.* 88 (2000) 148.
- [16] S. Bühlmann, E. Blank, R. Haubner, B. Lux, *Diamond Relat. Mater.* 8 (1999) 194.
- [17] S.L. Heidger, *Mater. Res. Soc. Symp. Proc.* 383 (1995) 319.
- [18] Y. Muranaka, H. Yamashita, H. Miyadera, *J. Appl. Phys.* 69 (1991) 8145.
- [19] J. Wei, H. Kawarada, J. Suzuki, A. Hiraki, *J. Cryst. Growth* 99 (1990) 1201.
- [20] M. Yuasa, O. Arakaki, J.S. Ma, A. Hiraki, H. Kawarada, *Diamond Relat. Mater.* 1 (1992) 168.
- [21] J. Zemek, J. Houdkova, B. Lesiak, A. Jablonski, J. Potmesil, M. Vanecek, *J. Optoelectron. Adv. Mater.* 8 (2006) 2133.
- [22] A. Kromka, J. Janik, F. Balon, M. Kubovič, I. Červeň, V. Dubravcová, *Thin Solid Films* 433 (2003) 73.
- [23] Kromka et al., (in preparation).
- [24] S. Potocky, A. Kromka, J. Potmesil, Z. Remes, Z. Polackova, M. Vanecek, *Phys. Status Solidi, A* 203 (2006) 3011.
- [25] J. Stiegler, Z.T. Lang, Y. von Kaenel, J. Michler, E. Blank, *Appl. Phys. Lett.* 70 (1997) 173.
- [26] B.V. Derjaguin, D.V. Fedoseev, *Surf. Coat. Technol.* 38 (1989) 131.
- [27] R.A. Bauer, N.M. Shrockey, W.E. Brower, *J. Mater. Res.* 8 (1993) 2858.
- [28] G.S. Yang, M.A. Siam, *Appl. Phys. Lett.* 66 (1995) 311.
- [29] W. Piekarczyk, *J. Cryst. Growth* 119 (1992) 345.
- [30] D.G. Kim, H.C. Lee, J.Y. Lee, *J. Mater. Sci.* 28 (1993) 6704.
- [31] P. Ascarelli, S. Fontana, *Diamond Relat. Mater.* 2 (1993) 990.

A.3

Linear antenna microwave plasma CVD diamond
deposition at the edge of no-growth region of C-H-O ternary
diagram

Linear antenna microwave plasma CVD diamond deposition at the edge of no-growth region of C–H–O ternary diagram

Štěpán Potocký*, Oleg Babchenko, Karel Hruška, and Alexander Kromka**

Institute of Physics AS CR, v.v.i., Cukrovarnická 10, 16200 Praha, Czech Republic

Received 30 April 2012, revised 20 September 2012, accepted 21 September 2012

Published online 6 November 2012

Keywords C–H–O phase diagram, nanocrystalline diamond, plasma enhanced CVD, Raman spectroscopy, SEM

* Corresponding author: e-mail potocky@fzu.cz, Phone: +420 220 318 437, Fax: +420 233 343 184

** e-mail kromka@fzu.cz, Phone: +420 220 318 437, Fax: +420 233 343 184

The process parametric window for diamond deposition using the chemical vapor deposition at low pressures is quite limited where addition of oxygen in the gas phase broadens this window. The lower boundary of the lens-shaped domain in C–H–O ternary diagram concurs with the H₂–CO tie-line ($C/(C+O)=0.5$). In this work, we present the set of experiments where the ratio of $C/(C+O)$ was kept at a constant value 0.385. The effect of hydrogen concentration (ratio $O/(O+H)$)

varied from 0.047 to 0.364) on plasma characteristics and deposited NCD films were investigated. Raman spectroscopy confirmed the diamond character of all deposited coatings while scanning electron microscopy showed transformation from not closed to continuous film and further decrease of grain size and finally growth of diamond nanowires while decreasing hydrogen concentration in a gas mixture.

© 2012 WILEY-VCH Verlag GmbH & Co. KGaA, Weinheim

1 Introduction New routes of diamond depositions are of interest due to demands of a high quality and quantity samples. Diamond exhibits a unique combination of physical, mechanical, chemical, optical, and electrical properties while keeping its high biocompatibility [1]. In the chemical vapor deposition (CVD) of diamond films, oxygen in the precursor gases either as a pure O₂ or in the form of some oxides like CO₂ or CO is added to a CH₄/H₂ system to obtain higher growth rate and/or an improvement of quality of resultant films [2–5]. Several authors have discussed the role of oxygen in improved diamond growth due to (i) increasing of concentration of atomic hydrogen [4], (ii) higher reactivity of –OH radicals [5–7], or (iii) change of electron temperature/density in the plasma [8, 9].

The first C–H–O phase diagram introduced by Bachmann et al. [10], and revised later on [11], provides a common scheme for diamond CVD methods based on experimental results. The calculated phase diagram was presented by Wang et al. [12] where further specifications and modifications were done [13, 14].

In this work, we present the CVD deposition of diamond coatings at the growth/no-growth edge of “phase diagram”. The CVD growth is done by using a low-pressure linear antenna microwave plasma CVD system.

2 Experimental Diamond thin films were grown on (100) oriented silicon substrates in size $10 \times 10 \text{ mm}^2$. Before the CVD growth, Si substrates were ultrasonically pretreated in a suspension of deionized water and ultradispersed detonation diamond powder (diameter 5–10 nm, New Metals and Chemicals Corp. Ltd., Kyobashi) [15]. Previously, we have shown that this procedure yields high seeding densities in the range up to 10^{11} cm^{-2} . The growth of diamond coatings was realized by the linear antenna microwave plasma enhanced CVD deposition system [16]. This system utilizes a lower pressure range than the commonly known “ball” shaped plasma. Thus, the diamond deposition is done at much larger distance substrate-to-plasma. Diamond coatings were grown from a gas mixture of methane in hydrogen (up to 20% in H₂) and carbon dioxide (up to 80% in H₂). Process parameters: microwave power $P = 2 \times 1700 \text{ W}$, total gas pressure $p = 0.1 \text{ mbar}$, gas ratio $\text{CH}_4/\text{CO}_2 = 0.25$, the substrate temperature $T_s \approx 550 \text{ }^\circ\text{C}$ and deposition time $t = 15 \text{ h}$, were kept constant for all the experiments. Series of experiments were prepared where H₂ flow varied to keep the gas ratios summarized in Table 1.

Surface morphology, grain size, and thickness of the deposited coatings were characterized by scanning electron

Table 1 The deposition process gas flow concentrations, atomic ratios and corresponding description of the samples.

sample	[CH ₄] in H ₂ (%)	[CO ₂] in H ₂ (%)	O/(O+H)	H/(H+C)
S1	1.25	5	0.047	0.970
S2	2.5	10	0.087	0.944
S3	5	20	0.154	0.898
S4	10	40	0.250	0.828
S5	20	80	0.364	0.737

microscopy in top and cross section views (SEM, e_LiNE writer, Raith GmbH). Diamond character of films was determined by Raman spectroscopy (Renishaw In Via Reflex Raman spectrometer, excitation wavelength of 325 nm). Optical emission spectroscopy (OES) measurements were done during the deposition process. Imaging spectrometer Jobin Yvon with a focal length 500 mm and a diffraction grating 1200 g mm⁻¹ was used. The emitted light was studied at the distance $z = 10$ mm perpendicular to the axis of the linear antenna tube. The emissions were collected by means of fiber-optic cable fitted with a 50 mm long, cylindrical ($\phi 10$ mm) collimator, pointing perpendicularly toward the antenna–substrate axis. The diffracted light was detected by CCD detector which's sensitivity was calibrated on relative spectral intensity by tungsten lamp.

3 Results and discussion According to nomenclature in Bachman et al. [10], Table 1 summarizes carbon:hydrogen:oxygen ratios of the corresponding gas phases, i.e. coordinates of data points in the atomic C–H–O phase diagram shown in Fig. 1.

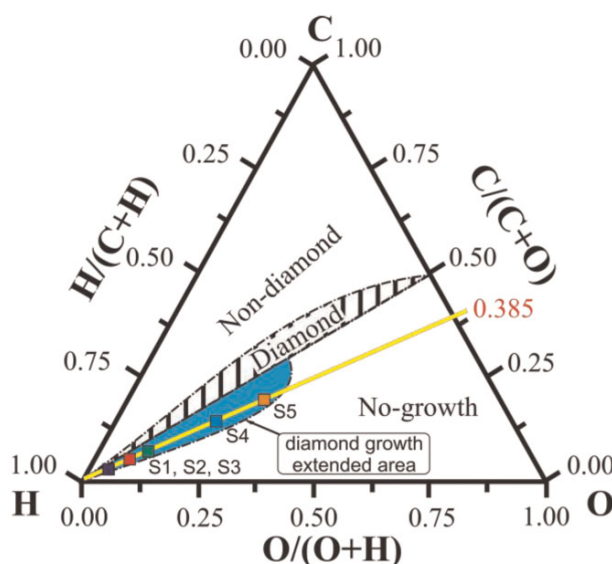
**Figure 1** (online color at: www.pss-b.com) The modified C–H–O feed gas compositional ternary plot based on Bachman et al. [11] with depicted sample S1 to S5 positions.

Figure 1 shows feed gas composition points in the modified lens-shaped C–H–O phase diagram by Bachman et al. [11]. Regions of diamond growth, non-diamond growth, and no deposition are depicted. Due to the fact that only H₂ gas flow was changed in our experiments, all coordinates lie in the gas mixture line $C/(C+H) = 0.385$ (see yellow line in Fig. 1). Although this line falls into the no deposition region we have still observed and confirmed a deposition of diamond coatings with varied morphologies. The origin for this observation can have few explanations. First one is a different design of linear antenna plasma system, which utilizes lower-pressure plasma than commonly used “ball” shaped plasmas where substrate is not in a “close” contact with plasma [16]. Over the longer plasma–substrate distance, the active oxygen containing species might recombine, i.e. the reaction chemistry with them should be lower. Second one, a total pressure should be taken into account during the construction of Bachman diagram as the diamond domain widens with decreasing pressure which in our case is by one to two orders lower than in common diamond deposition systems [13]. Last, the deposition temperature has to be also taken into account, which was lower in our experiments as compared to common ones. The calculated phase diagrams by Wang et al. [12] showed that for the process conditions as temperature higher than 700 K and the pressure range from 0.01 to 100 kPa, the $C/(C+H) = 0.385$ line copied the edge between diamond and no diamond region.

The development of the layer morphology with decreasing H₂ gas flow, i.e. H/(H+C) ratio is shown in Fig. 2. First, morphology of sample S1 reveals the nanocrystalline diamond grains in size 20–40 nm and not fully closed layer is observed. An estimated surface coverage is about 80%. The suppression of grain growth accompanied by decreasing in nucleation density should be caused by a “high” amount of hydrogen and thus, etching by hydrogen atoms can dominate over the diamond deposition. Sample S2 shows high quality polycrystalline diamond film with the grain size in the range of 50–150 nm and a visible development of diamond nanocrystal faceting is well observed. Due to reduced H/(H+C) ratio, the deposition of diamond phase dominates above the etching (sample S1). We assume that the nucleation layer survived at its high density (up to 10¹¹ cm⁻²) [17] and the growing grains compose fully closed diamond film. Further, reduce of the H/(H+C) (i.e. to 0.898) gives a rise to the influence of CO₂ in the gas mixture. The SEM image of sample S3 reveals a flat surface with fine granular structures (20–40 nm), i.e. morphology similar to our previous results [16]. Further decrease of hydrogen concentration exhibits a similar surface morphology while finer structures is observed (sample S4).

A drastic change in the film morphology is seen for sample S5 where formation of diamond nanowires is observed. We assume that at such high CH₄ concentration (20% in H₂), which would usually cause the deposition of “black” sp² rich diamond films is effectively compensated by a high value of CO₂ concentration (80% in H₂). It is well

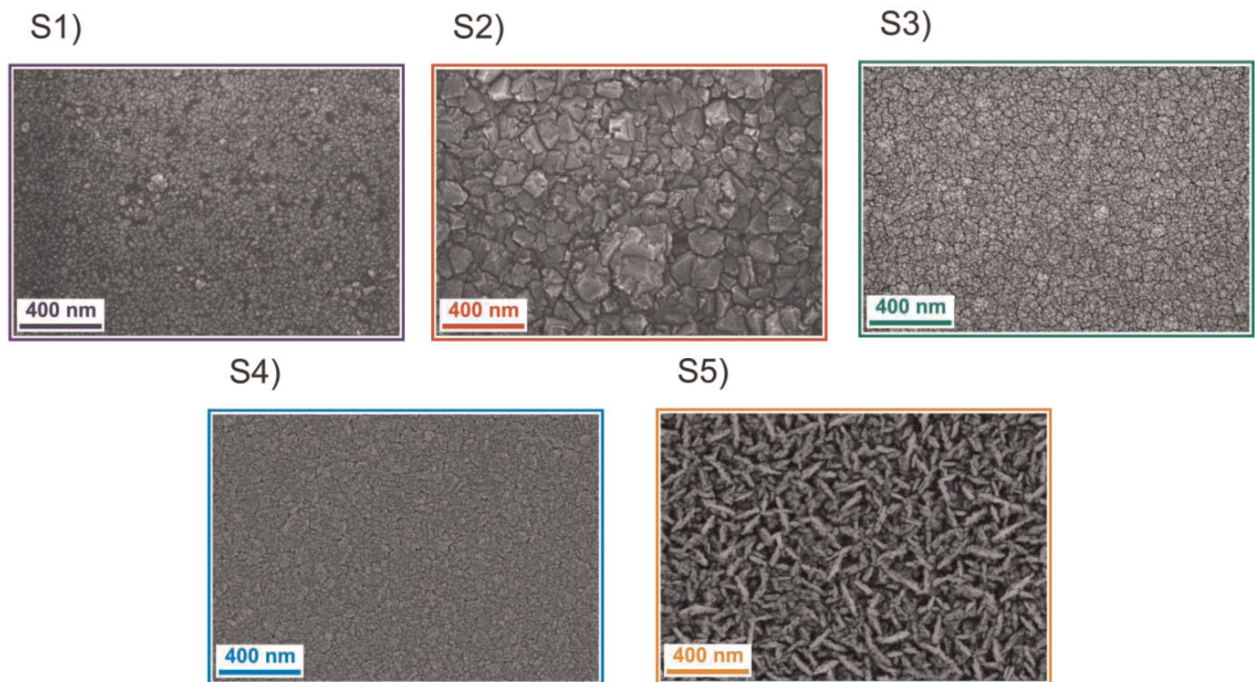


Figure 2 (online color at: www.pss-b.com) SEM images of the deposited samples S1 to S5.

known that oxygen etching occurs also at lower temperatures and proceeds at much higher rates [18].

Figure 3 shows Raman spectra of diamond coatings for a varied hydrogen flow. In the Raman spectra are identified three basic peaks. The diamond characteristic peak centered at 1331 cm^{-1} [19] is observed for all samples. Two broad bands centered at 1350 and 1580 cm^{-1} are attributed to D and G bands [20]. Left shoulder of D band indicates the presence of additional broad sub-band centered at

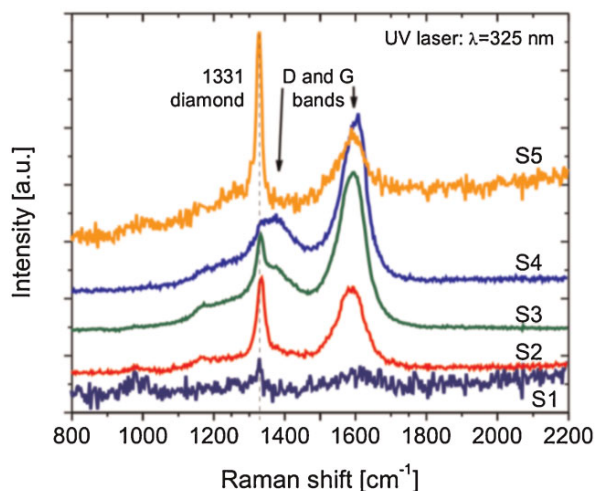


Figure 3 (online color at: www.pss-b.com) Raman spectra of deposited samples S1 to S5.

1160 cm^{-1} which should be attributed to the trans-polyacetylene groups (C–H bonds).

Sample S1 reveals only diamond 1331 cm^{-1} peak because other non-diamond phases are effectively etched by hydrogen. Low intensity is given only due to time integration constant and low film thickness. For decrease of H concentration in the samples S2, S3, and S4, increasing of D and G bands is observed which is most probably due to the increase of methane concentration. Also, formed films consisted of smaller grains, i.e. grain boundary surfaces increased (see SEM images Figs. 2-S2 to 2-S4) and it is known that sp^2 bonded phases of carbon are preferentially localized along grain boundaries [21]. For sample S5, a sharp diamond peak becomes dominant, D and G bands become lower in their intensity and band at approx. 1160 cm^{-1} is significantly suppressed down to the resolution limits of our measurement set-up. This indicates a clear diamond character of grown nanorods.

It should be noted that the deposition rate (resp. thickness) monotonically increased from 3 to 30 nm h^{-1} with lowering the concentration of H_2 in the gas mixture. Saturation of growth rate was observed for Sample S5. We experimentally observed that the CVD process running without using H_2 gas (CH_4 only as a source of H atoms), no diamond growth was achieved, i.e. the deposition rate was 0 nm h^{-1} .

Further, we calculated the excitation temperature in the close vicinity of the plasma source, which was $\approx 4500\text{ K}$ independent on the gas mixture composition. Saturation level of CO/H_β emission intensity was found until hydrogen

reduction $H/(H + C)$ down to 0.898. The CO/H_p emission intensity decreased by factor 0.5 at the lowest H_2 gas flow.

4 Conclusions In the presented work, we have investigated the influence of gas feed composition in C–H–O system for diamond deposition at the edge of diamond growth and no-growth regions. The deposition process was monitored by OES. Diamond coatings were characterized by Raman spectroscopy and SEM.

According to diamond peak in Raman measurements, we have successfully grown diamond coatings in/along the no diamond growth region due to the specific system set-up. Decreasing of the hydrogen concentration caused (i) increase in deposition rate maintaining good quality, (ii) change of morphology from discrete diamond grains over hundred nanometer well faceted grains, finer tens nanometer granular structures (≈ 30 nm) to porous diamond nanowires, (iii) the presence of the non-diamond phases mostly located along grain boundaries which is later reduced by substituted oxygen.

An interesting feature was a monotonic increase in the deposition rate with increasing CH_4 and CO_2 concentration in the gas mixture. It is still an opened question if the CVD process is dominated by carbon from CO_2 or by suppressing of H_2 etching due to lower concentration. The influence of substrate temperature (not discussed in this article) to the deposition rate is prominent due to a temperature controlled growth process [22].

Acknowledgements This work was financially supported by the research projects P205/12/0908 (GAČR) and P108/12/G108 (GAČR). This work occurred in frame of the LNSM infrastructure.

References

- [1] C. E. Nebel, *Nature Mater.* **2**, 431 (2003).
- [2] Y. Hirose and Y. Terasawa, *Jpn. J. Appl. Phys.* **25**, L519 (1986).
- [3] T. Kawato and K. Kondo, *Jpn. J. Appl. Phys.* **26**, 1429 (1987).
- [4] J. A. Mucha, D. L. Flamm, and D. E. Ibbotson, *J. Appl. Phys.* **65**, 3448 (1989).
- [5] M. Frenklach and H. Wang, *Phys. Rev. B* **43**, 1520 (1991).
- [6] K. Teii, H. Ito, M. Hori, T. Takeo, and T. Goto, *J. Appl. Phys.* **87**, 4572 (2000).
- [7] Y. Kouzuma, K. Teii, K. Uchino, and K. Muraoka, *Phys. Rev. B* **68**, 064104 (2003).
- [8] T. Gries, S. de Persis, L. Vandenbulcke, C. Met, J. L. Delfau, and M. I. De Barros-Bouchet, *Diam. Relat. Mater.* **18**, 730 (2009).
- [9] T. Gries, L. Vandenbulcke, S. de Persis, O. Aubry, and J. L. Delfau, *J. Vac. Sci. Technol. B* **27**, 2309 (2009).
- [10] P. K. Bachmann, D. Leers, and H. Lydtin, *Diam. Relat. Mater.* **1**, 1 (1991).
- [11] P. K. Bachmann, H.-J. Hagemann, H. Lade, D. Leers, F. Picht, D. U. Wiechert, and H. Wilson, *MRS Proc.* **339**, 267 (1994).
- [12] J.-T. Wang, Y.-Z. Wan, D. W. Zhang, Z.-J. Liu, and Z.-Q. Huang, *J. Mater. Res.* **12**, 3250 (2011).
- [13] S. C. Eaton and M. K. Sunkara, *Diam. Relat. Mater.* **9**, 1320 (2000).
- [14] G. Bhimarasetti and M. K. Sunkara, *Thin Solid Films* **440**, 78 (2003).
- [15] A. Kromka, S. Potocký, J. Cermák, B. Rezek, J. Potmesil, J. Zemek, and M. Vanecek, *Diam. Relat. Mater.* **17**, 1252 (2008).
- [16] A. Kromka, O. Babchenko, T. Izak, K. Hruska, and B. Rezek, *Vacuum* **86**, 776 (2012).
- [17] A. Kromka, B. Rezek, M. Kalbacova, V. Baresova, J. Zemek, C. Konak, and M. Vanecek, *Adv. Eng. Mater.* **11**, B71 (2009).
- [18] A. J. Neves and M. H. Nazaré, *Properties, Growth and Applications of Diamond* (INSPEC, EMIS Group, London, 2001).
- [19] S. Bühlmann, E. Blank, R. Haubner, and B. Lux, *Diam. Relat. Mater.* **8**, 194 (1999).
- [20] S. L. Heidger, *MRS Online Proc. Library* **383**, 319 (1995).
- [21] P. J. Fallon and L. M. Brown, *Diam. Relat. Mater.* **2**, 1004 (1993).
- [22] S. Potocký, A. Kromka, J. Potmesil, Z. Remes, Z. Polackova, and M. Vanecek, *Phys. Status Solidi A* **203**, 3011 (2006).

A.4

Influence of surface wave plasma deposition conditions on
diamond growth regime



Influence of surface wave plasma deposition conditions on diamond growth regime



O. Babchenko^{a,b,*}, Š. Potocký^a, T. Ižák^a, K. Hruška^a, Z. Bryknar^b, A. Kromka^a

^a Institute of Physics, ASCR, v.v.i., Cukrovarnická 10, 16200 Prague, Czech Republic

^b Czech Technical University in Prague, Faculty of Nuclear Sciences and Physical Engineering, Trojanova 13, 12000 Prague, Czech Republic

ARTICLE INFO

Available online 10 January 2015

Keywords:

Surface wave plasma
Diamond thin films
Growth kinetics
Scanning electron microscopy
Raman spectroscopy
Optical emission spectroscopy

ABSTRACT

The influence of deposition conditions on the diamond thin film growth in linear antenna microwave plasma system, also known as surface wave plasma reactor, is presented in this study. Depending on the process pressure the two growth regimes were identified. At high pressures (over 50 Pa) dominates the re-nucleation regime that results in ultra-small diamond crystals, while at low pressures (below 10 Pa) dominates the lateral growth regime that leads to formation of large diamond crystals. Next, it was shown that the distance of substrates from “hot” plasma region influences the diamond growth kinetics and results in growth regimes shift. Altogether, the observed results contribute to a better understanding of the diamond growth phenomena in surface wave plasma systems. Thus, it allows controllable growth of diamond films with tailored properties (morphology, roughness, etc.).

© 2015 Elsevier B.V. All rights reserved.

1. Introduction

Diamond thin films due to inherent combination of outstanding properties are traditionally considered as promising candidates for a wide range of applications, e.g. micro-electro-mechanical systems, surface acoustic wave devices, optical elements, and biosensors. [1–3]. On the other hand, there are several limitations for their broad usage. One of them is the lack of a reliable technique for uniform diamond deposition on industrially relevant areas. This demand could be covered, for instance, by using of surface wave plasma (SWP) systems.

The SWP systems are well working for solar cells and semiconductor industries, however, their use for diamond film deposition started only recently [4–7]. As it was found, SWP has a great advantage comparing to focused plasma [8,9] or hot filament [10,11] reactors which are generally used for diamond chemical vapour deposition (CVD). Potentially, the deposition area of the diamond films in the SWP system could be as large as 1 m² or even more, depending on the antennas' configuration. The next important advance of SWP reactors comparing to standard focused plasma or hot filament systems is a lower substrate loading by temperature and plasma in general [4,12]. This, for example, gives opportunity to deposit diamond on temperature sensitive optical elements [13]. Moreover, the large distance to plasma region (several cm) allows diamond deposition on the 3D substrates [14] or substrates with complicated geometry.

However, together with the aforementioned advances, the SWP systems have their own drawbacks. For example, the plasma density

and the expansion in the SWP reactor chamber are significantly affected by the process pressure [15]. Next, the maximal diamond growth rate in the SWP system is much lower comparing to focused plasma [8,9] or hot filament [10,11] reactors. Thus, the issue of successful diamond CVD in SWP systems is attractive but challenging. For example, one of the possible solutions to enhance the growth rate is the addition of oxygen containing gases to the process gas mixture [7,9,16]. The other possibility is increasing the microwave power [6]. However, in this case the substrate heating by plasma will increase as well. Therefore, the aim of any technological effort is to determine the stable SWP conditions suitable for CVD of diamond films of required properties.

In the present work we discuss the effect of pressure on the diamond growth by linear antenna pulsed microwave plasma CVD system. Depending on the process pressure we identify two main diamond growth regimes. In the case of diamond deposition at high pressure (over 50 Pa, low plasma volume) we observed the dominance of the so-called re-nucleation regime which led to the growth of ultra-small diamond crystals. On the other hand, the larger diamond crystals formed at low pressure processes (below 10 Pa, high plasma volume) are attributed to the dominance of lateral growth. Complementary to pressure dependence the influence of distance from antennas to the substrate (4 or 7 cm) was also studied.

2. Material and methods

The one-side polished Si (100) wafers (in size of 1 × 1 cm²) were used as substrates. The ultrasound agitation in water based diamond nano-powder suspension (powder from Metals and Chemicals Corp. Ltd., Kyobashi with size distribution 4–5 nm) was utilized as the seeding technology [7]. The diamond depositions were performed in the large

* Corresponding author at: Cukrovarnická 10, 16200 Prague, Czech Republic. Tel.: +420 220 318 482; fax: +420 220 318 468.

E-mail address: babchenko@fu.cz (O. Babchenko).

area linear antenna microwave plasma (LAMWP) system (modified AK 400, Roth & Rau MicroSystems). As it was aforementioned this system is based on the surface wave propagation and plasma ignition along linear antennas. The process gas mixture was 2.5% of CH₄ and 10% of CO₂ in hydrogen atmosphere [7,13]. The process pressure was set at a value within the range from 8 Pa to 100 Pa. The other growth parameters were as follows: microwave power 1700 W and substrate temperature maintained in the range 550–560 °C by resistive heating adjusting. The time of each deposition was 20 h while the films thickness varied from 60 nm to 280 nm. The experiments were realized at two constant distances of the substrate holder from antennas: far position (the distance from substrate holder to antennas is 7 cm) and close position (the distance is 4 cm).

The study on plasma discharge was realized by optical emission spectroscopy (OES) using Jobin Yvon imaging spectrometer with focal length of 500 mm and diffraction grating of 1200 g/mm. The spectral resolution in this configuration is 0.06 nm in the collected spectral region (280 nm to 890 nm). The emitted light was collected at two positions (far and close) related to the substrate holder position during the deposition process. The emissions were collected by the fibre-optic cable with 50 mm long, cylindrical (ø10 mm) collimator, placed perpendicularly to the antennas axis. The diffracted light was detected by CCD detector (1024 × 512 pixels). For atomic hydrogen amount evaluation spectra were collected within the pressure range from 7 Pa to 150 Pa using Ar addition to the process gas mixture. The sensitivity of CCD detector was calibrated on relative spectral intensity by tungsten lamp with known relative spectral radiation distribution.

After the diamond deposition the samples were analyzed by Raman spectroscopy (inVia Reflex Raman microscope, Renishaw, excitation wavelength 325 nm) and scanning electron microscopy (SEM, e_LiNE system writer, Raith).

3. Results

Fig. 1 shows the distribution of the Ar plasma discharge in LAMWP system at two different pressures: 100 Pa and 10 Pa. From the photos it is evident that at high pressure the plasma is localized in a close vicinity to the antennas (Fig. 1a), while at low pressure it expands towards the substrate holder (Fig. 1b) which in this case is at the distance 7 cm from antennas. In our previous study it was observed that when the pressure is reduced from 150 Pa to 10 Pa, the plasma density at the

proximity of the substrate holder increased by 3 orders of magnitude [15]. This gives the evidence of pressure effect on plasma species distribution in the process chamber.

The representative plasma emission spectra in the region of 350–700 nm collected by OES at three different pressures are shown in Fig. 2. While Fig. 2a shows spectra related to the far distance of substrate holder from antennas, Fig. 2b shows spectra related to the close distance of substrate holder to antennas.

All measured emission spectra are dominated by the H_α line (off scale) at 656.3 nm and H_β line at 486.1 nm (Balmer series) [21,22]. A broad region from 580 nm to 640 nm in the spectra is attributed to the hydrogen molecular bands (Fulcher-α region) [6,23]. The other observable spectral lines are attributed to H_γ at 434.1 nm, H_δ at 410.2 nm (Balmer series), C₂ emission bands between 450 and 475 nm, CO at 493.7 nm and 518.7 nm, CH⁺ between 417 nm and 422 nm and C₃ at 406 nm [21,22,24]. In the shown spectra (Fig. 2) the highest intensity of all spectral lines in the case of far distance position was at 8 Pa while in the case of close distance position the highest intensity was observed at 20 Pa.

The evaluation of hydrogen amount in the chamber was done according to the calculated ratio of H_α line (656.3 nm) to Ar line (750 nm) intensities (Fig. 3) in the pressure range of 7–150 Pa for far and close substrate holder distances from antennas respectively. The calculated ratio in both cases with pressure increasing from 7 Pa to 150 Pa increases up to the maximum value (estimated as the highest hydrogen amount) and then decreases. For the far distance the highest value was found at pressure 15 Pa while for the close distance position it was found at pressure 20 Pa (i.e. shifted towards the higher pressures). From the pressure 75 Pa to 150 Pa the calculated ratios for far and close distances were similar.

The morphologies of diamond films deposited at different pressures (arranged from 100 Pa to 8 Pa) and two distances of the substrate holder from antennas are shown in Fig. 4. The insets give detailed image of samples with small grains. The far distance samples (substrate holder distance from antennas is 7 cm) grown at pressures from 100 Pa to 30 Pa have similar morphology where diamond crystal size is estimated as <30 nm (Fig. 4a–c). Besides, for pressures 50 Pa and 30 Pa the non-negligible formation of ballas-like structures [2] in size of up to 200 nm for 50 Pa and up to 300 nm for 30 Pa was observed. For sample deposited at 20 Pa, the 100 nm large irregular clusters are observed (Fig. 4d). The deposition at 10 Pa resulted in the growth of large

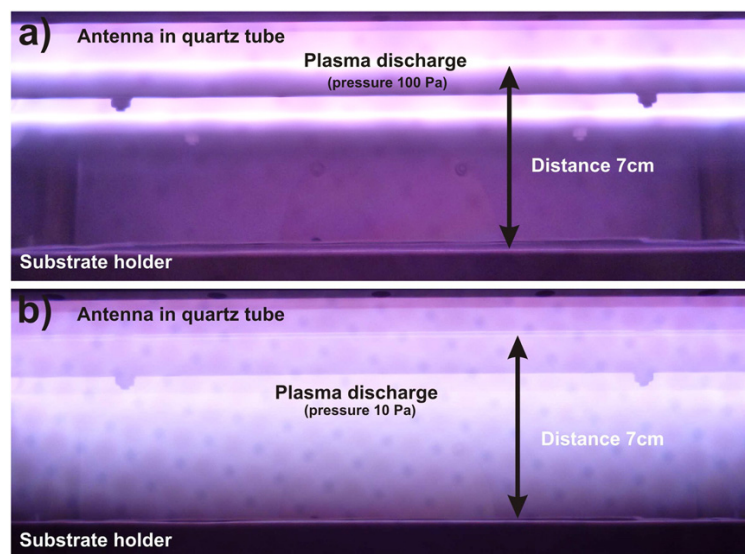


Fig. 1. The Ar plasma discharge in the linear antenna microwave plasma system at high (a) and low (b) process pressure (100 Pa and 10 Pa, respectively).

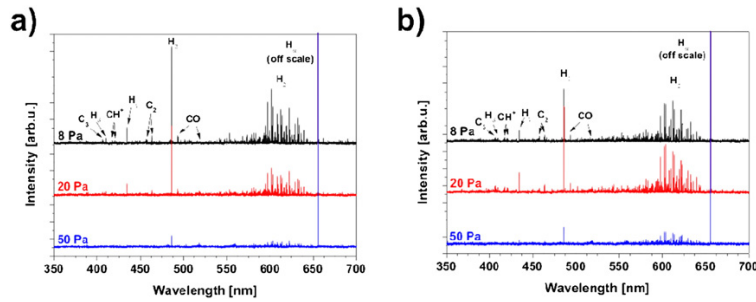


Fig. 2. The representative plasma discharge spectra from LAMWP system collected by OES at different pressures and far (a) and close (b) distance to antennas.

diamond crystals (up to 200 nm) with cracks and defects (Fig. 4e). Further pressure decreasing to 8 Pa led to the growth of diamond film consisting of randomly oriented diamond crystals with clear facets (Fig. 4f). The maximal size of the crystals is up to 200 nm.

Concerning the close distance samples (substrate holder distance from antennas is 4 cm) they have similar morphologies comparing to far distance samples, but the evidence of large diamond crystals formation is shifted towards higher pressures (Fig. 4g–l). Formation of ballas-like structures (up to 300 nm in size) was found only for samples deposited at a pressure of 100 Pa. The other important difference between close distance and far distance samples is found for films deposited at 8 Pa (Fig. 4f,l). In this case, for close distance samples (Fig. 4l) the porous layer formation with features up to 600 nm in size was observed.

Raman spectra of the grown films are shown in Fig. 5 and they correlate well with the SEM images. The measured spectra are typical for diamond films: the G-band (graphitic) centred at 1570–1600 cm^{-1} , D-band (disordered) at 1350–1400 cm^{-1} , diamond peak at $\sim 1332 \text{ cm}^{-1}$, and the band related to transpolyacetylene residues at grain boundaries (1150–1170 cm^{-1}) [17–19]. The intensity of the detected peaks depends on the ratio of sp^2 to sp^3 carbon bonds in the film. The presence of sp^2 carbon bonds (graphitic phases) is attributed to bands around 1570–1600 cm^{-1} and 1350–1400 cm^{-1} [17,18], while the diamond peak at 1332 cm^{-1} is related to sp^3 carbon phase. The quality of diamond is usually characterized by the ratio of sp^3 to sp^2 carbon bonds, i.e. by ratio of diamond to non-diamond phases. The diamond films quality was evaluated regarding to collected Raman spectra. The low ratio of diamond to non-diamond phase is often attributed to the nanocrystalline character of diamond films with a large amount of grain boundaries (rich in graphitic phase) [17–19]. On the other hand, high ratio of sp^3/sp^2 (i.e. dominating peak at 1332 cm^{-1}) indicates higher quality of diamond films with larger grains and less grain boundaries [17–19].

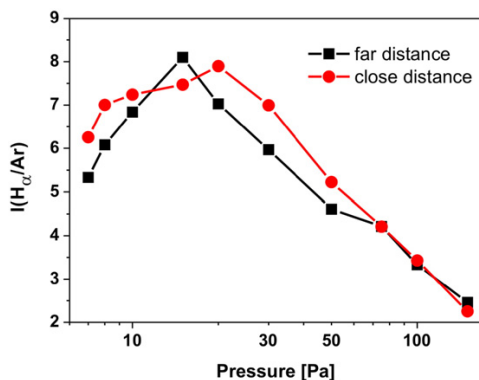


Fig. 3. The calculated from emission spectra ratio of H_α line (656.3 nm) intensity to Ar line (750 nm) intensity as the function of pressure.

Fig. 6a shows the ratio of diamond to non-diamond phases of the deposited diamond films (extrapolated from Raman spectra) as the function of pressure. The diamond film quality (primarily attributed to amount of diamond phase) was evaluated according to calculations from the fitted Raman spectra of samples using the following equation: $I_{\text{diam}} / (I_D + I_G)$, where I_{diam} is the diamond peak area at a frequency of $\sim 1332 \text{ cm}^{-1}$, while I_D and I_G represent the band areas at $\sim 1340\text{--}1380 \text{ cm}^{-1}$ and $\sim 1500\text{--}1600 \text{ cm}^{-1}$, respectively (the origin of these bands was described above). No correlation factor for sp^3 or sp^2 was used, thus the ratio represents only the trend in film quality and is a qualitative data. At high pressures, i.e. $\geq 30 \text{ Pa}$ for far distance sample and $\geq 50 \text{ Pa}$ for close distance sample, the ratio of $I_{\text{diam}}/(I_D + I_G)$ is low which indicates high amount of non-diamond phase in the films [20]. This ratio increases with pressure decreasing (Fig. 6a). The slope of the plotted data from 10 Pa to 30 Pa for far distance samples and from 20 Pa to 50 Pa for close distance samples copies each other, which also indicates the shift of growth kinetic for different distances to antennas. The decrease of sp^3/sp^2 ratio for close distance samples at low pressures $\leq 10 \text{ Pa}$ in the graph is not clear yet; we supposed, it could be related to the porous-like character of this film (Fig. 4l) or decreased film thickness.

Fig. 6b summarizes the growth rates of deposited samples calculated from the film thicknesses. The growth rate reaches maximum (i.e. 13–14 nm/h) at process pressure of 20 Pa or 30 Pa for far and close distances, respectively.

4. Discussion

The spectra collected by OES in the LAMWP system (Fig. 2) is a combination of emission caused by a continuous recombination radiation emission in the UV region, spectral emission lines from excited atoms and spectral emission bands from excited molecules. Concerning the observed emission lines it is necessary to mention the following. Although, typical for diamond CVD, C_2 emission bands between 450 and 475 nm were observed in the spectra, they were rather weak comparing to those reported by other authors [21]. On the other hand, we observe evidence of CO lines at 493.7 nm and 518.7 nm (more evident for higher pressures) and CH^+ lines between 417 and 422 nm in the spectra [21,22,24]. Surprisingly, we found no (or negligibly weak) evidence of CH line at 431 nm [21,22]. The emission related to molecular hydrogen was observed in the range of 580–640 nm [6,23]. For now the role of these differences between typical CVD process and process in LAMWP system is not clear, primarily due to not many publications related to OES in SWP systems. We propose that better understanding of possible chemical reaction in SWP requires the simulational study that will take into account chemical composition changes with increasing distance from hot plasma region (near antennas). Nevertheless, the SEM (Fig. 4) observation and Raman spectra (Fig. 5) measurements confirmed diamond growth by the LAMWP system and give practical output for diamond growth with tailored properties.

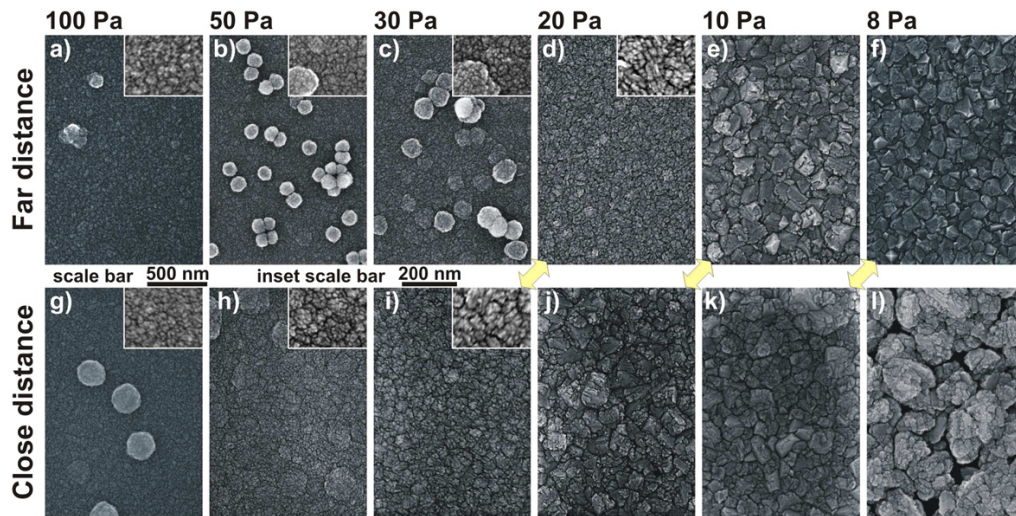


Fig. 4. SEM images of diamond films deposited at far (a–f) and close (g–l) distance of substrates to antennas and at different pressures varied from 100 Pa to 8 Pa; i.e. a), g) 100 Pa, b), h) 50 Pa, c), i) 30 Pa, d), j) 20 Pa, e), k) 10 Pa, and f), l) 8 Pa. The insets give detailed view of films with small grains. The arrows in the figure highlight the same morphology (i.e. the same growth regime) of diamond films deposited at ‘close distance’ compared to ‘far distance’.

With regard to our previous observations of plasma density increasing [15] and changes of emission line intensity depending on distance to antennas and pressure (Figs. 2 and 3) we assume changing of process chemistry in the close vicinity of substrates. Based on SEM and Raman measurements (Figs. 4 and 5) we propose that the diamond renucleation is the dominating growth process at the high pressure (≥ 50 Pa) depositions which results in diamond films with ultra-small crystals [2,20]. The low pressure depositions (≤ 10 Pa) are characterized by the dominance of the lateral diamond growth [2,20]. These differences in the growth processes can be explained by the following. It is recognized that atomic hydrogen is one of the most important components for successful diamond growth [2], involved in: (i) etching of non-diamond phases, (ii) stabilization of sp^3 dangling bonds and (iii) enhancing of the dissociation reactions [11,25,26]. At high pressures the recombination rate of atomic hydrogen increases, thus its concentration decreases [27]. On the other hand, at low pressures the plasma density and thus species concentration is low [26]. This statement is supported by the trend shown in Fig. 3. Here, with pressure increasing from 7 Pa to 150 Pa the ratio of H_{α} line to Ar line intensities increases up to the maximal value (correspond to observed high growth rate in Fig. 6b) which is estimated as the peak of atomic hydrogen amount and then decreases which let us claim that hydrogen concentration in the substrate vicinity decrease as well. Tsugawa et al. pointed out the importance of hydrogen and growth species diffusion out from the hot plasma region [28,29] which allows diamond deposition at far distance. The indication of this could be found in Fig. 3 where the ratio of H_{α} line

to Ar line intensities for close position generally are higher than that for far position (higher hydrogen amount). Lowering the process pressure from high values leads to increasing the mean free path of particles in plasma and thus change in the amount of atomic hydrogen and growth species (or simply plasma density [15]) in the close vicinity to the substrate [11,25,27] and Fig. 2. Besides, in our gas mixture we used 10% of CO_2 (regarding to hydrogen) that also influenced the growth regime [9,16]. The oxygen-based species partially replaces the role of hydrogen (e.g. etching of non-diamond phases) which is mainly taking the role at low temperature processes [16] and enhances the growth rates [9].

On the basis of calculated growth rates (Fig. 6b) and keeping in mind our previous observation of plasma density behaviour [15] and measured OES data (Figs. 2 and 3) we can compare the growth kinetics for different pressures. As it was shown, despite the similar morphology of diamond films grown at far distance and pressures ≥ 30 Pa (Fig. 4a–c), the growth rate is increased from approximately 3 nm/h at pressure 100 Pa to 6 nm/h at 30 Pa (Fig. 6b), together with diamond quality (i.e. slightly increased amount of sp^3 carbon forms, Fig. 6a). That is well agreed with the increasing of the growth species concentration (due to plasma expansion) according to Refs. [11,15,25,27] and OES observation (Figs. 2a and 3) and thus faster carbon deposition. However, the lack of proper species for the lateral growth (e.g. atomic hydrogen as can be seen from Fig. 3) leads to the formation of small diamond crystals [11,20]. The origin of larger clusters (Fig. 4b, c) observed on the films deposited at pressures 50 Pa (clusters up to 200 nm) and 30 Pa (clusters up to 300 nm) is not fully clear yet. As it can be seen from

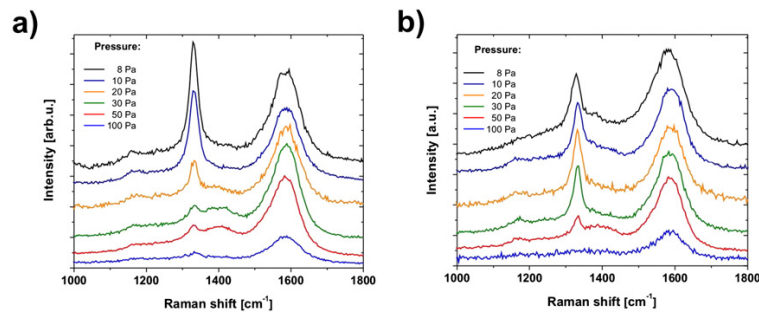


Fig. 5. Raman spectra of diamond films deposited at different pressures and at far (a) and close (b) distance of the substrates from the antennas.

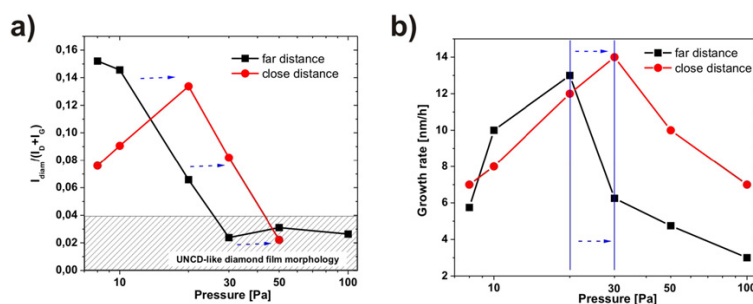


Fig. 6. The intensity ratio of diamond phase (I_{diam}) to non-diamond carbon (I_D – disordered, I_G – graphitic) evaluated from deconvoluted Raman spectra (a). The calculated growth rates of deposited diamond films as the function of pressure at different distance to antennas (b).

the insets these features are formed (or covered) from the small diamond crystals. We assume that its formation could be attributed to plasma-nucleated crystals as proposed by Tsugawa et al. [28] or dust particles [22]. The growth rate reaches the maximum value (13 nm/h) for sample deposited at 20 Pa (Fig. 6a), and the diamond film quality increases too. The highest growth rate supposes the optimal surface reactions, i.e. diamond film deposition and by-products removing [11,26], which agrees with the relatively high amount of hydrogen according Fig. 3. Further decrease of the pressure to 10 Pa resulted in the formation of diamond crystals with evident facets (Fig. 4e) and higher sp^3/sp^2 ratio (Fig. 6a), but lower growth rate (10 nm/h in Fig. 5). In this case, the atomic hydrogen localized at substrate surface due to low pressure in high concentration [27], etches sp^2 carbon forms and enhances the formation of higher quality diamond crystals. The growth rate decrease, probably, is the indication of growth species decreasing affected by pressure [26].

Finally, the highest quality diamond film was observed at the pressure of 8 Pa, but its growth rate decreased to 6 nm/h. This could be attributed to the drop of the plasma density (i.e. less growth species) rather than to high atomic hydrogen amount [16,27–29]. Indeed, in Fig. 3 it is shown that intensity of hydrogen signal is decreasing with pressure decreasing from 15 Pa to 7 Pa. Nevertheless, the amount of atomic hydrogen should be high enough for crystal formation.

In the case of diamond films deposited at close distance to antennas, similar dependences were observed. However, due to the shorter distance from the substrates to the hot plasma region the growth regimes are shifted to higher pressures. This is attributed to the distribution of growth species and active radicals whose density changes “vertically” in the plasma (compare spectra in Fig. 2 and trends in Fig. 3 for far and close distance). The diamond growth rates for pressures up to 20 Pa are nearly the same as in the case of far distance samples or slightly lower (Fig. 6b). Probably, this is affected by process chemistry near the samples’ surface (more efficient etching) because plasma density (and thus concentration growth species) must be high enough [15]. The growth rates from 20 Pa are slightly higher for close distance than for far distance. It is supposed that this effect appears only due to the increased amount of growth species (e.g. hydrogen according Fig. 3), because the temperature increasing (due to closer position to hot plasma region) was compensated by lower resistive heating of the substrate holder.

It should be mentioned that the substrate holder position clearly influences the morphology of grown diamond films and the growth rates (shift of large grain formation towards the higher pressure for close position). The high influence of substrate holder position was observed for the deposition homogeneity within the process area as well. The temperature and plasma load of samples placed closer to antennas (hot plasma region) is increased comparing to those at far position. In our case the system design prohibits sample positioning at close vicinity to antennas due to low plasma stability. It seems to be that further approaching of the samples towards the antennas (hot plasma region) will approximate the process conditions to focused plasma systems,

i.e. the case of Bachman’s diagram and no diamond growth due to very high etching rate caused by oxygen [2,20,26]. In the hot filament system the distance to filaments (hot active species) significantly affects the diamond film morphologies and growth rate trends [25,27,30]. Nevertheless, the formation of small grained diamond films at low pressures is generally observed [25,27,30]. The observed trends of diamond film growth in the LAMWP system demonstrate the difference of this system from typical focused MW plasma or hot filament reactors.

5. Conclusions

We studied the influence of pressure on the diamond film growth by the linear antenna pulsed microwave plasma CVD system at two different distances of the substrates from antennas (i.e. 7 and 4 cm). We observed that depending on the process pressure two main diamond growth regimes are identified. In the case of high pressure deposition (over 50 Pa, at low plasma volume) we suggest the dominance of the re-nucleation regime and thus growth of diamond film with ultra-small crystals. On the other hand, the larger diamond crystals formed at low pressure (below 10 Pa, at high plasma volume) were attributed to the dominance of the lateral growth. We demonstrated that closer substrate distance to the antennas shift the formation of large diamond crystal towards the higher pressures. We proposed that these observations are caused by different plasma densities or concentration of the growth species in the substrate vicinity. Altogether, the observed results contribute to better understanding of the diamond growth phenomena and mastering of diamond film growth in the surface wave plasma systems.

Acknowledgements

Authors acknowledge the financial support of Czech Science Foundation project 14-05053S. This work occurred in the frame of the LNSM infrastructure.

References

- [1] E. Kohn, P. Gluche, M. Adamschik, *Diam. Relat. Mater.* 8 (1999) 934–940.
- [2] P.W. May, *Philos. Trans. R. Soc. A Math. Phys. Eng. Sci.* 358 (2000) 473–495.
- [3] B. Rezek, M. Kratka, E. Ukraintsev, O. Babchenko, A. Kromka, A. Broz, et al., in: P.A. Serra (Ed.), *New Perspect. Biosens. Technol. Appl. InTech*, 2011.
- [4] K. Tsugawa, M. Ishihara, J. Kim, M. Hasegawa, Y. Koga, *New Diamond Front. Carbon Technol.* 16 (2006) 337–346.
- [5] J. Kim, K. Tsugawa, M. Ishihara, Y. Koga, M. Hasegawa, *Plasma Sources Sci. Technol.* 19 (2010) 015003.
- [6] F. Fendrych, A. Taylor, L. Peksa, I. Kratochvilova, J. Vleck, V. Rezacova, et al., *J. Phys. D: Appl. Phys.* 43 (2010) 374018.
- [7] A. Kromka, O. Babchenko, T. Izak, K. Hruska, B. Rezek, *Vacuum* 86 (2012) 776–779.
- [8] F. Silva, K. Hassouni, X. Bonnin, A. Gicquel, *J. Phys. Condens. Matter* 21 (2009) 364202.
- [9] Y. Liou, A. Inspektor, R. Weimer, D. Knight, R. Messier, *J. Mater. Res.* 5 (1990) 2305–2312.
- [10] V. Malcher, A. Mrška, A. Kromka, A. Šatka, J. Janík, *Curr. Appl. Phys.* 2 (2002) 201–204.

- [11] P.W. May, M.N.R. Ashfold, Y.A. Mankelevich, J. Appl. Phys. 101 (2007) 053115.
- [12] T. Izak, O. Babchenko, M. Varga, S. Potocky, A. Kromka, Phys. Status Solidi B 249 (2012) 2600–2603.
- [13] O. Babchenko, Z. Remes, T. Izak, B. Rezek, A. Kromka, Phys. Status Solidi B 248 (2011) 2736–2739.
- [14] Z. Remes, H. Kozak, B. Rezek, E. Ukrainsev, O. Babchenko, A. Kromka, et al., Appl. Surf. Sci. 270 (2013) 411–417.
- [15] Š. Potocký, M. Čada, O. Babchenko, T. Ižák, M. Davydova, A. Kromka, Phys. Status Solidi B 250 (2013) 2723–2726.
- [16] J. Stiegler, T. Lang, M. Nygard-Ferguson, Y. von Kaenel, E. Blank, Diam. Relat. Mater. 5 (1996) 226–230.
- [17] A. Ferrari, J. Robertson, Phys. Rev. B 61 (2000) 14095–14107.
- [18] S. Prawer, R.J. Nemanich, Philos. Trans. R. Soc. A Math. Phys. Eng. Sci. 362 (2004) 2537–2565.
- [19] H. Kuzmany, R. Pfeiffer, N. Salk, B. Günther, Carbon 42 (2004) 911–917.
- [20] J.J. Gracio, Q.H. Fan, J.C. Madaleno, J. Phys. D: Appl. Phys. 43 (2010) 374017.
- [21] M.A. Elliott, P.W. May, J. Petherbridge, S.M. Leeds, M.N.R. Ashfold, W.N. Wang, Diam. Relat. Mater. 9 (2000) 311–316.
- [22] T. Gries, L. Vandenbulcke, J.N. Rouzaud, S. de Persis, Plasma Sources Sci. Technol. 19 (2010) 025015.
- [23] Z. Qing, D.K. Otorbaev, G.J.H. Brussaard, M.C.M. vandeSanden, D.C. Schram, J. Appl. Phys. 80 (1996) 1312–1324.
- [24] C. Patacsil, G. Malapit, H. Ramos, J. Plasma Fusion Res. Ser. 7 (2006) 145–149.
- [25] S. Schwarz, S.M. Rosiwal, M. Frank, D. Breidt, R.F. Singer, Diam. Relat. Mater. 11 (2002) 589–595.
- [26] L. Gueroudji, N.M. Hwang, Diam. Relat. Mater. 9 (2000) 205–211.
- [27] R. Brunsteiner, R. Haubner, B. Lux, Diam. Relat. Mater. 2 (1993) 1263–1270.
- [28] K. Tsugawa, M. Ishihara, J. Kim, Y. Koga, M. Hasegawa, Phys. Rev. B 82 (2010) 125460.
- [29] K. Tsugawa, S. Kawaki, M. Ishihara, J. Kim, Y. Koga, H. Sakakita, et al., Diam. Relat. Mater. 20 (2011) 833–838.
- [30] X. Liang, L. Wang, H. Zhu, D. Yang, Surf. Coat. Technol. 202 (2007) 261–267.

A.5

Perspectives of linear antenna microwave system for growth of various carbon nano-forms and its plasma study

Perspectives of linear antenna microwave system for growth of various carbon nano-forms and its plasma study

Štěpán Potocký*, Martin Čada, Oleg Babchenko, Tibor Ižák, Marina Davydova, and Alexander Kromka**

Institute of Physics AS CR, v.v.i., Cukrovarnická 10, 16253 Praha, Czech Republic

Received 17 April 2013, revised 5 October 2013, accepted 15 October 2013

Published online 13 November 2013

Keywords CNT, Langmuir probe, nanocrystalline diamond, plasma enhanced CVD, Raman spectroscopy, SEM

* Corresponding author: e-mail potocky@fzu.cz, Phone: +420 220 318 437, Fax: +420 233 343 184

** e-mail kromka@fzu.cz, Phone: +420 220 318 437, Fax: +420 233 343 184

The versatility of linear antenna microwave plasma system, growth of diamond films with variable grain sizes, and efficient synthesis of oriented carbon nanotubes when combined with radiofrequency substrate bias were studied. Grown diamond films and carbon nanotubes are characterized by Raman spectroscopy and scanning electron microscopy. Successful surface functionalization of carbon nanotubes without their

destruction is shown in agreement to plasma state as measured by Langmuir probe. We show that diamond growth from large to ultra-small size grains can be easily driven by total gas pressure. Langmuir probe measurements indicate low electron effective energy at substrate position and higher ion energy at the lowest total gas pressure.

© 2013 WILEY-VCH Verlag GmbH & Co. KGaA, Weinheim

1 Introduction Demand on the growth of diamond, CNT, graphene, and other carbon allotropes over large areas with tunable morphological properties are a driving force for relatively matured state of classical microwave plasma chemical vapor deposition (CVD) techniques. A versatile deposition system can benefit from the multicomponent material deposition by a simple change of process parameters. Design and optimization of microwave plasma reactors is dominated by high pressure systems (10–100 kPa). However, such high pressure microwave plasma [1] is limited in the plasma volume represented either by a ball or an ellipsoid in a typical diameter up to 7 cm [2].

Instead of high pressure systems, microwave surface wave (MW-SW) plasma utilizing linear antenna(s), or slot window(s) become an attractive CVD method for growth of carbon allotropes over large areas ($>500\text{ cm}^2$) [3–5]. The deposition area can be simple enlarged by increased number of antennas or by prolonging their length. Moreover, MW-SW plasma combined with DC or RF bias extends specific plasma parameters [6] and hence properties of formed materials.

The growth of CNT becomes a routine by variety of deposition techniques [7, 8]. In these CVD techniques, catalytic materials are used as nickel, iron, cobalt or their

derivatives [9]. Among several techniques of CNT synthesis available today, plasma CVD is the most popular and widely used technique [10].

The large area diamond growth, an additional carbon allotrope form, is also routinely achieved by standard or modified hot filament CVD processes [11]. Unfortunately, filaments limit their usage for specific applications due to filament mechanical non-stabilities and chemical sensitivities to reactive gases as oxygen, etc.

In this work, we present the large area CVD deposition system where the growth of diamond films and CNTs is altered by optimized process parameters within one deposition apparatus. The CVD growth is done by using a low pressure linear antenna microwave plasma CVD system [12]. Requirements of scale-up, high production yield and versatility of deposited material (diamond, CNT, or even graphene) are satisfied on various substrates [13].

2 Experimental Carbon nanotubes were grown on (100) oriented Si substrates (in size of $10 \times 10\text{ mm}^2$) with thin SiO_2 layer (approx. 1200 nm) on which Ni catalytic layer (6 nm) was evaporated. First, the substrate with nickel catalyst was pretreated for 10 min in hydrogen plasma at following process conditions: total MW power $P = 1700\text{ W}$

at each antenna side, total gas pressure $p = 20$ Pa, and substrate temperature $T_s = 650$ °C. The CNT growth was done at parameters: $P = 1700$ W at each antenna side, RF induced negative substrate bias voltage $U_b = -200$ V, $p = 6$ Pa, $\text{CH}_4/\text{CO}_2 = 2/1$ ratio, $T_s = 650$ °C and antenna to substrate distance $z = 70$ mm. The process duration was varied between 10 and 40 min. Both, the pretreatment and growth steps, including oxygen termination of CNTs, were performed in linear antenna microwave plasma enhanced CVD (LA-MW-PECVD) deposition system [12]. Oxygen termination of CNTs for 5 min was applied to control their surface wettability as described in previous studies [14].

LA-MW-PECVD was used also for deposition of diamond thin films on (100) oriented Si substrates in size of 10×10 mm². Before the CVD growth, Si substrates were ultrasonically pretreated in a suspension of deionized water and ultradispersed detonation diamond powder (diameter 5–10 nm, New Metals and Chemicals Corp. Ltd., Kyobashi) [15] giving density of seeds in up to 10^{11} cm⁻². Thin diamond layers were grown from $\text{H}_2/\text{CH}_4/\text{CO}_2$ gas mixture (CH_4 up to 2.5%, CO_2 up to 10%). Other process parameters were as follows: $P = 2500$ W at each antenna side, total gas pressure p varied between 6 and 200 Pa and $T_s \approx 750$ °C. The substrate table was on floating potential. The antenna to substrate distance z was kept at 70 mm.

Surface morphology, thickness, and grain size of the deposited coatings were characterized by scanning electron microscopy in top and cross-section views (SEM, e_LiNE writer, Raith GmbH). The films were examined by Raman spectroscopy (Renishaw In Via Reflex Raman spectrometer, excitation wavelength of 325 nm). Surface Energy Evaluation System (Advex Instruments, s.r.o.) was used for contact angle measurements. Spatially resolved Langmuir probe measurements were carried out to estimate plasma temperature, plasma density and plasma potential at three different distances between antenna and substrate, i.e. $z = 16, 33,$ and 65 mm. High purity wolfram cylindrical probe of 100 μm diameter and 1 mm length was used. Selective time resolved measurements were done due to the time modulation of MW power source with $f = 111$ Hz.

3 Results and discussion Figure 1a and b shows surface morphology of densely packed and vertically aligned CNTs. In this case, both MW and RF generators of LA-MW-PECVD system were used (i.e. dual plasma configuration). The length of CNTs, as measured from 45° angle-view SEM image, was evaluated to ≈ 0.9 and ≈ 3.6 μm for 10 min (Fig. 1a) and 40 min (Fig. 1b) growth. The insets in Fig. 1b show the influence of plasma post-growth treatment on wettability of CNTs. As grown CNTs reveal hydrophobic properties with a contact angle value up to 130°. On the other hand, oxygen treated CNTs reveal contact angle $< 10^\circ$. We observed that surface wettability of CNTs can be controlled by the treatment procedure up to certain time duration until which nearly no degradation of CNTs is observed [14, 16]. Figure 1c shows the Raman spectrum of CNTs grown for 40 min. In this spectrum, three peaks are identified. The intensity ratio between D and G bands indicates good quality of CNT [17].

Figure 2 shows SEM morphology of diamond films as function of total gas pressure p in the LA-MW-PECVD system. In accordance to our previous results [12] the transition between large grain lateral-like growth regime (Fig. 2a and b) to ultra-small crystal size growth regime (Fig. 2c and d) was observed in the pressure range of 10–100 Pa. By comparison of films grown at 6 Pa (Fig. 2a) and 10 Pa (Fig. 2b), we can conclude that in both cases the diamond crystals have similar sizes up to 400 nm while the diamond faceting is pronounced at the lowest pressure (Fig. 2a). The growth rate was evaluated from cross section SEM images up to 40 nm h⁻¹. The diamond films deposited at $p > 100$ Pa are flat with clustered-like features consisting of grains in size < 50 nm. In this case, the growth rate decreased two times to the value of ≈ 20 nm h⁻¹.

Raman spectra shown in Fig. 3 well agree with SEM measurements. A sharp diamond peak at 1330 cm⁻¹ [18] is dominant for samples grown at $p = 6$ and 10 Pa. On the other hand, D and G bands [19] dominate the spectrum for films deposited at high pressure. In this case, diamond peak is resolvable but at low relative intensity. Moreover, broad bands centred at 1160 cm⁻¹ (*trans*-polyacetylene group) and 1480 cm⁻¹ are observed too.

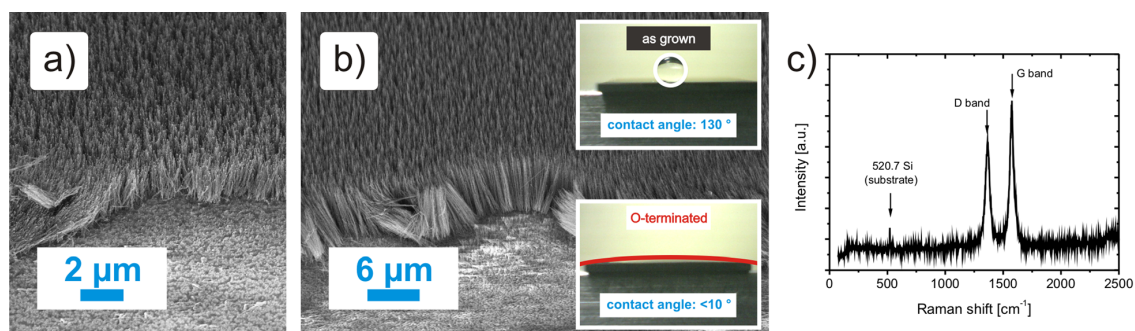


Figure 1 SEM images of CNTs grown by CVD method combining MW and RF plasma source for (a) 10 min and (b) 40 min with insets of water contact angle variation by oxygen-treatment, and (c) corresponding Raman spectrum.

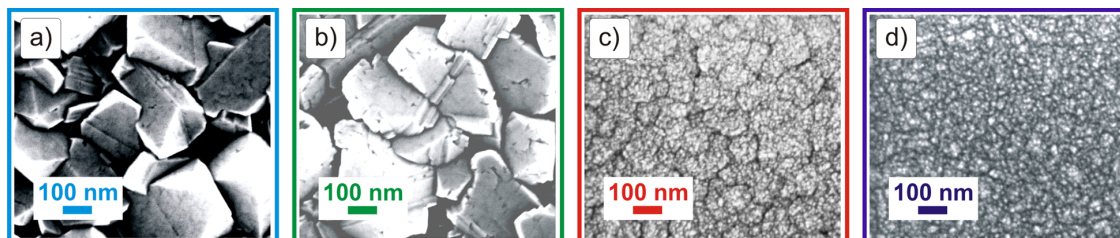


Figure 2 SEM images of the diamond surface morphology changes induced by change of total gas pressure p . From the left (a) to the right (d) the total gas pressure increased from 6 Pa to 10 Pa, 100 Pa and 200 Pa where transition from lateral, large grain growth regime (a and b) to ultra-small crystal size growth regime (c and d) is prominent.

For a better understanding of growth differences at different pressures, we focused on plasma characterization. Figure 4 shows the plasma density N_e as a function of total gas pressure p and distance z from antenna during diamond depositions. It is evident that when p is increasing, the N_e decreases. For the substrate localized at $z = 70$ mm, it means a drop of N_e by three orders of magnitude in the range of 10–150 Pa. The drop of N_e is faster at $z = 65$ mm while for shorter distances z the dependence of N_e on p is nearly linear.

Figure 5 shows the effective electron temperature T_{eff} (i.e. mean electron energy in unit of $k_B \times T$) as a function of pressure p and distance from the antenna z . In the close vicinity to the antenna and for the lowest pressure, the T_{eff} reaches the value of 4.5 eV and exponentially drops with increasing pressure. For higher distance z , the value of T_{eff} drops by 2 eV and saturates at value of $T_{\text{eff}} \approx 1.2$ eV for pressures $p > 50$ Pa. Higher values of T_{eff} for $z = 65$ mm then for $z = 33$ mm by 0.35 eV are most probably caused by the measurement resolution of our set-up and can represent measurement perturbation by plasma instability.

These results clearly indicate that the LA-MW-PECVD system exhibits properties of cold plasma with low T_{eff} . The advantage of low T_{eff} plasma is in low power loading of the

substrates during the CVD growth. This property allow us to grow diamond films at T_s as low as 250 °C [20, 21] or nondestructive plasma treatment of CNTs [14]. Increase of the T_{eff} values for $p < 50$ Pa most probably corresponds with the morphology transformation from the ultra-small crystal size growth regime to the lateral one. At such low pressures the concentration of atomic hydrogen is increased which shifts the growth conditions to hydrogen-rich plasma conditions.

When the pressure increases above certain value (in our case ≈ 100 Pa), the nanocrystalline growth regime prevails. Moreover, presence of CO_2 can lead to frequent inelastic electron collisions with CO_2 molecules and excitation of their vibration and rotation states. Because these excitation energies are relatively lower in comparison with ionization energy of other gas atoms, the electron gas temperature has to decrease. Moreover, the density of atomic hydrogen and diamond growth species is very low near the substrate.

Plasma potential U_{pl} at $z = 16$ mm reaches value of 30 V at $p = 10$ Pa, drops to 20 V at 50 Pa and then linearly decreases to 14 V at 150 Pa. With increasing distance z the values systematically decreases by ≈ 4 V for each distance step. A floating potential U_{fl} decreases from 16 to 8 V at

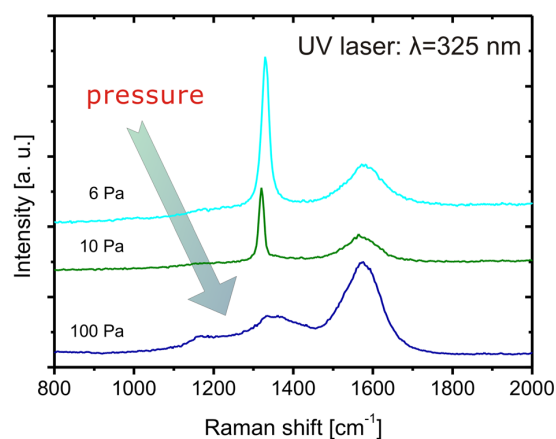


Figure 3 Raman spectra of the diamond films as a function of total gas pressure.

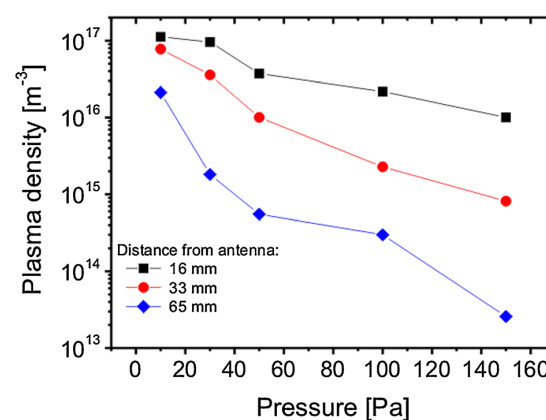


Figure 4 Plasma densities as a function of total gas pressure p and distance z from the antenna.

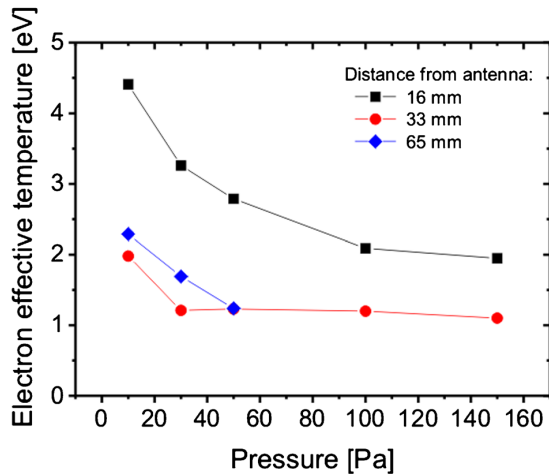


Figure 5 Electron effective temperatures as a function of total gas pressure p and distance from the antenna z .

$z = 16$ mm. With increasing distance z the values systematically increases by ≈ 3 V for each distance step. Thus the potential difference $U_{pl} - U_{fl}$ is smaller for larger distance z , i.e. closer to the substrate holder. Thus, energy of cations bombarding substrate can be varied by substrate to antenna distance, i.e. power loading of substrate can be optimized. Moreover, due to the U_{pl} drop at 50 Pa the potential difference $U_{pl} - U_{fl}$ is larger for lower pressures p . This indicates higher cation energy at pressures < 50 Pa which can supports higher crystallinity and grain size of grown diamond films [22].

4 Conclusions In the presented work, we have investigated the versatility of the linear antenna MW plasma CVD system for growth of CNTs and diamond and their surface functionalization. The used system can be simply scale up by number of antennas or by prolonging their length. Efficient synthesis of oriented CNTs was achieved at dual plasma conditions when RF substrate bias was used in the LA-MW-PECVD system. The length of CNTs increased with the deposition time. The LA-MW-PECVD system can be also used for CNTs surface treatment without their damaging after finding optimal treatment conditions.

By changing processing parameters, we have successfully grown diamond films as confirmed by Raman spectroscopy. The transition from lateral, large grain growth regime to ultra-small crystal size growth regime was found between 10 and 100 Pa. The plasma parameters during diamond deposition process were monitored by Langmuir probe measurements. Simultaneously plasma parameters calculations indicate that the transition pressure p is ≈ 50 Pa. Moreover, Langmuir probe measurements confirm lower energy of particles together with decrease of plasma density above the substrates with increased gas pressure influencing morphology of grown diamond films.

Acknowledgments We thank Dr. P. Adámek for helpful discussions and realization of Langmuir probe measurements. This work was financially supported by the Czech Science Foundation research projects P205/12/0908 (SP) and Technology Agency of the Czech Republic TA01011740 (AK, MC, MD). This work was carried out in the frame of the LNSM infrastructure.

References

- [1] J. J. Gracio, Q. H. Fan, and J. C. Madaleno, *J. Phys. D* **43**, 374017 (2010).
- [2] S. Potocký, A. Kromka, J. Potmesil, Z. Remes, Z. Polackova, and M. Vanecek, *Phys. Status Solidi A* **203**, 3011–3015 (2006).
- [3] F. Silva, K. Hassouni, X. Bonnin, and A. Gicquel, *J. Phys.: Condens. Matter* **21**, 364202 (2009).
- [4] K. Tsugawa, M. Ishihara, J. Kim, M. Hasegawa, and Y. Koga, *New Diam. Frontier Carbon Technol.* **16**, 337–346 (2006).
- [5] Š. Potocký, O. Babchenko, K. Hruška, and A. Kromka, *Phys. Status Solidi B* **249**, 2612–2615 (2012).
- [6] K. Tsugawa, S. Kawaki, M. Ishihara, J. Kim, Y. Koga, H. Sakakita, et al., *Diam. Relat. Mater.* **20**, 833–838 (2011).
- [7] S. B. Sinnott, and R. Andrews, *Crit. Rev. Solid State Mater. Sci.* **26**, 145–249 (2001).
- [8] A. N. Obratsov, A. A. Zolotukhin, A. O. Ustinov, A. P. Volkov, Y. Svirko, and K. Jefimovs, *Diam. Relat. Mater.* **12**, 917–920 (2003).
- [9] A. V. Melechko, V. I. Merkulov, T. E. McKnight, M. A. Guillorn, K. L. Klein, D. H. Lowndes, and M. L. Simpson, *J. Appl. Phys.* **97**, 041301 (2005).
- [10] M. Kumar, and Y. Ando, *J. Nanosci. Nanotechnol.* **10**, 3739–3758 (2010).
- [11] S. Matsumoto, Y. Sato, M. Kamo, and N. Setaka, *Jpn. J. Appl. Phys.* **21**, L183–L185 (1982).
- [12] A. Kromka, O. Babchenko, T. Izak, K. Hruska, and B. Rezek, *Vacuum* **86**, 776–779 (2012).
- [13] O. Babchenko, Z. Remes, T. Izak, B. Rezek, and A. Kromka, *Phys. Status Solidi B* **248**, 2736–2739 (2011).
- [14] M. Kalbacova, A. Broz, A. Kromka, O. Babchenko, and M. Kalbac, *Carbon* **49**, 2926–2934 (2011).
- [15] A. Kromka, Š. Potocký, J. Čermák, B. Rezek, J. Potměšil, J. Zemek, and M. Vaněček, *Diam. Relat. Mater.* **17**, 1252–1255 (2008).
- [16] A. Kromka, O. Babchenko, T. Izak, S. Potocký, M. Davydova, N. Neykova, H. Kozak, Z. Remes, K. Hruska, and B. Rezek, *Pulsed Linear Antenna Microwave Plasma – A Step Ahead in Large Area Material Depositions and Surface Functionalization* (Tanger Ltd., Slezska, 2011).
- [17] S. Costa, E. Borowiak-Palen, M. Kruszynska, A. Bachmatiuk, and R. J. Kalenczuk, *Mater. Sci.* **26**, 433–441 (2008).
- [18] S. Bühlmann, E. Blank, R. Haubner, and B. Lux, *Diam. Relat. Mater.* **8**, 194–201 (1999).
- [19] S. L. Heidger, *MRS Proc.* **383**, 319 (1995).
- [20] K. Tsugawa, M. Ishihara, J. Kim, Y. Koga, and M. Hasegawa, *Phys. Rev. B* **82**, 125460 (2010).
- [21] T. Izak, O. Babchenko, M. Varga, S. Potocký, and A. Kromka, *Phys. Status Solidi B* **249**, 2600–2603 (2012).
- [22] V. Mortet, L. Zhang, M. Eckert, J. D’Haen, A. Soltani, M. Moreau, D. Troadec, E. Neyts, J.-C. De Jaeger, J. Verbeeck, A. Bogaerts, G. Van Tendeloo, K. Haenen, and P. Wagner, *Phys. Status Solidi A* **209**, 1675–1682 (2012).

A.6

Great Variety of Man-Made Porous Diamond Structures:
Pulsed Microwave Cold Plasma System with a Linear
Antenna Arrangement



Great Variety of Man-Made Porous Diamond Structures: Pulsed Microwave Cold Plasma System with a Linear Antenna Arrangement

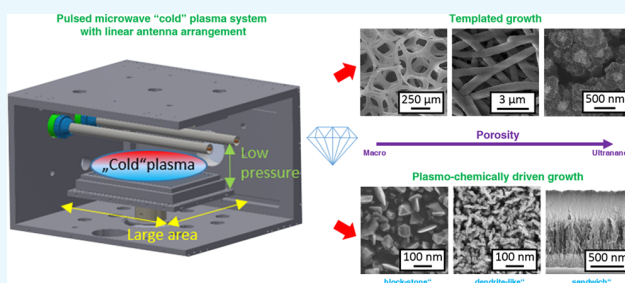
Marián Varga,^{*,†,‡,§} Štěpán Potocký,[†] Mária Domonkos,^{†,§} Tibor Ižák,[†] Oleg Babčenko,^{†,‡} and Alexander Kromka^{†,§}

[†]Institute of Physics, Czech Academy of Sciences, Cukrovarnická 10, 162 00 Prague 6, Czech Republic

[‡]Department of Physics, Faculty of Electrical Engineering, Czech Technical University in Prague, Technická 2, 166 27 Prague 6, Czech Republic

[§]Department of Physics, Faculty of Civil Engineering, Czech Technical University in Prague, Thákurova 7, 166 29 Prague 6, Czech Republic

ABSTRACT: Synthetic diamond films are routinely grown using chemical vapor deposition (CVD) techniques. Due to their extraordinary combination of intrinsic properties, they are used as the functional layers in various bio-optoelectronic devices. It is a challenge to grow the dimensional layers or porous structures that are required. This study reviews the fabrication of various porous diamond-based structures using linear antenna microwave plasma (LAMWP) chemical vapor deposition (CVD), a low-cost technology for growing diamond films over a large area (>1 m²) at low pressure (<100 Pa) and at low temperature (even at 350 °C). From a technological point of view, two different approaches, i.e., templated diamond growth using three different prestructured (macro-, micro-, and nanosized) porous substrates and direct bottom-up growth of ultra-nanoporous diamond (block-stone and dendritelike) films, are successfully employed to form diamond-based structures with controlled porosity and an enhanced surface area. As a bottom-up strategy, the LAMWP CVD system allows diamond growth at as high as 80% CO₂ in the CH₄/CO₂/H₂ gas mixture. In summary, the low-pressure and cold plasma conditions in the LAMWP system facilitate the growth on three-dimensionally prestructured substrates of various materials that naturally form porous self-standing diamond structures.



1. INTRODUCTION

Because of their superior properties, synthetic monocrystalline diamonds and polycrystalline diamond thin films have for decades been the focus of interest of various research teams.^{1–3} At the same time, diamond is used in numerous industrial fields. As a consequence, various diamond structuring strategies have been developed to fit specific requirements,^{4–6} e.g., large surface areas, geometrically ordered microstripes or meshes,⁷ nano-objects or nanostructures (wires, rods, and whiskers),^{8,9} porous films and membranes,^{10,11} etc.

Recently, nanoscaled fibrous materials have been attracting attention due to their specific characteristics, such as high bending performance, flexibility in surface functionalities, a high surface-area-to-volume ratio, and controllable pore size.¹² These advantages make them interesting candidates for a wide variety of applications, e.g., filtration, separation, catalysis, storage and transportation, adsorption, tissue engineering, drug delivery systems, sensors, etc.^{8,9,13–15} For example, tailorable pore size is a key requirement in filtration and/or separation.^{16,17}

However, fabricating these nanostructures from diamond remains a technological challenge, due to the great hardness of diamond and its chemical inertness or due to undesired diamond graphitization. Ongoing studies have therefore

focused on fabricating nanostructures, explaining specific growth phenomena, and developing appropriate technological procedures.

There are two main approaches to diamond film structuring: (i) postgrowth processing (top-down) and (ii) pregrowth (bottom-up) processing. These two approaches differ in the number of technological steps and also in the dimensionality and the geometrical aspect ratios that can be achieved in the structures that are fabricated. Top-down processing involves technological steps, such as depositing a masking material (Al, Ni, Au, Cu, and Pt) followed by plasma etching (generally oxygen with Ar, CF₄, or CHF₃)^{5,14} or by thermocatalytically induced etching (graphitization or burning).^{11,18} The first study on top-down fabrication of porouslike diamond films was reported by Kriele et al.¹⁶ They fabricated freestanding diamond films consisting of nanopores localized between diamond grains. The porouslike structure was achieved by etching nondiamond carbon forms (mainly localized along grain boundaries) by annealing in air at elevated temperatures (530–560 °C).

Received: February 4, 2019

Accepted: April 19, 2019

Published: May 14, 2019

Bottom-up processing is either guided by selective area nucleation/deposition or is achieved by direct growth on prestructured substrates, porous membranes, or nanofibers.^{4,6,15} Key benefits are minimal technological steps and a larger variety of complex geometries. However, the main limitation is the less precise fabrication of structures, due to (i) the pyramidlike diamond growth of the crystals and (ii) the hard-to-control vertical and lateral diamond growth. Using the bottom-up approach, porosity of the diamond films is achieved by either (i) employing geometrically prestructured substrates (i.e., templated growth) or (ii) optimized chemical vapor deposition (CVD) by providing suitable growth conditions (mainly by varying the gas mixture). The variety of supporting substrates includes fully or partially transformable polymers,^{19–21} various non-carbon-based templates,^{14,17,22,23} carbon-based templates,^{24–28} or SiO_x-based templates.^{29–31} The important advantage of templated diamond growth is that the porosity is generally guided by the template that is used.^{27,30,32} In the course of the development and usage of these supports, various aspects of procedures that can be used and specific applications have already been discussed. For example, diamond nanoparticles in a polymer matrix can be used for fabricating porous diamond structures,^{7,19} for enhancing the seeding efficiency in planar diamond deposition and for diamond growth on vertical structures.^{20,33,34} In the case of diamond deposition on graphitelike materials, the proper seeding technology and the chemical stability of these materials has a direct effect on the final geometry of the structure that is formed.^{26,27} In addition, the pore size of the templates has a strong influence on the penetration of the growth species in depth (i.e., in the Z-direction) during chemical vapor deposition (CVD). Pore size therefore has an impact on the final thickness of a porous diamond-based structure.^{10,30,35}

This can be overcome by using layer-by-layer deposition,^{29,31,32} but it is a time-consuming and expensive procedure. For direct growth of thick porous diamond layers, steady kinetic reactions during CVD are required to achieve porous growth rather than micro- or nanocrystalline growth.^{36,37} A reliable technique for templated and direct fabrication of porous diamond structures is highly sought after.

In this paper, we introduce the linear antenna microwave plasma (LAMWP) CVD system as a promising “4L” (low-pressure, low-temperature, low-cost, and large-area) technology for fabricating a great variety of porous diamond-based structures. We present and summarize five complementary bottom-up technological processes suitable for fabricating diamond-based structures with different porosities. Two approaches are involved: (1) templated diamond growth on porous substrates, including (i) carbon foam (C-foam) with macrosized porosity, (ii) a nonwoven nanofibrous SiO_x mat with microsized porosity, (iii) buckypaper (BP) composed of single-wall carbon nanotubes (SWCNT) with nanosized porosity, and (2) direct plasmochemically driven growth of (i) block-stone-like and (ii) dendritelike diamond films with ultra-nanosized porosity. All of these approaches allow the fabrication of self-standing three-dimensional (3D) diamond-based porous structures with the use of just one CVD system.

2. EXPERIMENTAL PART

2.1. Materials and Preparation. The LAMWP CVD system consists of a water-cooled chamber with two linear Cu conductors (≈ 60 cm in length) located inside quartz tubes. A distributed gas inlet enables a homogeneous precursor input

over the complete length of the antennas. Microwave power is delivered from both sides by two microwave generators (2.45 GHz, Muegge) working at pulse-frequency up to 500 Hz and at maximum power up to 4.4 kW in a pulse, using a specially designed splitter-adaptor (Muegge GmbH). The plasma is generated in an asymmetric way between the two electrodes and ground.³⁸ This configuration provides homogeneous plasma distribution at low working pressure (units of Pa) over the water-cooled graphite substrate holder 30×20 cm² in area.³⁹ The design principle and corresponding reaction mechanism (simplified for H₂ plasma) of such a deposition system can be found in ref 40. The distance between the substrate holder and the antennas (Z-axis distance) can be adjusted in the range of several centimeters and was fixed at 7 cm in this work. At this distance, the effective electron temperature T_{eff} is about 1.5 eV,⁴¹ i.e., the LAMWP system is characterized by a cold MW plasma process at the surface of the substrate. This setup allows diamond growth at low temperature (250 °C).⁴² However, if needed, the substrate temperature can be controlled independently of the CVD process by a resistively heated substrate holder up to 800 °C.⁴³ In this study, we performed diamond deposition at temperatures in the range between 350 and 650 °C in a CH₄/CO₂/H₂ gas mixture. The porous diamond structures were fabricated either by novel CVD growth on a planar substrate or by low-pressure CVD growth on macro-, micro-, and nanoporous templates.

A commercially available rigid and highly porous (80 pores per in.) C-foam was used as a macrosized porous template.⁴⁴ The C-foam ($15 \times 10 \times 3$ mm³) was first oxidized by RF oxygen plasma to make its surface hydrophilic. On the basis of the previously optimized nucleation and growth procedures,²⁷ the C-foam was seeded for 10 min in a poly(vinyl alcohol)/nanodiamond (50:50 ratio) mixture, using an ultrasonic bath.

The microsized porous template was a silica (SiO_x) nonwoven three-dimensional nanofibrous mat produced by needleless electrospinning (NanoSpider, Elmarco Ltd.). The mat consisted of randomly oriented submicron fibers ($\phi \approx 100$ nm) weighing 20 g m⁻², and the total thickness of the mat was about 60–70 μm . The large SiO_x mat was cut into smaller pieces (3×4 cm²) and was treated in RF oxygen plasma to achieve a hydrophilic character. The prepared mats were then seeded by soaking in a dispersion of deionized water and ultradispersed detonation diamond (UDD, $\phi \approx 5$ –10 nm, New Metals and Chemicals Corp. Ltd.).

Finally, a buckypaper (BP) composed of single-wall carbon nanotubes (SWCNTs) was used as the nanosized porous template. The fabrication procedure is described in ref 45. In brief, the SWCNTs were first dispersed in an *n*-methyl pyrrolidone solution and were then filtered through the nylon membrane by vacuum filtration to fabricate a self-standing dense SWCNT BP. The BP substrate was approximately 8 μm in thickness. Before the diamond CVD, the BPs were immersed in deionized water with UDD for 30 min.

The ultra-nanoporous (block-stone and dendritelike) diamond films were fabricated on mirror-polished Si(100) substrates 1×1 cm² in size, which were ultrasonically seeded in a suspension of deionized water and UDD. Similarly, silicon substrates coated with ultrananocrystalline diamond (UNCD) and microcrystalline diamond (MCD) layers were also used, but no ultrasonic treatment was performed on them.

The substrates with various porosities and diamond CVD growth conditions are presented in Table 1.

Table 1. Different Porosities and Applied Diamond Growth Conditions of the Substrates

description	diamond film porosity	deposition time (h)	microwave power (kW)	CH ₄ /CO ₂ /H ₂ gas flow (sccm)	substrate temperature (°C)
SET 1 diamond growth on C-foam	macroporous (substrate template)	60	2 × 2	10:0:100	650
SET 2 diamond growth on SiO _x mat	microporous (substrate template)	60	2 × 2	5:20:150	550
SET 3 diamond growth on SWCNT BP	nanoporous (substrate template)	15	2 × 1.7	5:20:50	450
SET 4 growth of porous (block-stone and dendritelike) diamond films	ultra-nanoporous (self-template)	15	2 × 1.7	5:20:50	450
				5:20:25	650
					550
					450
					350

2.2. Materials Characterization. The surface morphology and the grain size of the fabricated diamond films/structures were analyzed using a field-emission scanning electron microscope (SEM) operating in secondary electron mode (MAIA3, Tescan Ltd.) and in semi-in-lens mode (JSM7500F, JEOL). The diamond character of the deposited films was determined by Raman spectroscopy (InVia, Renishaw) using a He–Cd laser with 325 and/or 442 nm excitation wavelengths.

3. RESULTS AND DISCUSSION

3.1. Templated Diamond Growth. *3.1.1. Macrosized Porosity: Diamond Growth on C-Foam.* The structure with macrosized porosity was produced by templated growth of a diamond film on C-foam. In general, it is not a simple task to grow diamonds on this kind of graphite-based material using high-density MW plasma CVD, due to the presence of atomic hydrogen and oxygen species in the plasma, which degrades and etches this material. One solution is to use a poly(vinyl alcohol) and UDD mixture for the nucleation of C-foams, followed by diamond growth.²⁷ It should be noted that successful overgrowth of porous C-foams by a continuous diamond film within the whole volume of the substrate (3D growth) was achieved only by the LAMWP CVD. Representative SEM images of the bare and diamond-coated C-foams are shown in Figure 1a,b. The presence of the diamond film is confirmed by Raman spectroscopy (Figure 1c). The Raman spectrum of the bare C-foam consists of two bands known as the D band (defect sp² phases), centered at 1356 cm⁻¹, and the G band (graphitic phases) centered at 1585 cm⁻¹. Compared with the bare C-foam, the Raman spectra of the diamond-coated C-foam taken from the top and the bottom side reveal a red-shift of the position of the D band from 1356 to 1332 cm⁻¹. Additionally, the band at 1150 cm⁻¹, which is attributed to *trans*-polyacetylene (*t*-PA) chains at diamond grain boundaries, is also present. The diamond morphology taken at three different depths through the C-foam is shown in Figure 1d. The diamond coating is present throughout the bulk of the macroporous C-foam framework. However, due to the variations in the penetration efficiency of the active species within the Z-scale (~3 mm), a visible difference in the thickness of the diamond film is observed, i.e., delayed closing/growing of the diamond film was achieved at the bottom of the substrate. However, this delay can easily be solved by a prolonged deposition time. Similar results (not shown here) were also observed for C-foams with lower porosity (60 pores per in.) and with higher porosity (100 pores per in.).

We will now discuss the homogeneity of the deposited diamond film within the C-foam volume (bulk) achieved in our LAMWP system. Marton et al.²⁵ also exposed C-foam to

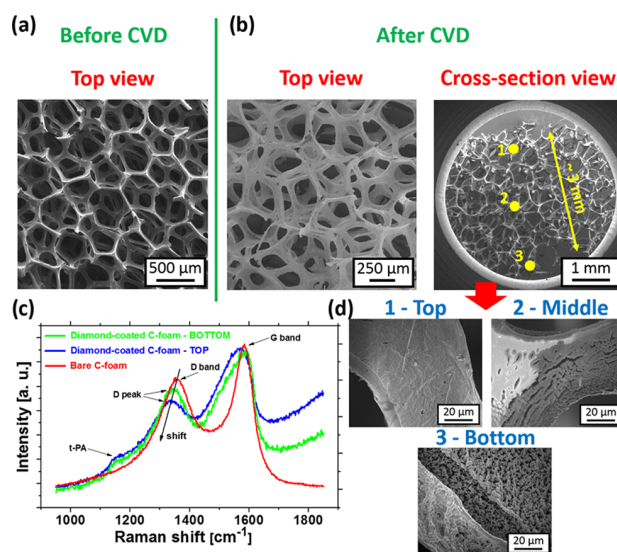


Figure 1. SEM images of the (a) bare and (b) diamond-coated C-foams. (c) Raman spectra of the bare and diamond-coated C-foams (top and bottom side) measured with the 442 nm excitation wavelength. (d) SEM images of the diamond-coated C-foam taken from the top to the bottom of the substrate (i.e., Z-depth profiling).

the diamond growth process in a hot filament (HF) CVD system. They observed the formation of various carbon-based materials (diamond, carbon nanowalls, graphite nanosheets, etc.) within the volume of the C-foam, depending on the Z-distance from the hot filaments. Marton et al. also reported a strong influence of the porosity of the foam on the deposited structures. The diamond growth rate decreased rapidly or there was even no diamond growing inside the C-foam volume with increased porosity. This was attributed to a lack of atomic hydrogen penetrated into the C-foam. Thanks to the significantly lower working pressure in the LAMWP CVD system than that in the HF CVD system (i.e., 10 vs 3000 Pa), deeper penetration of the growth species into the C-foam volume should be achieved and any formation of nondiamond forms is effectively suppressed. Other types of materials with similar porosity (e.g., silicon carbide or alumina foam, etc.) can be used to minimize any complications related to carbon-based substrates (damage to the substrate and substrate etching).

3.1.2. Microsized Porosity: Diamond Growth on a SiO_x Mat. Self-standing porous diamond membranes were fabricated using templated growth on three-dimensional microporous SiO_x fiber mats. The template (mat thickness, average fiber diameter, pore size, and the relative spacing between the fibers) was primarily defined by the parameters of the electrospinning process. Figure 2a shows a top-view SEM

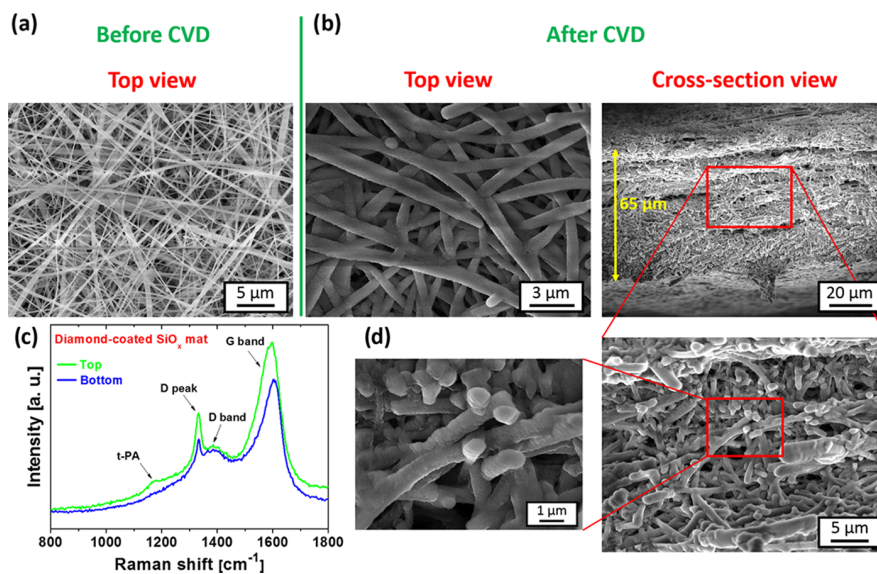


Figure 2. (a) Top-view SEM image of the bare SiO_x fiber mat. (b) Top-view, cross-sectional view, and (d) detailed-view SEM images of the SiO_x fiber mat after diamond deposition. (c) Raman spectra of the top and the bottom of the diamond-coated SiO_x mat measured with the 442 nm excitation wavelength.

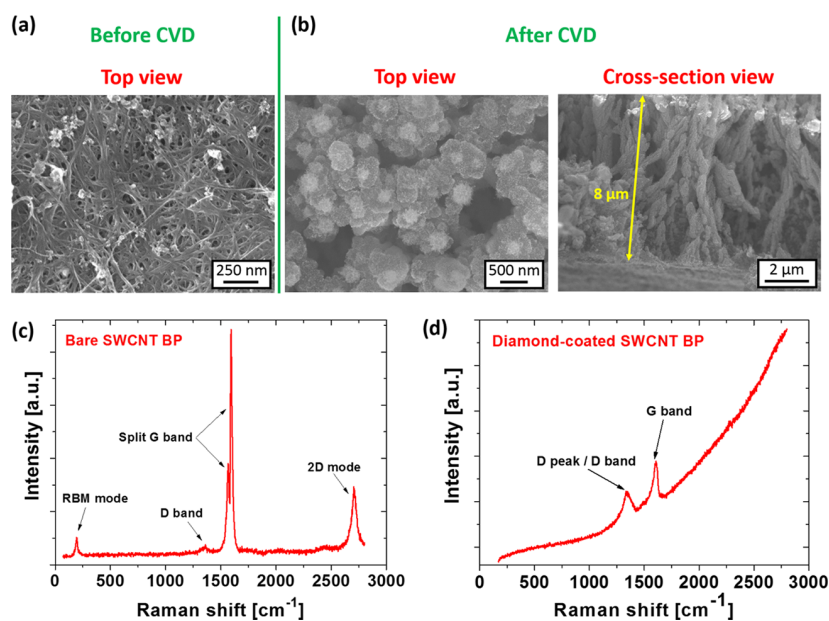


Figure 3. (a) Top-view SEM image of the bare SWCNT BP. (b) Top-view and cross-sectional-view SEM images of the diamond-coated SWCNT BP. The corresponding Raman spectra of the (c) bare and (d) diamond-coated SWCNT BP samples, measured with the 442 nm excitation wavelength.

image of the electrospun fiber mat, which comprises randomly oriented SiO_x fibers with submicron diameter and a smooth surface. Figure 2b shows top and cross-sectional views of the nanofiber mat after the diamond CVD process. Detailed views (see Figure 2d) confirm a hermetic coating of SiO_x fibers with the diamond film.

Some authors have reported that diamond deposition on a fibrous template dominates only on the top surfaces whereas other layers shield the inner part from plasma, resulting in nonuniform diamond growth within the Z-depth.^{10,31} The reason for this was assigned to hindered diffusion and penetration of reactive species into the bulk of the densely packed fibrous template.^{30,32} To improve the homogeneity of

the diamond film growth with the template bulk, polymers have been used as the seeding layer³⁰ or a layer-by-layer deposition process has been used.³¹ As has already been demonstrated above, the LAMWP system naturally forces diamond growth also on 3D substrates (i.e., on perpendicular walls of prestructured substrates). Its low-pressure operation mode (10 Pa) prolongs the mean free path of active species and therefore naturally suppresses any limitations in diffusion.^{10,30,32}

It should be noted that oxygen plasma pretreatment and subsequent seeding with diamond nanoparticles also ensured homogeneous nucleation throughout the volume of the template by the opposite surface charges of UDD⁴⁶ and SiO_x

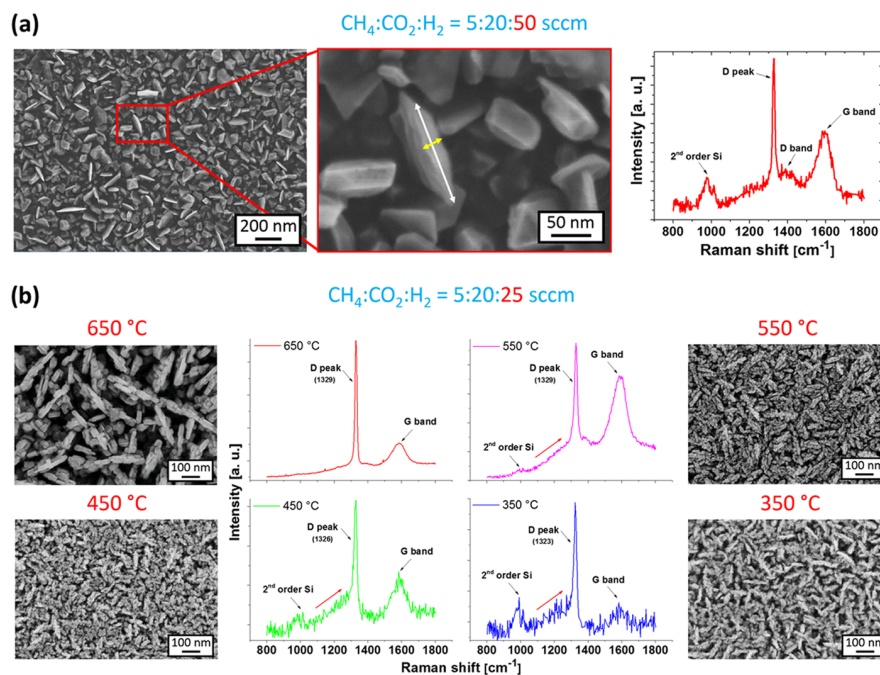


Figure 4. (a) SEM images and the Raman spectrum of a block-stone diamond film deposited at a temperature of 450 °C from a gas mixture of $\text{CH}_4/\text{CO}_2/\text{H}_2 = 5:20:50$ sccm. (b) Top-view SEM images and the corresponding Raman spectra of dendritelike diamond films grown at different deposition temperatures and with a higher $\text{CH}_4 + \text{CO}_2$ content in a gas mixture ($\text{CH}_4/\text{CO}_2/\text{H}_2 = 5:20:25$ sccm). The Raman spectra were measured with the 325 nm excitation wavelength.

fibers. No mixing with polymer matrix^{30,31} was therefore necessary in our case. The fibers were well-overgrown by the diamond film throughout the 65 μm thickness of the substrate; see Figure 2b. Moreover, the diamond film well copied the initial microstructure of each individual fiber. We were also able to coat the whole membrane efficiently, using two-sided deposition in a single run. In this case, the fiber mats were mounted on a special substrate holder (i.e., the templates “hovered” ~ 1 cm above the substrate holder), which enabled simultaneous chemical vapor deposition on both sides, i.e., on the top side and on the bottom side. No major morphological changes were observed for the top and bottom parts of the diamond-coated SiO_x mat, which indicates almost identical films.

These results are also supported by Raman measurements, i.e., the Raman spectra from the top and from the rear side are similar (see Figure 2c). In general, both Raman spectra are dominated by the diamond characteristic peak centered at 1332 cm^{-1} and by two broad bands at 1385 and 1600 cm^{-1} , which are attributed to the D band and the G band, representing the nondiamond carbon bonds (sp^2 phases) in the diamond film.⁴⁷ The weak band centered at 1168 cm^{-1} corresponds to *trans*-polyacetylene groups localized mainly at grain boundaries. The LAMWP system also ensured excellent deposition homogeneity over large areas; i.e., 18 samples 3 \times 4 cm^2 in size were coated within a single deposition run.

3.1.3. Nanosized Porosity: Diamond Growth on SWCNT Bucky paper. Finally, we report on templated diamond growth on very densely packed SWCNT buckypaper with nanosized porosity. Figure 3a shows the top-view SEM image of the bare buckypaper substrate, which is primarily composed of SWCNT bundles, with only a small amount of impurities (amorphous and carbonaceous residues). The corresponding Raman spectrum (Figure 3c) reveals four characteristic peaks/bands:

(i) radial breathing mode at 193 cm^{-1} , (ii) the D band at 1360 cm^{-1} , (iii) the split G band (G^- and G^+ at 1566 and 1593 cm^{-1} , respectively), and (iv) two-dimensional (2D) mode at 2705 cm^{-1} . After the diamond CVD process, the SWCNT bundles were homogeneously coated with a nanocrystalline diamond (NCD) film (Figure 3b) not only on the top of the substrate but also throughout the volume of the porous BP (see the cross-sectional SEM image in Figure 3b). This compact diamond coverage led to significant changes in the Raman spectrum (Figure 3d), which is now dominated by two bands recognized as the D band (a broad band combining the diamond peak 1333 cm^{-1} and the red-shifted defect band 1348 cm^{-1}) and the blue-shifted G band to 1607 cm^{-1} .

In the case of diamond growth on SWCNT BP, both the low working pressure and the gas composition are crucial parameters. The gas composition has to be chosen very properly to avoid the formation of a two-layer compartment heterostructure, due to the rapid diamond growth rate and, at the same time, to avoid the rapid substrate etching by atomic hydrogen. Moreover, the typically used $\text{CH}_4/\text{CO}_2/\text{H}_2$ gas mixture in the LAMWP system results in more complex plasmachemical reactions than in the conventionally used CH_4/H_2 atmosphere. The main role of the added CO_2 gas is to increase the diamond growth rate and to improve the diamond quality.⁴⁸ However, the presence of oxygen species together with atomic hydrogen species makes the plasma environment more aggressive, especially for the nondiamond carbon-based substrates.⁴⁹ However, unconventional diamond growth can be achieved at an unusually high ratio of CO_2 to H_2 (see Section 3.2).

As a summary of Section 3.1, the pulsed microwave cold plasma system with a linear antenna arrangement is versatile for the production of various porous diamond structures with adjustable morphologies. The low-pressure operation length-

ens the homogeneity of the diamond growth in the substrate Z-depth and also enhances the penetration of the growth species into the porous templates. However, the pore size is still a substantial parameter because penetration of the growth species is clearly easier (simpler) for large (macro-) pores than for smaller (micro- and nano-) pores. Thanks to the large distance of the microwave plasma from the substrate, the LAMWP system also enables two-sided deposition in a single run and homogeneous diamond growth in the volume of thick or densely packed porous templates. Moreover, the LAMWP system can vary the deposition conditions (temperature and gas composition) in a wide range to tailor the thickness, the morphology, and the crystalline quality of the diamond coating to specific needs. It should be noted that boron-doped diamond films can also be prepared by this system, which widens the applicability of porous diamond structures.

3.2. Ultra-Nanosized Porosity: Plasmochemically Driven Porous Diamond Growth. Porous (block-stone and dendritelike) diamond films were also directly grown on standard seeded polished silicon substrates or on polycrystalline diamond films deposited on silicon in the pulsed microwave cold plasma system with a linear antenna arrangement. Using the same deposition conditions (see Table 1) as those for the overgrowth of the SWNCT BP templates, we observed homogeneous coverage of Si with well-faceted block-stone diamond crystals (Figure 4a). Some crystals exhibit platelike structures, i.e., quasi 2D diamond crystallites around 20 nm in thickness (yellow arrow) and up to 200 nm in lateral dimension (white arrow). The length-to-thickness aspect ratio was approximately 10. Although the surface is homogeneously covered with diamond crystals, these plates are sparsely located (see Figure 4a). The Raman spectrum consists of the diamond characteristic peak centered at 1329 cm^{-1} and two broad bands centered at 1388 and 1588 cm^{-1} , known as the D band and the G band, respectively (Figure 4a). The band at around 981 cm^{-1} is attributed to the second order of silicon.

Similar block-stone diamond crystals have already been prepared at high temperatures ($>850\text{ }^{\circ}\text{C}$) using the ASTeX resonant cavity MW plasma enhanced CVD system.^{50–53} However, high-temperature diamond growth is applicable only for limited substrate materials, e.g., silicon. Drijkoningen et al. have recently reported the growth of diamond plates in a linear antenna microwave plasma system at a lower temperature ($410\text{ }^{\circ}\text{C}$), using MW continuous wave power of 2.8 kW, a gas mixture of $\text{CH}_4/\text{CO}_2/\text{H}_2$ (2.5% CH_4 and 6% CO_2 to H_2), and a low working pressure of 23 Pa.³⁷ The diamond plates were randomly oriented and were up to 130 nm in height after 18 h. For the prolonged deposition time (up to 64 h), the individual plates disappeared and only a continuous layer consisting of microcrystalline diamond grains was observed. The driving force for the anisotropic growth of the plates was assigned to the stacking faults present in the early stages of the diamond growth.³⁶ Drijkoningen et al. proposed a model in which the formation of diamond plates is related to silicon atoms, i.e., “impurity traces” coming from the quartz tubes. Here, Si atoms were involved as a catalyst that either blocks diamond layer growth or enhances the selective etching of $\{111\}$ diamond facets (for details, see ref 37). Drijkoningen et al. reported that once the diamond crystals enlarged their size enough, the plate growth collapsed and microcrystalline grains dominated the surface morphology of the sample. On the basis of their model, the growth of thick porous structures (500 nm and larger)

therefore seems to be unfavorable at these process parameters. However, this contrasts with our findings.

Note that the gas mixture and the total gas pressure are crucial process parameters that influence the quality and the morphology of the diamond films. In our previous studies, we have demonstrated that the addition of a small amount of CO_2 to the CH_4/H_2 gas mixture substantially improved the diamond growth.³⁹ Next, taking into account the Bachmann ternary diagram, the diamond growth should be suppressed usually at a high oxygen content ($>40\%$ CO_2 in the CH_4/H_2 gas mixture).⁵⁴ However, the diamond growth in LAMWP CVD does not strictly follow the Bachmann ternary diagram and the diamond also grows at higher CO_2 , i.e., outside the forbidden region.⁵⁵

Another issue is the total gas pressure in the LAMWP system. At process pressure $>100\text{ Pa}$, the diamond growth was dominated by the renucleation mode and the films that formed consisted of nanosized diamond crystals ($<50\text{ nm}$) with a high content of sp^2 -bonded carbon on grain boundaries.⁴¹ However, reducing the pressure to 10 Pa (in our case) suppressed the renucleation mode⁴³ and the crystal size increased in proportion with the deposition time. In this case, the Raman spectrum revealed a sharp diamond peak. In this sense, the combination of high CO_2 content (40% to hydrogen) and low process pressure (10 Pa) allows the formation of a high-quality diamond in a block-stone form (Figure 4a), whereas higher CO_2 content (80%) results in the formation of a dendritelike form (Figure 4b). In general, the low working pressure increases the concentration of atomic hydrogen, thus locating the points on the triangular Bachmann diagram closer to the hydrogen vertex.⁵⁶ We assume that the increased CO_2 content, i.e., the increased amount of oxygen-based species (such as CO, CO_2 , O_2 , or alcohol) supports the role of atomic hydrogen and has a beneficial effect on the diamond growth regime. In addition, the higher CO_2 content led to formation of a higher amount of OH radicals⁵⁷ and in combination with a low-pressure regime, it finally switched the diamond growth regime from a block-stone to dendritelike form. In comparison with the block-stone diamond, the growth of the dendritelike diamond can be tailored by the deposition temperature. Although all of the Raman spectra reveal a high-quality diamond film with just a small amount of sp^2 hybridized carbon, some changes can be still observed. The diamond films deposited at higher temperatures (650 and 550 $^{\circ}\text{C}$) are characterized by three Raman features: (i) the diamond peak centered at around 1329 cm^{-1} , (ii) the D band with a maximum at 1388 cm^{-1} , and (iii) the G band at 1585 cm^{-1} . Lowering the deposition temperature resulted in a red-shift of the diamond peak to a value of 1323 cm^{-1} and a clear increase in the diamond peak shoulder around 1250 cm^{-1} . This feature most likely originates from a disordered sp^3 phase, which is typically found in dynamically synthesized nanodiamonds and may be a part of the sp^3/sp^2 near-surface stress-releasing transient layer.⁵⁸

For the growth of isolated diamond nanowires, (111) nanowires were proposed as the unstable form whereas $\text{C}(100)(2 \times 1)$ dimer rows parallel to the axis of the nanowire should ideally fulfill the stability requirements.⁵⁹ Theoretical calculations later showed that certain morphological criteria must be fulfilled for structurally and thermodynamically stable diamond nanowires or nanorods.⁶⁰ This may be the reason why the chemical and kinetic reactions are in thermodynamic equilibrium with the etching process and the growth of the

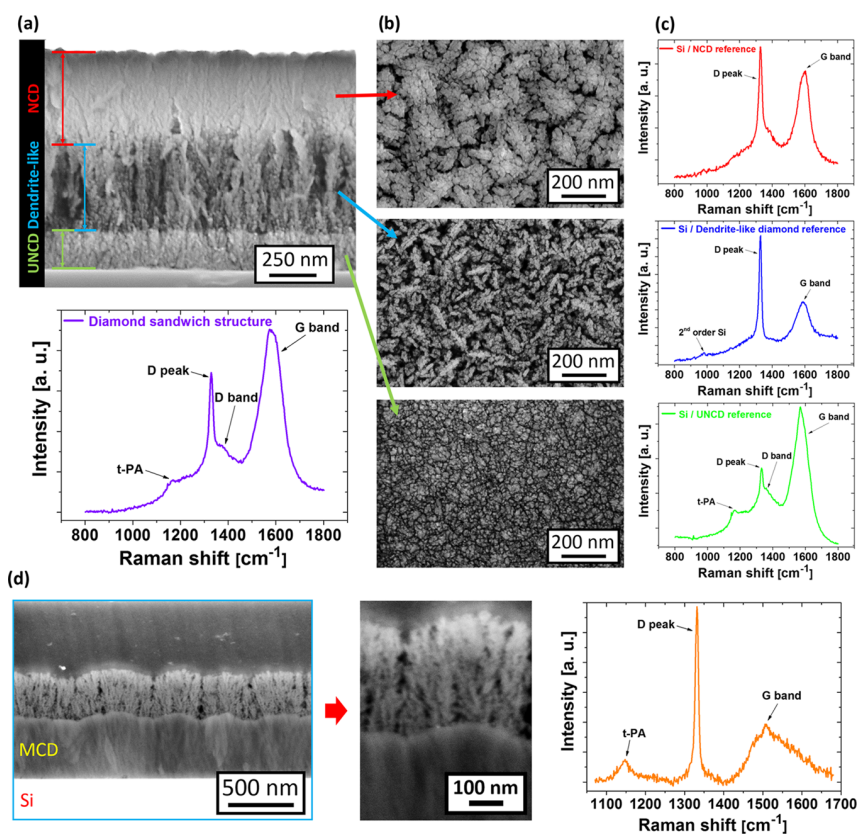


Figure 5. (a) Cross-sectional view of the diamond sandwich structure (UNCD/dendritelike/NCD) and the corresponding Raman spectrum of the final sandwich structure. (b) Top-view SEM images of the diamond structures after an individual deposition step during fabrication of the sandwich structure, and (c) the corresponding Raman spectra of the reference diamond films deposited on silicon substrates measured with the 325 nm excitation wavelength. (d) Cross-sectional SEM images and the Raman spectrum measured with the 442 nm excitation wavelength of the MCD/dendritelike diamond structure.

preferential crystallographic orientation. This type of specific equilibrium could also be required for dendritelike diamond growth, as presented in this work. Dendritelike diamond growth seems to be driven only by plasmochemical processes (and not to be influenced by the substrate material), and it does not collapse into micro- or nanocrystalline diamond growth for prolonged deposition times.

Further evidence for a plasmo-chemical driven process is demonstrated by the dendritelike diamond growth on ultranano- (UNCD) and microcrystalline (MCD) diamond films. Figure 5a shows a cross-sectional view of a diamond sandwich structure. The diamond sandwich structure starts with the UNCD base layer, which was further used as a substrate for the growth of dendritelike diamond. Finally, the dendritelike porous structure was overgrown with nanocrystalline diamond (NCD). Figure 5b shows top-view SEM images of individually deposited diamond films on planar Si substrates (the reference). The dendritelike diamond growth is not conditioned by the UNCD morphology and reveals the same morphology as in the previous section (Figure 4b). However, the NCD film well copies the top profile of the dendritelike diamond layer.

Figure 5a shows the Raman spectrum of the final sandwich structure. For comparison, Figure 5c shows the corresponding Raman spectra of each diamond type deposited on Si substrates. It is evident that the Raman spectrum of the sandwich structure is primarily influenced by the UNCD layer. However, the diamond peak intensity and the contempora-

neous lower G band intensity seem to be related to higher-quality diamond films (dendritelike and NCD films).

Finally, a two-layer compartment of the dendritelike diamond film (deposited at $T = 450\text{ }^{\circ}\text{C}$) on a rough microcrystalline diamond film was also fabricated. It is evident from the cross-sectional SEM images that the dendritelike growth is not disturbed (influenced) by the base MCD layer (Figure 5d). The Raman spectrum is characterized by three typical features: *t*-PA, the diamond peak, and the G band. Unlike in the sandwich structure, the position of the diamond peak (1331 cm^{-1}) is preferentially influenced by the MCD layer (Figure 5d). Finally, it should be noted that dendritelike diamond growth was also observed on nonseeded Si substrates, due to spontaneous nucleation (not shown here).

To summarize Section 3.2, the unconventional diamond growth regime that is outside the Bachmann ternary diagram led to the direct growth of porous block-stone and dendritelike diamond films. Both of these growth modes are affected by the low total gas pressure (10 Pa) and by the composition of the gas, with a high content of CO_2 gas (40% CO_2 to H_2 for porous block-stone and 80% CO_2 to H_2 for dendritelike diamond films). The diamond growth itself is mainly driven by plasmochemical reactions, i.e., it is not conditioned by the substrate material. Moreover, the dendritelike diamond growth does not collapse after reaching a certain diamond film thickness. This is in contrast to the block-stone growth model.³⁷ This unique bottom-up porous diamond growth, observed only when there is a high CO_2 content in the

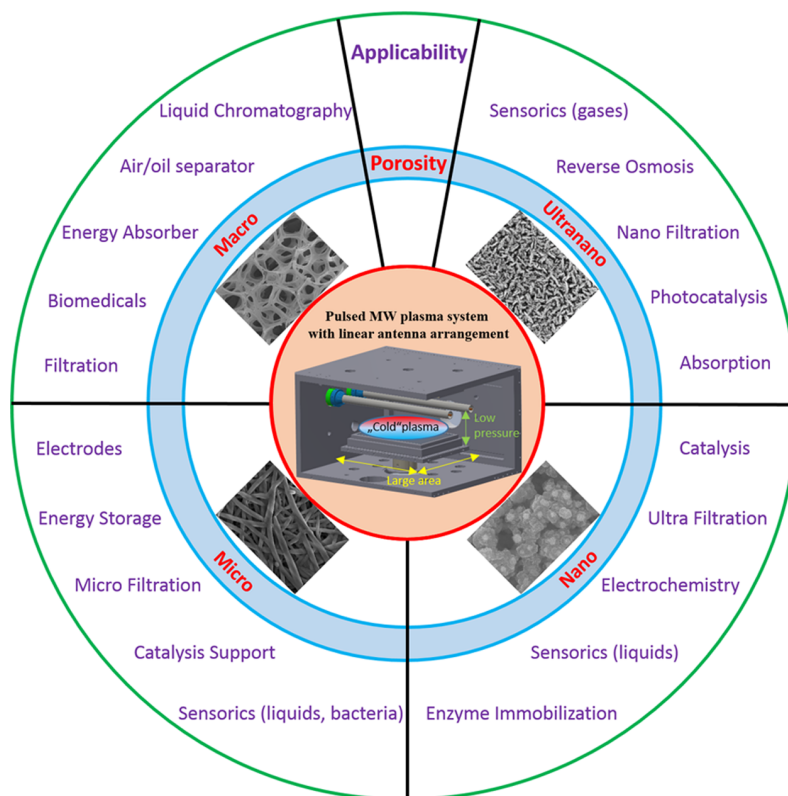


Figure 6. Classification of porous diamond structures by pore size and their potential applicability.

LAMWP system, is minimally affected by the deposition temperature. In this sense, the LAMWP system is suitable for porous diamond growth on temperature-sensitive substrates over a large area. The multilayered structures (sandwich and two-layer compartment structures) can be prepared within a single deposition run by simply varying the gas chemistry during the CVD process. This saves fabrication time. It should be noted that all of the fabricated and presented diamond-based porous structures were thick enough to be self-standing.

3.3. Applicability of Porous Diamond Structures.

Generally, porous materials are of significant interest due to their wide applications. They can be used for various targets in solar energy systems containing adsorption materials, thermal energy storage materials, insulation materials, evaporation materials, or heat transfer augmentation materials.⁶¹ The distribution of the sizes, shapes, and volumes of the void spaces in porous materials is directly related to their ability to perform the desired function in a particular application.⁶² In addition, the material of the porous structure itself is a key factor for its usability. Porous diamond-based structures in various forms, as well as their applicability, have already been presented as promising electrodes,²⁶ as separators in biotechnology and biomedicine,¹⁷ as electrochemical separators,⁶³ and as supercapacitors.³² In a wider manner, Figure 6 summarizes the classification of porous diamond structures grown by LAMWP on the basis of their pore sizes and outlines their potential applicability.

Driven by the demand for porous structures based on intrinsic or boron-doped diamond, the last two decades have seen an enormous effort by researchers to prepare and optimize the fabrication procedures. For example, Kondo et al. reported a two-step thermal treatment method for the fabrication of porous conductive boron-doped diamond

electrodes,⁶⁴ Ruffinatto et al. reported that heavily boron-doped diamond porous membranes were fabricated using low-cost commercial fiber glass filters seeded through the Buchner filtration process,³⁰ Shimoni et al. presented recipes for the creation of various diamond-based patterns using a lithography-based procedure,⁶⁵ and Gao et al. reported the preparation of a porous diamond foam by a fabrication procedure consisting of several steps.²⁹ Generally, a complex fabrication procedure was needed.

In this sense, we believe that our summary of the fabrication (with or without a template) of a wide range of 3D porous diamond structures using the pulsed microwave cold plasma system with a linear antenna arrangement can promote the potential use of porous diamond in industrial applications.

4. CONCLUSIONS

In this work, we reviewed two different fabrication approaches (top-down and bottom-up) of porous diamond structures in one unique CVD system, the large-area pulsed microwave plasma system with a linear antenna arrangement. In the first approach, templated diamond growth on macro-, micro-, and nanoporous substrates was presented. Low-pressure operation (10 Pa) lengthened the diamond growth in the substrate Z-depth and thus enhanced the penetration of the growth species into the porous templates. Moreover, thanks to the larger distance between antennas and substrate, the LAMWP system also enabled quite homogeneous two-sided deposition growth in the volume of thick or very dense porous templates within a single deposition run. In the second approach, the new plasmachemically driven growth for a high CO₂ content (80% to H₂) in the gas mixture led to an unconventional formation of dendritelike diamond films. This unique bottom-up porous

diamond growth was not dependent on the substrate material, the deposition time, or the film thickness. The results presented here demonstrate that the large-area pulsed microwave plasma system with a linear antenna arrangement is a promising and industrially compatible versatile tool for the fabrication of a great variety of porous diamond structures in a broad range of temperatures.

AUTHOR INFORMATION

Corresponding Author

*E-mail: varga@fzu.cz.

ORCID

Marián Varga: [0000-0002-9613-4614](https://orcid.org/0000-0002-9613-4614)

Author Contributions

M.V. and A.K. conceived and supervised the work. M.V. was primarily responsible for preparing the macro- and nanosized structures. M.D. was responsible for the microsized structures. O.B. and Š.P. were responsible for preparing the block-stone and dendritelike structures. T.I. measured the Raman spectra. All authors contributed to preparing the manuscript and have approved the final version.

Notes

The authors declare no competing financial interest.

ACKNOWLEDGMENTS

This work was supported by the Ministry of Health of the Czech Republic grant No. AZV 15-33018A (A.K., T.I.). M.V. acknowledges GACR-FWF bilateral project (16-34856L, AI0234421), and S.P. acknowledges the Operational Programme Research, Development and Education, financed by European Structural and Investment Funds and the Czech Ministry of Education, Youth and Sports (Project No. SOLID21—CZ.02.1.01/0.0/0.0/16_019/0000760). The authors would like to thank K. Hruska, R. Jackivova, and M. Kotlar for the SEM measurements. The authors would like to thank the JEOL European training center (Paris, France) for the cross-sectional SEM measurements of the MCD/dendrite-like diamond structure. Robin Healey (Czech Technical University in Prague) is gratefully acknowledged for his language revision of the manuscript.

REFERENCES

- (1) May, P. W. Diamond thin films: a 21st-century material. *Philos. Trans. R. Soc., A* **2000**, *358*, 473–495.
- (2) Gicquel, A.; Hassouni, K.; Silva, F.; Achard, J. CVD diamond films: from growth to applications. *Curr. Appl. Phys.* **2001**, *1*, 479–496.
- (3) Nebel, C. E.; Rezek, B.; Shin, D.; Uetsuka, H.; Yang, N. Diamond for bio-sensor applications. *J. Phys. D: Appl. Phys.* **2007**, *40*, 6443–6466.
- (4) Liu, H.; Wang, C.; Gao, C.; Han, Y.; Luo, J.; Zou, G.; Wen, C. New insights into selected-area deposition of diamond films by means of selective seeding. *J. Phys.: Condens. Matter* **2002**, *14*, 10973–10977.
- (5) Huff, M. A.; Aidala, D. A.; Butler, J. E. MEMS applications using diamond thin films. *Solid State Technol.* **2006**, *49*, 45–46.
- (6) Kromka, A.; Babchenko, O.; Rezek, B.; Ledinsky, M.; Hruska, K.; Potmesil, J.; Vanecek, M. Simplified procedure for patterned growth of nanocrystalline diamond micro-structures. *Thin Solid Films* **2009**, *518*, 343–347.
- (7) Gavrilov, S. A.; Dzbansky, N. N.; Il'ichev, É. A.; Minakov, P. V.; Poltoratsky, É. A.; Rychkov, G. S.; Suetin, N. V. Electron flow enhancement with a diamond membrane. *Tech. Phys.* **2004**, *49*, 108–113.
- (8) Davydova, M.; Kromka, A.; Rezek, B.; Babchenko, O.; Stuchlik, M.; Hruska, K. Fabrication of diamond nanorods for gas sensing applications. *Appl. Surf. Sci.* **2010**, *256*, 5602–5605.
- (9) Yang, N.; Uetsuka, H.; Osawa, E.; Nebel, C. E. Vertically Aligned Diamond Nanowires for DNA Sensing. *Angew. Chem., Int. Ed.* **2008**, *47*, 5183–5185.
- (10) Kondo, T.; Lee, S.; Honda, K.; Kawai, T. Conductive diamond hollow fiber membranes. *Electrochem. Commun.* **2009**, *11*, 1688–1691.
- (11) Mehedi, H.; Arnault, J.-C.; Eon, D.; Hébert, C.; Carole, D.; Omnes, F.; Gheeraert, E. Etching mechanism of diamond by Ni nanoparticles for fabrication of nanopores. *Carbon* **2013**, *59*, 448–456.
- (12) Matsumoto, H.; Tanioka, A. Functionality in Electrospun Nanofibrous Membranes Based on Fiber's Size, Surface Area, and Molecular Orientation. *Membranes* **2011**, *1*, 249–264.
- (13) Hébert, C.; Scorsone, E.; Bendali, A.; Kiran, R.; Cottance, M.; Girard, H. A.; Degardin, J.; Dubus, E.; Lissorgues, G.; Rousseau, L.; Mailley, P.; Picaud, S.; Bergonzo, P. Boron doped diamond biotechnology: from sensors to neurointerfaces. *Faraday Discuss.* **2014**, *172*, 47–59.
- (14) Siuzdak, K.; Bogdanowicz, R. Nano-engineered Diamond-based Materials for Supercapacitor Electrodes: A Review. *Energy Technol.* **2018**, *6*, 223–237.
- (15) Yang, N.; Foord, J. S.; Jiang, X. Diamond electrochemistry at the nanoscale: A review. *Carbon* **2016**, *99*, 90–110.
- (16) Kriele, A.; Williams, O. A.; Wolfer, M.; Hees, J. J.; Smirnov, W.; Nebel, C. E. Formation of nano-pores in nano-crystalline diamond films. *Chem. Phys. Lett.* **2011**, *507*, 253–259.
- (17) Aramesh, M.; Fox, K.; Lau, D. W. M.; Fang, J.; Ken Ostrikov, K.; Praver, S.; Cervenka, J. Multifunctional three-dimensional nanodiamond-nanoporous alumina nanoarchitectures. *Carbon* **2014**, *75*, 452–464.
- (18) Smirnov, W.; Hees, J. J.; Brink, D.; Müller-Sebert, W.; Kriele, A.; Williams, O. A.; Nebel, C. E. Anisotropic etching of diamond by molten Ni particles. *Appl. Phys. Lett.* **2010**, *97*, No. 073117.
- (19) Potocký, Š.; Ižák, T.; Rezek, B.; Tesárek, P.; Kromka, A. Transformation of polymer composite nanofibers to diamond fibers and films by microwave plasma-enhanced CVD process. *Appl. Surf. Sci.* **2014**, *312*, 188–191.
- (20) Scorsone, E.; Saada, S.; Arnault, J. C.; Bergonzo, P. Enhanced control of diamond nanoparticle seeding using a polymer matrix. *J. Appl. Phys.* **2009**, *106*, No. 014908.
- (21) Hébert, C.; Scorsone, E.; Mermoux, M.; Bergonzo, P. Porous diamond with high electrochemical performance. *Carbon* **2015**, *90*, 102–109.
- (22) Suo, N.; Huang, H.; Wu, A.; Cao, G.; Hou, X.; Zhang, G. Porous boron doped diamonds as metal-free catalysts for the oxygen reduction reaction in alkaline solution. *Appl. Surf. Sci.* **2018**, *439*, 329–335.
- (23) Yang, K.-H.; Nguyen, A. K.; Goering, P. L.; Sumant, A. V.; Narayan, R. J. Ultrananocrystalline diamond-coated nanoporous membranes support SK-N-SH neuroblastoma endothelial cell attachment. *Interface Focus* **2018**, *8*, No. 20170063.
- (24) Varga, M.; Vretenar, V.; Izak, T.; Skakalova, V.; Kromka, A. Carbon nanotubes overgrown and ingrown with nanocrystalline diamond deposited by different CVD plasma systems. *Phys. Status Solidi B* **2014**, *251*, 2413–2419.
- (25) Marton, M.; Vojs, M.; Kotlár, M.; Michniak, P.; Vančo, L.; Veselý, M.; Redhammer, R. Deposition of boron doped diamond and carbon nanomaterials on graphite foam electrodes. *Appl. Surf. Sci.* **2014**, *312*, 139–144.
- (26) Zanin, H.; May, P. W.; Fermin, D. J.; Plana, D.; Vieira, S. M. C.; Milne, W. L.; Corat, E. J. Porous Boron-Doped Diamond/Carbon Nanotube Electrodes. *ACS Appl. Mater. Interfaces* **2014**, *6*, 990–995.
- (27) Varga, M.; Stehlik, S.; Kaman, O.; Izak, T.; Domonkos, M.; Lee, D. S.; Kromka, A. Templated diamond growth on porous carbon foam decorated with poly(vinyl alcohol)-nanodiamond composite. *Carbon* **2017**, *119*, 124–132.

- (28) Silva, A. A.; Pinheiro, R. A.; do Amaral Razzino, C.; Trava-Airoldi, V. J.; Corat, E. J. Thin-film nanocomposites of BDD/CNT deposited on carbon fiber. *Diamond Relat. Mater.* **2017**, *75*, 116–122.
- (29) Gao, F.; Wolfer, M. T.; Nebel, C. E. Highly porous diamond foam as a thin-film micro-supercapacitor material. *Carbon* **2014**, *80*, 833–840.
- (30) Ruffinatto, S.; Girard, H. A.; Becher, F.; Arnault, J.-C.; Tromson, D.; Bergonzo, P. Diamond porous membranes: A material toward analytical chemistry. *Diamond Relat. Mater.* **2015**, *55*, 123–130.
- (31) Petrák, V.; Vlčková Živcová, Z.; Krýsová, H.; Frank, O.; Zukal, A.; Klimša, L.; Kopeček, J.; Taylor, A.; Kavan, L.; Mortet, V. Fabrication of porous boron-doped diamond on SiO₂ fiber templates. *Carbon* **2017**, *114*, 457–464.
- (32) Gao, F.; Nebel, C. E. Diamond-Based Supercapacitors: Realization and Properties. *ACS Appl. Mater. Interfaces* **2015**, *8*, 28244–28254.
- (33) Kromka, A.; Babchenko, O.; Kozak, H.; Hruska, K.; Rezek, B.; Ledinsky, M.; Potmesil, J.; Michalka, M.; Vanecek, M. Seeding of polymer substrates for nanocrystalline diamond film growth. *Diamond Relat. Mater.* **2009**, *18*, 734–739.
- (34) Varga, M.; Potocký, S.; Tesarek, P.; Babchenko, O.; Davydova, M.; Kromka, A. Diamond growth on copper rods from polymer composite nanofibres. *Appl. Surf. Sci.* **2014**, *312*, 220–225.
- (35) Kato, H.; Hees, J.; Hoffmann, R.; Wolfer, M.; Yang, N.; Yamasaki, S.; Nebel, C. E. Diamond foam electrodes for electrochemical applications. *Electrochem. Commun.* **2013**, *33*, 88–91.
- (36) Alexeev, A. M.; Ismagilov, R. R.; Ashkinazi, E. E.; Orekhov, A. S.; Malykhin, S. A.; Obraztsov, A. N. Diamond platelets produced by chemical vapor deposition. *Diamond Relat. Mater.* **2016**, *65*, 13–16.
- (37) Drijkoningen, S.; Pobedinskas, P.; Korneychuk, S.; Momot, A.; Balasubramaniam, Y.; Van Bael, M. K.; Turner, S.; Verbeeck, J.; Nesládek, M.; Haenen, K. On the Origin of Diamond Plates Deposited at Low Temperature. *Cryst. Growth Des.* **2017**, *17*, 4306–4314.
- (38) Schlemm, H.; Fritzsche, M.; Roth, D. Linear radio frequency plasma sources for large scale industrial applications in photovoltaics. *Surf. Coat. Technol.* **2005**, *200*, 958–961.
- (39) Kromka, A.; Babchenko, O.; Izak, T.; Hruska, K.; Rezek, B. Linear antenna microwave plasma CVD deposition of diamond films over large areas. *Vacuum* **2012**, *86*, 776–779.
- (40) Obrusnik, A.; Bonaventura, Z. Studying a low-pressure microwave coaxial discharge in hydrogen using a mixed 2D/3D fluid model. *J. Phys. D: Appl. Phys.* **2015**, *48*, No. 065201.
- (41) Tsugawa, K.; Ishihara, M.; Kim, J.; Hasegawa, M.; Koga, Y. Large-Area and Low-Temperature Nanodiamond Coating by Microwave Plasma Chemical Vapor Deposition. *New Diamond Front. Carbon Technol.* **2006**, *16*, 337–346.
- (42) Izak, T.; Babchenko, O.; Varga, M.; Potocký, S.; Kromka, A. Low temperature diamond growth by linear antenna plasma CVD over large area. *Phys. Status Solidi B* **2012**, *249*, 2600–2603.
- (43) Babchenko, O.; Potocký, S.; Ižák, T.; Hruška, K.; Bryknař, Z.; Kromka, A. Influence of surface wave plasma deposition conditions on diamond growth regime. *Surf. Coat. Technol.* **2015**, *271*, 74–79.
- (44) www.ergaerospace.com.
- (45) Varga, M.; Vretenar, V.; Kotlar, M.; Skakalova, V.; Kromka, A. Fabrication of free-standing pure carbon-based composite material with the combination of sp²–sp³ hybridizations. *Appl. Surf. Sci.* **2014**, *308*, 211–215.
- (46) Kromka, A.; Jira, J.; Stenclova, P.; Kriha, V.; Kozak, H.; Beranova, J.; Vretenar, V.; Skakalova, V.; Rezek, B. Bacterial response to nanodiamonds and graphene oxide sheets: Bacterial response to nanodiamonds and graphene oxide. *Phys. Status Solidi B* **2016**, *253*, 2481–2485.
- (47) Filik, J. Raman spectroscopy: a simple, non-destructive way to characterise diamond and diamond-like materials. *Spectrosc. Eur.* **2005**, *17*, 10–17.
- (48) Kromka, A.; Babchenko, O.; Izak, T.; Varga, M.; Davydova, M.; Krata, M.; Rezek, B. Diamond Films Deposited by Oxygen-Enhanced Linear Plasma Chemistry. *Adv. Sci. Eng. Med.* **2013**, *5*, 509–514.
- (49) Joshi, A.; Nimmagadda, R. Erosion of diamond films and graphite in oxygen plasma. *J. Mater. Res.* **1991**, *6*, 1484–1490.
- (50) Angus, J. C.; Sunkara, M. K.; et al. Twinning and faceting in early stages of diamond growth by chemical vapor deposition. *J. Mater. Res.* **1992**, *7*, 3001–3009.
- (51) Chen, H.-G.; Chang, L.; Cho, S.-Y.; Yan, J.-K.; Lu, C.-A. Growth of Diamond Nanoplatelets by CVD. *Chem. Vap. Deposition* **2008**, *14*, 247–255.
- (52) Chen, H.-G.; Chang, L. Characterization of diamond nanoplatelets. *Diamond Relat. Mater.* **2004**, *13*, 590–594.
- (53) Lu, C.-A.; Chang, L. Microstructural investigation of hexagonal-shaped diamond nanoplatelets grown by microwave plasma chemical vapor deposition. *Mater. Chem. Phys.* **2005**, *92*, 48–53.
- (54) Bachmann, P. K.; Leers, D.; Lydtin, H. Towards a general concept of diamond chemical vapour deposition. *Diamond Relat. Mater.* **1991**, *1*, 1–12.
- (55) Potocký, Š.; Babchenko, O.; Hruška, K.; Kromka, A. Linear antenna microwave plasma CVD diamond deposition at the edge of no-growth region of C-H-O ternary diagram. *Phys. Status Solidi B* **2012**, *249*, 2612–2615.
- (56) Eaton, S. C.; Sunkara, M. K. Construction of a new C–H–O ternary diagram for diamond deposition from the vapor phase. *Diamond Relat. Mater.* **2000**, *9*, 1320–1326.
- (57) Wei, J.; Kawarada, H.; Suzuki, J.; Hiraki, A. Growth of diamond films at low pressure using magneto-microwave plasma CVD. *J. Cryst. Growth* **1990**, *99*, 1201–1205.
- (58) Stehlik, S.; Varga, M.; Ledinsky, M.; Miliaieva, D.; Kozak, H.; Skakalova, V.; Mangler, C.; Pennycook, T. J.; Meyer, J. C.; Kromka, A.; Rezek, B. High-yield fabrication and properties of 1.4 nm nanodiamonds with narrow size distribution. *Sci. Rep.* **2016**, *6*, No. 38419.
- (59) Barnard, A. S.; Russo, S. P.; Snook, I. K. Surface structure of cubic diamond nanowires. *Surf. Sci.* **2003**, *538*, 204–210.
- (60) Barnard, A. S. Structural properties of diamond nanowires: Theoretical predictions and experimental progress. *Rev. Adv. Mater. Sci.* **2004**, *6*, 94–119.
- (61) Rashidi, S.; Esfahani, J. A.; Rashidi, A. A review on the applications of porous materials in solar energy systems. *Renewable Sustainable Energy Rev.* **2017**, *73*, 1198–1210.
- (62) Davis, M. E. Ordered porous materials for emerging applications. *Nature* **2002**, *417*, 813–821.
- (63) Gao, F.; Nebel, C. E. Electrically Conductive Diamond Membrane for Electrochemical Separation Processes. *ACS Appl. Mater. Interfaces* **2016**, *8*, 18640–18646.
- (64) Kondo, T.; Kodama, Y.; Ikezoe, S.; Yajima, K.; Aikawa, T.; Yuasa, M. Porous boron-doped diamond electrodes fabricated via two-step thermal treatment. *Carbon* **2014**, *77*, 783–789.
- (65) Shimoni, O.; Cervenkova, J.; Karle, T. J.; Fox, K.; Gibson, B. C.; Tomljenovic-Hanic, S.; Greentree, A. D.; Prawer, S. Development of a Templated Approach to Fabricate Diamond Patterns on Various Substrates. *ACS Appl. Mater. Interfaces* **2014**, *6*, 8894–8902.

A.7

Influence of the growth temperature on the Si-V photoluminescence in diamond thin films



Influence of the growth temperature on the Si-V photoluminescence in diamond thin films

Kateřina Dragounov^{1,2} · Tibor Izak¹ · Alexander Kromka¹ · Zdenek Potuček² · Zdenek Bryknař² · Štepan Potocky¹

Received: 10 October 2017 / Accepted: 1 February 2018 / Published online: 8 February 2018
© Springer-Verlag GmbH Germany, part of Springer Nature 2018

Abstract

The influence of growth temperature (350 ÷ 1100 °C) on the intensity of Si-V colour centres photoluminescence was studied in diamond thin films. The films were grown by a microwave plasma enhanced chemical vapour deposition system. The film quality and surface morphology were characterised by Raman spectroscopy and scanning electron microscopy, respectively. For selected samples, the temperature behaviour of steady-state photoluminescence emission spectra was studied within the range 11 ÷ 300 K as well. The photoluminescence properties are related to the film growth temperature. We found that 800 °C is the optimal growth temperature, at which the highest intensity of the Si-V centre photoluminescence was observed. For all the samples, the blue shift in the position of the Si-V centre photoluminescence zero-phonon line is observed with decreasing temperature, which is attributed to the effects of lattice contraction and quadratic electron–phonon coupling. The zero-phonon line narrowing is discussed regarding vibrations of the perturbed lattice.

1 Introduction

The outstanding properties inherent to diamond [1] are multiplied by optically active impurities [2]. Silicon-vacancy (Si-V) colour centres are naturally incorporated into all types of diamonds prepared by the chemical vapour deposition (CVD) technique, due to etching of Si substrates or quartz windows or even quartz bell-jars themselves [3]. The exceptionality of the Si-V centres resides in the spectrally narrow photoluminescence (PL) in the NIR spectral region, with the short decay time of 1.2 ns [4] and their high photo-stability [5, 6]. The Si-V centre PL is dominated at room temperature by the very intensive and narrow zero-phonon line (ZPL) (full width at half maximum (FWHM) even 0.7 nm [7]) that is located in the spectral window of biological tissues [8]. Moreover, the Si-V centres PL can be effectively excited by red light, which reduces biological tissue auto-fluorescence. Such properties predetermine Si-V centres doped diamond for applications as solid-state light emitters [7], especially

single-photon sources [4, 9], or biocompatible fluorescent markers for bio-imaging [6, 10], where they could surpass recently used nitrogen-vacancy centres [4].

To achieve PL intensity enhancement and controlled reproducible fabrication of the Si-V doped CVD diamond, attention was paid to the influence of the deposition conditions, such as substrate material quality [11, 12], gas mixture [13–15], or substrate structure [16–18]. Despite this great effort, a reproducible fabrication of diamond films with controllable concentration and PL activity of Si-V centres is still a technological challenge.

In addition, many works devoted to ab initio calculations [19], electron paramagnetic resonance measurements, and studies of optical properties in polarised light [7, 20, 21] deal with the other important questions concerning the nature of electronic transitions, structure, and geometry of the Si-V centres. In this context, valuable information is also provided by the temperature behaviour of the Si-V centre PL ZPL, which was reported for the low-stress homo-epitaxial CVD diamond thin films [22] and diamond nanoparticles [23].

In this work, we present a controllable preparation of Si-V centres in nano-crystalline diamond (NCD) films. The influence of NCD film deposition temperature on PL activity of the Si-V colour centres is analysed. The study of steady-state PL and Raman scattering of NCD films is correlated, and attention is also paid to the temperature behaviour of the Si-V centres PL.

✉ Kateřina Dragounov
katerina.dragounova@fjfi.cvut.cz

¹ Institute of Physics AS CR, v. v. i., Cukrovarnick 10,
16200 Prague, Czech Republic

² Faculty of Nuclear Sciences and Physical Engineering, Czech
Technical University in Prague, Trojanova 13, 12000 Prague,
Czech Republic

2 Experimental

Diamond thin films were grown on Si (100) substrates with an area of $10 \times 10 \text{ mm}^2$. Before the CVD growth, substrates were ultrasonically pretreated in a suspension of deionised water and ultra-dispersed detonation diamond powder (diameter 5–10 nm, New Metals and Chemicals Corp. Ltd., Kyobashi). The CVD deposition of diamond was performed in a microwave plasma enhanced CVD reactor using the cavity resonator with focused plasma [24]. This system enables the diamond deposition at substrate temperatures T_S ranging from 1100 °C down to 350 °C [25]. All NCD films were deposited in hydrogen-rich plasma with methane (1% with respect to H_2 flow) and had approximately the same thickness ($\sim 200 \text{ nm}$). Notice that no silicon-containing gas mixture was used during the CVD deposition. Thus, Si atoms were incorporated into the NCD films mainly as a result of chemical etching of the exposed silicon substrate or possibly of components of the CVD reactor chamber (quartz bell jar) [11, 26].

Surface morphology was characterised by scanning electron microscopy (SEM) (e_LiNE writer, Raith GmbH). The thickness of the diamond films was determined using reflectance interferometry and evaluated by commercial Film Wizard software (Scientific Computing International) by fitting to a predefined model of the Si substrate/diamond/air system. The error in the thickness was estimated to be about 5%. The Raman and PL spectra of the films were measured at room temperature by a Renishaw In Via Reflex Raman spectrometer using a CCD camera and an excitation wavelength of 442 nm. Temperature-dependent PL emission spectra of diamond films excited by 442 nm line of He–Cd laser were measured in the reflection geometry within 11–300 K temperature range using a set-up based on a Carl Zeiss SPM2 monochromator. The PL intensity was measured with a cooled RCA31034 photomultiplier (GaAs photo-cathode) operating in the photon-counting mode, and the emission spectra were corrected for the spectral dependence of the apparatus response.

3 Results and discussion

Figure 1 shows a selection of SEM images of NCD films deposited in the range of $T_S = 350\text{--}1100 \text{ °C}$, that are reported and discussed in detail in [27]. The sample deposited at 350 °C (Fig. 1a) reveals the smallest grain sizes ($< 50 \text{ nm}$). Samples grown at temperatures from 450 to 900 °C displayed nearly identical grain size ($150 \div 200 \text{ nm}$), as illustrated for $T_S = 800 \text{ °C}$ in Fig. 1b. For the highest T_S (1100 °C), the grain size reduction is

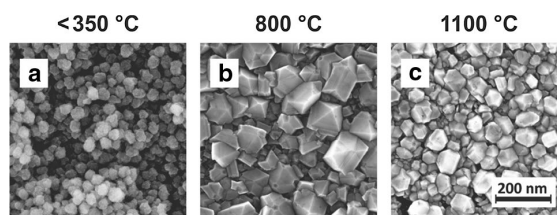


Fig. 1 Surface morphology of NCD film deposited at growth temperatures **a** 350 °C, **b** 800 °C, and **c** 1100 °C (scale bar corresponds to 200 nm for all images). Adopted from [27]

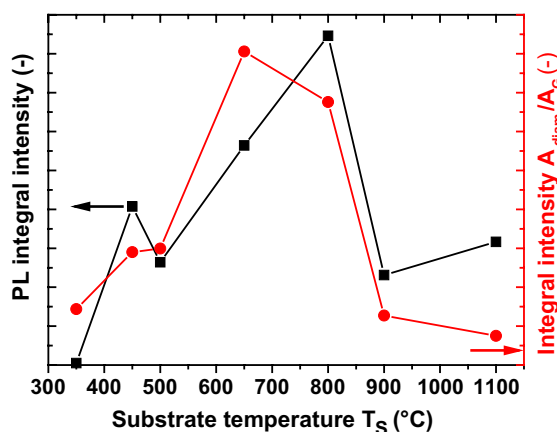


Fig. 2 Integral intensity of Si-V PL (squares) and the ratio of the integral intensity of diamond peak and G band (circles) in the Raman spectra of NCD films deposited at various growth temperatures T_S . PL integral intensity was normalised to its value for $T_S = 350 \text{ °C}$. PL and Raman spectra were measured at room temperature with excitation by 442 nm line of He–Cd laser

obvious in Fig. 1c, but formed crystals still reveal good faceting in contrast to the sample grown at the lowest $T_S = 350 \text{ °C}$. The deposition temperature-dependent grain size can be explained as follows. The small grain size at the lowest T_S is a consequence of a high re-nucleation rate during the growth stage caused by sp^2 bonded carbon atoms [28, 29]. In the T_S range $450 \div 900 \text{ °C}$, increasing grain size is observed due to suppressed re-nucleation. The grain size decrease observed at $T_S = 1100 \text{ °C}$ is assigned to raised graphitisation due to too high T_S [30].

Figure 2 shows the integral intensity of ZPL of the Si-V centre PL at room temperature (full symbols) and the ratio A_{diam}/A_G of the integral intensities of diamond peak and graphite band (empty symbols) in the Raman spectra of NCD films for various deposition temperatures T_S . The integral intensity of ZPL corresponding to the electronic transition ${}^2E_u \rightarrow {}^2E_g$ in Si-V centres [21] was determined from the PL spectra already presented in [27]. FWHM of ZPL peaking at room temperature in the vicinity of 738 nm was

found ~ 6 nm in the studied NCD films [7, 15]. Taking into account an overlap of the emission bands in the PL spectra, the evaluation of the integral ZPL intensity further revealed its dependence on the deposition temperature T_S which was not seen in the previous work using only normalised PL spectra [27]. The ZPL intensity is weak for the sample deposited at $T_S = 350$ °C, but it increases by more than one order of magnitude with increasing the temperature to $T_S = 450$ °C, and then three times as much, with a subsequent T_S increase reaching the maximum at $T_S = 800$ °C. Further, a T_S increase to 900 °C results in the ZPL intensity decrease to the level observed for samples deposited at 450 °C. The ZPL intensity did not significantly change for the highest examined $T_S = 1100$ °C.

The Raman spectra of selected NCD films can be found in [27]. A pronounced diamond peak at 1332 cm^{-1} , which denotes good film quality, and an additional four bands centred at 1150, 1360, 1450 and 1580 cm^{-1} were identified in the Raman spectra. The bands at 1150 and 1450 cm^{-1} are attributed to trans-polyacetylene groups (C–H bonds) [31], whereas bands at 1360 and 1580 cm^{-1} correspond to D and G bands [32, 33], respectively. Overlapping bands at 1450 and 1580 cm^{-1} , both originate from the sp^2 hybridised carbon phase and are most pronounced for the highest T_S . The inconspicuous sub-band in the vicinity of 1150 cm^{-1} is typically seen on nano- or ultranano-crystalline diamond films [32]. A broad G band is most pronounced for samples grown at the lowest (350 °C) and the highest T_S (1100 °C). In the case of $T_S = 350$ °C, the high content of the sp^2 hybridised phase is ascribed to the high amount of grain boundaries due to the smallest grain size. For the highest T_S , the graphitisation dominates and once again, a high amount of the sp^2 hybridised phase is

detected [34]. Thus, the behaviour of the integral intensity of the diamond peak, relative to that of identified Raman graphite peak, is in agreement with SEM measurements.

Increased intensity of the Si-V centre PL observed for the deposition temperatures within the range $650 \div 800$ °C is most probably caused by the increased concentrations of the PL active Si-V centres in NCD films. It results partly from increasing Si concentration due to more efficient substrate etching, partly from increasing the content of diamond phase, and partly from the vacancy motion through the NCD film [3, 4, 35]. A higher deposition temperature contributes to re-ordering and stabilisation of carbon vacancies [36]. Thus, with rising T_S , more Si is introduced into the NCD film, and the number of mobile vacancies also increases, leading to the higher amount of vacancies trapped by silicon impurities that can form the PL active colour centres in the diamond phase. At the same time, exceeding the optimal NCD deposition temperature creates a more graphitic phase in the films. Consequently, maximal intensity of Si-V centre PL is observed at temperature T_S , which does not correspond to the maximal value of ratio A_{diam}/A_G . Besides, changes to the local environment of Si atoms due to graphitic phases could result in the change of the Si-V charge state to a PL inactive one (Si-V^0) or the creation of PL inactive Si centres.

Figure 3a shows the temperature development of the PL emission spectra for NCD film deposited at $T_S = 800$ °C. The spectrum measured at 300 K shows a sharp ZPL of Si-V centre PL with a broad, hardly visible, phonon sideband. After cooling down to 200 K, well-pronounced phonon replicas at 757 nm ($13,210$ cm^{-1}) and 767 nm ($13,038$ cm^{-1}) are resolved. The band at 767 nm could be attributed to the local resonance phonon mode of the

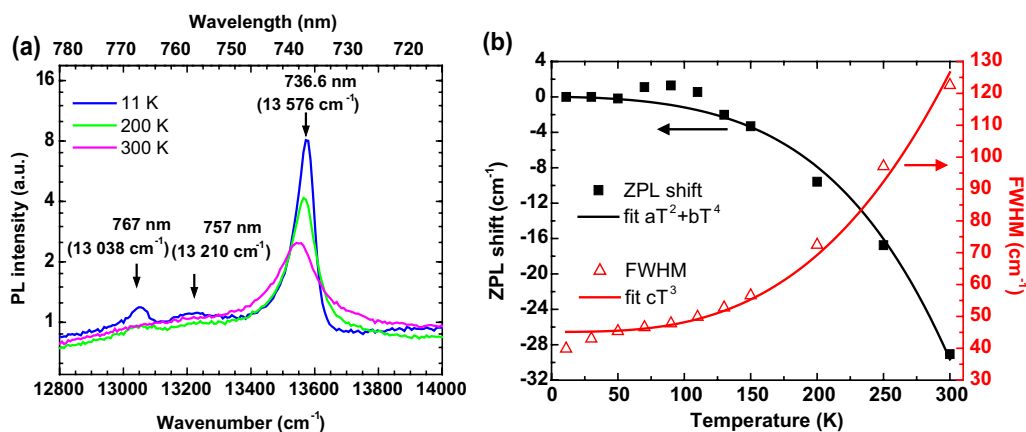


Fig. 3 PL emission spectra (a) and ZPL peak position (full symbols) and FWHM (empty symbols) (b) as a function of temperature obtained under excitation by 442 nm line of He–Cd laser for NCD

film deposited at $T_S = 800$ °C. The ZPL shift is referred to the ZPL position at 11 K that is 736.6 nm

Si-V centre (without much participation of distant carbon nuclei), and the band in the vicinity of 757 nm to delocalized phonon mode [37].

To identify the temperature development of the ZPL parameters, the broad emission band and phonon sidebands were fitted outside the ZPL spectral range by Gaussian functions. Then the sum of these Gaussian curves was subtracted from the measured PL emission spectra as a ZPL background. The determination of the ZPL position was performed using the method of moments described in [38], FWHM was obtained directly from the ZPL profile. For the ZPL shift expression, the ZPL position (736.6 nm) obtained at the lowest temperature was taken as the reference value. All NCD samples revealed the blue shift and narrowing of ZPL with temperature decrease. Figure 3b shows the dependence of the ZPL position and FWHM on the temperature for NCD film deposited at $T_S = 800$ °C. During sample cooling from room temperature down to 110 K, crucial changes of these ZPL parameters took place. The peak position shifts to higher energies by 29 cm^{-1} ($\sim 1.5\text{ nm}$) and FWHM decreases from 123 cm^{-1} ($\sim 6\text{ nm}$) to 50 cm^{-1} ($\sim 2.5\text{ nm}$). Further cooling down to 11 K did not significantly influence the ZPL position and FWHM. The ZPL position is nearly constant, and FWHM that primarily results in inhomogeneous broadening at these temperatures reduces from 50 to 40 cm^{-1} ($\sim 2\text{ nm}$). Our results are in agreement with works [22, 39] where ZPL shifts by $19\text{--}31\text{ cm}^{-1}$ and FWHM decrease to 40 cm^{-1} was observed for temperature $< 100\text{ K}$.

The development of the ZPL position could be explained as a result of two synergetic processes, lattice contraction and quadratic electron–phonon coupling [22]. The ZPL temperature shift is consistent with the dependence $aT^2 + bT^4$ ($a, b = \text{const.}$) similarly as in [22, 40], where T^2 term represents an effect of bonds softening in an excited state, and T^4 dependence describe contributions of hard phonon modes in electron–phonon coupling along with lattice contraction. The following values of a and b parameters were determined: $a = -9.0 \times 10^{-5}\text{ cm}^{-1}\text{ K}^{-2}$, $b = -2.6 \times 10^{-9}\text{ cm}^{-1}\text{ K}^{-4}$ by fitting the data in Fig. 3b. Unfortunately, to the best of our knowledge, in the available literature, no values have been published for a comparison.

The temperature dependence of FWHM at low temperatures follows in general T^7 dependence, expressing the effect of phonon spectrum of perturbed lattice on non-degenerate electronic states. Temperature-dependent PL study on N-V centres performed by Hizhnyakov et al. [40] showed that for degenerate electronic states, the phonon interaction induces a dynamic Jahn–Teller effect and softening of bonds in an excited state. The contribution of these effects to FWHM could be expressed by two other additional terms $\sim T^5$ and $\sim T^3$, respectively. Thus, a homogeneous line broadening is described by the polynomial formula $cT^3 + dT^5 + eT^7$ ($c, d, e = \text{const.}$). Nevertheless, Neu et al. [22] found that for

the Si-V colour centres, the term $\sim T^3$ rather comes from the effect of fluctuating fields between the centre and other defects. Apparently, the dominant term in this formula determines the main mechanism of the FWHM broadening. The same work [22] assigned the predominant contribution to the T^3 dependence, which was also confirmed for our sample (see Fig. 3b). The evaluated fitting parameter of the FWHM temperature dependence is $c = 3.02 \times 10^{-6}\text{ cm}^{-1}\text{ K}^{-3}$. As for the ZPL position, no values have been found in the literature for a comparison.

4 Conclusion

Thin nanocrystalline diamond films deposited at various growth temperatures were analysed using steady-state photoluminescence, Raman scattering, and SEM measurements. The NCD growth kinetic, surface morphology and PL were influenced by the deposition temperature T_S . Especially for the lowest (350 °C), and the highest (1100 °C) deposition temperatures, grain size reduction and graphitisation dominated the deposition. The NCD films deposited within the medium temperature range ($450\text{--}900$ °C) showed well-faceted diamond crystals. The correlation between the integral intensity of ZPL of the Si-V centre PL and quality of the diamond film reveals the key role of the diamond carbon phase for the Si-V centre PL. The highest intensity of the Si-V centres PL was found for the sample deposited at the temperature of 800 °C. For this sample, the ZPL narrowing from $\text{FWHM} = 123\text{ cm}^{-1}$ ($\sim 6\text{ nm}$) to $\text{FWHM} = 40\text{ cm}^{-1}$ ($\sim 2\text{ nm}$) was observed for a temperature decrease from 300 to 11 K, respectively. This behaviour was well described by the T^3 dependence expressing the homogenous broadening determined by vibrations of the perturbed host lattice. Additionally, the blue shift by 29 cm^{-1} ($\sim 1.5\text{ nm}$) in the ZPL position from room temperature to 11 K was observed. This blue shift follows the $T^2 + T^4$ polynomial dependence reflecting effects of lattice contraction and weakening of the strength of electron–phonon coupling.

Acknowledgements This work was supported by the Grant agency of the Czech Republic 15-22102J (SP) and grant agency of Czech Technical University in Prague SGS16/244/OHK4/3T/14.

References

1. J. Mort, *Mater. Des.* **11**, 115 (1990)
2. I. Aharonovich, E. Neu, *Adv. Opt. Mater.* **2**, 911 (2014)
3. K. Iakubovskii, G.J. Adriaenssens, M. Nesladek, *J. Phys. Condens. Matter.* **12**, 189 (2000)
4. E. Neu, D. Steinmetz, J. Riedrich-Möller, S. Gsell, M. Fischer, M. Schreck, C. Becher, *New J. Phys.* **13**, 025012 (2011)
5. E. Neu, M. Agio, C. Becher, *Opt. Express.* **20**, 19956 (2012)

6. T.D. Merson, S. Castelletto, I. Aharonovich, A. Turbic, T.J. Kilpatrick, A.M. Turnley, *Opt. Lett.* **38**, 4170 (2013)
7. E. Neu, R. Albrecht, M. Fischer, S. Gsell, M. Schreck, C. Becher, *Phys. Rev. B* **85**, 245207 (2012)
8. A.M. Smith, M.C. Mancini, S. Nie, *Nat. Nanotechnol.* **4**, 710 (2009)
9. M. Leifgen, T. Schröder, F. Gädeke, R. Riemann, V. Métillon, E. Neu, C. Hepp, C. Arend, C. Becher, K. Lauritsen, O. Benson, *New J. Phys.* **16**, 023021 (2014)
10. M. Amaral, P.S. Gomes, M.A. Lopes, J.D. Santos, R.F. Silva, M.H. Fernandes, *Acta Biomater.* **5**, 755 (2009)
11. M.G. Donato, G. Faggio, G. Messina, S. Santangelo, M. Marinelli, E. Milani, G. Pucella, G. Verona-Rinati, *Diam. Relat. Mater.* **13**, 923 (2004)
12. V.S. Sedov, I.I. Vlasov, V.G. Ralchenko, A.A. Khomich, V.I. Konov, A.G. Fabbri, G. Conte, *Bull. Lebedev Phys. Inst.* **38**, 291 (2011)
13. I. Sakaguchi, M. Nishitani-Gamo, K.P. Loh, H. Haneda, S. Hishita, T. Ando, *Appl. Phys. Lett.* **71**, 629 (1997)
14. S. Singh, S.A. Catledge, *J. Appl. Phys.* **113**, 044701 (2013)
15. T.Y. Ko, Y.L. Liu, K.W. Sun, Y.J. Lin, S.-C. Fong, I.N. Lin, N.H. Tai, *Diam. Relat. Mater.* **35**, 36 (2013)
16. S. Singh, V. Thomas, D. Martyshkin, V. Kozlovskaya, E. Kharlampieva, S.A. Catledge, *Nanotechnology.* **25**, 045302 (2014)
17. J. Song, H. Li, F. Lin, L. Wang, H. Wu, Y. Yang, *Cryst. Eng. Comm.* **16**, 8356 (2014)
18. J. Riedrich-Möller, C. Arend, C. Pauly, F. Mücklich, M. Fischer, S. Gsell, M. Schreck, C. Becher, *Nano Lett.* **14**, 5281 (2014)
19. A. Gali, J.R. Maze, *Phys. Rev. B* **88**, 235205 (2013)
20. U.F.S. D'Haenens-Johansson, A.M. Edmonds, B.L. Green, M.E. Newton, G. Davies, P.M. Martineau, R.U.A. Khan, D.J. Twitchen, *Phys. Rev. B* **84**, (2011)
21. L.J. Rogers, K.D. Jahnke, M.W. Doherty, A. Dietrich, L.P. McGuinness, C. Müller, T. Teraji, H. Sumiya, J. Isoya, N.B. Manson, F. Jelezko, *Phys. Rev. B* **89**, (2014)
22. E. Neu, C. Hepp, M. Hauschild, S. Gsell, M. Fischer, H. Sternschulte, D. Steinmüller-Nethl, M. Schreck, C. Becher, *New J. Phys.* **15**, 043005 (2013)
23. K.D. Jahnke, A. Sipahigil, J.M. Binder, M.W. Doherty, M. Metsch, L.J. Rogers, N.B. Manson, M.D. Lukin, F. Jelezko, *New J. Phys.* **17**, 043011 (2015)
24. M. Füner, C. Wild, P. Koidl, *Appl. Phys. Lett.* **72**, 1149 (1998)
25. A. Kromka, Š. Potocký, J. Čermák, B. Rezek, J. Potměšil, J. Zemek, M. Vaněček, *Diam. Relat. Mater.* **17**, 1252 (2008)
26. L. Bergman, B.R. Stoner, K.F. Turner, J.T. Glass, R.J. Nemanich, *J. Appl. Phys.* **73**, 3951 (1993)
27. Š. Potocký, T. Ižák, M. Varga, A. Kromka, *Phys. Status Solidi B* **252**, 2580 (2015)
28. J.R. Petherbridge, P.W. May, S.R.J. Pearce, K.N. Rosser, M.N.R. Ashfold, *J. Appl. Phys.* **89**, 1484 (2001)
29. O. A. Williams ed. *Nanodiamond* (Royal Society of Chemistry, Cambridge, 2014)
30. V. Ralchenko, L. Nistor, E. Pleuler, A. Khomich, I. Vlasov, R. Khmel'nitskii, *Diam. Relat. Mater.* **12**, 1964 (2003)
31. R. Pfeiffer, H. Kuzmany, N. Salk, B. Günther, *Appl. Phys. Lett.* **82**, 4149 (2003)
32. A.C. Ferrari, J. Robertson, *Phys. Rev. B* **63**, (2001)
33. I.I. Vlasov, E. Goovaerts, V.G. Ralchenko, V.I. Konov, A.V. Khomich, M.V. Kanzyuba, *Diam. Relat. Mater.* **16**, 2074 (2007)
34. S.A. Grudinkin, N.A. Feoktistov, K.V. Bogdanov, M.A. Baranov, A.V. Baranov, A.V. Fedorov, V.G. Golubev, *Semiconductors* **48**, 268 (2014)
35. I. Kiflawi, G. Sittas, H. Kanda, D. Fisher, *Diam. Relat. Mater.* **6**, 146 (1997)
36. Z. Remes, A. Kromka, J. Potmesil, M. Vanecek, *Phys. Status Solidi A* **205**, 2158 (2008)
37. A. Dietrich, K.D. Jahnke, J.M. Binder, T. Teraji, J. Isoya, L.J. Rogers, F. Jelezko, *New J. Phys.* **16**, 113019 (2014)
38. B. Henderson, G.F. Imbush, *Optical spectroscopy of inorganic solids* (Clarendon Press, Oxford, 1989)
39. A.A. Gorokhovskiy, A.V. Turukhin, R.R. Alfano, W. Phillips, *Appl. Phys. Lett.* **66**, 43 (1995)
40. V. Hizhnyakov, H. Kaasik, I. Sildos, *Phys. Status Solidi B* **234**, 644 (2002)

A.8

Si-related color centers in nanocrystalline diamond thin films

Si-related color centers in nanocrystalline diamond thin films

Štěpán Potocký*, Jakub Holovský, Zdeněk Remeš, Martin Müller, Jan Kočka, and Alexander Kromka**

Institute of Physics AS CR, v.v.i., Cukrovarnická 10, 16253 Praha, Czech Republic

Received 15 April 2014, revised 25 July 2014, accepted 11 August 2014

Published online 5 September 2014

Keywords chemical vapor deposition, color center, diamond, photoluminescence, plasma

* Corresponding author: e-mail potocky@fzu.cz, Phone: +420 220 318 437, Fax: +420 233 343 184

** e-mail kromka@fzu.cz, Phone: +420 220 318 437, Fax: +420 233 343 184

The successful growth of nanocrystalline diamond (NCD) thin films with optically active Si-related color centers was realized on glass and molybdenum substrates by the microwave plasma chemical vapor deposition (CVD) with focused or linear antenna plasma reactors. Diamond coatings were characterized by Raman spectroscopy, scanning electron microscopy, and photolumin-

escence (PL) spectroscopy. Increased of a-Si interlayer thickness resulted in reduction of stress in NCD film and increased renucleation of NCD films. The PL spectra showed that the Si-color center is only observed in the focused plasma system. The influence of the substrate material as well as the a-Si interlayer on the density of Si-related color center was not confirmed in our setup.

© 2014 WILEY-VCH Verlag GmbH & Co. KGaA, Weinheim

1 Introduction The photoluminescence (PL) properties of optical centers in diamond are outstanding due to high quantum yields and little photobleaching [1]. In addition, optical centers in diamond are promising as single photon emitters [2, 3]. Many impurities are known to form optically active defects in diamond. These include N, Si, and Cr [4], and recently, N-vacancy centers with pronounced zero-phonon line (ZPL) with a relatively strong phonon sideband [5]. Silicon vacancy (SiV) defects with ZPL at 738 nm [6] have weak interaction with phonons of the host [7]. Several studies have reported on the excellent PL of nanodiamond particles in cells without photobleaching even at room temperatures [8, 9]. A nanosized island-like diamond film with nonuniform spatially localized SiV centers can be prepared by microwave (MW) plasma chemical vapor deposition (CVD) [10]. The size of nanodiamonds influences the shift of SiV emission [11]. In addition, due to carbon–carbon bonds diamond can be easily functionalized with various chemical groups [12] and color center activity can be controlled.

In this paper, we present a controllable and reproducible method for the preparation of SiV centers in nanocrystalline diamond (NCD). A comparison of two MW plasma deposition systems utilizing quite distinctive setup and process parameters is also done.

2 Experimental Diamond thin films were grown on fused silica (UQG) and Mo substrates in size $10 \times 10 \text{ mm}^2$.

Before the CVD growth, substrates were ultrasonically pretreated in a suspension of deionized water and ultra-dispersed detonation diamond powder (diameter 5–10 nm, New Metals and Chemicals Corp. Ltd., Kyobashi) [13]. The CVD deposition of diamond was performed in a MW plasma enhanced CVD reactor using either cavity resonator with focused plasma (Aixtron P6) [14, 15] or the linear antenna system (AK400, Roth & Rau), which exhibits unique characteristics compared to focused plasma systems [16–18]. Amorphous Si (a-Si) interlayers (5, 10, and 20 nm) were prepared by a custom RF plasma enhanced CVD system by Aurion.

Three sets of samples were prepared and studied for the influence of a-Si interlayer thickness, substrate type, and deposition system on SiV color center activity (see Table 1).

Samples with defined a-Si interlayer thickness were prepared using the focused plasma reactor as follows: (a) first, approx. 50 nm NCD film was deposited using 1% of methane (3 sccm) diluted in hydrogen (300 sccm), total gas pressure $p = 5 \text{ kPa}$, substrate temperature $T_s \approx 730 \text{ }^\circ\text{C}$, using the total power $P = 2.5 \text{ kW}$ and 45 min deposition time, (b) then transferred for a-Si growth, and (c) finally redeposited by approx. 100 nm NCD layer using 1% of methane (3 sccm) diluted in hydrogen (300 sccm), $p = 6 \text{ kPa}$, $T_s \approx 900 \text{ }^\circ\text{C}$, $P = 3 \text{ kW}$, and 1 h deposition time.

Samples comparing the focused and linear plasma reactor were prepared using two nucleation procedures:

Table 1 The parameters of prepared samples.

sample name	deposition system	substrate type	a-Si interlayer (nm)
S1a	focused	UQG	0
S1b	focused	UQG	5
S1c	focused	UQG	10
S1d	focused	UQG	20
S2a	focused	Mo	0
S2b	focused	Mo	5
S2c	focused	Mo	10
S3a	focused	UQG	10 nm a-Si/nucleated
S3b	focused	UQG	nucleated/10 nm a-Si
S3c	linear antenna	UQG	10 nm a-Si/nucleated
S3d	linear antenna	UQG	nucleated/10 nm a-Si

(a) nucleated substrate was redeposited by 10 nm a-Si layer and (b) clean substrate with 10 nm a-Si was nucleated. Only UQG substrates were used. These pretreated substrates were then loaded for NCD growth in both deposition systems. In the case of the focused plasma system, the deposition parameters were the same as in the third step when 1% of CH₄ in H₂, $p = 6$ kPa, $T_s \approx 900$ °C, $P = 3$ kW, and 1 h deposition time were used. The process parameters of the linear antenna system were as follows: H₂/CH₄/CO₂ gas mixture (2.5% of CH₄ and 10% CO₂ in 200 sccm H₂), $P = 2$ kW at each antenna side, $p = 100$ Pa, and $T_s \approx 450$ °C. The substrate table was on floating potential at a distance of 70 mm from antennas [18].

Surface morphology was characterized by scanning electron microscopy (SEM, e_LiNE writer, Raith GmbH). The layer thickness was characterized by the reflectance interferometry and evaluated using the commercial Film Wizard (Scientific Computing International) software. The thickness of selected samples was also confirmed by SEM in cross-section view.

The diamond character of films as well as their PL was determined at room temperature by the Renishaw In Via Reflex Raman spectrometer using a CCD camera, the UV excitation wavelength of 325 nm for Raman spectra and blue excitation light 442 nm for the PL spectra. Steady state PL was also measured at room temperature in 550–1050 nm spectral range under oblique incidence 60° in our micro-spectroscopic setup with TTL triggered green excitation

laser operating at 532 nm and 200 mW, the fused silica aspheric lens collecting PL ($f = 20$ mm, N.A. 0.5), Horiba H10 monochromator and fW photodiode receiver locked-in to the laser reference frequency.

3 Results and discussion The development of the layer morphology with increasing a-Si interlayer thickness is shown in Fig. 1. Shown images are for UQG substrates.

Figure 1a shows the surface morphology of NCD film without a-Si interlayer. The grains are well faceted with average size 170 nm. Figure 2a shows surface morphology of NCD film with 5 nm a-Si interlayer. Renucleation and a decrease of average grain size are observed due to the a-Si interlayer. As will be shown later in Fig. 2a, the a-Si layer is too thin or it is reduced during the growth of diamond to observe its recrystallization. Due to this fact further growth of the upper diamond layer is only weakly influenced by the a-Si layer. In Fig. 1c and d, the effect of renucleation is more evident with the average grain size decreasing to ≈ 100 nm (Fig. 1c) and ≈ 75 nm (Fig. 1d). The pronounced renucleation with 20 nm of a-Si interlayer is mostly caused by recrystallization of Si (see sample S1d in Fig. 2a). Another effect of increased a-Si interlayer is stress compensation. This problem is caused by lattice mismatch and is emphasized when growing thicker NCD films and/or high thermal cooling after the deposition occurs. We have tested higher sample cooling after the NCD deposition on UQG substrates. Cracking and delamination of NCD was reduced with increased a-Si layer thickness. Morphology changes of sample S3a and S3c versus S3b and S3d confirm that 10 nm a-Si layer on top of nucleated sample increase renucleation of diamond grains.

Figure 2 shows Raman spectra of diamond coatings for increasing a-Si interlayer thickness both for UQG and Mo substrates. In the Raman spectra, six peaks are identified. The diamond characteristic peak centered at 1332 cm⁻¹ [19]. Broad bands centered at 1350 and 1580 cm⁻¹ are attributed to D and G bands [20]. The broad sub-band centered at 1150 cm⁻¹, which is attributed to the *trans*-poly-acetylene groups (C–H bonds). The peak at 520.7 cm⁻¹ corresponds to crystalline Si with a shoulder from amorphous phase at 480 cm⁻¹, where the peak at approx. 960 cm⁻¹ reflects its second order [21, 22].

All samples show high quality NCD film were prepared independent on substrate material and the thickness of a-Si

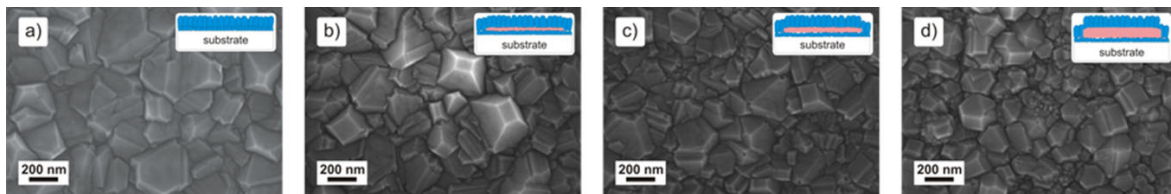


Figure 1 SEM images of the diamond surface morphology changes induced by increasing thickness of a-Si interlayer. From left (a) to right (d), the a-Si thickness increased from 0 nm (sample S1a) to 5 nm (S1b), 10 nm (S1c) and 20 nm (S1d) where the renucleation of diamond is pronounced.

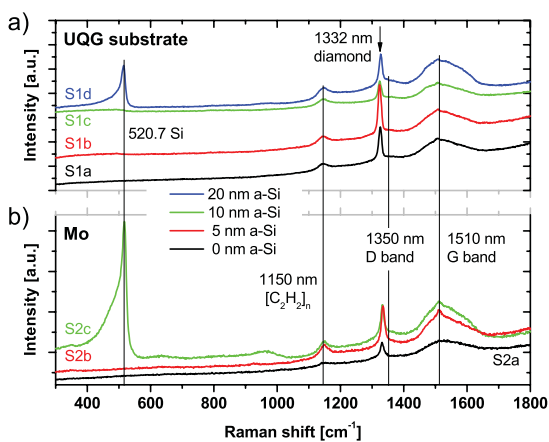


Figure 2 Raman spectra of the diamond films (S1x and S2x) as a function of a-Si layer thicknesses on both substrates.

layer owing to constant process parameters and confirms the high reproducibility of the deposition system [14]. Recrystallization of the a-Si interlayer is observed with increasing a-Si thickness as confirmed by the peak at 520.7 cm^{-1} . This is due to the equilibrium between enough high amount of Si atoms [23], optimal temperature and detection limit of Raman measurement setup. Recrystallized Si grains are attributed to increasing renucleation of the upper NCD film as shown in Fig. 1.

Figure 3 shows PL spectra of diamond coatings as a function of a-Si interlayer thickness both for UQG and Mo substrates. The PL spectrum shows the ZPL from SiV center at 738 nm, and associated satellites merged into a broad shoulder at 757 nm [6]. Activity of the SiV center was also confirmed for the sample without a-Si interlayer, see Fig. 3a. To eliminate the effect of glass substrate sputtering as a source of Si, Mo substrates were used. Since the 738 nm

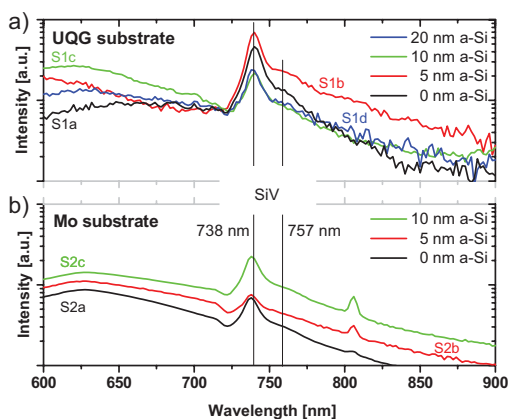


Figure 3 PL emission spectra taken at RT under 532 nm excitation on NCD samples (S1x and S2x) with various a-Si layer thicknesses on both substrates.

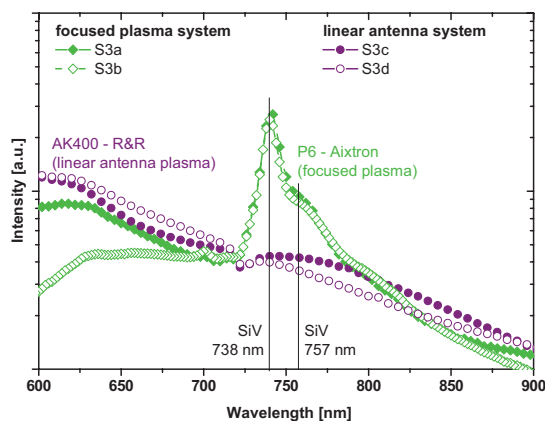


Figure 4 PL emission spectra at RT taken under 532 nm excitation on NCD samples (S3x) comparing focused and linear antenna plasma system.

PL peak is present in NCD grown on Mo, see Fig. 3b, the substrate is not the source of Si atoms. The idea of pronounced fabrication of SiV centers by immersing the a-Si layer into NCD film was also not confirmed. Thus, we speculate that the source of Si remains in the quartz bell jar of the focused plasma system. Indeed, the electrical field strength in the two focal maxima of the ellipsoidal cavity resonator is three times greater than side maxima [24]. These side maxima in close vicinity to the bell jar can ignite weak plasma, which etches Si from it. This contamination was detected previously [25] but it was not understood as a feature of the system that created optically active centers in diamond.

Moreover, for Mo substrate also a peak at 806 nm was detected and its activity decreased with decreasing thickness of a-Si interlayer. However, the origin of this peak is unclear at the moment.

Figure 4 shows PL spectra of diamond coatings for two pretreatment layers in the focused and linear antenna plasma deposition systems. Since the a-Si layer was not found to cause a detectable improvement in the fabrication of SiV centers, we have focused on the other deposition system utilizing linear antenna MW plasma source [16–18]. By comparing PL activity of the samples grown in the focused plasma system (S3a and S3b) with samples from the linear antenna plasma system (S3c and S3d) in Fig. 4, we can conclude that no detectable PL is present in the samples S3c and S3d. This observation further indicates that the Si-color center is closely related to the focused plasma system. The future outlook includes the study of SiV activity as a function of the substrate temperature and gas composition.

4 Conclusions In the presented work, we have investigated the reproducible method of SiV color center preparation in diamond. The PL activity of single phonon centers in diamond layers was achieved and correlated with process parameters and deposition system characteristics.

Our observations indicate that the Si-color center is closely related to the focused plasma system. The idea of pronounced fabrication of SiV centers by the presence of the a-Si interlayer in the NCD film was not confirmed. On the other hand, we observed that the increased a-Si thickness results in reduction of stress in NCD film and increased renucleation of NCD film.

Acknowledgements This work was financially supported by the Czech Science Foundation research projects 14-04790S (SP), Technology Agency of the Czech Republic TA01011740 (SP), and by the MSMT project LH12186 (ZR) (KONTAKT II). This work was carried out in the frame of the LNSM infrastructure.

References

- [1] A. Schrand, S. A. C. Hens, and O. Shenderova, *Crit. Rev. Solid State Mater. Sci.* **34**, 18–74 (2009).
- [2] F. Jelezko and J. Wrachtrup, *Phys. Status Solidi A* **203**, 3207–3225 (2006).
- [3] E. Neu, D. Steinmetz, J. Riedrich-Möller, S. Gsell, M. Fischer, M. Schreck, and C. Becher, *New J. Phys.* **13**, 025012 (2011).
- [4] A. M. Zaitsev, *Optical Properties of Diamond: A Data Handbook* (Springer, Berlin, 2001).
- [5] J. R. Rabeau, A. Stacey, A. Rabeau, S. Praver, F. Jelezko, I. Mirza, and J. Wrachtrup, *Nano Lett.* **7**, 3433–3437 (2007).
- [6] T. Feng and B. D. Schwartz, *J. Appl. Phys.* **73**, 1415–1425 (1993).
- [7] T. Gaebel, I. Popa, A. Gruber, M. Domhan, F. Jelezko, and J. Wrachtrup, *New J. Phys.* **6**, 98 (2004).
- [8] Y.-K. Tzeng, O. Faklaris, B.-M. Chang, Y. Kuo, J.-H. Hsu, and H.-C. Chang, *Angew. Chem. Int. Ed.* **50**(10), 2262–2265 (2011).
- [9] C.-Y. Fang, V. Vijayanthimala, C.-A. Cheng, S.-H. Yeh, C.-F. Chang, C.-L. Li, and H.-C. Chang, *Small* **7**, 23 (2011).
- [10] A. A. Basov, M. Rahn, M. Pärs, I. I. Vlasov, I. Sildos, A. P. Bolshakov, V. G. Golubev, and V. G. Ralchenko, *Phys. Status Solidi A* **206**, 2009–2011 (2009).
- [11] I. I. Vlasov, A. A. Shiryayev, T. Rendler, S. Steinert, S.-Y. Lee, D. Antonov, M. Vörös, F. Jelezko, A. V. Fisenko, L. F. Semjonova, J. Biskupek, U. Kaiser, O. I. Lebedev, I. Sildos, P. R. Hemmer, V. I. Konov, A. Gali, and J. Wrachtrup, *Nature Nanotechnol.* **9**, 54–58 (2014).
- [12] S. Szunerits and R. Boukherroub, *J. Solid State Electrochem.* **12**, 1205–1218 (2008).
- [13] A. Kromka, Š. Potocký, J. Čermák, B. Rezek, J. Potměšil, J. Zemek, and M. Vaněček, *Diamond Relat. Mater.* **17**, 1252 (2008).
- [14] M. Fünér, C. Wild, and P. Koidl, *Appl. Phys. Lett.* **72**, 1149–1151 (1998).
- [15] S. Potocký, A. Kromka, J. Potmesil, Z. Remes, Z. Polackova, and M. Vanecek, *Phys. Status Solidi A* **203**, 3011–3015 (2006).
- [16] A. Kromka, O. Babchenko, T. Izak, K. Hruska, and B. Rezek, *Vacuum* **86**, 776–779 (2012).
- [17] Š. Potocký, O. Babchenko, K. Hruška, and A. Kromka, *Phys. Status Solidi B* **249**, 2399–2403 (2012).
- [18] Š. Potocký, M. Čada, O. Babchenko, T. Ižák, M. Davydova, and A. Kromka, *Phys. Status Solidi B* **250**, 2717–2722 (2013).
- [19] S. Bühlmann, E. Blank, R. Haubner, and B. Lux, *Diamond Relat. Mater.* **8**, 194 (1999).
- [20] S. L. Heidger, *MRS Proc.* **383**, 319 (1995).
- [21] H. K. Woo, C. S. Lee, I. Bello, and S. T. Lee, *Diamond Relat. Mater.* **8**, 1737–1740 (1999).
- [22] C. Smit, R. A. C. M. M. van Swaaij, H. Donker, A. M. H. N. Petit, W. M. M. Kessels, and M. C. M. van de Sanden, *J. Appl. Phys.* **94**, 3582 (2003).
- [23] M. Zacharias and P. Streitenberger, *MRS Proc.* **638**, F6.2.1 (2000).
- [24] M. Fünér, C. Wild, and P. Koidl, *Surf. Coat. Technol.* **116–119**, 853–862 (1999).
- [25] A. Kromka, R. Kravetz, A. Poruba, J. Zemek, V. Perina, J. Rosa, and M. Vanecek, *Phys. Status Solidi A* **199**, 108–112 (2003).

A.9

Influence of gas chemistry on Si-V color centers in diamond films

Influence of gas chemistry on Si-V color centers in diamond films

Štěpán Potocký*, Tibor Ižák, Marian Varga, and Alexander Kromka**

Institute of Physics AS CR, v.v.i., Cukrovarnická 10, 16200 Praha, Czech Republic

Received 17 April 2015, revised 23 June 2015, accepted 25 June 2015

Published online 20 July 2015

Keywords chemical vapor deposition, diamond, photoluminescence, plasma, silicon optical centers

* Corresponding author: e-mail potocky@fzu.cz, Phone: +420 220 318 437, Fax: +420 233 343 184

** e-mail kromka@fzu.cz, Phone: +420 220 318 437, Fax: +420 233 343 184

In this paper, we studied the influence of process parameters on the incorporation and optical activity of the silicon vacancy (Si-V) zero phonon line (ZPL) in diamond films. The ZPL intensity at 738 nm is studied in nano- and micro-crystalline diamond films deposited by microwave plasma enhanced CVD as a function of a substrate temperature, gas composition, i.e. CO₂ and N₂ concentrations in the gas mixture. We found that the ZPL intensity of Si-V center is independent in a broad deposition temperature range from 450 °C to 1100 °C with a

full width of half maxima (FWHM) of 6 nm. For the lowest deposition temperature (350 °C), the ZPL intensity decreases and the FWHM doubles. The Si-V center ZPL vanished for admixtures of 1% CO₂ or 2.5% of N₂ and higher in the gas mixture. For smaller concentrations, the ZPL intensity gradually decreased while keeping the ZPL peak position and FWHM constant. The influence of CO₂ and N₂ addition on the diamond morphology is also discussed with respect to the presence of Si-V centers.

© 2015 WILEY-VCH Verlag GmbH & Co. KGaA, Weinheim

1 Introduction Optical centers in diamond reveal outstanding photoluminescence (PL) properties as high quantum yields, negligible photobleaching, and no blinking [1]. The zero-phonon line (ZPL) of Si-V centers in diamond is predominantly localized at approximately 738 nm [2–4]. Its sharp and short-lived emission line makes diamond a promising single-photon source material [5] or material suitable for bio-imaging due to its near infrared emission [6, 7]. Si-related centers are often and commonly incorporated in all chemically vapor deposited (CVD) diamonds by the etching of Si substrates, quartz windows, and bell jars [3, 4] or by addition of Si containing gasses to the gas mixture [8]. To achieve PL enhancement and reproducible fabrication, studies related to the substrate material morphology [5, 9] and quality [10], gas composition [11–13] or creating special structures [14–16] were carried out. Due to carbon–carbon sp³ hybridized bonds, diamond can be easily functionalized with various chemical groups [17] which can also influence the optical activity of nearly localized color centers. A high interest is seen in fabrication of nanodiamonds. They can be fabricated directly [8, 11] or from solid films [18]. Molecular-sized fluorescent nanodiamonds with Si-V centers were theoretically predicted [19] and experimentally confirmed [20].

This concerns applications in drug delivery [21] or fluorescent labeling [22, 23].

In the diamond CVD process, oxygen is added to a source gas mixture to increase the growth rate and/or to improve the quality of the resultant films [24, 25] due to faster etching of non-diamond phases. Oxygen containing gas species are also very effective for low temperature diamond growth [26–28]. On the other hand, the addition of nitrogen into the gas mixture resulted in quite significant morphological changes in diamond films [29, 30].

In this contribution, we present a reproducible method for the preparation of diamond films with controllable enhanced photoluminescence corresponding to Si-V color centers. The influence of process parameters (substrate temperature and gas composition – CO₂ or N₂ addition) on the Si-V center ZPL intensity is studied.

2 Experimental Thin diamond films were grown on 10 × 10 mm² Si (100) substrates. Before the CVD growth, substrates were ultrasonically pre-treated in a suspension of deionized water and ultra-dispersed detonation diamond powder (diameter 5–10 nm, New Metals and Chemicals Corp. Ltd., Kyobashi) [31]. The CVD deposition of diamond was performed in a microwave plasma-enhanced

CVD reactor using the ellipsoidal resonator with focused plasma [32]. Three sets of samples were prepared. Diamond films were grown from hydrogen rich plasma from two various gas compositions (i.e., $\text{H}_2/\text{CH}_4/\text{CO}_2$ and $\text{H}_2/\text{CH}_4/\text{N}_2$) and at varied substrate temperatures (T_s) from 350 °C to 1100 °C.

For the study of the T_s influence on the Si-V center ZPL intensity, the diamond films were deposited from 1% CH_4/H_2 gas mixture. Variation of T_s (350, 500, 650, 800, 900, and 1100 °C) was controlled by changing total gas pressure p , total microwave power P , and heat transfer efficiency to the cooled substrate holder [33]. The growth time t was 15 min to 12 h to achieve the same diamond thickness (approximately 200 nm).

For the study of the CO_2/H_2 concentration (0, 0.5, 1.5, 2.5, 3.5, and 4.5%) in the gas mixture on the Si-V center activity, diamond films were deposited at 5% CH_4/H_2 , $p = 6$ kPa, $T_s \approx 900$ °C, $P = 3$ kW, and $t = 4$ h.

For the study of the N_2/H_2 concentration (0, 0.5, 1, 2, 4, and 6%) in the gas mixture on the Si-V center activity, diamond films were deposited at 5% CH_4/H_2 , $p = 7$ kPa, $T_s \approx 800$ °C, $P = 3$ kW, and $t = 2$ h.

In the gas composition experiments ($[\text{CO}_2]$ and $[\text{N}_2]$ studies), the diamond deposition was first 10 min without CO_2 or N_2 addition to the gas mixture to prevent etching of the seeding layer.

The diamond character of films as well as their photoluminescence was determined at room temperature by the Renishaw In Via Reflex Raman spectrometer using CCD camera with 442 nm excitation wavelength. Surface morphology was characterized by a scanning electron microscopy (SEM, e_LiNE writer, Raith GmbH). The film thickness was measured by a reflectance interferometry and evaluated using the Film Wizard software (Scientific Computing International).

3 Results and discussion

3.1 Influence of substrate temperature T_s

The influence of the substrate temperature T_s on the Si-V color center ZPL intensity was studied for 1% CH_4 in H_2 gas mixture. Figure 1 shows the dependence of surface morphology on the varied T_s from 350 °C to 1100 °C. It is well-known that an increased T_s results in an increased deposition rate and a pronounced crystal faceting [34]. In our case, all the films had the thickness approximately 200 nm. This was achieved by variation of the deposition time. The sample deposited at 350 °C (Fig. 1a) reveals the smallest grains (<50 nm). For higher T_s up to 900 °C, the grain size remains nearly constant with the size between 150 and 200 nm (see Fig. 1b–e). Similar grain size is mainly given by the same film thickness and effective growth process without renucleation during the diamond growth. For the highest T_s , a reduction of grain size is observed (Fig. 1f). This crystal size decrease is attributed to a too high (1100 °C) substrate temperature which is already behind an optimal deposition temperature where the graphitization occurs [35].

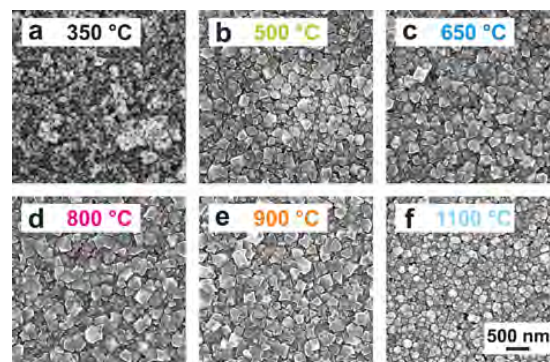


Figure 1 Surface morphology of diamond films deposited at different substrate temperatures T_s from the H_2/CH_4 gas mixture (scale bar corresponds to 500 nm for all images).

Figure 2 shows selected Raman spectra of samples deposited at four different substrate temperatures. Typical features for diamond films are observed, i.e., one sharp peak centered at ~ 1332 cm^{-1} and three bands centered at the frequencies of ~ 1150 , ~ 1360 , and ~ 1580 cm^{-1} . Intensity of the diamond peak at 1332 cm^{-1} (sp^3 diamond phase) increases with increasing T_s . The D-band at 1360 cm^{-1} is observed when small graphite crystallites are present.

A broad band from approximately 1450 to 1630 cm^{-1} is a superposition of several bands, including trans-polyacetylene band (1450 cm^{-1}) and G-band (related to sp^2 graphite phase) at 1550 – 1620 cm^{-1} [36, 37]. The G-band increases for the sample deposited at the highest T_s (1100 °C), which is attributed to high sp^2 content due to a too high substrate temperature when microcrystalline graphite may be also formed [35]. For the $T_s = 350$ °C, the trans-polyacetylene band (at 1150 cm^{-1}) is attributed to a high

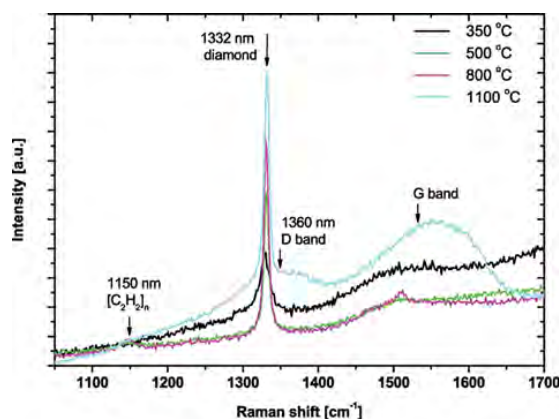


Figure 2 Raman spectra of diamond films deposited at different substrate temperatures T_s from the H_2/CH_4 gas mixture.

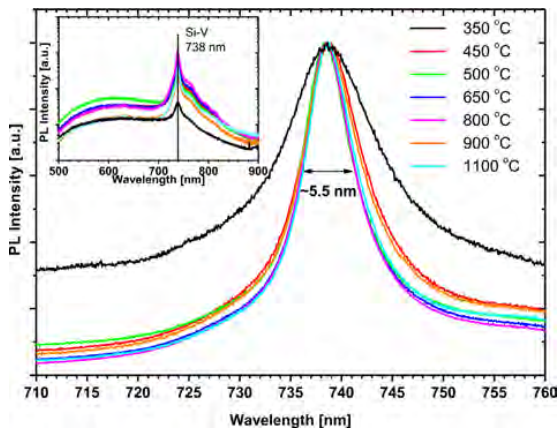


Figure 3 The normalized photoluminescence emission spectra from diamond films deposited at various substrate temperatures T_s . The PL spectra were taken at RT using the 442 nm excitation wavelength. The inset shows as-measured spectra.

amount of grain boundaries as the average grain size is the lowest [38].

The normalized photoluminescence spectra of diamond films as a function of substrate temperatures T_s are shown in Fig. 3. The photoluminescence spectra show the Si-V center ZPL line at 738 nm, and associated satellites merged into a broad shoulder at 757 nm [3, 4]. The diamond films deposited at $T_s \geq 450$ °C reveal comparable ZPL intensities as well as the FWHMs (6 nm) independently on T_s . These observations are similar to previously published results [9]. For the $T_s = 350$ °C, the FWHM of the 738 nm Si-V center peak is doubled while the intensity decreased to 70%. Based on SEM and Raman measurements (as seen in Figs. 1 and 2), this can be attributed to structural defects and increased amount of non-diamond phases within the formed diamond film. The presence of NV centers in the grown films was not detected (as seen in the inset of Fig. 3).

3.2 Influence of gas composition As introduced, the addition of other gases to standard H_2/CH_4 chemistry can change the diamond morphology from micro- to nano- or even to an ultra-nanocrystalline character. Similarly, film quality, growth rate, and the most importantly, the presence and activity of the Si-V center will be influenced too. Based

on our previous work [30], we fixed CH_4/H_2 concentration at 5% at different CO_2 and N_2 added concentrations.

Figure 4 shows SEM images of diamond films deposited at CO_2 varied from 0 to 4.5%. No significant change of diamond growth or surface morphology is observed up to 3.5% CO_2 . On the other hand, the deposition is slowed down already at 4.5% CO_2 due to the prevailing etching process promoted by CO_2 addition [27].

Figure 5a shows the photoluminescence spectra of the diamond films deposited at various CO_2 concentrations while the inset in Fig. 5a shows the corresponding Raman spectra. The Raman spectra prove the good quality of the diamond films with dominating sharp diamond peak. In contrast to the Raman results, the PL spectra show a strong sensitivity to the CO_2 . An addition of 0.5% CO_2 into the gas mixture reduces the ZPL intensity by more than 50%. The Si-V center position and the FWHM did not change. A further increase of CO_2 concentration to 1.5% and higher resulted in a total quenching of Si-V centers. No qualitative change in the diamond peak (1332 cm^{-1}) was observed for various CO_2 concentrations (see inset in Fig. 5a) confirming the good quality of the diamond films.

Figure 5b shows a dependence of the ZPL intensity after the N_2 addition to the gas mixture. In this case, the addition of 0.5% N_2 into the gas mixture already led to reduction of the ZPL intensity by 50%. The ZPL intensity decreased to 30% for 1% of N_2 . The position and FWHM of the Si-V ZPL were insensitive to these N_2 concentrations. No active Si-V centers were detected for N_2 concentrations higher than 1%. Competitive vacancy creation processes with oxygen or nitrogen might be the reason for ZPL intensity decrease due to the lack of vacancies. The observed decrease in the Si-V intensity can be caused by changed plasmochemistry (preferential formation of SiO_x complexes in the gas phase) or changed growth kinetics (higher N_2 content enhances the renucleation which leads to the formation of a larger amount of grain boundaries). It is well known that the diffusion of any element into diamond lattice is very low (nearly zero). Moreover, the dopants should be preferentially segregated along the impurities induced by additional element rather than substitutionary incorporated in the diamond crystal lattice. Thus, the decrease of Si-V intensity with higher N_2 concentration could be attributed to the quenching of the Si-V PL as a result of N_2 clustering and/or too high amount of non-diamond carbon phases [11, 39].

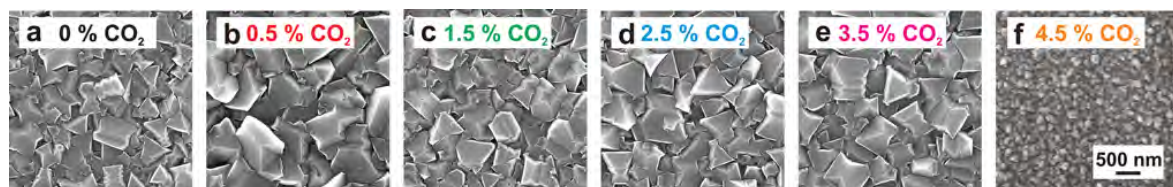


Figure 4 Surface morphology of diamond films as a function of CO_2 addition to the H_2/CH_4 gas mixture (scale bar corresponds to 500 nm for all images).

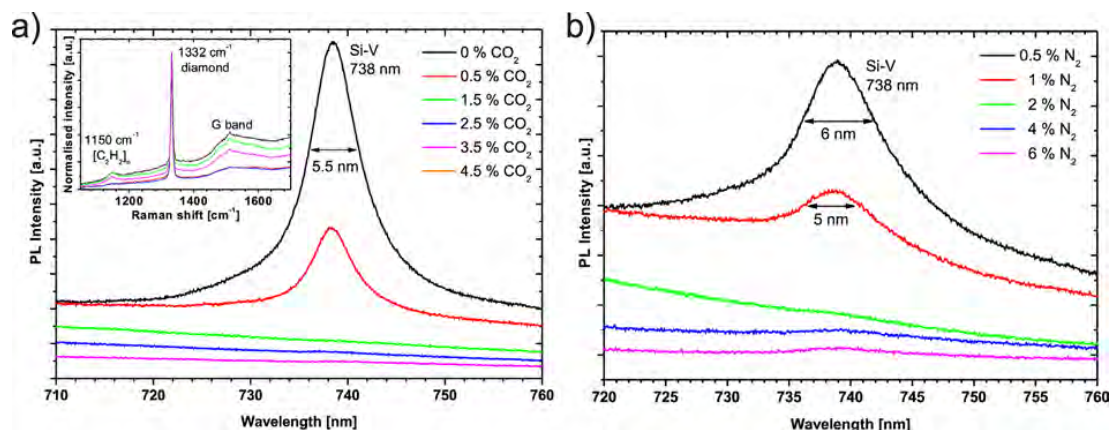


Figure 5 Photoluminescence emission spectra and Raman spectra (inset) of the diamond films as a function of: (a) CO₂ addition, (b) N₂ addition to the H₂/CH₄ gas mixture.

The surface morphology changed significantly and revealed a transformation from well-faceted diamond film (without N₂) to a nanowire-like diamond structure ($\geq 4\%$ of N₂). As previously observed by SEM and Raman spectra, the diamond growth was hindered for 10% N₂ [30]. In contrast to the Singh and Catledge findings [11], we did not observe any increase of Si-V emission after nitrogen addition. It is assumed that this difference might be attributed to much lower N₂ concentrations used in their work. On the other hand in their work [11], enhancement of the ZPL diminished for 0.115% N₂. These different findings might be assigned to the deposition apparatus. Moreover, the main source of Si atoms is coming from the Si substrate [11, 40].

The SIMS measurements (SIMS TOF IV. ION TOF Muenster) revealed the Si content at the detection limit of our setup (i.e., more or less comparable with the noise signal – not shown here). On the other hand, the depth profiling indicated a nearly linear Si increase at the diamond/Si interface. This dependence could be assigned to the plasma etching of the Si substrate before its coating with a continuous diamond film.

Our results indicate the technological possibility to deposit diamond films at high quality and defined morphologies with or without optically active Si-V color centers fabricated within one deposition process.

4 Conclusion We studied the influence of process parameters on the Si-V color center ZPL intensity correlated with the quality and morphology changes of diamond films. The intensity of Si-V centers ZPL was independent of the substrate temperature T_s . Similar grain size (~ 175 nm) was obtained for T_s in the range of 450–900 °C. For the lowest (350 °C) and the highest (1100 °C) substrate temperatures, the grain size was reduced and graphitization occurred at 1100 °C. By a small addition of CO₂ or N₂ into the gas mixture, the Si-V ZPL intensity gradually decreased. Moreover, morphology of

the diamond films with active Si-V centers was insensitive to the CO₂ admixture. In the case of nitrogen addition, the diamond film morphology changed from micro- to nanocrystalline structure still revealing active Si-V centers. In all cases, no shift of the ZPL was observed. The FWHM of the ZPLs was 5–6 nm except for the sample deposited at 350 °C when it was doubled.

These experiments indicate that a gradient intensity of Si-V color centers within the diamond film can be prepared by precise control of the gas mixture and still keeping good enough film quality and morphology. Using this strategy, sandwich-like structures consisting of optically active and not active Si-V centers can be fabricated. Moreover, micro- or nanocrystalline diamond character can be tailored by the gas admixture while still keeping optical activity of the Si-V centers.

Acknowledgements The authors would like to thank A. Vincze for the SIMS measurements (ILC in Bratislava). This work was financially supported by the Czech Science Foundation research project 14-04790S (SP). This work was partially supported by the COST Action MP1403 “Nanoscale Quantum Optics”. This work was carried out in the frame of the LNSM infrastructure.

References

- [1] A. Schrand, S. A. C. Hens, and O. Shenderova, *Crit. Rev. Solid State Mater. Sci.* **34**(1), 18–74 (2009).
- [2] A. M. Zaitsev, *Optical Properties of Diamond: A Data Handbook* (Springer, Berlin, 2001).
- [3] H. Sternschulte, K. Thonke, R. Sauer, P. Münzinger, and P. Michler, *Phys. Rev. B* **50**(19), 14554–14560 (1994).
- [4] T. Feng and B. D. Schwartz, *J. Appl. Phys.* **73**(3), 1415 (1993).
- [5] I. I. Vlasov, A. S. Barnard, V. G. Ralchenko, O. I. Lebedev, M. V. Kanzyuba, A. V. Saveliev, V. I. Konov, and E. Goovaerts, *Adv. Mater.* **21**(7), 808–812 (2009).
- [6] R. J. Narayan, R. D. Boehm, and A. V. Sumant, *Mater. Today* **14**(4), 154–163 (2011).
- [7] A. M. Smith, M. C. Mancini, and S. Nie, *Nature Nanotechnol.* **4**(11), 710–711 (2009).

- [8] S. A. Grudinkin, N. A. Feoktistov, A. V. Medvedev, K. V. Bogdanov, A. V. Baranov, A. Y. Vul', and V. G. Golubev, *J. Phys. D, Appl. Phys.* **45**(6), 062001 (2012).
- [9] V. Sedov, V. Ralchenko, A. A. Khomich, I. Vlasov, A. Vul, S. Savin, A. Goryachev, and V. Konov, *Diam. Relat. Mater.* **56**, 23–28 (2015).
- [10] M. G. Donato, G. Faggio, G. Messina, S. Santangelo, M. Marinelli, E. Milani, G. Pucella, and G. Verona-Rinati, *Diam. Relat. Mater.* **13**(4–8), 923–928 (2004).
- [11] S. Singh, S. A. Catledge, *J. Appl. Phys.* **113**(4), 044701 (2013).
- [12] T. Y. Ko, Y. L. Liu, K. W. Sun, Y. J. Lin, S.-C. Fong, I. N. Lin, and N. H. Tai, *Diam. Relat. Mater.* **35**, 36–39 (2013).
- [13] I. Sakaguchi, M. Nishitani-Gamo, K. P. Loh, H. Haneda, S. Hishita, and T. Ando, *Appl. Phys. Lett.* **71**(5), 629 (1997).
- [14] J. Song, H. Li, F. Lin, L. Wang, H. Wu, and Y. Yang, *CrystEngComm* **16**(36), 8356 (2014).
- [15] A. A. Basov, M. Rähn, M. Pärs, I. I. Vlasov, I. Sildos, A. P. Bolshakov, V. G. Golubev, and V. G. Ralchenko, *Phys. Status Solidi A* **206**(9), 2009–2011 (2009).
- [16] S. Singh, V. Thomas, D. Martyshkin, V. Kozlovskaya, E. Kharlampieva, and S. A. Catledge, *Nanotechnology* **25**(4), 045302 (2014).
- [17] S. Szunerits and R. Boukherroub, *J. Solid State Electrochem.* **12**(10), 1205–1218 (2008).
- [18] E. Neu, C. Arend, E. Gross, F. Guldner, C. Hepp, D. Steinmetz, E. Zscherpel, S. Ghodbane, H. Sternschulte, D. Steinmüller-Nethl, Y. Liang, A. Krueger, and C. Becher, *Appl. Phys. Lett.* **98**(24), 243107 (2011).
- [19] A. S. Barnard, I. I. Vlasov, and V. G. Ralchenko, *J. Mater. Chem.* **19**(3), 360–365 (2009).
- [20] I. I. Vlasov, A. A. Shiryayev, T. Rendler, S. Steinert, S.-Y. Lee, D. Antonov, M. Vörös, F. Jelezko, A. V. Fisenko, L. F. Semjonova, J. Biskupek, U. Kaiser, O. I. Lebedev, I. Sildos, P. R. Hemmer, V. I. Konov, A. Gali, and J. Wrachtrup, *Nature Nanotechnol.* **9**(1), 54–58 (2013).
- [21] O. Faklaris, D. Garrot, V. Joshi, F. Druon, J.-P. Boudou, T. Sauvage, P. Georges, P. A. Curmi, and F. Treussart, *Small* **4**(12), 2236–2239 (2008).
- [22] T. D. Merson, S. Castelletto, I. Aharonovich, A. Turbic, T. J. Kilpatrick, and A. M. Turnley, *Opt. Lett.* **38**(20), 4170 (2013).
- [23] D. Evanko, *Nature Meth.* **5**(3), 218–219 (2008).
- [24] M. Frenklach and H. Wang, *Phys. Rev. B* **43**(2), 1520 (1991).
- [25] J. A. Mucha, D. L. Flamm, and D. E. Ibbotson, *J. Appl. Phys.* **65**(9), 3448 (1989).
- [26] Y. Muranaka, H. Yamashita, and H. Miyadera, *Diam. Relat. Mater.* **3**(4–6), 313–318 (1994).
- [27] A. Kromka, O. Babchenko, T. Izak, M. Varga, M. Davydova, M. Kratka, and B. Rezek, *Adv. Sci. Eng. Med.* **5**(6), 509–514 (2013).
- [28] Š. Potocký, O. Babchenko, K. Hruška, and A. Kromka, *Phys. Status Solidi B* **249**(12), 2612–2615 (2012).
- [29] C.-R. Lin, W.-H. Liao, D.-H. Wei, J.-S. Tsai, C.-K. Chang, and W.-C. Fang, *Diam. Relat. Mater.* **20**(3), 380–384 (2011).
- [30] T. Izak, M. Davydova, M. Varga, S. Potocky, and A. Kromka, *Adv. Sci. Eng. Med.* **6**(7), 749–755 (2014).
- [31] A. Kromka, Š. Potocký, J. Čermák, B. Rezek, J. Potměšil, J. Zemek, and M. Vaněček, *Diam. Relat. Mater.* **17**(7–10), 1252–1255 (2008).
- [32] M. Fünér, C. Wild, and P. Koidl, *Appl. Phys. Lett.* **72**(10), 1149–1151 (1998).
- [33] S. Potocky, A. Kromka, J. Potmesil, Z. Remes, Z. Polackova, and M. Vanecek, *Phys. Status Solidi A* **203**(12), 3011–3015 (2006).
- [34] D. Das and R. N. Singh, *Int. Mater. Rev.* **52**(1), 29–64 (2007).
- [35] H. Liu, D. S. Dandy, *Diamond Chemical Vapor Deposition: Nucleation and Early Growth Stages* (Noyes Publications, Park Ridge, N.J., 1995).
- [36] I. I. Vlasov, E. Goovaerts, V. G. Ralchenko, V. I. Konov, A. V. Khomich, and M. V. Kanzyuba, *Diam. Relat. Mater.* **16**(12), 2074–2077 (2007).
- [37] A. C. Ferrari and J. Robertson, *Philos. Trans. R. Soc. A, Math. Phys. Eng. Sci.* **362**(1824), 2477–2512 (2004).
- [38] S. Praver and R. J. Nemanich, *Philos. Trans. R. Soc. A, Math. Phys. Eng. Sci.* **362**(1824), 2537–2565 (2004).
- [39] K. Iakoubovskii and G. J. Adriaenssens, *Diam. Relat. Mater.* **9**(7), 1349–1356 (2000).
- [40] L. Bergman, B. R. Stoner, K. F. Turner, J. T. Glass, and R. J. Nemanich, *J. Appl. Phys.* **73**(8), 3951 (1993).

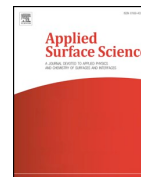
A.10

Nucleation of diamond micro-patterns with photoluminescent SiV centers controlled by amorphous silicon thin films



Contents lists available at ScienceDirect

Applied Surface Science

journal homepage: www.elsevier.com/locate/apsusc

Full length article

Nucleation of diamond micro-patterns with photoluminescent SiV centers controlled by amorphous silicon thin films



Jan Fait^{a,b,*}, Štěpán Potocký^a, Štěpán Stehlík^a, Jiří Stuchlík^a, Anna Artemenko^a, Alexander Kromka^a, Bohuslav Rezek^b

^a Institute of Physics, CAS, Cukrovarnická 10, 16200 Prague, Czech Republic

^b Faculty of Electrical Engineering, Czech Technical University in Prague, Technická 27, 16627 Prague, Czech Republic

ARTICLE INFO

Keywords:

Spontaneous nucleation
Diamond
Hydrogenated amorphous silicon
Selective growth
Focused microwave CVD

ABSTRACT

Selective deposition of diamond allows bottom-up growth of diamond nanostructures and nanoscale devices. However, it remains challenging to reduce the size of the patterns and to suppress parasitic spontaneous nucleation. We show here that thin layers of hydrogenated amorphous silicon (down to 40 nm) efficiently suppress spontaneous nucleation of diamond. The suppression of diamond nucleation does not depend on the substrate materials below hydrogenated amorphous silicon (Si, SiO₂, Pt, Ni). We attribute the suppressed diamond nucleation to surface disorder on atomic scale. By using a structured layer of hydrogenated amorphous silicon, highly selective growth of diamond micro-patterns with optically active SiV centers by low-temperature microwave plasma chemical vapor deposition is achieved.

1. Introduction

Diamond has many outstanding properties – optical, thermal, electrochemical, chemical, electronic [1] – which are very promising for many potential applications. One of the most interesting and intensively studied features are diamond colour centers [2,3]. They are investigated for many reasons such as detection of very weak magnetic fields [4,5] and quantum computing [6] by nitrogen-vacancy (NV) centers, and biomarkers and (bio-)sensing by silicon-vacancy (SiV) centers [7]. Many of these applications require, or may benefit from, precise placement of luminescent diamonds on a substrate.

When chemical vapor deposition (CVD) of diamond is carried out on a non-diamond substrate, stable clusters of carbon atoms with a diamond structure (called nuclei) must first be created. In order to become stable, clusters must overcome the energetic barrier (i.e. to achieve a critical size). This process is called spontaneous nucleation [8,9]. The height of the energetic (or nucleation) barrier is determined by the deposition conditions – the deposition system, the gas mixture, pressure or temperature [10]. The spontaneous nucleation rate is usually characterized by the nucleation density – the number of spontaneously created diamond grains per unit surface area. Spontaneous nucleation depends not only on the deposition conditions, but also on the properties of the substrate material. CVD diamonds usually start to grow after the formation of a carbide buffer layer on the substrate (e.g. SiC on

Si substrates). Moreover, the same material can lead to different nucleation densities if defects are present on the surface. For example, spontaneous nucleation is markedly enhanced near the scratches on an otherwise smooth surface [11].

The substrate is often seeded with diamond nanoparticles before deposition (e.g. in an ultrasonic bath), because the spontaneous nucleation process is typically slow and the nucleation density is relatively low and insufficient for growing thin, continuous films. Subsequently, the diamond grows directly on diamond grains. Lateral structuring of the seeding layer can be used for selective growth of diamond devices [12]. However, it is challenging to reduce the size of the patterns in the seeding layer to nanoscale, to control the position of the seeding particles in order to prepare small clusters of diamond crystals, as well as to reduce unwanted growth outside the defined areas [13].

A mask made of material that suppresses diamond nucleation can be used instead of lateral structuring of the seeding layer in order to achieve selective growth. There are several requirements on the material of the mask. 1. It must suppress spontaneous nucleation in order to achieve growth only within predefined areas. 2. It must be compatible with the conditions that are used for the diamond growth. 3. The material should be easily deposited, structured on nanoscale and, preferably, easily removable.

In this respect, hydrogenated amorphous silicon (a-Si:H) thin films are appealing. A layer of a-Si:H can easily be deposited by chemical

* Corresponding author at: Institute of Physics ASCR, Cukrovarnická 10, 16200 Prague, Czech Republic.
E-mail address: fait@fzu.cz (J. Fait).

<https://doi.org/10.1016/j.apsusc.2019.03.064>

Received 5 December 2018; Received in revised form 20 February 2019; Accepted 7 March 2019

Available online 08 March 2019

0169-4332/ © 2019 Elsevier B.V. All rights reserved.

vapor deposition, can easily be etched chemically, and can be locally structured by photolithography or even by a conductive atomic force microscope (AFM) [14–16].

In this study, we first investigate the effect of a-Si:H thin film coating on the spontaneous nucleation of diamond on various substrate materials. In order to quantify the effect, the nucleation density on a-Si:H is compared with the nucleation density on a bare Si wafer, as a reference. Low temperature diamond growth [17,18] was used for deposition in order to avoid thermally-induced changes in a-Si:H layers. We show that spontaneous nucleation of diamond is completely suppressed on amorphous silicon in contrast to monocrystalline silicon, where high spontaneous nucleation density can be achieved. In this sense, the a-Si:H film can work as a mask for selective diamond deposition, as demonstrated. Moreover, we show that the chemical purity of the diamond is high enough for optically active SiV centers to be observed. The method presented here can thus be highly beneficial for bottom-up growth of diamond photonic [19] or electronic devices [12].

2. Experimental

Spontaneous nucleation was investigated on the following substrates: standard polished monocrystalline p-type Si (100) wafers, or Si wafers with additional interlayer made of Ni (40 nm by evaporation), of Pt (40 nm by sputtering) or of SiO₂ (900 nm). All of these substrates were covered by a thin layer (40 nm–230 nm) of a-Si:H. The a-Si:H layers were deposited by chemical vapor deposition (CVD), using 0.02% of SiH₄ (1 sccm) diluted in helium (5000 sccm), and a low substrate temperature (50 °C). This process leads to a high hydrogen content in the a-Si:H layers (20–45 at. %). The thickness of the a-Si:H layer was controlled by the CVD deposition time, with a linear increase in thickness with deposition time, and was determined by atomic force microscopy (AFM). A bare monocrystalline silicon wafer (placed side-by-side with the a-Si:H covered samples) was used as a reference during subsequent diamond deposition, and the nucleation density on a-Si:H was compared with the nucleation density on this reference sample.

The diamond deposition was carried out in a focused microwave plasma CVD (MP-CVD) reactor (Aixtron P6) using an ellipsoidal cavity resonator. For the setup scheme of the reactor, see Fig. S1 in Supplementary Information. The plasma is located close (1–2 mm) to the substrate surface [8]. This proximity of the plasma limits the lowest substrate temperature that can be achieved during CVD deposition. The substrate temperature was kept low (approximately 430 °C; monitored by a *Williamson, PRO 92-20-C-23* type IR pyrometer) in order to reduce possible thermally-induced changes to the a-Si:H. In some cases, a higher surface temperature (approximately 560 °C) was used while keeping the deposition conditions unchanged. This was achieved by using a hollow substrate holder with lower thermal conductivity.

The deposition conditions were adjusted so that the nucleation density on the reference polished monocrystalline silicon substrates was higher than 10^6 cm^{-2} , which is the maximum that we could achieve while keeping the substrate temperature low. The reference substrates were cleaned using O₂ plasma treatment before depositions. The parameters used for diamond deposition were as follows: deposition time $t = 3 \text{ h}–12 \text{ h}$, total gas pressure $p = 4 \text{ kPa}$, gas flow of hydrogen H₂ equal to 300 sccm, gas flow of methane CH₄ equal to 3 sccm (or 15 sccm), power of the MW source $P = 4 \text{ kW}$. Three different deposition scenarios were used. In the first scenario (labeled as *long*), the deposition time was 12 h. All parameters were kept constant during the deposition. In the second scenario (labeled as *methane*), the deposition was shortened to 4 h. In order to enhance and accelerate spontaneous nucleation, the methane concentration was increased to 5% during the first hour. In the third scenario (labeled as *interrupted*), the deposition was interrupted after 0.5 h. Deposition was restarted after 0.25 h, and lasted a further period 3 h.

Scanning electron microscopy (SEM; *Tescan Maia3*) was used to determine the nucleation density of the diamond grains and the

morphology of the samples after deposition. The particles on randomly selected regions (each $1500 \mu\text{m}^2$ in area) over the surface of the sample were manually counted. Subsequently, the number of particles was divided by the total area of these regions.

The material and chemical composition of grains was characterized by Raman micro-spectroscopy (*Renishaw inVia Reflex*, excitation wavelength 442 nm, objective 100×; *Horiba XploRA*, excitation wavelength 325 nm, objective 100×). The micro-photoluminescence of the structures was also measured in the same setup (*Renishaw inVia Reflex*). The chemical composition of some samples was analyzed by X-ray photoelectron spectroscopy (XPS; *AXIS Supra, Kratos* spectrometer with a hemispheric analyzer and a monochromatic Al K α X-ray source, 1486.6 eV; high resolution spectra pass energy 20 eV). The XPS spectra were acquired from an area of $700 \times 300 \mu\text{m}^2$ with a 90° take-off angle 90°.

The selective growth of diamond was demonstrated on samples consisting of a Si wafer covered by 40 nm of Pt. We used FDP (Fumed Diamond Powder, $3.1 \pm 0.6 \text{ nm}$; NanoCarbon Research Institute) detonation nanodiamonds, which were dispersed in DI water by means of ultrasonication (200 W, 1 h; Hielscher UP200S) for seeding. The samples to be seeded were immersed in a colloidal solution (1 mg/ml) of FDP diamond nanoparticles for 30 min, were rinsed in DI water, blown by nitrogen and covered with a layer of a-Si:H (230 nm). Part of this layer was removed using a standard photolithographic process (positive photoresist, 6 s exposition with UV light, 40 s in the developer) and dry etching in SF₆ plasma. SF₆ plasma, which is not harmful for the diamond seeding layer, was used to selectively remove a-Si:H in places where the resist was removed in the photolithographic process, revealing the diamond seeding layer. The rest of the photoresist was removed in an acetone bath. The final samples consisted of a Pt layer (on a Si wafer) seeded with diamond nanocrystals and partially covered with a-Si:H layer.

Subsequently, diamond deposition was carried out in the focused MP-CVD reactor. The deposition parameters were: power 4 kW, pressure 4 kPa, concentration of methane in hydrogen 1%, and deposition time 3.5 h. The samples were characterized using SEM, Raman micro-spectroscopy and micro-photoluminescence measurements.

3. Results

3.1. Spontaneous nucleation on monocrystalline silicon

We detected clusters of nanocrystalline diamond (NCD) spontaneously nucleated on the surface of monocrystalline Si (Fig. 1). The size of the clusters differed according to the deposition scheme. The largest clusters (up to 2 μm) were observed on the sample with long deposition. The surface of this sample was also covered by a thin layer of non-diamond carbon particles. The larger clusters were composed of smaller diamond grains 50 nm–100 nm in size. Solitary grains were also observed on the samples.

The nucleation density on the reference sample (monocrystalline silicon) achieved by three different growth scenarios was determined from SEM images. The deposition scenarios are described in detail in the Experimental section. The diamond nucleation density is roughly the same ($4 \times 10^6 \text{ cm}^{-2}$) for all three scenarios (Table 1). The uncertainty of the spontaneous nucleation was estimated on the basis of the slightly different number of particles in several SEM images taken in various places over the sample.

The chemical composition of the nucleated particles was determined by Raman micro-spectroscopy. The diamond peak is clearly visible in the spectra of the particles, confirming their diamond composition. Raman spectroscopy also revealed different ratios of the sp³ to sp² bonds for the three scenarios. The highest concentration of sp² bonds was detected on the sample with interrupted deposition (relatively, in comparison with the other two depositions). The absolute height of the diamond peak cannot be compared, as the Raman spectra

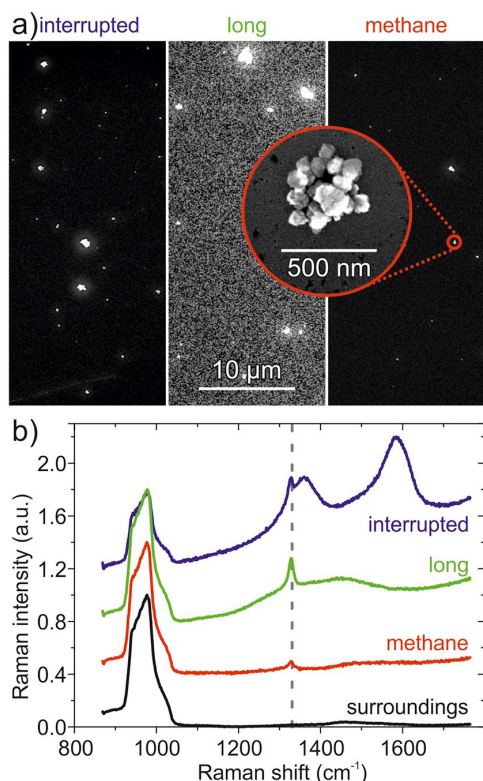


Fig. 1. Monocrystalline silicon samples with spontaneously nucleated diamond clusters (three different deposition scenarios): (a) SEM images, (b) Raman spectra of clusters; the grey dashed line denotes the position of the diamond peak.

Table 1

Nucleation density on monocrystalline silicon for three different deposition scenarios. The estimated uncertainty is $1 \times 10^6 \text{ cm}^{-2}$.

Temperature	approx. 430 °C
Interrupted	5×10^6
Long	4×10^6
Methane	5×10^6

were measured on clusters of different sizes.

The diamond nature of the nucleated particles was also confirmed indirectly by the micro-photoluminescence measurements [20]. The photoluminescence spectra show that optically active SiV centers were created in diamond crystals formed on monocrystalline silicon (Fig. 2). The zero phonon line (ZPL) is centered at approximately 738 nm. The characteristic phonon band (wavelength $> 750 \text{ nm}$) is also present. The luminescence of the SiV centers was detected for all deposition scenarios. However, the luminescence intensity varied in different scenarios. This is most probably due to the different sizes of the particles. The highest intensity was detected for the long deposition scenario with the biggest clusters, which supports this assumption. However, the role of different chemical composition (e.g. a different ratio of the sp^2 bonds) cannot be excluded.

Some carbon deposits were detected even in the surroundings of diamond grains on the sample with the long deposition scenario. However, these carbon deposits are not composed of diamond, as evidenced by both Raman and PL spectra (Fig. 1(b) and 2). Note that even very small diamonds may contain optically active SiV centers [20,21]

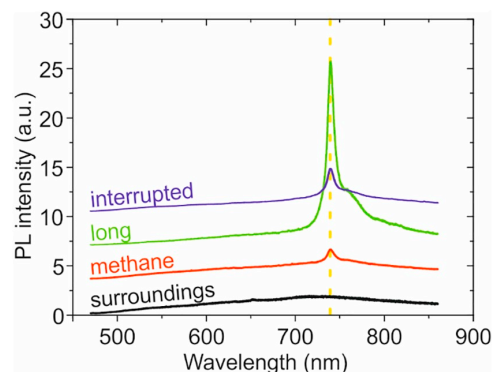


Fig. 2. Photoluminescence of spontaneously nucleated diamond clusters (various scenarios). The yellow dashed line denotes the position of SiV centers ZPL (738 nm).

and the PL spectra can thus confirm the presence/absence of diamond nanoparticles.

3.2. Spontaneous nucleation on a-Si:H

SEM images of a-Si:H coated samples with various thicknesses and interlayers after diamond deposition (interrupted deposition) are shown in Fig. 3. The results of other deposition scenarios were similar. The first four samples were placed side-by-side inside the reactor chamber. Deposition on the other two samples was carried out separately, using the same deposition conditions.

The nucleation density was determined from SEM images (the number of all particles in a given area). The nucleation density on samples with microcrystalline silicon (a 40 nm layer of a-Si:H which crystallized during diamond deposition due to the metal-induced crystallization process [22]) is at least one order of magnitude lower than on monocrystalline silicon (Table 2). A few particles can be seen on the SEM image (Fig. 3(c), bottom right corner). However, not all the particles were composed of diamond, as was revealed by Raman spectroscopy. Detailed pictures of some particles can be found in Fig. S2, in Supplementary Information. Some of the particles may be diamonds. However, the diamond sp^3 peak was observed only in a few cases in the Raman spectra of the particles. The absence of a diamond peak in other cases is not caused by the small size of the particles, since different Raman peaks (e. g. crystalline Si, carbon G-band, examples given in Figs. S3 – S5, in Supplementary Information) were observed on the particles.

No presence of spontaneously nucleated diamond particles was observed on the samples with a thicker (150–230 nm) a-Si:H layer, which remained amorphous during diamond deposition, as detected by Raman micro-spectroscopy. Nevertheless, the layer was wrinkled in some cases (Ni interlayer) due to the elevated temperature during deposition (Fig. 3(d)).

Fig. 4 shows the Raman spectra of the samples presented above. These spectra were taken on parts of the samples that did not contain any particles (observable in the optical microscope). The spectrum of a diamond particle nucleated on monocrystalline silicon is plotted at the top for comparison. There is no sign of carbon in the spectra of the other samples, with the exception of the sample with a 40 nm a-Si:H layer on a Ni interlayer, which is covered with a continuous carbon film. Moreover, a layer of carbon nanostructures composed of diamond-like carbon (see Supplementary Information for details) was repeatedly observed by SEM on this sample at high magnification. Luminescence of the SiV centers was not detected on either of the samples with an amorphous/microcrystalline silicon layer.

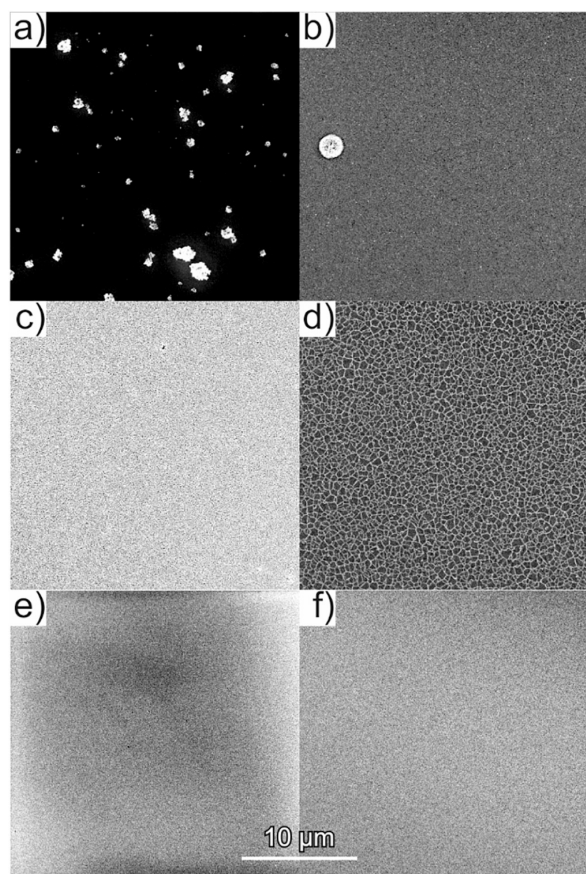


Fig. 3. SEM images of samples on different substrates after diamond deposition (interrupted deposition): (a) Monocrystalline silicon (reference and carrier substrate); (b) Si/Ni/a-Si:H (40 nm); (c) Si/Pt/a-Si:H (40 nm); (d) Si/Ni/a-Si:H (230 nm); (e) Si/SiO₂/a-Si:H (150 nm); (f) Si/a-Si:H (150 nm). Note that the contrast on the samples was intentionally increased in order to show details on the surface of the sample.

Table 2

Diamond nucleation density (N_D) on six different samples after diamond deposition (interrupted deposition). Based on data from SEM. * denotes that the a-Si:H layer crystallized during diamond deposition due to elevated temperature.

Substrate	N_D (cm ⁻²)
Reference	$5 \times 10^6 \pm 1 \times 10^6$
Si + Ni + a-Si:H* (40 nm)	Non-diamond carbon particles (see Supplementary material)
Si + Pt + a-Si:H* (40 nm)	$< 2 \times 10^5$
Si + Ni + a-Si:H (230 nm)	No diamond particles
Si + SiO ₂ + a-Si:H (150 nm)	No diamond particles
Si + a-Si:H (150 nm)	No diamond particles

3.3. Selective growth of diamond

Based on knowledge of suppressed diamond nucleation on a-Si:H, the application of an a-Si:H layer as a mask for diamond deposition was tested. Fig. 5 shows the sample, which was seeded by diamond nanocrystals and was selectively covered by an a-Si:H layer (approx. 230 nm in thickness) during diamond deposition. The SEM image and the Raman spectra clearly show that the diamond is growing only on areas that are not covered by an a-Si:H layer. The detailed SEM image shows that the deposited layer has the form of nanocrystalline diamond with

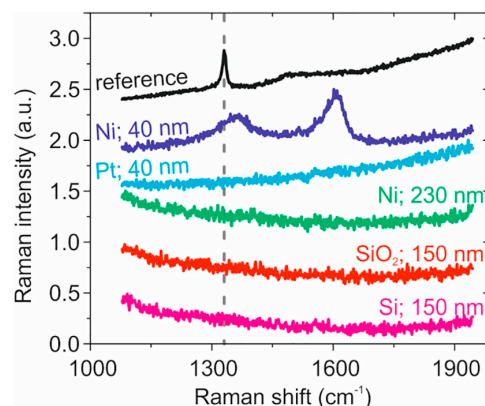


Fig. 4. Raman spectra of the surface of the sample after diamond deposition (interrupted deposition, temperature approx. 430 °C). From the top: Monocrystalline silicon (reference - diamond particle); Ni/a-Si:H (40 nm); Pt/a-Si:H (40 nm); Ni/a-Si:H (230 nm); SiO₂/a-Si:H (150 nm); Si/a-Si:H (150 nm).

grain size between 20 and 50 nm. Moreover, the diamond contains optically active SiV centers that are clearly evidenced by the micro-photoluminescence measurement. No diamond crystals were detected on the a-Si:H part of the sample.

When a thinner layer of a-Si:H (40 nm) was deposited on the sample, we observed some growth of nanocrystalline diamond even on the masked areas of the sample. This is most likely because the thickness of the a-Si:H layer tends to decrease during diamond CVD growth, due to an escape of hydrogen or due to crystallization. The diamond nanoparticles in the seeding layer can thus be partially uncovered, and diamond grows directly on them without the spontaneous nucleation process.

4. Discussion

The nature of the a-Si:H films remained amorphous during diamond deposition if the layer was sufficiently thick (150 nm–230 nm). Thicker a-Si:H layers on the Ni interlayer were wrinkled (Fig. 3(d)), which is very likely caused by the different coefficient of thermal expansion of Ni and a-Si:H. The situation was different for thinner layers of a-Si:H (40 nm). These layers crystallized during diamond deposition (temperature approx. 430 °C). The crystallization was probably caused by the presence of metals (Ni, Pt), both of which significantly reduce the temperature at which amorphous silicon crystallizes [22]. In addition, the high concentration of hydrogen reduces the crystallization temperature [23]. However, both the metal interlayer and a high hydrogen content are essential for templating a-Si:H layers with AFM [14].

We propose the following explanation of the observed phenomenon of suppressed or reduced spontaneous nucleation on amorphous Si layer and on a microcrystalline Si layer, in comparison with a monocrystalline Si wafer. On monocrystalline Si, diamond nuclei are created on preferential sites on its surface, such as defects or nano-scratches, where the concentration of carbon atoms is increased. Between these sites, carbon atoms can migrate relatively freely over the surface. However, the nucleation in the immediate neighborhood (10 nm) of nucleation sites is suppressed, because they act as sinks for the diffusing adatoms [24].

In contrast to crystalline Si, there are many more surface defects on amorphous/microcrystalline Si that may act as potential preferential sites [25]. However, all preferential sites also act as sinks for diffusing adatoms and prevent nucleation in their neighborhood. The high surface density of the preferential sites results in high competition between them, and in the slow growth of carbon clusters. The slow growth rate causes the diamond nuclei to be dissolved or destroyed by the

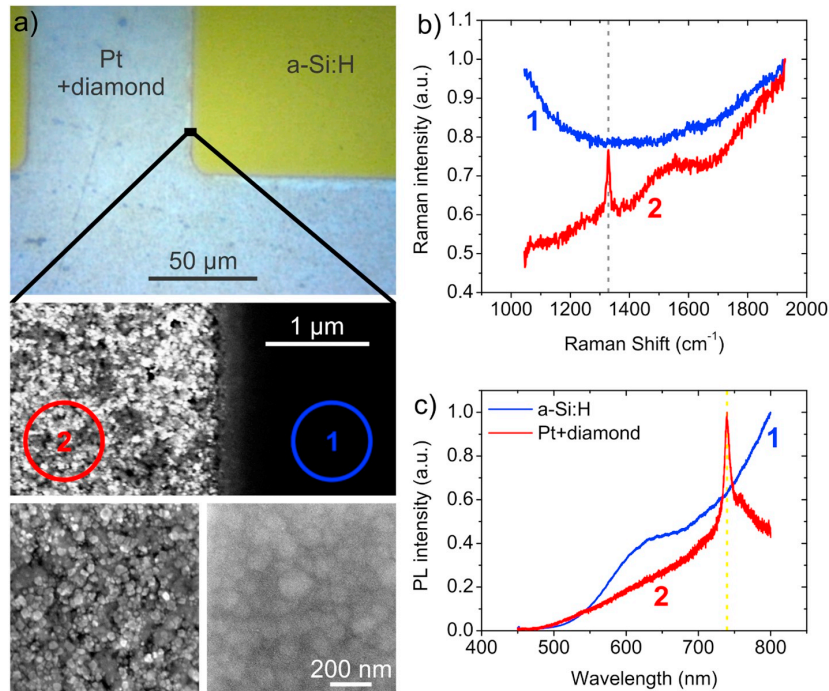


Fig. 5. (a) Optical microscope image (top) and SEM morphology (middle) of the sample with an a-Si:H layer patterned by photolithography after diamond growth. The pictures at the bottom shows SEM details of the NCD structure (left) and the a-Si:H morphology (right). (b) Raman spectra taken on the a-Si:H and on the NCD part of the sample; the grey dashed line denotes the position of the diamond peak. (c) PL intensity taken on the a-Si:H and on the NCD part of the sample; the yellow dashed line denotes the spectral position of the SiV peak.

bombarding energetic species [26] before they reach the diamond nucleation critical size. The low temperature of the substrate may play an important role in this process, because it further reduces the diffusion rate of adatoms or of clusters of adatoms over the surface.

The role of surface termination and the surface energy difference between monocrystalline Si and a-Si:H was also considered. The surfaces of both materials were covered by a native oxide layer prior to deposition. The thickness of the oxide layer on a-Si:H was roughly the same as on monocrystalline Si [27], taking into account that there were several days between the deposition of a-Si:H and the diamond deposition. The surface energy is about 50 mJ/m² both for microcrystalline Si [28] and for a-Si:H [29] covered with native oxide, which is significantly lower than the surface energy of diamond [30]. Thus, there is no significant difference in surface termination or in surface energy. Note that it cannot be only the amorphous structure of the surface that suppresses the spontaneous nucleation of diamond, because low nucleation density was also observed on microcrystalline Si (a thin layer of a-Si:H that crystallized during deposition). However, the number of surface defects is still significantly higher on microcrystalline Si than on the monocrystalline reference. This can again lead to limited diffusion of carbon atoms over the surface.

Some carbon nanostructures were observed only on Ni samples with a thin (40 nm) layer of a-Si:H. The carbon layer is probably composed of diamond-like carbon (DLC), as evaluated by Raman micro-spectroscopy and XPS analysis (see Supplementary Information for details). At the same time, there was no such nucleation of carbon on other types of samples (a different material below a-Si:H, or a thicker a-Si:H layer). The nucleation is, therefore, caused by the presence of Ni in the vicinity of the surface. Similar structures were observed on Fe substrates in [31]. We suppose that the a-Si:H layer (40 nm) shrinks and crystallizes during deposition, due to the elevated temperature. Layer shrinkage was observed after local application of an electric field in [16], and was assigned to an escape of hydrogen atoms from the layer. Increased temperature (400 °C) also leads to the effusion of hydrogen atoms from hydrogen-rich layers [32]. The crystallization was evidenced by Raman micro-spectroscopy. Subsequently, Ni atoms can diffuse through the

crystallized Si layer towards the surface. The Ni diffusion rate is significantly higher for crystalline Si than for amorphous Si [33], which explains why we observed the effect of Ni only for the case of the thin layer that crystallized during diamond deposition. This observation shows that the a-Si:H layer must be thick enough in order to prevent nucleation of carbon nanoparticles. If the layer is too thin, it crystallizes during diamond deposition and the substrate material may affect the deposition process and catalyze the growth of carbon species.

Similarly, a thicker layer (> 150 nm) must also be deposited for the use of a-Si:H as an efficient mask over the diamond seeding layer. We have demonstrated that thick layers block the growth of diamond and at the same time reduce unwanted spontaneous nucleation. When very thin layers (20 nm) of amorphous Si were used, they crystallized during diamond deposition, and diamond growth was observed [34]. This is in accordance with our observation here. This fact limits the maximal deposition temperature (approx. 500 °C) that can be used during diamond deposition. On the other hand, it means that an a-Si:H layer does not have to be completely removed in order to achieve diamond deposition on selected areas. This could be very important for the use of AFM for a-Si:H lithography [16], where the a-Si:H is structurally modified but is not completely removed. The process is therefore also not so sensitive to the accuracy of dry etching in conventional patterning by photolithography or electron beam lithography.

5. Conclusion

Coating various substrates (Si, SiO₂, Pt, Ni) with a thin (150–230 nm) a-Si:H films leads to complete suppression of the spontaneous nucleation of diamond at deposition conditions when diamond spontaneously nucleates and grows on monocrystalline Si. Reduced nucleation density was also detected on microcrystalline silicon thin films. The suppression of spontaneous nucleation was explained by the amorphous nature and, therefore, the large number of surface defects, which greatly hinder the surface diffusion of C atoms. The suppression of spontaneous nucleation by a-Si:H films opens a new way for highly selective deposition of diamond nanostructures. By patterning the a-

Si:H layer with the use of photolithography, highly selective growth of nanocrystalline diamond with optically active SiV centers was achieved even at relatively low substrate temperatures. This method can be further miniaturized to nanoscale by using conductive AFM for creating patterns in a-Si:H thin films. The results presented here thus open prospects for various applications in photonics and in sensor systems.

Acknowledgements

The work has been supported by GACR project 17-19968S, by CTU project SGS18/179/OHK4/3T/13, and by European projects CZ.02.1.01/0.0/0.0/15 003/0000464 and CZ.02.1.01/0.0/0.0/16 019/0000760. The work has been carried out within the frame of the LNSM infrastructure. Technical support from P. Bauerová (SEM images and photolithography) and Ondřej Rezek (diamond deposition) is gratefully acknowledged. We thank Oleksandr Romanyuk for his kind help in interpreting the XPS spectra.

Appendix A. Supplementary data

Supplementary data to this article can be found online at <https://doi.org/10.1016/j.apsusc.2019.03.064>.

References

- [1] R.S. Balmer, J.R. Brandon, S.L. Clewes, H.K. Dhillon, J.M. Dodson, I. Friel, P.N. Inglis, T.D. Madgwick, M.L. Markham, T.P. Mollart, N. Perkins, G.A. Scarsbrook, D.J. Twitchen, A.J. Whitehead, J.J. Wilman, S.M. Woollard, Chemical vapour deposition synthetic diamond: materials, technology and applications, *J. Phys. Condens. Matter* 21 (2009) 364221, <https://doi.org/10.1088/0953-8984/21/36/364221>.
- [2] E. Neu, D. Steinmetz, J. Riedrich-Möller, S. Gsell, M. Fischer, Matthias Schreck, C. Becher, Single photon emission from silicon-vacancy colour centres in chemical vapour deposition nano-diamonds on iridium, *New J. Phys.* 13 (2011) 025012, <https://doi.org/10.1088/1367-2630/13/2/025012>.
- [3] I. Aharonovich, S. Castellotto, D.A. Simpson, C.-H. Su, A.D. Greentree, S. Prawer, Diamond-based single-photon emitters, *Rep. Prog. Phys.* 74 (2011) 076501, <https://doi.org/10.1088/0034-4885/74/7/076501>.
- [4] A. Gruber, A. Dräbenstedt, C. Tietz, L. Fleury, J. Wrachtrup, C. von Borzyskowski, Scanning confocal optical microscopy and magnetic resonance on single defect centers, *Science* 276 (1997) 2012–2014, <https://doi.org/10.1126/science.276.5321.2012>.
- [5] D.A. Redman, S. Brown, R.H. Sands, S.C. Rand, Spin dynamics and electronic states of N-V centers in diamond by EPR and four-wave-mixing spectroscopy, *Phys. Rev. Lett.* 67 (1991) 3420–3423, <https://doi.org/10.1103/PhysRevLett.67.3420>.
- [6] M.D. Eisaman, J. Fan, A. Migdall, S.V. Polyakov, Invited review article: single-photon sources and detectors, *Rev. Sci. Instrum.* 82 (2011) 071101, <https://doi.org/10.1063/1.3610677>.
- [7] V. Sedov, V. Ralchenko, A.A. Khomich, I. Vlasov, A. Vul, S. Savin, A. Goryachev, V. Konov, Si-doped nano- and microcrystalline diamond films with controlled bright photoluminescence of silicon-vacancy color centers, *Diam. Relat. Mater.* 56 (2015) 23–28, <https://doi.org/10.1016/j.diamond.2015.04.003>.
- [8] A. Kromka, O. Babchenko, Š. Potocký, B. Rezek, Sveshnikov, Diamond nucleation and seeding techniques for tissue regeneration, in: *Diam.-Based Mater. Biomed. Appl.*, Elsevier, 2013.
- [9] R.P. Sear, Nucleation: theory and applications to protein solutions and colloidal suspensions, *J. Phys. Condens. Matter* 19 (2007) 033101, <https://doi.org/10.1088/0953-8984/19/3/033101>.
- [10] T. Izak, A. Sveshnikov, P. Demo, A. Kromka, Enhanced spontaneous nucleation of diamond nuclei in hot and cold microwave plasma systems, *Phys. Status Solidi B* 250 (2013) 2753–2758, <https://doi.org/10.1002/pssb.201300117>.
- [11] H. Liu, D.S. Dandy, Studies on nucleation process in diamond CVD: an overview of recent developments, *Diam. Relat. Mater.* 4 (1995) 1173–1188, [https://doi.org/10.1016/0925-9635\(96\)00297-2](https://doi.org/10.1016/0925-9635(96)00297-2).
- [12] H. Kozak, A. Kromka, O. Babchenko, B. Rezek, Directly grown nanocrystalline diamond field-effect transistor microstructures, *Sens. Lett.* 8 (2010) 482–487, <https://doi.org/10.1166/sl.2010.1298>.
- [13] O. Babchenko, T. Izak, E. Ukrainsev, K. Hruska, B. Rezek, A. Kromka, Toward surface-friendly treatment of seeding layer and selected-area diamond growth, *Phys. Status Solidi B* 247 (2010) 3026–3029, <https://doi.org/10.1002/pssb.201000124>.
- [14] B. Rezek, E. Šípek, M. Ledinský, P. Krejza, J. Stuchlík, A. Fejfar, J. Kočka, Spatially localized current-induced crystallization of amorphous silicon films, *J. Non-Cryst. Solids* 354 (2008) 2305–2309, <https://doi.org/10.1016/j.jnoncrysol.2007.10.045>.
- [15] E. Verveniotis, E. Šípek, J. Stuchlík, J. Kočka, B. Rezek, Generating ordered Si nanocrystals via atomic force microscopy, *J. Non-Cryst. Solids* 358 (2012) 2118–2121, <https://doi.org/10.1016/j.jnoncrysol.2011.12.018>.
- [16] J. Fait, J. Čermák, J. Stuchlík, B. Rezek, Complex nano-patterning of structural, optical, electrical and electron emission properties of amorphous silicon thin films by scanning probe, *Appl. Surf. Sci.* (2018), <https://doi.org/10.1016/j.apsusc.2017.09.228>.
- [17] F. Piazza, G. Morell, Synthesis of diamond at sub 300 °C substrate temperature, *Diam. Relat. Mater.* 16 (2007) 1950–1957, <https://doi.org/10.1016/j.diamond.2007.08.038>.
- [18] K. Tsugawa, M. Ishihara, J. Kim, Y. Koga, M. Hasegawa, Nanocrystalline diamond film growth on plastic substrates at temperatures below 100°C from low-temperature plasma, *Phys. Rev. B* 82 (2010) 125460, <https://doi.org/10.1103/PhysRevB.82.125460>.
- [19] L. Ondič, M. Varga, K. Hruška, J. Fait, P. Kapusta, Enhanced extraction of silicon-vacancy centers light emission using bottom-up engineered polycrystalline diamond photonic crystal slabs, *ACS Nano* (2017), <https://doi.org/10.1021/acsnano.6b08412>.
- [20] S. Stehlik, M. Varga, P. Stenclova, L. Ondic, M. Ledinsky, J. Pangrac, O. Vanek, J. Lipov, A. Kromka, B. Rezek, Ultrathin Nanocrystalline diamond films with silicon vacancy color centers via seeding by 2 nm detonation nanodiamonds, *ACS Appl. Mater. Interfaces* 9 (2017) 38842–38853, <https://doi.org/10.1021/acsnami.7b14436>.
- [21] I.I. Vlasov, A.A. Shiryayev, T. Rendler, S. Steinert, S.-Y. Lee, D. Antonov, M. Vörös, F. Jelezko, A.V. Fisenko, L.F. Semjonova, J. Biskupek, U. Kaiser, O.I. Lebedev, I. Sildos, P.R. Hemmer, V.I. Konov, A. Gali, J. Wrachtrup, Molecular-sized fluorescent nanodiamonds, *Nat. Nanotechnol.* 9 (2014) 54–58, <https://doi.org/10.1038/nnano.2013.255>.
- [22] S.Y. Yoon, S.J. Park, K.H. Kim, J. Jang, Metal-induced crystallization of amorphous silicon, *Thin Solid Films* 383 (2001) 34–38, [https://doi.org/10.1016/S0040-6090\(00\)01790-9](https://doi.org/10.1016/S0040-6090(00)01790-9).
- [23] P. Fojtík, K. Dohnalová, T. Mates, J. Stuchlík, I. Gregora, J. Chval, A. Fejfar, J. Kočka, I. Pelant, Rapid crystallization of amorphous silicon at room temperature, *Philos. Mag. B* 82 (2002) 1785–1793, <https://doi.org/10.1080/13642810208222940>.
- [24] X. Jiang, K. Schifmann, C.-P. Klages, Nucleation and initial growth phase of diamond thin films on (100) silicon, *Phys. Rev. B* 50 (1994) 8402–8410, <https://doi.org/10.1103/PhysRevB.50.8402>.
- [25] D.M. Tanenbaum, A.L. Laracuenta, A. Gallagher, Surface roughening during plasma-enhanced chemical-vapor deposition of hydrogenated amorphous silicon on crystal silicon substrates, *Phys. Rev. B* 56 (1997) 4243–4250, <https://doi.org/10.1103/PhysRevB.56.4243>.
- [26] Y. Lifshitz, T. Köhler, T. Frauenheim, I. Guzman, A. Hoffman, R.Q. Zhang, X.T. Zhou, S.T. Lee, The mechanism of diamond nucleation from energetic species, *Science* 297 (2002) 1531–1533, <https://doi.org/10.1126/science.1074551>.
- [27] R.A. Street, *Hydrogenated Amorphous Silicon*, Cambridge University Press, 2005.
- [28] S.R. Narayan, J.M. Day, H.L. Thinakaran, N. Herbots, M.E. Bertram, C.E. Cornejo, T.C. Diaz, K.L. Kavanagh, R.J. Culbertson, F.J. Ark, S. Ram, M.W. Mangus, R. Islam, Comparative study of surface energies of native oxides of Si(100) and Si(111) via three liquid contact angle analysis, *MRS Adv.* 3 (2018) 3379–3390, <https://doi.org/10.1557/adv.2018.473>.
- [29] F. Mussano, T. Genova, M. Laurenti, L. Munaron, C.F. Pirri, P. Rivolo, S. Carossa, P. Mandracci, Hydrogenated amorphous silicon coatings may modulate gingival cell response, *Appl. Surf. Sci.* 436 (2018) 603–612, <https://doi.org/10.1016/j.apsusc.2017.11.283>.
- [30] J.-M. Zhang, F. Ma, K.-W. Xu, X.-T. Xin, Anisotropy analysis of the surface energy of diamond cubic crystals, *Surf. Interface Anal.* 35 (2003) 805–809, <https://doi.org/10.1002/sia.1605>.
- [31] N.M. Hwang, J.H. Hahn, D.Y. Yoon, Charged cluster model in the low pressure synthesis of diamond, *J. Cryst. Growth* 162 (1996) 55–68, [https://doi.org/10.1016/0022-0248\(95\)00943-4](https://doi.org/10.1016/0022-0248(95)00943-4).
- [32] W. Beyer, Diffusion and evolution of hydrogen in hydrogenated amorphous and microcrystalline silicon, *Sol. Energy Mater. Sol. Cells* 78 (2003) 235–267, [https://doi.org/10.1016/S0927-0248\(02\)00438-5](https://doi.org/10.1016/S0927-0248(02)00438-5).
- [33] A.Y. Kuznetsov, B.G. Svensson, Nickel atomic diffusion in amorphous silicon, *Appl. Phys. Lett.* 66 (1995) 2229–2231, <https://doi.org/10.1063/1.113175>.
- [34] Š. Potocký, J. Holovský, Z. Remeš, M. Müller, J. Kočka, A. Kromka, Si-related color centers in nanocrystalline diamond thin films, *Phys. Status Solidi B* 251 (2014) 2603–2606, <https://doi.org/10.1002/pssb.201451177>.

A.11

Uptake and intracellular accumulation of diamond nanoparticles – a metabolic and cytotoxic study



Uptake and intracellular accumulation of diamond nanoparticles – a metabolic and cytotoxic study

Antonín Brož¹, Lucie Bačáková¹, Pavla Štenclová², Alexander Kromka² and Štěpán Potocký^{*2}

Full Research Paper

[Open Access](#)**Address:**

¹Institute of Physiology of the Czech Academy of Sciences, v.v.i., Vídeňská 1083, 142 20, Praha 4, Czech Republic and ²Institute of Physics of the Czech Academy of Sciences, v.v.i., Cukrovarnická 10, 162 00 Praha 6, Czech Republic

Email:

Štěpán Potocký* - potocky@fzu.cz

* Corresponding author

Keywords:

cell viability; FTIR; live-cell imaging; MTS; nanodiamond; SAOS-2 cells

Beilstein J. Nanotechnol. **2017**, *8*, 1649–1657.

doi:10.3762/bjnano.8.165

Received: 15 July 2016

Accepted: 17 July 2017

Published: 10 August 2017

This article is part of the Thematic Series "Self-assembly of nanostructures and nanomaterials II".

Guest Editor: I. Berbezier

© 2017 Brož et al.; licensee Beilstein-Institut.

License and terms: see end of document.

Abstract

Diamond nanoparticles, known as nanodiamonds (NDs), possess several medically significant properties. Having a tailorable and easily accessible surface gives them great potential for use in sensing and imaging applications and as a component of cell growth scaffolds. In this work we investigate in vitro interactions of human osteoblast-like SAOS-2 cells with four different groups of NDs, namely high-pressure high-temperature (HPHT) NDs (diameter 18–210 nm, oxygen-terminated), photoluminescent HPHT NDs (diameter 40 nm, oxygen-terminated), detonation NDs (diameter 5 nm, H-terminated), and the same detonation NDs further oxidized by annealing at 450 °C. The influence of the NDs on cell viability and cell count was measured by the mitochondrial metabolic activity test and by counting cells with stained nuclei. The interaction of NDs with cells was monitored by phase contrast live-cell imaging in real time. For both types of oxygen-terminated HPHT NDs, the cell viability and the cell number remained almost the same for concentrations up to 100 µg/mL within the whole range of ND diameters tested. The uptake of hydrogen-terminated detonation NDs caused the viability and the cell number to decrease by 80–85%. The oxidation of the NDs hindered the decrease, but on day 7, a further decrease was observed. While the O-terminated NDs showed mechanical obstruction of cells by agglomerates preventing cell adhesion, migration and division, the H-terminated detonation NDs exhibited rapid penetration into the cells from the beginning of the cultivation period, and also rapid cell congestion and a rapid reduction in viability. These findings are discussed with reference to relevant properties of NDs such as surface chemical bonds, zeta potential and nanoparticle types.

Introduction

Carbon-based materials in the form of nanostructures are showing great promise as engineering and biomedical materials [1]. Moreover, diamond represents a new class of material with

properties that are tailorable on demand [2]. This work investigates the use of diamond nanomaterials, or nanodiamonds (NDs), especially in life sciences, tissue engineering and regen-

erative medicine [3-6]. Diamond is biocompatible [7,8], and for advanced biomedical applications, it is particularly promising in its nanostructured forms (nanoparticles, nanostructured diamond films and composite scaffolds) [9].

ND particles can act in the single particle form (bioimaging and biosensing) [10,11], can serve as a stable delivery platform for therapeutic antibodies [12], or can be incorporated into various materials, for example, films for potential implant coatings [13]. Nanodiamond-based drug delivery has been mainly developed for advanced tumour therapies and for localized drug delivery [3,14]. Due to their stable and controllable photoluminescence, NDs are also highly promising for advanced photonic and bio-imaging techniques [15,16] and for nanoscale sensing [17,18].

There are various types of NDs, but two main groups can be identified on the basis of their synthesis procedure. The first group of NDs are those synthesized by the detonation method [19], where even sub-nanometer detonation nanodiamond particles (DNDs) are produced [20]. A typical size distribution has a maximum DND diameter of around 5 nm. The second group of NDs are prepared by mechanical grinding of high-pressure high-temperature (HPHT) diamond crystals [21]. The HPHT ND particle size distribution can be mechanically controlled down to approximately 20 nm, or by further post-processing down to 1 nm, as has recently been reported [22].

NDs typically contain impurities, such as other carbon allotropes, various oxides or carbides (i.e., carriers of various functional surface groups) [3,23]. Therefore, for use in biological or biomedical studies, NDs need to be extensively purified. Numerous methods exist for removing non-diamond carbon components based on treatment with various oxidizers, such as peroxides, acids and ozone-enriched air [3,24,25]. Oxidation in air at elevated temperature is a good method for effective sp^2 carbon removal [26,27], particle size reduction [22] and surface oxidation (i.e., the surface is covered by defined starting functional groups).

The cytotoxicity of NDs depends on their origin (i.e., DNDs or HPHT NDs), their size (distribution), their tendency to form aggregates (surface charge), the presence of impurities, and surface functionalization groups. Adverse effects on cell viability have been reported when using DNDs [24,28-32], while HPHT NDs often appear to be nontoxic [33,34]. Factors influencing the cytotoxicity of nanoparticles are their size [24,35,36] and surface functionalization [37].

In this work, we focus on cytotoxicity studies of NDs as a function of their synthesis route (DNDs versus HPHT NDs), their concentration in the medium (from 10 to 1000 mg/mL, 3 to

300 $\mu\text{g}/\text{cm}^2$), their size (5 nm DND, 18–210 nm HPHT NDs) and their surface potential/termination (as-received and oxygen-terminated). The cytotoxicity of NDs against the SAOS-2 human osteoblastic cell line is evaluated in this work by counting adherent cells and by a mitochondrial metabolic activity test (MTS) after 3 and 7 days. Both the cell count and mitochondrial activity are positively correlated with the cell viability and are negatively correlated with the material cytotoxicity. The live-cell imaging method was used for observing the intake of NDs into the cells. The results were evaluated on the basis of particle size, surface potential, surface functional groups, and the concentration of the ND suspension.

Results and Discussion

Influence of particle size and concentration

Figure 1 shows the results of a cell mitochondrial activity test (upper row) and a cell nuclei count (lower row) after 3 days of cultivation for three different concentrations of 10, 100 and 1000 $\mu\text{g}/\text{mL}$ (3, 30, and 300 $\mu\text{g}/\text{cm}^2$) as a function of HPHT ND (labeled as MR-xx) particle size. Both tests proved almost no ND size or concentration dependence on cell viability after 3 days of cultivation within the measurement error. Only at the highest concentration of NDs (1000 $\mu\text{g}/\text{mL}$, 300 $\mu\text{g}/\text{cm}^2$), the mitochondrial activity and the cell number showed a tendency to decrease in certain ND groups. However, these differences were not statistically significant. This decrease could be due to the obstruction of access to nutrients or scavenging of nutrients and growth factors from the cultivation medium by the NDs. A high ND concentration can also express chemical toxicity based on the production of reactive oxygen species.

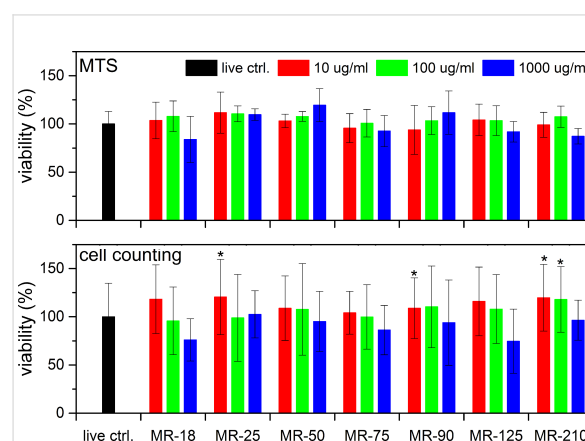


Figure 1: Viability of SAOS-2 cells incubated with HPHT NDs for three concentrations as a function of the mean particle diameter after 3 days. (Upper row) results of an MTS assay, (lower row) results of cell counting after cell staining. The results are given as the mean \pm SD from 3 experiments, each performed in sextuplicate. ANOVA, Tukey HSD post-hoc test. “*” indicates a significant difference from MR-18 at a concentration of 1000 $\mu\text{g}/\text{mL}$ ($p < 0.05$).

Figure 2 shows the results of a cell mitochondrial activity test (upper row) and counting of the cell nuclei (lower row) after 7 days of cultivation for three different concentrations of 10, 100 and 1000 $\mu\text{g}/\text{mL}$ (3, 30, 300 $\mu\text{g}/\text{cm}^2$) as a function of HPHT ND particle size. Again, no dependence of the ND size or concentration was observed for 10 and 100 $\mu\text{g}/\text{mL}$ (3 and 30 $\mu\text{g}/\text{cm}^2$) suspension concentrations after 7 days. However, a concentration-dependent toxic effect of HPHT NDs was revealed after 7 days of cultivation, where the viability of the cells cultivated in the 1000 $\mu\text{g}/\text{mL}$ (300 $\mu\text{g}/\text{cm}^2$) suspension reduced by 25% when evaluated by MTS and by 35% when evaluated by the cell counting experiment. This pronounced effect may have been caused by the previously mentioned obstruction of access to nutrients by nutrient scavenging or by reactive oxygen species. Alternatively, it could have been caused just by mechanical obstruction of the cell adhesion and division by ND agglomerates, as confirmed by live-cell imaging. A similar effect was also observed in human osteoblast-like MG 63 cells cultured in a medium with multi-walled carbon nanotubes (MWCNTs) at concentrations of 4, 40, 400, 4000 and 40000 $\mu\text{g}/\text{mL}$. On days 1, 3 and 7 after seeding, the number of MG 63 in the media with 4 and 40 $\mu\text{g}/\text{mL}$ of MWCNTs was similar to or even higher than in the control cultures without MWCNTs, while at higher concentrations of MWCNTs, it decreased in a concentration-dependent manner. This was explained by the fact that MWCNTs at higher concentrations covered most of the bottom of the culture well and left only limited space for cell attachment and spreading [38].

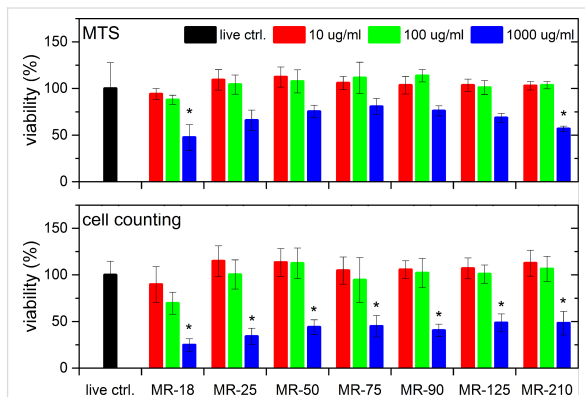


Figure 2: Viability of SAOS-2 cells incubated with HPHT NDs at three concentrations as a function of the mean particle diameter after 7 days. (Upper row) results of the MTS assay; (lower row) results of cell counting after cell staining. The results are given as the mean \pm SD from 3 experiments, each performed in sextuplicate. ANOVA, Tukey HSD post-hoc test. “*” indicates a significant difference from MR-18 at a concentration of 1000 $\mu\text{g}/\text{mL}$ ($p < 0.05$).

Influence of particle type

Figure 3 and Figure 4 show a comparison between the cell metabolic activity test (upper row) and counting of the cell

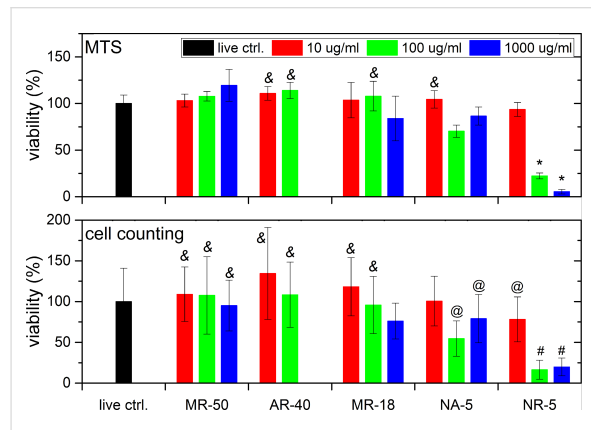


Figure 3: Viability of SAOS-2 cells incubated with NDs at three concentrations as a function of ND type and surface treatment after 3 days. (Upper row) results of the MTS assay; (lower row) results of cell counting after nuclei staining. The results are given as the mean \pm SD from 3 experiments, each performed in sextuplicate. ANOVA, Tukey HSD post-hoc test. “&” - significant difference from NA-5 100 $\mu\text{g}/\text{mL}$ ($p < 0.05$), “***” - significant difference from all other measurements ($p < 0.01$), “#” - significant difference from all other measurements except for NA-5 100 $\mu\text{g}/\text{mL}$ ($p < 0.01$), “@” - significant difference from MR-50 10 and 100 $\mu\text{g}/\text{mL}$, AR-40 10 $\mu\text{g}/\text{mL}$ ($p < 0.05$).

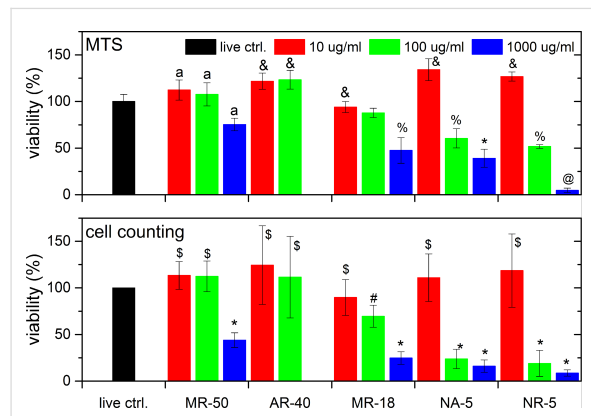


Figure 4: Viability of SAOS-2 cells incubated with NDs for three concentrations as a function of ND type and surface treatment after 7 days. (Upper row) results of the MTS assay; (lower row) results of cell counting after nuclei staining. The results are given as the mean \pm SD from 3 experiments, each performed in sextuplicate. ANOVA, Tukey HSD post-hoc test. “a” - significant difference from NA-5 1000 $\mu\text{g}/\text{mL}$ and NR-5 1000 $\mu\text{g}/\text{mL}$ $p < 0.01$, “&” - significant difference from MR-18 1000 $\mu\text{g}/\text{mL}$, NA-5 100 and 1000 $\mu\text{g}/\text{mL}$, NR-5 100 and 1000 $\mu\text{g}/\text{mL}$ ($p < 0.05$), “%” - significant difference from AR-40, MR-18 10 $\mu\text{g}/\text{mL}$, NA-5 10 $\mu\text{g}/\text{mL}$ and NR-5 10 $\mu\text{g}/\text{mL}$ ($p < 0.05$), “***” - significant difference from control, all 10 $\mu\text{g}/\text{mL}$ measurements and all MR and AR 100 $\mu\text{g}/\text{mL}$ measurements ($p < 0.01$), “@” - same as “***” + MR-50 1000 $\mu\text{g}/\text{mL}$ ($p < 0.01$), “\$” - significant difference from 1000 $\mu\text{g}/\text{mL}$ ($p < 0.01$), “#” - significant difference from all AR-40 and from all 100 and 1000 $\mu\text{g}/\text{mL}$ concentrations, with the exception of MR-50 ($p < 0.05$).

nuclei (lower row) for three different concentrations of 10, 100 and 1000 $\mu\text{g}/\text{mL}$ (3, 30 and 300 $\mu\text{g}/\text{cm}^2$) as a function of ND type and surface treatment after 3 days (Figure 3) and 7 days

(Figure 4) of cultivation. Three ND types with differing characteristics were selected: non-luminescent HPHT NDs of two diameters as described in the previous section (MR-18 and MR-50), HPHT NDs with photoluminescent nitrogen-vacancy (N-V) centers (AR-40), and detonation NDs with hydrogen termination (NR-5, as-received) and with oxygen termination (NA-5, annealed).

First, we compared the photoluminescent HPHT NDs (AR-40) with non-luminescent HPHT NDs of similar size (MR-50) and of smaller size (MR-18). The photoluminescent NDs AR-40 were available only in two concentrations: 10 and 100 $\mu\text{g/mL}$ (3 and 30 $\mu\text{g/cm}^2$). Both HPHT ND types were oxidized. Neither of the HPHT NDs are cytotoxic in low and medium concentrations after 3 and 7 days of cultivation. A visible decrease in cell viability can be observed with the highest ND concentration of MR-50 and 18. The decrease was statistically insignificant after 3 days (Figure 3). However, after 7 days the cell viability had decreased significantly (Figure 4) in comparison with the control cells in the pure culture medium and in comparison with the other concentrations of MR. The similar cytotoxicity of these HPHT NDs is probably caused by the similar production method, which results in oxidized surface termination and surface energy of the NDs. The presence of photoluminescent N-V centers had no negative effect on cell viability in the concentrations studied (3 $\mu\text{g/cm}^2$ and 30 $\mu\text{g/cm}^2$).

Similar to the other HPHT NDs with an oxidized surface, the NDs with N-V optical centers expressed no significant toxicity when compared with the ND-free living control (i.e., cells grown in polystyrene wells in a medium without diamond nanoparticles). Similar results were also obtained in a study by Vijayanthimala et al. [11], in which the proliferation of HeLa cells and 3T3-L1 pre-adipocytes exhibited no significant difference in cultures exposed and unexposed to photoluminescent nanodiamonds. This positive effect can be attributed to the fact that the mechanism of the ND uptake was clathrin-mediated endocytosis, that is, a physiological cellular mechanism for internalization of various bioactive substances from the extracellular environment. The negligible difference in cytotoxicity is caused by the similar production method, surface termination and energy of the NDs.

The surface termination of the two HPHT ND types is similar, despite the fact that the photoluminescent NDs were further postprocessed utilising methods influencing the bulk of the NDs (formation of vacancies, and N-V sites supported by high-temperature annealing in vacuum) [39]. This was confirmed by the fact that there was no obvious difference in the FTIR spectra between the MR-18 sample and the AR-40 sample. The zeta potential of MR-type NDs were negative, typically in the range

of -20 to -40 mV [40,41], comparable with the -37 mV zeta potential value of the AR-40 sample. The stock concentration of AR-40 did not allow us to test the effect of the highest ND concentration (1000 $\mu\text{g/mL}$, 300 $\mu\text{g/cm}^2$).

Next, we compared the influence of surface treatment by evaluating NR-5 and NA-5 samples (i.e., samples of detonation NDs as-received and treated by annealing, respectively). These detonation NDs in their as-received state have a positive zeta potential, which is characteristic for hydrogenated NDs. The XPS analysis indicated a mixture of hydrogen and oxygen states on the surface. They were fully oxygenated by annealing at high temperature. The viability of the cells cultivated with NR-5 (100 and 1000 $\mu\text{g/mL}$, 30 and 300 $\mu\text{g/cm}^2$) had already reduced by 80–85% after 3 days of cultivation. However, the annealing of these DNDs (NA-5) reduced their toxicity significantly by 30%. This effect could still be observed after 7 days of cultivation, where the cytotoxicity of air-annealed DNDs decreased by 25% for a 100 $\mu\text{g/mL}$ (30 $\mu\text{g/cm}^2$) suspension, and by 30% for a 1000 $\mu\text{g/mL}$ (300 $\mu\text{g/cm}^2$) suspension. The particle size should be same as these samples are produced from the same batch of DND powder. The main difference lies in the surface termination and energy. The surface termination differs mainly in antisymmetric and symmetric CH_2 , CH_3 (decrease), C=O (increase) and strong overlapping C–O, C–C bonds with air oxidation [42]. The oxidation of DNDs has a strong impact on their zeta potential, which influences the aggregation or the selection of adhered proteins from the culture medium. The as-received DNDs have a strongly positive zeta potential of ≈ 40 mV, while oxidation reverses it to approximately -40 mV [41].

The cell surface charge is influenced by the actual biochemical composition of the cytoplasmic membrane and the state of the cell. It is an important biophysical parameter influencing the interaction with the cell surroundings.

The cell surface charge (zeta potential) of human cells was between -20 and -30 mV caused by the presence of nonionogenic groups within phospholipids, proteins, and their polysaccharide conjugates [43]. Thus, we can expect similar zeta potential values for SAOS-2 cells, which are comparable with HPHT NDs and annealed DNDs, (i.e., negatively charged nanoparticles). It is known that negatively charged nanoparticles are less attractive for binding to the cell membrane than positively charged nanoparticles, which can be internalized more rapidly [44]. Positively charged nanoparticles have been reported to improve the efficacy of imaging, gene transfer and drug delivery. However, at the same time, negative effects like impaired integrity of cytoplasmic membrane and damage of other membranous organelles like mitochondria and lysosomes were observed. Also, more autophagosomes were produced by

the cells cultivated with positively charged nanoparticles ([45] or for a review see [46]). Hydrogenated positively charged ND particles impaired the radio-resistance of cancer cells and potentiated radiation-caused DNA damage and the generation of cytotoxic reactive oxygen species [47]. Thus, the positive charge of our as-received DNDs could, at least partly, explain their more pronounced cytotoxic effect than that observed in negatively charged annealed DNDs.

Finally, we can compare the NDs produced by mechanical grinding and by the detonation method, MR-18 and NR-5, respectively. Here, the main differences are in the production method and the particle size (18 nm and 5 nm), while the effect of surface termination is minimized due to air annealing [42]. We have shown that air annealing of as-received DNDs reduced mainly bands in the 2800–3000 cm^{-1} region corresponding to CH_2 and CH_3 stretching vibrations, and they give rise to a $\text{C}=\text{O}$ stretch at 1775 cm^{-1} , $\text{C}-\text{O}$ stretch at 1294 cm^{-1} , and a $\text{C}-\text{O}-\text{C}$ stretch at 1077 cm^{-1} .

This produces surface termination similar to that of the as-received HPHT NDs (compare Figs. 1 in [42] and [40]). The zeta potentials have almost the same value of -40 mV for both ND types [41]. This explains the similarity in cytotoxic behaviour, where annealing of DNDs reduced their toxicity significantly. A decrease in the cytotoxicity is still observable after 7 days of cultivation (a 40% reduction), likely because some CH_2 , CH_3 and $\text{C}-\text{H}$ stretch bands remain and some differences in particle diameter. Finally, the dependence of the concentration on the cell viability was again most pronounced for the highest concentration (1000 $\mu\text{g}/\text{mL}$, 300 $\mu\text{g}/\text{cm}^2$).

Live-cell imaging of diamond nanoparticle uptake

Live-cell imaging (see Supporting Information File 1 and Supporting Information File 2 for full experimental data) confirmed the formation of DND aggregates in the suspension

(10 $\mu\text{g}/\text{mL}$, 3 $\mu\text{g}/\text{cm}^2$). Particle aggregates are collected by cells from their surroundings. DNDs then accumulate on their surface and are endocytosed during the experiment. The accumulation and the cytotoxicity of the DNDs in the cell depends on their surface termination.

Live-cell imaging of SAOS-2 cells with as-received DNDs (NR-5, see Supporting Information File 1) reveals rapid uptake of NDs by the cells. The DNDs penetrated the cells early in the experiment. The video begins with six living cells. The cells are soon congested by the nanoparticles then their viability drops rapidly. Five cells undergo cytokinesis, but at least half of the cells are dead at the end of the experiment. In at least one or two of the cases of cell death, an expelled cytoplasm can be seen exiting the cell membrane. This indicates uncontrolled cell death and rupture. The remaining living cells have an elongated shape due to the accumulated NDs which mechanically restrain their spreading and migration [38].

Unlike NR-5, the air-annealed DND aggregates (NA-5, see Supporting Information File 2) are not taken up by the cells as rapidly as their non-annealed counterparts. The video starts with a similar number of living cells as described above. The cells undergo 14 cytokineses, and most of them survive until the end of the video sequence. Only two or three cell death events can be recognized in the video.

Photoluminescence of diamond nanoparticles

Figure 5 shows fluorescence phase contrast images of osteoblasts and photoluminescent NDs (AR-40, 100 $\mu\text{g}/\text{mL}$, 30 $\mu\text{g}/\text{cm}^2$) grown for 3 and 7 days. The images reveal the presence of NDs in the cells. The red photoluminescence signal around the outside of the cell nuclei indicate that the NDs could not penetrate the nuclear envelope and stay in the cytoplasm. A certain amount of NDs are present outside the cells, probably in the loose serum protein/ND aggregates or in cell debris. The

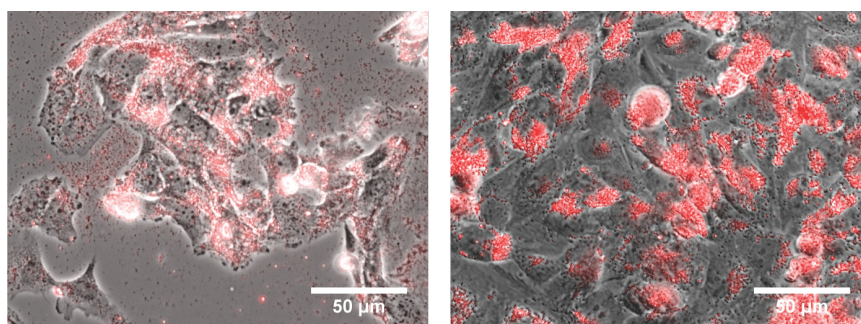


Figure 5: Phase contrast images of photoluminescent NDs (AR-40, 100 $\mu\text{g}/\text{mL}$) incubated with SAOS-2 cells after 3 days (left) and after 7 days (right).

well-spread osteoblasts are homogeneously and confluent distributed. Good cell adhesion and division confirms the viability of the cells with photoluminescent NDs (AR-40).

Conclusion

A comparison of cell viability with various types of NDs (HPHT, HPHT PL, DND) and surface termination and energy showed that the toxicity is mostly dependent on particle surface modification. In our study, oxygen termination emerges as the best surface modification for ND particles from the point-of-view of their biocompatibility. The viability of cells cultivated with positively charged as-received DNDs (100 and 1000 $\mu\text{g}/\text{mL}$, 30 and 300 $\mu\text{g}/\text{cm}^2$) had already decreased after 3 days of cultivation. However, annealing these NDs reduced their toxicity significantly. This effect could still be observed after 7 days of cultivation.

A concentration-dependent toxic effect of HPHT NDs was revealed after 7 days of cultivation when the viability of the cells cultivated at a 1000 $\mu\text{g}/\text{mL}$ (300 $\mu\text{g}/\text{cm}^2$) concentration reduced by 25–30% in comparison with 100 $\mu\text{g}/\text{mL}$ and 10 $\mu\text{g}/\text{mL}$ (30 $\mu\text{g}/\text{cm}^2$ and 3 $\mu\text{g}/\text{cm}^2$). This was associated with the mechanical obstruction by NDs preventing cell adhesion, migration and division.

In comparison with the results of our previous studies, the air annealing of as-received DNDs reduced bands mainly corresponding to CH_2 and CH_3 stretching vibrations, and gave rise to $\text{C}=\text{O}$, CO and $\text{C}-\text{O}-\text{C}$ stretch bands [41,42]. The zeta potential was also reversed from positive values to negative values. Thus the surface state of as-received DNDs is rendered similar to the state of HPHT NDs with similar cytotoxicity results. A decrease in viability was still observable after 7 days of cultivation, mostly due to the remaining CH_2 , CH_3 and $\text{C}-\text{H}$ stretching bands. The dependence of concentration on cell viability was again observed.

The comparison of the viability of the cells cultivated with various types of NDs indicates that the toxicity of NDs is probably dependent on the surface functional groups and the zeta potential rather than on the diameter of the particles.

Live-cell imaging showed that as-received DNDs penetrated rapidly into cells and caused rupture. O-terminated DNDs aggregated into large clusters, and the cells internalized them at a slower rate with a low impact on their viability for the first 3 days. After 7 days of cultivation, the MTS test revealed lower cell viability for ND concentrations of 100 $\mu\text{g}/\text{mL}$ and 1000 $\mu\text{g}/\text{mL}$ (30 $\mu\text{g}/\text{cm}^2$ and 300 $\mu\text{g}/\text{cm}^2$). Nevertheless, O-termination increases the biocompatibility of diamond nanoparticles and can be considered an advantageous modification.

Experimental

Origin and surface modification of diamond nanoparticles

Nanodiamond particles produced by two different methods were used: NanoAmando DNDs (NanoCarbon Research Institute, Japan) with a nominal diameter of 5 nm, HPHT NDs (Microdiamant AG, Switzerland) with median sizes from 18–210 nm, and 40 nm HPHT NDs with N-V-based photoluminescence (Adámas Nanotechnologies, USA). The particles were used either as-received or were oxidized by air annealing at 450 °C for 30 min [48]. For the detonation nanodiamonds purchased from NanoCarbon, the as-received nanodiamonds had a mixture of hydrogen and oxygen states on the surface with a positive zeta potential (characteristic for hydrogenated NDs). A fully oxidized state was achieved by air annealing, which resulted in oxygen-termination. The other diamond nanoparticles, namely high-pressure high-temperature (HPHT) DNDs and photoluminescent HPHT NDs, were oxidized in their as-delivered state.

Characterization of diamond nanoparticles

The size of the ND particles and their zeta potential was determined by dynamic light scattering (DLS) measurements in water at 25 °C using a Nano-ZetaSizer (Malvern, UK) equipped with an He-Ne laser. A separate disposable folded capillary cell was used for each set of ND measurements to eliminate sample cross contamination.

A Nicolet 8700 FTIR spectrometer (Thermo Scientific, USA) was equipped with N_2 purging, a KBr beamsplitter and an MCT detector cooled by liquid nitrogen. 50 μL of the water suspension with NDs was applied on the Au mirror by the drop-casting method just prior to the grazing angle reflectance FTIR measurements. The optical absorbance was calculated in standard absorbance units as $A = -\log(R/R_0)$, where R is the spectrum measured with NDs and R_0 is the reference (background) spectrum recorded using the clean Au mirror before the NDs were applied. In all cases, the spectra represent an average of 128 scans recorded with a resolution of 4 cm^{-1} .

The basic characteristics and the notation of the NDs that were used are summarized in Table 1. More data on ND characterization by FTIR and XPS can be found in our previous works [42,49].

Evaluation of cell viability

The cell viability upon exposure to the NDs was evaluated using the SAOS-2 human osteoblastic cell line (European Collection of Cell Cultures, Salisbury, UK, Cat. No. 89050205). The SAOS-2 cell line was used for biocompatibility experiments based on cell anchorage dependency and homogeneity.

Table 1: Characteristics and notation of diamond nanoparticle (ND) samples.

ND type	Particle size [nm]	Treatment	Notation
HPHT NDs	18	as-received	MR-18
	25		MR-25
	50		MR-50
	75		MR-75
	90		MR-90
	125		MR-125
DNDs	210	as-received	MR-210
	5		NR-5
	5		NA-5
HPHT PL NDs	40	as-received	AR-40

Two complementary methods were used. The first method was based on the mitochondrial metabolic activity test (MTS), while the second method was based on counting adherent cells. The cells were cultivated in the recommended McCoy's 5A medium (Sigma-Aldrich, USA) with 15% fetal bovine serum (FBS, Sigma-Aldrich, USA). The cells were seeded at a density of 15000 cells/cm² in a sterile 96-well plate (TPP, Switzerland) and were cultivated for 24 h before the nanoparticles were added. Cells from the 82nd passage to the 86th passage were used for the experiments. The NDs were sonicated in a UP 100H sonicator (Hielscher, Germany) in sterile distilled water in a stock concentration of 10 mg/mL, at 80 W for 30 min. The stock ND suspension was sterilized by exposure to UVC light (Esco germicidal lamp, spectrum peak at 253.7 nm) for 30 min. The working concentrations of 10, 100 and 1000 µg/mL were then diluted in the cultivation medium with FBS. The original medium was aspirated off the cells, and the medium with NDs was pipetted onto the cells. The cells were cultivated with the NDs for 3 and 7 days under standard cultivation conditions (37 °C, 5% CO₂). The cell metabolic activity (a marker of cell viability and growth) was measured using the colorimetric MTS test (CellTiter 96® - Promega, USA). The absorbance of the colorimetric MTS test was measured at 490 nm, and a reference measurement was taken at 650 nm. This experiment was repeated three times in sextuplicate for each experimental group. The cells on the samples were then washed with phosphate buffered saline and were fixed with 4% paraformaldehyde for 10 min. The nuclei of the fixed cells were then stained using Hoechst 33258 dye for cell counting. Micrographs of the stained nuclei were acquired using an IX71 microscope (Olympus, Japan) with a 10× lens. 12 micrographs were taken for each sample. The cell nuclei were automatically counted using open source ImageJ image processing software. Photoluminescence microphotographs of fixed cells co-cultivated with photoluminescent NDs (AR-40), 100 µg/mL (30 µg/cm²), were

also taken using an IX71 microscope (Olympus, Japan) with a 40× lens. The AR-40 NDs were excited by green excitation light, and their red photoluminescence was collected through a U-MWG2 filter cube (Olympus, Japan).

The statistical significance of the differences in the cell metabolic activity and in cell number among the samples was evaluated using ANOVA with the Tukey HSD post-hoc test.

Live-cell imaging

The live-cell imaging method was used for observing the ND uptake in the cells. Live-cell imaging was again performed on the SAOS-2 cell line. The cells were seeded on a 35 mm diameter Petri dish with a 0.17 mm glass bottom and were cultivated for 24 h. The ND suspension was prepared in the same way as for the viability test. For live-cell imaging, only 10 µg/mL and 100 µg/mL concentrations were used. The live-cell imaging was performed on the TE2000 microscope with 40× magnification, (Nikon, Japan), Plan Fluor, ELWD objective (Nikon, Japan) with phase contrast installed. The microscope was equipped with a cell incubation chamber (Solent Scientific, UK) with humidity regulation (95%), controlled temperature (37 °C) and CO₂ concentration (5%). The cells were photographed for 72 h at 2 min intervals for the first 6 h and thereafter at 10 min intervals.

Supporting Information

Supporting Information File 1

Live-cell imaging of NR-5 (10 µg/mL, 3 µg/cm²) uptake by the SAOS-2 cells.

[<http://www.beilstein-journals.org/bjnano/content/supplementary/2190-4286-8-165-S1.avi>]

Supporting Information File 2

Live-cell imaging of NA-5 (10 µg/mL, 3 µg/cm²) uptake by the SAOS-2 cells.

[<http://www.beilstein-journals.org/bjnano/content/supplementary/2190-4286-8-165-S2.avi>]

Supporting Information File 3

FTIR comparison of MR-18 and AR-40 nanodiamonds.

[<http://www.beilstein-journals.org/bjnano/content/supplementary/2190-4286-8-165-S3.png>]

Supporting Information File 4

Live-cell imaging of SAOS-2 cells after three days without nanodiamonds.

[<http://www.beilstein-journals.org/bjnano/content/supplementary/2190-4286-8-165-S4.avi>]

Acknowledgements

This work was financially supported by the Czech Science Foundation research project 17-19968S (Š.P.). The work also received support from project No. LD15003 (Ministry of Education, Youth and Sports) within the frame of the COST Action MP1403 "Nanoscale Quantum Optics". This work was carried out in the framework of the LNSM infrastructure. The biological part of this work was supported by the Czech Health Research Council, Ministry of Health of the Czech Republic, project No. 15-32497A (A.B., L.B.). Mr. Robin Healey (Czech Technical University in Prague) is gratefully acknowledged for his language revision of the manuscript.

References

- Monaco, A. M.; Giugliano, M. *Beilstein J. Nanotechnol.* **2014**, *5*, 1849–1863. doi:10.3762/bjnano.5.196
- May, P. W. *Philos. Trans. R. Soc., A* **2000**, *358*, 473–495. doi:10.1098/rsta.2000.0542
- Kaur, R.; Badea, I. *Int. J. Nanomed.* **2013**, *8*, 203–220. doi:10.2147/IJN.S37348
- Ho, D., Ed. *Nanodiamonds: applications in biology and nanoscale medicine*; Springer: Berlin, Germany, 2010.
- Bacakova, L.; Kopova, I.; Stankova, L.; Liskova, J.; Vacik, J.; Lavrentiev, V.; Kromka, A.; Potocky, S.; Stranska, D. *Phys. Status Solidi A* **2014**, *211*, 2688–2702. doi:10.1002/pssa.201431402
- Bacakova, L.; Broz, A.; Liskova, J.; Stankova, L.; Potocky, S.; Kromka, A. The Application of Nanodiamond in Biotechnology and Tissue Engineering. In *Diamond and Carbon Composites and Nanocomposites*; Aliofkhaezrai, M., Ed.; InTech: Rijeka, Croatia, 2016. doi:10.5772/63549
- Tang, L.; Tsai, C.; Gerberich, W. W.; Kruckeberg, L.; Kania, D. R. *Biomaterials* **1995**, *16*, 483–488. doi:10.1016/0142-9612(95)98822-V
- Paget, V.; Sergent, J. A.; Grall, R.; Altmeyer-Morel, S.; Girard, H. A.; Petit, T.; Gesset, C.; Mermoux, M.; Bergonzo, P.; Arnault, J. C.; Chevillard, S. *Nanotoxicology* **2014**, *8*, 46–56. doi:10.3109/17435390.2013.855828
- Mochalin, V. N.; Shenderova, O.; Ho, D.; Gogotsi, Y. *Nat. Nanotechnol.* **2012**, *7*, 11–23. doi:10.1038/nnano.2011.209
- Liu, K.-K.; Wang, C.-C.; Cheng, C.-L.; Chao, J.-I. *Biomaterials* **2009**, *30*, 4249–4259. doi:10.1016/j.biomaterials.2009.04.056
- Vaijayanthimala, V.; Tzeng, Y.-K.; Chang, H.-C.; Li, C.-L. *Nanotechnology* **2009**, *20*, 425103. doi:10.1088/0957-4484/20/42/425103
- Yan, L.; Yang, Y.; Zhang, W.; Chen, X. *Adv. Mater.* **2014**, *26*, 5533–5540. doi:10.1002/adma.201305683
- Lam, R.; Ho, D. *Expert Opin. Drug Delivery* **2009**, *6*, 883–895. doi:10.1517/17425240903156382
- Vaijayanthimala, V.; Lee, D. K.; Kim, S. V.; Yen, A.; Tsai, N.; Ho, D.; Chang, H.-C.; Shenderova, O. *Expert Opin. Drug Delivery* **2015**, *12*, 735–749. doi:10.1517/17425247.2015.992412
- Chao, J.-I.; Perevedentseva, E.; Chung, P.-H.; Liu, K.-K.; Cheng, C.-Y.; Chang, C.-C.; Cheng, C.-L. *Biophys. J.* **2007**, *93*, 2199–2208. doi:10.1529/biophysj.107.108134
- Aharonovich, I.; Neu, E. *Adv. Opt. Mater.* **2014**, *2*, 911–928. doi:10.1002/adom.201400189
- Balasubramanian, G.; Lazariev, A.; Arumugam, S. R.; Duan, D.-w. *Curr. Opin. Chem. Biol.* **2014**, *20*, 69–77. doi:10.1016/j.cbpa.2014.04.014
- Schirhagl, R.; Chang, K.; Lorez, M.; Degen, C. L. *Annu. Rev. Phys. Chem.* **2014**, *65*, 83–105. doi:10.1146/annurev-physchem-040513-103659
- Dolmatov, V. Yu. *Russ. Chem. Rev.* **2007**, *76*, 339–360. doi:10.1070/RC2007v076n04ABEH003643
- Osawa, E. *Pure Appl. Chem.* **2008**, *80*, 1365–1379. doi:10.1351/pac200880071365
- Boudou, J.-P.; Curmi, P. A.; Jelezko, F.; Wrachtrup, J.; Aubert, P.; Sennour, M.; Balasubramanian, G.; Reuter, R.; Thorel, A.; Gaffet, E. *Nanotechnology* **2009**, *20*, 235602. doi:10.1088/0957-4484/20/23/235602
- Stehlik, S.; Varga, M.; Ledinsky, M.; Jirasek, V.; Artemenko, A.; Kozak, H.; Ondic, L.; Skakalova, V.; Argentero, G.; Pennycook, T.; Meyer, J. C.; Fejfar, A.; Kromka, A.; Rezek, B. *J. Phys. Chem. C* **2015**, *119*, 27708–27720. doi:10.1021/acs.jpcc.5b05259
- Krueger, A.; Stegk, J.; Liang, Y.; Lu, L.; Jarre, G. *Langmuir* **2008**, *24*, 4200–4204. doi:10.1021/la703482v
- Keremidarska, M.; Ganeva, A.; Mitev, D.; Hikov, T.; Presker, R.; Pramatarova, L.; Krasteva, N. *Biotechnol. Biotechnol. Equip.* **2014**, *28*, 733–739. doi:10.1080/13102818.2014.947704
- Schrand, A. M.; Hens, S. A. C.; Shenderova, O. A. *Crit. Rev. Solid State Mater. Sci.* **2009**, *34*, 18–74. doi:10.1080/10408430902831987
- Pichot, V.; Comet, M.; Fousson, E.; Baras, C.; Senger, A.; Le Normand, F.; Spitzer, D. *Diamond Relat. Mater.* **2008**, *17*, 13–22. doi:10.1016/j.diamond.2007.09.011
- Shenderova, O.; Petrov, I.; Walsh, J.; Grichko, V.; Grishko, V.; Tyler, T.; Cunningham, G. *Diamond Relat. Mater.* **2006**, *15*, 1799–1803. doi:10.1016/j.diamond.2006.08.032
- Puzyr', A. P.; Tarskikh, S. V.; Makarskaya, G. V.; Chiganova, G. A.; Larionova, I. S.; Detkov, P. Ya.; Bondar, V. S. *Dokl. Biochem. Biophys.* **2002**, *385*, 201–204. doi:10.1023/A:1019959322589
- Puzyr, A. P.; Neshumae, D. A.; Tarskikh, S. V.; Makarskaia, G. V.; Dolmatov, V. I.; Bondar, V. S. *Biofizika* **2005**, *50*, 101–106.
- Xing, Y.; Xiong, W.; Zhu, L.; Osawa, E.; Hussin, S.; Dai, L. *ACS Nano* **2011**, *5*, 2376–2384. doi:10.1021/nn200279k
- Zhu, Y.; Li, W.; Zhang, Y.; Li, J.; Liang, L.; Zhang, X.; Chen, N.; Sun, Y.; Chen, W.; Tai, R.; Fan, C.; Huang, Q. *Small* **2012**, *8*, 1771–1779. doi:10.1002/sml.201102539
- Wierzbecki, M.; Sawosz, E.; Grodzik, M.; Hotowy, A.; Prasek, M.; Jaworski, S.; Sawosz, F.; Chwalibog, A. *Int. J. Nanomed.* **2013**, *8*, 3427–3435. doi:10.2147/IJN.S49745
- Xing, Z.; Pedersen, T. O.; Wu, X.; Xue, Y.; Sun, Y.; Finne-Wistrand, A.; Kloss, F. R.; Waag, T.; Krueger, A.; Steinmüller-Nethl, D.; Mustafa, K. *Tissue Eng., Part A* **2013**, *19*, 1783–1791. doi:10.1089/ten.tea.2012.0336
- Eidi, H.; David, M.-O.; Crépeaux, G.; Henry, L.; Joshi, V.; Berger, M.-H.; Sennour, M.; Cadusseau, J.; Gherardi, R. K.; Curmi, P. A. *BMC Med.* **2015**, *13*, 144. doi:10.1186/s12916-015-0388-2
- Solarska, K.; Gajewska, A.; Bartosz, G.; Mitura, K. *J. Nanosci. Nanotechnol.* **2012**, *12*, 5117–5121. doi:10.1166/jnn.2012.4952
- Landgraf, L.; Müller, I.; Ernst, P.; Schäfer, M.; Rosman, C.; Schick, I.; Köhler, O.; Oehring, H.; Breus, V. V.; Basché, T.; Sönnichsen, C.; Tremel, W.; Hilger, I. *Beilstein J. Nanotechnol.* **2015**, *6*, 300–312. doi:10.3762/bjnano.6.28

37. Wehling, J.; Dringen, R.; Zare, R. N.; Maas, M.; Rezwan, K. *ACS Nano* **2014**, *8*, 6475–6483. doi:10.1021/nn502230m
38. Lombardi, S. L., Ed. *Nanoparticles: new research*; Nova Science Publishers: New York, NY, U.S.A., 2008.
39. Chang, Y.-R.; Lee, H.-Y.; Chen, K.; Chang, C.-C.; Tsai, D.-S.; Fu, C.-C.; Lim, T.-S.; Tzeng, Y.-K.; Fang, C.-Y.; Han, C.-C.; Chang, H.-C.; Fann, W. *Nat. Nanotechnol.* **2008**, *3*, 284–288. doi:10.1038/nnano.2008.99
40. Kozak, H.; Artemenko, A.; Čermák, J.; Švrček, V.; Kromka, A.; Rezek, B. *Vib. Spectrosc.* **2016**, *83*, 108–114. doi:10.1016/j.vibspec.2016.01.010
41. Jirásek, V.; Čech, J.; Kozak, H.; Artemenko, A.; Černák, M.; Kromka, A. *Phys. Status Solidi A* **2016**, *213*, 2680–2686. doi:10.1002/pssa.201600184
42. Kromka, A.; Jira, J.; Stenclova, P.; Kriha, V.; Kozak, H.; Beranova, J.; Vretenar, V.; Skakalova, V.; Rezek, B. *Phys. Status Solidi B* **2016**, *253*, 2481–2485. doi:10.1002/pssb.201600237
43. Bondar, O. V.; Saifullina, D. V.; Shakhmaeva, I. I.; Mavlyutova, I. I.; Abdullin, T. I. *Acta Naturae* **2012**, *4*, 78–81.
44. Platel, A.; Carpentier, R.; Becart, E.; Mordacq, G.; Betteder, D.; Nessler, F. *J. Appl. Toxicol.* **2016**, *36*, 434–444. doi:10.1002/jat.3247
45. Carmona-Ribeiro, A. M.; Dias de Melo Carrasco, L. *Int. J. Mol. Sci.* **2013**, *14*, 9906–9946. doi:10.3390/ijms14059906
46. Fröhlich, E. *Int. J. Nanomed.* **2012**, *7*, 5577–5591. doi:10.2147/IJN.S36111
47. Grall, R.; Girard, H.; Saad, L.; Petit, T.; Gesset, C.; Combis-Schlumberger, M.; Paget, V.; Delic, J.; Arnault, J.-C.; Chevillard, S. *Biomaterials* **2015**, *61*, 290–298. doi:10.1016/j.biomaterials.2015.05.034
48. Kozak, H.; Remes, Z.; Houdkova, J.; Stehlik, S.; Kromka, A.; Rezek, B. *J. Nanopart. Res.* **2013**, *15*, 1568. doi:10.1007/s11051-013-1568-7
49. Kromka, A.; Čech, J.; Kozak, H.; Artemenko, A.; Ižák, T.; Čermák, J.; Rezek, B.; Černák, M. *Phys. Status Solidi B* **2015**, *252*, 2602–2607. doi:10.1002/pssb.201552232

License and Terms

This is an Open Access article under the terms of the Creative Commons Attribution License (<http://creativecommons.org/licenses/by/4.0>), which permits unrestricted use, distribution, and reproduction in any medium, provided the original work is properly cited.

The license is subject to the *Beilstein Journal of Nanotechnology* terms and conditions: (<http://www.beilstein-journals.org/bjnano>)

The definitive version of this article is the electronic one which can be found at:
[doi:10.3762/bjnano.8.165](https://doi.org/10.3762/bjnano.8.165)

A.12

Alterations to the adhesion, growth and osteogenic differentiation of human osteoblast-like cells on nanofibrous polylactide scaffolds with diamond nanoparticles



Alterations to the adhesion, growth and osteogenic differentiation of human osteoblast-like cells on nanofibrous polylactide scaffolds with diamond nanoparticles

Lubica Stankova^a, Jana Musilkova^{a,*}, Antonin Broz^a, Stepan Potocky^b, Alexander Kromka^b, Halyna Kozak^b, Tibor Izak^b, Anna Artemenko^b, Denisa Stranska^c, Lucie Bacakova^a

^a Institute of Physiology of the Czech Academy of Sciences, Videnska 1083, 142 20 Prague 4-Krc, Czech Republic

^b Institute of Physics of the Czech Academy of Sciences, Cukrovarnicka 10, 16253 Prague 6, Czech Republic

^c InStar Technologies a.s., Mrstikova 399/2a, 460 07 Liberec, Czech Republic

ARTICLE INFO

Keywords:

Diamond nanoparticles
Nanofibers
Cell viability
Cell cycle regulation
Cytotoxicity
Gene expression

ABSTRACT

Nanofibrous scaffolds are promising materials for engineering various types of tissues, including bone tissue. The properties of nanofibers for bone tissue engineering can be improved by adding ceramic or carbon nanoparticles, including diamond nanoparticles (DNPs). In this study, poly(L-lactide) (PLLA) nanofibrous membranes reinforced with detonation DNPs (concentration from 0 to 12.28 wt%), provided by the NanoCarbon Research Institute (Japan) under the name NanoAmando[®], were prepared by a needle-less electrospinning process. The biocompatibility of these DNP-reinforced PLLA membranes was tested in vitro using two human lines of osteoblast-like cells, MG-63 and Saos-2. Microscopic and biochemical methods were used. In addition, the expression of cell survival markers, focal adhesion proteins and osteogenic markers were studied in both cell types at mRNA level and at protein level. The mitochondrial activity of both cells types decreased with increasing DNP concentration in the PLLA matrix. At the same time, the expression of cyclin D and survivin, i.e. factors supporting cell growth and survival were downregulated on the DNP-loaded PLLA scaffolds, while KLF6, an anti-proliferative factor, was often upregulated, at least in MG-63 cells. Thus, loading the nanofibrous polymeric scaffolds with detonation DNPs had rather adverse effects on the behavior of human bone-derived cell lines. These results are mostly in conflict with our earlier studies on poly(lactide-co-glycolide) (PLGA) scaffolds, loaded with DNPs prepared by etching the diamond layer fabricated by radiofrequency plasma-assisted chemical vapour deposition. The cell behavior on DNP-loaded scaffolds is therefore markedly influenced by the origin and the properties of the DNPs.

1. Introduction

In recent years, nanofiber materials reinforced with nanoparticles have been attracting interest in bone tissue engineering. The nanofibers for this purpose have been fabricated from natural or synthetic polymers [1]. To reinforce the nanofibers, and also to enhance their biological activity, ceramic particles have mainly been used, particularly particles based on silica and calcium phosphates [1,2]. In addition to ceramic particles, carbon nanoparticles, such as fullerenes, carbon nanotubes, graphene and nanodiamonds, are also promising for reinforcing polymeric nanofibrous scaffolds and for increasing their bioactivity. For example, modified fullerene nanoparticles have been used to form synthetic polymeric nanofibrous scaffolds designed for bone

reconstruction [3] or for bioimaging [4]. Multi-walled carbon nanotubes and particularly graphene nanoparticles incorporated into nanofibrous poly(L-lactic acid) (PLLA) scaffolds enhanced the osteogenic differentiation of mouse bone marrow mesenchymal stem cells in cultures on these scaffolds [5]. In our earlier studies, loading nanofibrous poly(lactide-co-glycolide) (PLGA) scaffolds with diamond nanoparticles (DNPs) accelerated the growth of human bone marrow mesenchymal stem cells [6], improved the mechanical properties of the scaffolds, and facilitated the formation of focal adhesion plaques in human osteoblast-like MG-63 cells in comparison with pure PLGA scaffolds [7]. Similarly, in a study by Mahdavi et al., adding DNPs into an electrospinning solution of chitosan and bacterial cellulose improved the tensile strength and the wettability of the resulting nanofibrous

* Corresponding author.

E-mail address: jana.musilkova@fgu.cas.cz (J. Musilkova).

<https://doi.org/10.1016/j.diamond.2019.05.007>

Received 26 February 2019; Received in revised form 15 April 2019; Accepted 7 May 2019

Available online 08 May 2019

0925-9635/ © 2019 Elsevier B.V. All rights reserved.

scaffolds and supported the growth of mouse skin L929 fibroblasts [8]. DNPs also had a favorable effect when incorporated into polymeric films or when attached to the surface of nanofibers in nanofibrous scaffolds. Thin poly(L-lactide) (PLLA) films with fluorescent nanodiamonds supported the adhesion, growth and osteogenic differentiation of murine bone marrow-derived cells to a similar extent as pure PLLA films, but showed considerably higher hardness and Young modulus [9]. Porous poly(L-lactide-co-ε-caprolactone) scaffolds coated with oxygen-terminated DNPs increased the adhesion and the osteogenic differentiation of human bone marrow mesenchymal stem cells in vitro, and also increased bone tissue formation in vivo using a sheep calvarial defect model [10]. Similar effects were observed when oxygen-terminated DNPs were added into β-tricalcium phosphate. The resulting scaffolds enhanced the attachment of ovine bone marrow stromal cells in vitro and improved guided bone regeneration after lateral augmentation of the mandible in sheep in vivo [11].

Diamond nanoparticles have also proved to be suitable for other applications, such as bioimaging, biosensing and targeted drug and gene delivery (for a review, see [12]), and also for coating biomaterials. In our earlier studies, and in studies by other authors, nanocrystalline diamond films provided excellent substrates for the adhesion, growth and osteogenic differentiation of cells [13,14]. The cell performance on these films, and on DNP-containing materials in general, can be further modulated by terminating NCD with hydrogen or oxygen [15,16], by functionalization with biologically active molecules, e.g. bone morphogenetic protein-2 [17] and angiogenic factors [18], or by boron doping [19].

In the study presented here, we constructed nanofibrous scaffolds with various concentrations of DNPs, ranging from 0 to 12.28 wt%, in order to investigate the behavior of bone-derived cells on these scaffolds. In studies by Zhang et al. [9], performed on PLLA foils with DNPs, the Young modulus and the hardness of the films increased and the creep decreased proportionally to the DNP concentration, ranging from 0 to 10 wt%. The deposition of minerals in simulated body fluid (SBF) also increased with increasing DNP concentration. We therefore expected different cell behavior on scaffolds with various DNP concentrations. The cell behavior was studied on two commercially available lines of human osteoblast-like cells, namely on human osteoblast-like MG-63 cells, which are considered to be a good model for cell adhesion and proliferation studies, and on human osteoblast-like Saos-2 cells, which are considered to be a good model for studies on osteogenic cell differentiation [20–22]. Our study provides an insight into the adhesion, growth, viability, mitochondrial activity, osteogenic cell differentiation and expression of genes regulating cell growth and apoptosis in cells on DNP-loaded nanofibrous PLLA scaffolds in correlation with the physical and chemical properties of these scaffolds.

2. Experimental

2.1. Preparation of the PLLA scaffolds

Poly(L-lactide) (PLLA, Ingeo™ Biopolymer 4032D) for preparing nanofibrous scaffolds was purchased from NatureWorks, Minnetonka, Minnesota, USA. Its molecular masses were $M_w = 124,000$ g/mol and $M_n = 48,000$ g/mol, as determined by size exclusion chromatography. Five grams of PLLA was dissolved in 100 ml of chloroform. The polymer solution was made to be electrically conductive with tetraethylammoniumbromide, which was first dissolved in dimethylformamide at a concentration of 3 wt%, and then 3 g of this solution were added to 100 g of the PLLA solution (for a review, see [2]). Diamond nanoparticles (DNPs; NanoAmando, Nanocarbon Research Institute Co., Ltd. Japan [23]) were then added in concentrations ranging from 0 to 0.7 g/100 ml of the polymer solution (these concentrations were set by successive division of 0.7 by two). After the solvent had evaporated, these concentrations corresponded to 0 to 12.28 wt% in the final dry PLLA scaffolds (Table 1). The as-received DNPs were used directly

Table 1

Concentrations of diamond nanoparticles (DNPs) added to the PLLA solution in chloroform, calculated in dry scaffolds after evaporation of the solvent, and the specific weight of the scaffolds.

Sample label	Concentration of DNPs (g/100 ml of PLLA solution)	Concentration of DNPs pure PLLA (wt %)	Membrane weight (g/m ²)
1	0	0	17.82
2	0.021875	0.44	18.97
3	0.04375	0.87	17.05
4	0.0875	1.72	16.44
5	0.175	3.38	15.1
6	0.35	6.54	19.6
7	0.7	12.28	29.3

without any pre-treatment. The DNPs were prepared by detonation of trinitrotoluene in an oxygen-deprived atmosphere. This method results in the production of hydrogen-terminated (i.e. hydrophobic) DNPs with the size median between 4 and 5 nm [23].

In our earlier studies, these DNPs were thoroughly characterized with Fourier-transform infrared spectroscopy (FTIR), X-ray photoelectron spectroscopy (XPS) and dynamic light scattering (DLS). FTIR spectra of as-received DNPs revealed vibrational modes of the hydroxyl groups of water at about 3500 cm⁻¹ (stretching) and 1630 cm⁻¹ (deformation) and C–O groups at about 1300–1000 cm⁻¹ [24]. XPS measurements were in good agreement with FTIR, and the concentrations of the chemical bonds calculated from the deconvoluted high-resolution C 1s peak were 7% for C–O, 2% for C=O and 91% for carbon, of which 24% was identified as sp²-hybridized carbon, and 66% was identified as sp³-hybridized carbon. The relatively high sp²/sp³ ratio (0.36) indicated an amorphous character of bulk DNPs or their outer carbon shell [25]. The presence of sp²-hybridized carbon seems to be responsible for the positive zeta potential of DNPs. Broad range XPS scans revealed the presence of 2% of nitrogen, which we attributed to contamination of the DNPs during their production [26]. The DLS measurements of the DNPs revealed nanoparticles as large as 13 nm and 77 nm, which was attributed to aggregates of DNPs [27]. As has later been confirmed by many authors, sonication & milling processes further decreased the average size of DNP aggregates to 6 nm [28].

The suspensions of DNPs in a PLLA solution were intensively vortexed and sonicated for 2 min using a Sonorex sonicator (Bandelin, Berlin, Germany), in order to prevent or at least reduce the aggregation of DNPs. The nanofibrous membranes were then prepared by a needleless electrospinning technology, using a Nanospider machine (NS Lab 500, Elmarco Ltd., Liberec, Czech Republic). The electrode distance was 200 mm, the voltage was 60 kV, the electric current was 0.07 mA, the relative humidity was 23.6%, and the process was performed at room temperature. The speed of the vessel with the DNP-PLLA mixture was 430 mm/s, and the speed of the polypropylene fabric, which served as the nanofiber collector, was 11 mm/min. The fiber density, i.e. the area weight of the nanofibrous membranes, ranged from 15.1 to 29.3 g/m². The fiber density was generally similar in membranes with a DNP concentration from 0 to 6.54 wt% (15.1 to 19.6 g/m² with no dependence on the DNP concentration), and increased markedly only in the membranes with 0.7 wt% of DNPs (29.3 g/m²; Table 1).

2.2. Physicochemical characterization of the scaffolds

The nanofibrous membranes were detached from their underlying polypropylene substrate, and their morphology was studied using scanning electron microscopy (SEM). The thickness (i.e., diameter) of the nanofibers was measured on SEM images using Atlas software (Tescan Ltd., Brno, Czech Republic). The chemical functional groups on the PLLA surface were studied by attenuated total reflection Fourier transform infrared (ATR-FTIR) spectroscopy. The presence of diamond

in the scaffolds was confirmed by Raman spectroscopy.

The chemical composition of the PLLA surfaces was characterized by X-ray photoelectron spectroscopy (XPS), using an Al K α X-ray source (1486.6 eV, Specs) equipped with a hemispherical energy analyzer (Phoibos 100, Specs, Berlin, Germany). The wettability of the scaffolds was estimated by the water drop contact angle measured by reflection goniometry [6].

2.3. Cell culture on the scaffolds

The nanofibrous membranes were detached from the underlying polypropylene substrate, were cut into square samples (2 × 2 cm), fixed in CellCrown inserts (Scaffdex Ltd., Tampere, Finland), disinfected in 70% ethanol in deionized water for 1 h, rinsed in deionized water, inserted into polystyrene 12-well culture plates (TPP, Trasadingen, Switzerland, well diameter 2.1 cm), and rinsed in phosphate-buffered saline (PBS). The samples were then seeded with human osteoblast-like MG-63 cells (European Collection of Cell Cultures, Salisbury, UK; Cat. No. 86051601) or with human osteoblast-like Saos-2 cells (European Collection of Cell Cultures, Salisbury, UK, Cat. No. 89050205). Both cell lines were seeded in a concentration of 40,000 cells/well, which corresponds to ca. 10,500 cells/cm² in 3 ml of the medium. The MG-63 cells were cultured in Dulbecco's modified Eagle's Minimum Essential Medium (DMEM; Sigma, USA, Cat. No. D5648), supplemented with 10% of fetal bovine serum (FBS; Sebak GmbH, Aidenbach, Germany). The Saos-2 cells were cultured in McCoy's 5A medium (Sigma-Aldrich, St. Louis, MO, USA), supplemented with 15% of FBS. Both media also contained gentamicin (40 µg/ml; LEK, Ljubljana, Slovenia). Nanofibrous PLLA membranes without DNPs and standard cell culture polystyrene wells served as control samples in the subsequent studies on cell adhesion, growth, viability and osteogenic differentiation.

2.4. An evaluation of the potential cytotoxicity of the scaffolds

The potential cytotoxicity of the scaffolds was evaluated in the cells on day 3 after seeding. For an evaluation of cell viability, the cells on the samples were stained by the LIVE/DEAD viability/cytotoxicity kit for mammalian cells (Thermo-Fisher Scientific, Waltham, MA, USA). The live cells were stained in green with calcein dye, and the dead or dying cells were stained in red with ethidium homodimer-1.

Microscopy images were acquired on an Olympus IX 51 microscope with a lens 10 × (N.A. = 0.3) and an Olympus DP 70 camera (Olympus Corp. Tokyo, Japan). The number of living cells (green) and dead or dying cells (red) in 3-day-old cultures on cell culture polystyrene and on PLLA nanofibrous scaffolds with 0 to 12.28 wt% of DNPs were automatically counted using ImageJ software [29]. The results were displayed as the arithmetical mean ± standard deviation. The data were taken from 3 experiments performed in triplicate, i.e. three independent samples were used for each experimental group. Statistical significance was evaluated by ANOVA with the Student-Newman-Keuls post-hoc test.

In addition to the LIVE/DEAD staining, a Cell Proliferation Kit II (XTT) (Roche Diagnostic GmbH, Mannheim, Germany, Cat. No. 11 465 015 001) was used to measure the activity of the mitochondrial enzymes in the studied cell lines. The experiments were performed according to the manufacturer's protocol.

2.5. Expression of specific markers of cell cycle regulation, adhesion and differentiation at mRNA level

The quantitative PCR method was used for detecting selected expressed genes taking part in cell adhesion, cell cycle regulation and cell differentiation. On day 14 after cell seeding, the nanofibrous membranes with cells were rinsed with PBS, were dismantled from the Scaffdex CellCrowns, were placed in Eppendorf tubes, and the cells were then lysed directly on the membranes using the lysis solution

enriched with mercaptoethanol (1%). Four samples were pooled for all types of samples in two independent experiments. Total RNA was subsequently isolated using the Total RNA Purification Micro Kit (Norgen Biotek Corp., Thorold, ON, Canada).

Individual mRNA samples were reversely transcribed using the Omniscript Reverse Transcription Kit (Qiagen, Venlo, Netherlands) and the Random primer kit (New England Biolabs Inc., Ipswich, MA, USA), and the relative mRNA expression of the target was tested. The mRNA levels were quantified using real-time 5xHOT FIREPol Probe qPCR Mix Plus (ROX) (Solis BioDyne, Tartu, Estonia) and TaqMan Gene Expression Assays (Life Technologies, Thermo-Fisher Scientific, Waltham, MA, USA) labelled with FAM reporter dye specific to the studied human genes.

The studied genes involved in the cell cycle and in apoptosis regulation were:

- cyclin D (probeID: CCND1, Hs00765553_m1), a member of the cyclin protein family that is involved in regulating the cell cycle progression;
- B-cell lymphoma 2 (Probe ID: Bcl-2 Hs00236329_m1), an important anti-apoptotic protein and proto-oncogene;
- survivin, also called a baculoviral inhibitor of apoptosis repeat-containing 5 (probe ID: BIRC5, Hs04194392_s1), an inhibitor of caspase activation;
- Krüppel-like factor 6 (probe ID: KLF6, Hs00810569_m1), a transcription factor involved in growth-related signal transduction, cell proliferation and differentiation, development, apoptosis and angiogenesis, postulated as an anti-proliferative tumor suppressor [30].

For an evaluation of the cell/material interaction, two structural proteins of cell focal adhesions were chosen:

- talin (probe ID: TLN1, Hs00196775_m1), a protein connecting either integrin dimers in focal adhesions or integrins and the actin cytoskeleton;
- vinculin (probe ID: VCL, Hs00419715_m1), a protein cooperating with talin in connecting the integrin molecules to the actin cytoskeleton.

The osteogenic differentiation was evaluated by measuring the concentrations of mRNA for the following proteins:

- collagen type I (Coll I, probe ID: COL1A1 Hs00164004_m1), a bone extracellular matrix (ECM) protein and an early differentiation marker,
- alkaline phosphatase (ALP, probe ID: ALPL Hs01029144_m1), an enzyme involved in the bone extracellular matrix calcification process,
- osteocalcin (Ocn, probe ID: BGLAP Hs01587814_g1), a non-collagenous ECM protein typically produced typically by osteoblasts. The data were presented as the means of 4–5 experimental points from two independent experiments.

The expression values were obtained from the C_t numbers. The target gene levels were expressed as a relative value, i.e. the ratio of the target gene expression to the reference gene GAPDH. The relative gene expression was calculated as 2^{-ΔC_t}, where ΔC_t was determined in each sample by subtracting the C_t value of the target gene from the C_t value of glutaraldehyde-3-phosphate dehydrogenase (probe ID: GAPDH, Hs02758991_g1). The data were presented as the arithmetic means ± standard deviation.

2.6. Production of specific markers of cell adhesion and differentiation at protein level

The concentration of molecular markers of cell adhesion and osteogenic differentiation was estimated by the enzyme-linked immunosorbent assay (ELISA). The markers of cell adhesion again included talin and vinculin, and the markers of osteogenic cell differentiation included collagen type I (Coll I) (an early marker), alkaline phosphatase (ALP) (a middle marker) and osteocalcin (Ocn) (a late marker). The concentration of all these markers was measured per mg of protein in homogenates of MG-63 cells and Saos-2 cells harvested on day 14 of cultivation. The total protein content was measured using a method developed by Lowry et al. [31], and the detailed protocol of ELISA was reported in our earlier studies [19,32].

2.7. Statistical analysis

The quantitative data were presented as the mean \pm S.D. (standard deviation). The statistical significance of the differences between the compared experimental groups was evaluated using the One Way Analysis of Variance (ANOVA), Student–Newman–Keuls method (SigmaStat for Windows, version 3.5 (Systat Software, Inc., San Jose, CA, USA)). *P* values equal to or < 0.05 were considered significant.

3. Results

3.1. Morphology and physicochemical properties of the scaffolds

In nanofibrous meshes, SEM revealed mainly straight and randomly distributed fibers ranging in diameter from 293 ± 167 nm to 466 ± 498 nm (mean \pm S.D.). The thickness of the fibers within the same sample was inhomogeneous, i.e. the minimum fiber diameter values ranged from 10 nm to 60 nm, while the maximum values reached from 1590 nm to 6140 nm (Figs. 1 and 2). However, the box plot indicates that the majority of the data is in a similar range in all tested groups of samples. The growing quantity of DNPs results in a higher maximum of the fiber diameter (Fig. 2). Material clusters, which formed mainly due to the aggregation of DNPs, were present predominantly in the nanofibrous meshes with the highest DNP concentration. However, small material clusters were also present in the

pure PLLA meshes (Fig. 1A, G).

The infrared absorbance spectra of selected PLLA nanofibers (zero, medium and the highest concentration of DNPs) revealed almost identical vibration fingerprints. A detailed description of the peaks and bands is documented in the supplementary data (Fig. S1).

Results of the Raman spectra of the nanofibrous PLLA scaffolds showed dependence on the diamond concentration in the PLLA in the broad luminescence background, as shown in the supplementary data (Fig. S2). The water drop contact angle increased from 45° to 139° with increasing DNP concentration, i.e. the addition of DNPs increased the hydrophobicity of the scaffolds (Table 2). More detailed descriptions of these approaches and their results are given in the supplementary data.

3.2. An evaluation of the potential cytotoxicity of the PLLA scaffolds

Staining the cells with the LIVE/DEAD Cell Viability Cytotoxicity kit on day 3 after seeding (Fig. 3) revealed that the number of MG-63 cells was basically similar in standard polystyrene cell culture wells, in pure PLLA scaffolds, and in scaffolds with a concentration of DNPs up to 1.72 wt%. These cells were mostly viable, well-spread and mostly polygonal in shape. However, from a concentration of 3.38 wt% of DNPs in the scaffolds, even the viable cells showed signs of detachment and their number decreased significantly in comparison with the standard tissue culture polystyrene. The lowest number of viable cells was observed on scaffolds with 12.28 wt% of DNPs (Fig. 3).

The number of Saos-2 cells on all tested materials was generally lower than the number of MG-63 cells (Fig. 3). At the same time, the number of Saos-2 cells was significantly lower on all types of nanofibrous scaffolds than in the polystyrene wells, and the cells were relatively poorly spread, being mostly rounded and with a smaller cell-material projected area.

The cell number and the cell viability were further estimated by the activity of mitochondrial enzymes, measured by the XTT test (Fig. 4). In MG-63 cells, the mitochondrial activity was significantly lower on all DNP-containing samples than on the pure PLLA membrane, whereas in Saos-2 cells, there was no difference in the mitochondrial activity of cells between the pure PLLA membrane and the sample with the lowest amount of DNPs (0.44 wt%). However, the mitochondrial activity of Saos-2 cells on the pure PLLA membrane was lower than on polystyrene, while in MG-63 cells, this value was similar as on polystyrene.

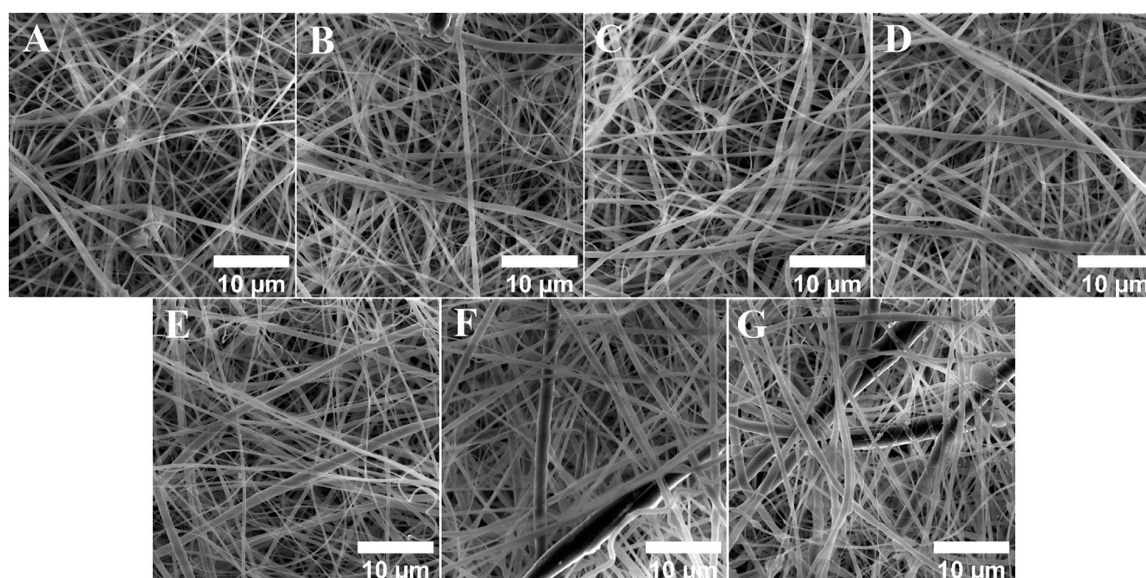


Fig. 1. Morphology of nanofibrous PLLA scaffolds with increasing concentrations of diamond nanoparticles: 0 wt% (A), 0.44 wt% (B), 0.87 wt% (C), 1.72 wt% (D), 3.38 wt% (E), 6.54 wt% (F) and 12.28 wt% (G). MAIA Tescan scanning electron microscope (Brno, Czech Republic), original magnification $500\times$, bar = 10 μm .

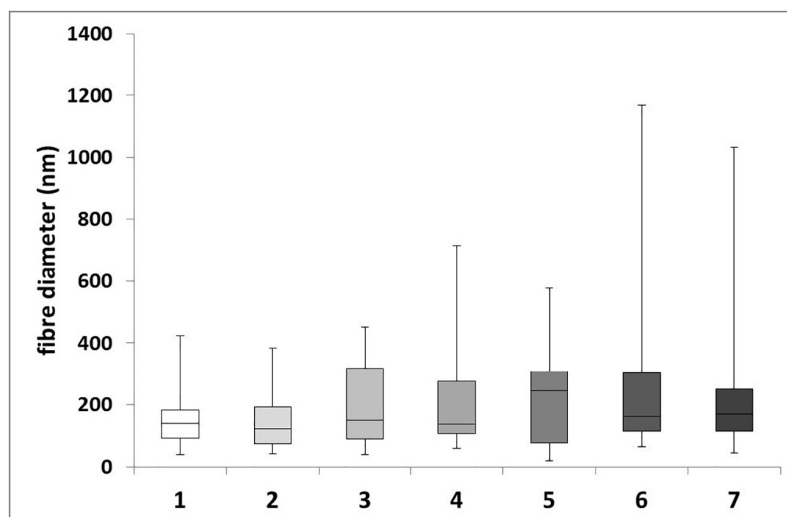


Fig. 2. Distribution of diameters of fibers of nanofibrous PLLA scaffolds with increasing concentrations of diamond nanoparticles: 0 wt% (1), 0.44 wt% (2), 0.87 wt% (3), 1.72 wt% (4), 3.38 wt% (5), 6.54 wt% (6) and 12.28 wt% (7).

Table 2

The static water drop contact angle of nanofibrous PLLA scaffolds with various concentrations of diamond nanoparticles (DNPs).

Sample label	Concentration of DNPs per pure PLLA (wt%)	Water drop contact angle (°)
1	0	51
2	0.44	45
3	0.87	70
4	1.72	129
5	3.38	133
6	6.54	127
7	12.28	130, 139
-	PLGA with 23 wt% of DNPs ^a	~70
-	Pure PLGA ^a	~70

^a For comparison, data from our earlier study [7] are provided.

Moreover, in Saos-2 cells, a significant drop in the mitochondrial activity in comparison with the sample containing 0.44 wt% of DNPs started already from the sample with 0.87 wt% of DNPs, while in MG-63 cells, the drop began from the sample with 3.38 wt% of DNPs (Fig. 4).

3.3. Gene expression of proteins involved in cell cycle regulation and apoptosis

In addition to biochemical and microscopic evaluations of the biocompatibility of the PLLA scaffolds, the gene expression of the proteins regulating the cell cycle progression and apoptosis was also evaluated at mRNA level using real-time PCR. These molecules included cyclin D, survivin and Bcl-2, i.e. factors supporting cell growth and survival, and Krueppel-like factor 6, a factor suppressing cell proliferation.

Cyclin D is synthesized during the G1 phase of the cell cycle, and drives the G1/S phase transition. The gene expression of cyclin D in MG-63 cells growing on pure PLLA nanofibers was comparable with the values in the cells growing on nanofibers loaded with DNPs up to a concentration of 6.54 wt% (Fig. 5). On nanofibers with 0.87 and 3.38 wt% of DNPs, the expression was even higher than on the nanofibers with the lowest DNP concentration. At the highest DNP concentration, the expression decreased to values significantly lower than for all other tested samples. In Saos-2 cells, the gene expression of cyclin D on samples with 0.44 to 6.54 wt% of DNPs was significantly lower than on pure PLLA samples, and on samples with the highest DNP

concentration of 12.28 wt%, this expression was significantly lower than on all other tested samples (Fig. 5A, B).

Survivin, encoded by the BIRC5 gene, is an inhibitor of caspase activation and apoptosis. The gene expression of survivin was mostly lower in the cells on DNP-loaded nanofibrous scaffolds than in the cells on the pure PLLA scaffolds. Only in MG-63 cells on scaffolds with 3.38 wt% of DNPs (Fig. 5C), and in Saos-2 cells on scaffolds with 0.87 and 6.54 wt% of DNPs (Fig. 5D), the mRNA expression level of survivin was relatively unchanged.

Bcl-2 is an important anti-apoptotic protein, which promotes cell survival by inhibiting the actions of pro-apoptotic proteins. The gene expression of Bcl-2 in MG-63 on DNP-loaded PLLA nanofibers was similar to, or even higher than, the expression in cells on pure PLLA nanofibers, namely on nanofibers with 0.87 wt% of DNPs, and even on nanofibers with a relatively high concentration of DNPs of 6.54 wt% (Fig. 5). In Saos-2 cells, the expression of Bcl-2 was also higher in the cells on nanofibers with a DNP concentration from 0.44 to 6.54 wt% than on the pure PLLA nanofibers, but after an initial increase on nanofibers with 0.87 wt% of DNPs, the expression of Bcl-2 decreased significantly with increasing DNP concentration. On the membranes with 12.28 wt% of DNPs, this expression became equal to the values in the cells on the pure PLLA scaffolds (Fig. 5E, F).

Krueppel-like factor 6, encoded by KLF6, is a transcription factor postulated as a tumor suppressor, i.e. a suppressor of cell growth. The expression of KLF6 showed a pattern surprisingly similar to the expression of Bcl-2, particularly in MG-63 cells. In these cells, it reached two maxima, at 0.87 wt% and at 6.54 wt% of DNPs, and was significantly higher than on the pure PLLA scaffolds (Fig. 5). In Saos-2 cells, the maximal expression of KLF6 was found on scaffolds with the lowest DNP concentration (0.44 wt%), and then this expression decreased with increasing DNP concentration to values significantly lower than on the pure PLLA scaffolds (at 6.54 wt% and 12.28 wt% of DNPs; Fig. 5G, H).

3.4. Markers of cell adhesion

The gene expression of talin both in MG-63 cells and in Saos-2 cells cultured on PLLA nanofibers with the lowest concentration of DNPs (0.44 wt%) was higher than in the cells on pristine PLLA nanofibers (Fig. 6A, B). However, the talin expression then decreased significantly in comparison with the sample containing 0.44 wt% of DNPs in both MG-63 and Saos-2 cells. In Saos-2 cells on samples with the highest

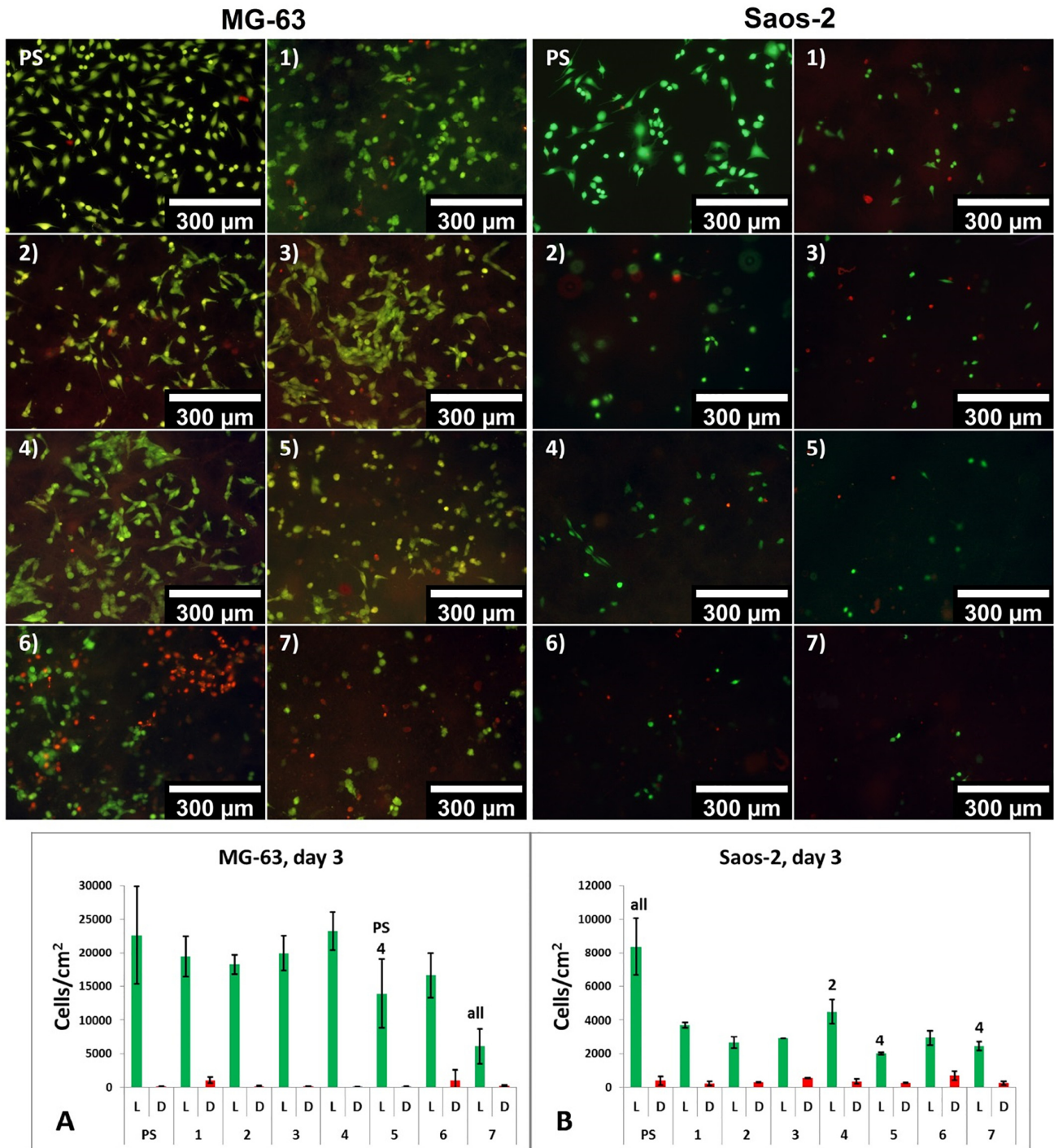


Fig. 3. Images: morphology and viability of human osteoblast-like cells MG-63 (left side, A) and Saos-2 (right side, B) on day 3 after seeding in standard cell culture polystyrene wells (PS) and on PLLA nanofibrous scaffolds with increasing concentrations of diamond nanoparticles: 0 wt% (1), 0.44 wt% (2), 0.87 wt% (3), 1.72 wt% (4), 3.38 wt% (5), 6.54 wt% (6) and 12.28 wt% (7). The cells were stained with a LIVE/DEAD Cell Viability Cytotoxicity kit (Life Technologies). Live cells are stained in green, and dead or dying cells are stained in red. Images were acquired with an Olympus IX 51 microscope, obj. 10×, DP 70 Olympus camera, scale bar = 100 µm. Graphs: The number of live (L, green) and dead/dying (D, red) cells per cm² in 3-day cultures on cell culture polystyrene wells and on PLLA. Mean ± S.D. from 3 experiments performed in triplicate. Statistical significance was evaluated by ANOVA with the Student-Newman-Keuls post hoc test. Statistical significance level: $P \leq 0.05$. (For interpretation of the references to color in this figure legend, the reader is referred to the web version of this article.)

concentration of DNPs (12.28 wt%), the talin expression became significantly lower than on all other groups of tested samples.

The dependence of the gene expression of vinculin on the DNP concentration was more complicated and rather biphasic. In MG-63

cells, the vinculin expression in cells on scaffolds with low concentrations of DNP (0.44 and 0.87 wt%) was similar as on the pure PLLA scaffolds. The expression then decreased significantly (at a DNP concentration of 1.72 wt%), then increased again, and finally decreased on

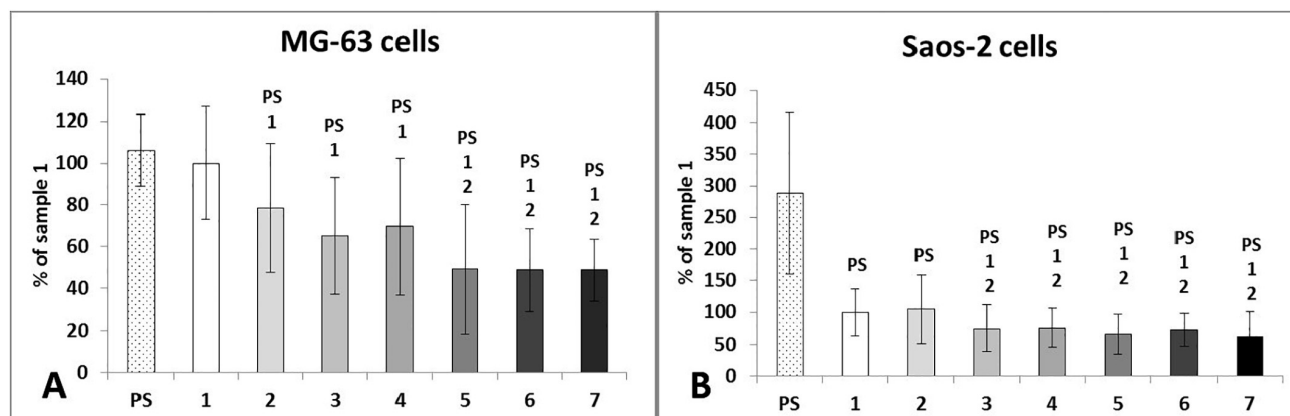


Fig. 4. Cell mitochondrial activity of human osteoblast-like cells measured by an XTT test on day 3 after seeding on MG-63 (A) and Saos-2 (B) cells lines cultivated on polystyrene dishes (PS) and PLLA nanofibrous membranes loaded with different concentrations of DNPs: 0 wt% (1), 0.44 wt% (2), 0.87 wt% (3), 1.72 wt% (4), 3.38 wt% (5), 6.54 wt% (6) and 12.28 wt% (7). The plotted values are the means of the absorbances \pm S.D. (from 17 to 21 values obtained from 4 independent experiments) related to the pure PLLA membranes (sample 1). Statistical significance was evaluated by ANOVA with the Student-Newman-Keuls post hoc test. Statistical significance level: $P \leq 0.05$.

the scaffolds with the highest DNP concentrations (6.34 and 12.28 wt %). A similar behavior was observed in Saos-2 cells. The vinculin expression decreased up to a concentration of 1.72 wt%, then increased, and at the highest concentration of DNPs (12.28 wt%), it finally decreased (Fig. 6A, B).

In spite of the remarkable differences found in the gene expression at mRNA level, the amount of talin and vinculin at protein level was not significantly influenced by the concentration of DNPs in almost all scaffolds in comparison with the pure PLLA scaffolds. The ELISA measurement results indicated that the concentrations of talin and vinculin in the MG-63 cells were similar on all samples. The only significant difference found in Saos-2 cells was in the amount of vinculin on the sample with the highest concentration of DNPs (12.28 wt%), which was lower than for most of DNP-containing samples (Fig. 6C, D).

3.5. Osteogenic differentiation

The expression of the collagen I gene in MG-63 cells decreased with increasing DNP concentration (Fig. 7A). In Saos-2 cells, the expression of collagen I first increased significantly in the cells on the scaffolds with DNP concentrations from 0.87 to 1.72 wt% in comparison with pristine scaffolds and scaffolds with lower DNP concentrations, but then decreased, and at the highest DNP concentration (12.28 wt%), the level decreased significantly below the values measured on the pure PLLA scaffolds. Similar results were also observed for the expression of osteocalcin in Saos-2 cells on scaffolds with the same DNP concentrations. However, the ALP expression in Saos-2 cells had a clear decreasing trend with increasing DNP concentration, which was apparent at higher DNP concentrations. At DNP concentrations of 3.38 and 6.54 wt%, the ALP expression was significantly lower than on scaffolds with 0 and 0.44 wt% of DNPs, and at the highest DNP concentration of 12.28 wt%, the ALP expression was significantly lower than on scaffolds with 0–3.38 wt% of DNPs (Fig. 6B). ALP and osteocalcin markers were measurable only in Saos-2 cells, which are a better model of osteogenic cell differentiation than MG-63 cells [21,22], where the concentrations of both markers were very low and at the limit of detection. They were therefore omitted in our graphs.

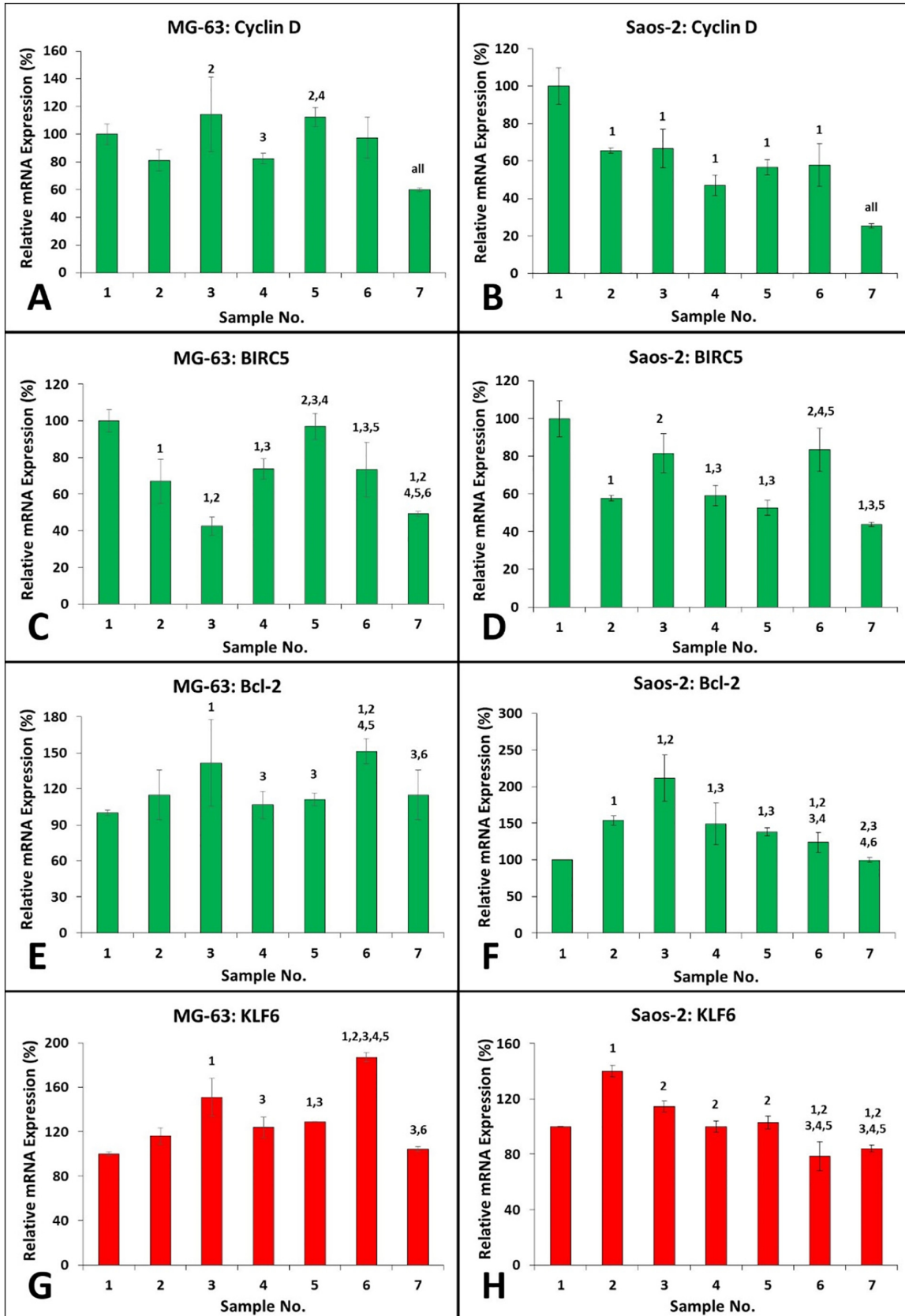
The concentrations of collagen I and alkaline phosphatase at protein level were similar in MG-63 cells on PLLA nanofibrous membranes with all concentrations of DNPs (Fig. 7C). In Saos-2 cells, the amount of collagen I was even significantly higher on the PLLA scaffolds with 3.38–12.28 wt% of DNPs. Similarly, the concentration of ALP protein was higher in Saos-2 cells on the membranes with 1.72 and 6.54 wt% of

DNPs (Fig. 7D), despite its lower expression on mRNA level (Fig. 7B). The concentration of osteocalcin, a marker of late osteogenic differentiation, decreased in MG-63 cells on scaffolds with medium and higher DNP concentrations (Fig. 7C), while in Saos-2 cells the amount of osteocalcin remained similar in the cells on scaffolds with all DNP concentrations (Fig. 7D).

4. Discussion

In this study, we created PLLA nanofibrous scaffolds with an increasing concentration of diamond nanoparticles (from 0 to 12.28 wt %). We found that an increasing concentration of DNPs in the PLLA nanofibrous scaffolds (from 0 to 12.28 wt%) had a negative effect on the viability, proliferation and mitochondrial activity of both human osteoblast-like cells lines used in this study. The number of living cells on the scaffolds and the activity of mitochondrial enzymes measured on the 3rd day of cultivation decreased progressively with increasing DNP concentration. The negative effect was more pronounced in Saos-2 cells, as the number of living cells after 3-day cultivation on the scaffolds was apparently lower than the number of living MG-63 cells (Fig. 3). We decided to identify the cause of this drop in cell viability, and we therefore investigated the expression of survival markers, cell adhesion markers and cell differentiation markers at mRNA level. In addition, the expression of the adhesion and differentiation markers was also evaluated at protein level.

First, we evaluated the expression of genes regulating the cell cycle, proliferation and apoptosis. The decrease in the expression of cyclin D, i.e. a protein stimulating the cell cycle progression, observed particularly in Saos-2 cells, is in good correlation with the decrease in the number of living cells, and particularly with the decrease in cell mitochondrial activity with increasing DNP concentration. Similar effects were observed in human fibroblasts and in HEK293 cells cultured in the presence of single-wall carbon nanotubes [33] and human mesenchymal stem cells in cultures with silica nanoparticles [34]. These effects were attributed to the oxidative stress generated by these nanoparticles [34] and to disturbances in the cell membrane integrity [35]. The expression of survivin, an antiapoptotic factor, was also downregulated in MG-63 and Saos-2 cells on most DNP-loaded PLLA scaffolds in comparison with the pure PLLA scaffolds. Similarly as in the case of cyclin D, the expression of survivin was also downregulated in response to various nanoparticles, such as alginate-enclosed, chitosan-conjugated, or calcium phosphate and iron-saturated bovine lactoferrin nanocarriers/nanocapsules [36]. By contrast, the expression of Bcl-2,



(caption on next page)

Fig. 5. 1st, 2nd and 3rd row (green graphs): The gene expression of factors supporting cell cycle progression (cyclin D) and inhibition of apoptosis (encoded by BIRC5 and Bcl-2 gene). 4th row (red graphs): gene expression of the anti-proliferative tumor suppressor KLF6 gene. All markers were measured for MG-63 and Saos-2 cells on PLLA scaffolds with various concentrations of diamond nanoparticles: 0 wt% (1), 0.44 wt% (2), 0.87 wt% (3), 1.72 wt% (4), 3.38 wt% (5), 6.54 wt% (6) and 12.28 wt% (7). The mRNA concentrations were measured 14 days after cell seeding, and were expressed as a % of the value obtained on pure PLLA (sample 1). The plotted values are the means ± S.D. of 4–5 experimental points obtained from 2 independent experiments. The statistical significance was evaluated by ANOVA with the Student-Newman-Keuls post hoc test. Numbers above the columns indicate statistical significance with P value ≤ 0.05. (For interpretation of the references to color in this figure legend, the reader is referred to the web version of this article.)

another anti-apoptotic factor, was similar or even higher in the cells on DNP-loaded scaffolds than on pure PLLA scaffolds, which suggested a certain resistance of the cells, particularly MG-63 cells, to the damage caused by DNPs. Similarly, fullereneol C₆₀(OH)₂₄ nanoparticles, which are promising anti-oxidative agents, also increased the Bcl-2 expression in irradiated K562 leukemic cells, and thus rendered these cells more tolerant to radiotherapy [37]. In Saos-2 cells on scaffolds with 0.87 to 12.28 wt% of DNPs, the Bcl-2 decreased with increasing DNP concentration, which suggests increased propensity of these cells to apoptosis. Apoptotic cell death, manifested by a decrease in Bcl-2 expression, was observed in human HeLa cells exposed to TiO₂ nanofibers [38], where this was attributed to oxidative stress, and in human lung cancer H1299 cells exposed to silver nanoparticles [39]. The expression of KLF6, a tumor suppressor, was also similar or even higher in cells on DNP-loaded scaffolds than on pure PLLA scaffolds. In this context, it should be pointed out that both MG-63 cells and Saos-2 cells are p53-deficient. In a study by Gehrau et al. [30], performed on a profiling array of cancer cell lines exposed to a variety of cell damaging stimuli at

growth inhibitory concentrations, KLF6 expression was significantly increased in 63% of the p53-deficient cell lines, and was decreased in > 70% of the p53-positive cells. High intensity of cell damage caused a p53-independent down-regulation of the KLF6 gene. In accordance with this, the expression of KLF6 in Saos-2 cells on the scaffolds with the highest concentrations of DNPs decreased below the level observed in cells on the pure PLLA scaffolds. Saos-2 cells are considered to be more differentiated and better resembling normal human osteoblasts [21,22]. They were therefore probably more sensitive than MG-63 cells to damage by DNPs.

Another phenomenon that could have influenced the cell survival on the scaffolds was cell adhesion. The focal adhesion protein talin plays a key role during inside-out signaling, namely in regulating the cell adhesion by binding to the cytoplasmic tail of the β-integrin subunit, and in this way, it allosterically regulates the affinity of integrins to their ligands in ECM molecules [40]. The decrease in the mRNA expression of talin in Saos-2 cells was proportional to the increase in the DNP concentration. The expression of talin in Saos-2 cells was higher

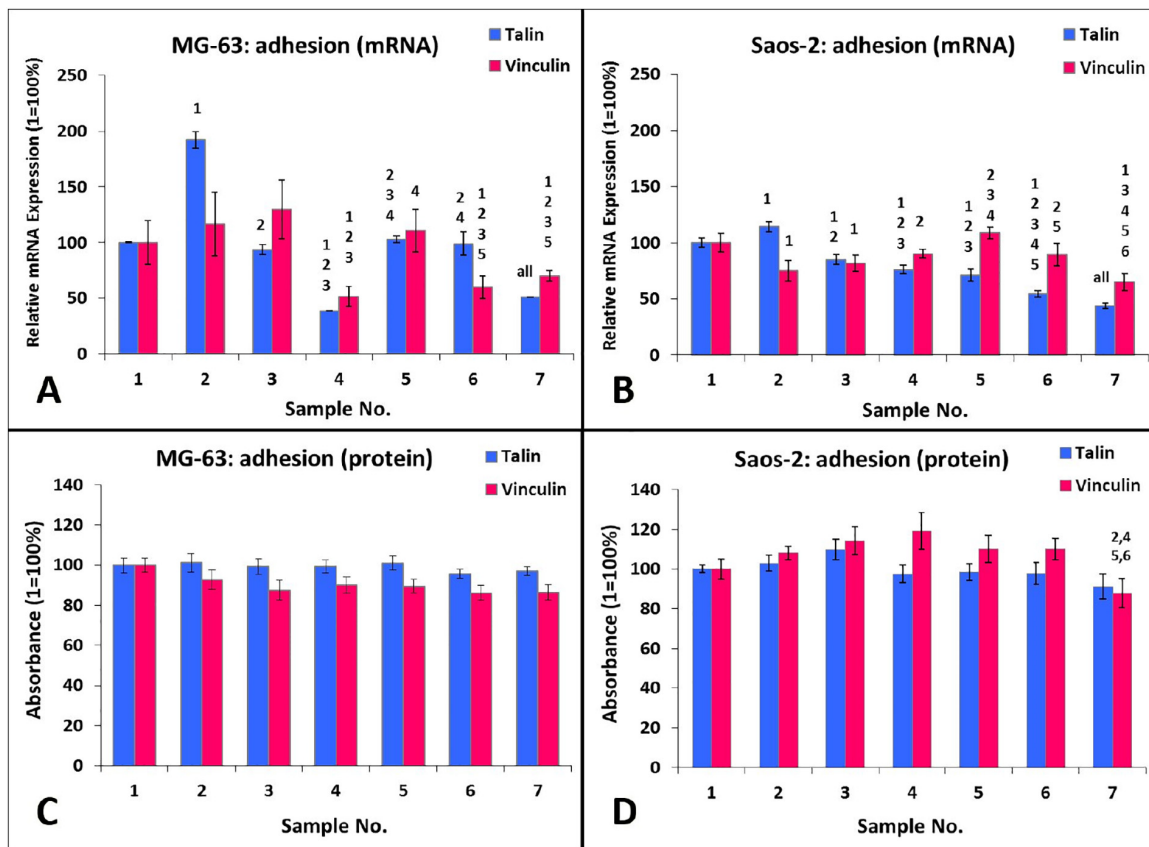


Fig. 6. Markers of cell adhesion measured 14 days after cell seeding: talin and vinculin gene expression measured by RT-PCR (upper row) and concentrations of talin and vinculin proteins measured by the ELISA assay (lower row) in MG-63 cells (left column) and in Saos-2 cells (right column) cultured on the PLLA nanofibrous membrane with different concentrations of diamond nanoparticles: 0 wt% (1), 0.44 wt% (2), 0.87 wt% (3), 1.72 wt% (4), 3.38 wt% (5), 6.54 wt% (6) and 12.28 wt% (7). The plotted values are the means ± S.D. of 4–5 experimental points obtained from 2 independent experiments. The values were expressed as a % of the value obtained on pure PLLA (sample 1). Statistical significance was evaluated by ANOVA with the Student-Newman-Keuls post-hoc test. Numbers above the columns indicate statistical significance with P value ≤ 0.05.

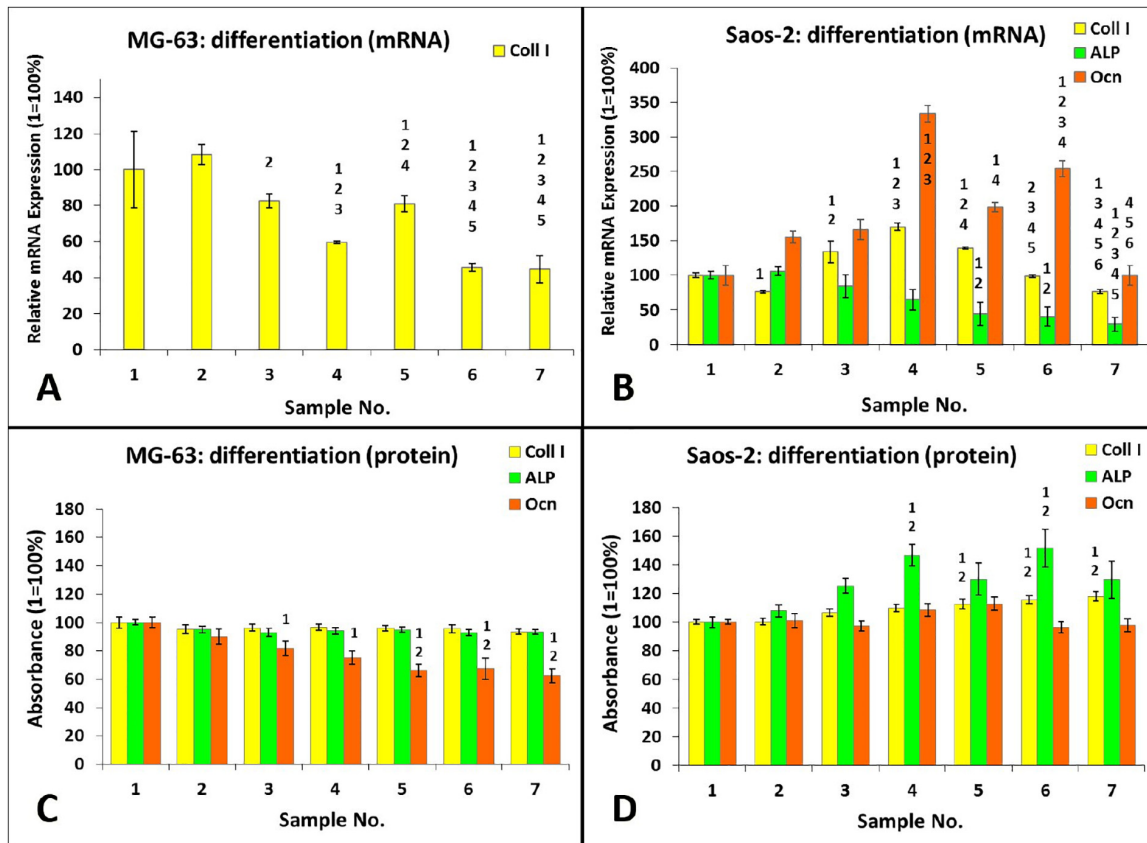


Fig. 7. Markers of cell differentiation measured 14 days after cell seeding: expression of the collagen I gene, the ALP gene (only in Saos-2) and the osteocalcin gene (only in Saos-2), measured by RT-PCR (upper row), and the concentrations of collagen I, ALP and osteocalcin proteins measured by the ELISA assay (lower row) in MG-63 cells (left column) and Saos-2 cells (right column) cultured on the PLLA nanofibrous membrane with different concentrations of diamond nanoparticles: 0 wt% (1), 0.44 wt% (2), 0.87 wt% (3), 1.72 wt% (4), 3.38 wt% (5), 6.54 wt% (6) and 12.28 wt% (7). The plotted values are the means \pm S.D. of 4–6 experimental points obtained from 2 independent experiments. The values were expressed as a % of the value obtained on pure PLLA (sample 1). Statistical significance was evaluated by ANOVA with the Student-Newman-Keuls post-hoc test. Numbers above the columns indicate statistical significance with P value \leq 0.05.

than on pure PLLA scaffolds only at the lowest DNP concentration (0.44 wt%). Similarly, the expression of vinculin in Saos-2 cells was higher on scaffolds with a medium concentration of DNPs (3.38 wt%) than on scaffolds with lower DNP concentrations. This could be explained by the increased stiffness of the PLLA-DNP scaffolds, which could improve the cell adhesion. In our earlier study, the formation of talin- and vinculin-containing plaques in MG-63 cells was better on DNP-loaded nanofibrous PLLA scaffolds than on pure scaffolds [7]. At higher nanoparticle concentrations, the adverse effects of DNPs probably prevailed over their beneficial effects on cell adhesion.

Surprisingly, the concentrations of talin and vinculin at protein level did not differ significantly from the control pure PLLA membrane in both cell types, with the exception of the concentration of vinculin in Saos-2 cells on scaffolds with 12.28 wt% of DNPs, which was significantly lower than on most DNP-loaded PLLA scaffolds. The proportions between the expression of focal adhesion proteins at mRNA level and at protein level can be explained by the fact that the expression at mRNA level reflects the current status of gene expression in a cell, while the total amount of a protein in a cell is usually a result of long-term accumulation.

Nevertheless, it can be summarized that the expression of talin and vinculin both on mRNA level and on protein level responded more sensitively to the increasing concentration of DNPs in Saos-2 cells than in MG-63 cells. In MG-63 cells, the dependence of the mRNA expression of both focal adhesion proteins on the DNP concentration was less regular, and there were no significant differences at protein level. In

addition, the adhesion and growth of Saos-2 cells was more dependent on the morphology of the adhesion substrate. The number and the spreading of Saos-2 cells on the pure nanofibrous PLLA scaffolds were significantly lower than on the control flat polystyrene dishes, while in MG-63 cells, these parameters were similar on both cultivation substrates. Therefore, MG-63 cells seem to be more stable in cell adhesion than Saos-2 cells.

The last possible reason studied here for the drop in cell viability and mitochondrial activity corresponding with the DNP concentration could be a progressive process of cell differentiation that could result in slowing down cell proliferation. The expression of the mRNA for the first studied osteogenic marker, collagen type I, decreased slowly in MG-63 cells with the DNP concentration, whereas in Saos-2 cells this marker rose up to 150% of the pure PLLA sample on sample 4 (1.72 wt % of DNPs). Together with the increase in osteocalcin expression in Saos-2 cells, which was even more pronounced, and with the rising concentration of alkaline phosphatase at least on the protein level, this could indicate that the cells were undergoing osteogenic differentiation. On the other hand, in studies by other authors, collagen I was produced by cells during foreign body reaction, wound healing and encapsulation of implants with less appropriate physical and chemical properties. For example, increased deposition of collagen has been observed around polymeric meshes for hernia repair [41] and in gingival fibroblasts after microplasma irradiation [42]. Therefore, it cannot be excluded that the expression of the collagen gene was produced by Saos-2 cells in our study, in response to the damaging effect of their growth support, rather

than as a marker of osteogenic cell differentiation. The reaction of the MG-63 cells on mRNA level or on protein level did not indicate any significant osteogenic differentiation.

A possible explanation for our rather negative results is the relatively high hydrophobicity of our PLLA-DNP scaffolds, which increased with increasing DNP concentration. In our scaffolds with 0.44 to 12.28 wt% of DNPs, the water drop contact angle ranged from 45° to 139°. By contrast, in PLGA scaffolds with 23 wt% of DNPs in our earlier studies, the water drop contact angle was only about 70°, which can be considered as a moderate level of hydrophilicity, optimal for cell adhesion and growth [7].

Another explanation is the potential cytotoxicity of the DNPs used in our study. The damaging effect of DNPs on cells depends on their origin, size, impurities and functionalization. In studies reporting adverse effects of DNPs, these nanoparticles were often prepared by detonation [43–45]. In our present study, too, the DNPs were of detonation origin. In other studies with non-toxic or even beneficial effects of DNPs on cell behavior, the DNPs were prepared by non-detonation methods, e.g. by milling of diamond microcrystals [10,46], or by the radiofrequency PACVD method, which was used in our earlier studies [6,7]. The detonation DNPs used in our present study were relatively small in diameter (4–5 nm) and were grayish in color, which suggested the presence of impurities. In a study by Keremidarska et al. [45], increased cytotoxicity of DNPs was associated with their smaller size and with the presence of impurities, such as other carbon allotropes and metals. In addition, the detonation DNPs used in our study had positive zeta potential [47]. It has been reported that positively-charged nanoparticles in general showed a higher cellular uptake and greater subsequent damage to subcellular structures than negatively-charged nanoparticles (for a review, see [47]). The biocompatibility of detonation DNPs can be improved by annealing at high temperature, which oxidizes these DNPs and changes their surface charge from positive to negative [47]. Other possible ways to achieve improvements include functionalization of detonation DNPs with various chemical groups or molecules, such as oxygen-containing groups (hydroxyl and carboxyl groups) or serum proteins (for a review, see [48]).

5. Conclusions

The nanofibrous PLLA-DNP scaffolds prepared in this study had rather negative effects on the adhesion, growth and osteogenic differentiation of human osteoblast-like MG-63 and Saos-2 cells. The number, spreading, viability and the mitochondrial activity of these cells decreased with an increasing concentration of DNPs in the scaffolds (from 0.44 to 12.28 wt%). In accordance with this, the expression of cyclin D and survivin, i.e. factors supporting cell growth and survival, were downregulated on DNP-loaded PLLA scaffolds. The expression of KLF6, a tumor suppressor, was mostly similar or even higher in cells on DNP-loaded scaffolds than on the pure PLLA scaffolds. However, the expression of Bcl-2, an antiapoptotic factor, was also similar or even higher in cells on DNP-loaded scaffolds. This suggested only a moderate cell damaging effect of the DNP-loaded scaffolds in this study.

The expression of mRNA for focal adhesion proteins vinculin and particularly talin decreased significantly on scaffolds with the highest DNP concentration (12.28 wt%) in comparison with the pure PLLA scaffolds and most of the DNP-loaded scaffolds. However, on scaffolds with the lowest DNP concentration (0.44 wt%), the expression of talin was even higher than on the pure PLLA scaffolds. This suggests a certain supportive effect of DNPs on the cell adhesion by increasing the stiffness of the scaffolds. Similarly, the expression of collagen I and osteocalcin at mRNA level, and collagen I and ALP at protein level, was increased in Saos-2 cells on the scaffolds with medium and high DNP concentrations. However, this could be due to the response of the cells to the cytotoxicity of the material, rather than due to osteogenic cell differentiation. Moreover, MG-63 cells showed impaired rather than improved osteogenic differentiation on DNP-loaded scaffolds.

In general, we can see a decrease in the mRNA expression of all studied markers of osteogenic cell differentiation at the highest DNP concentration (12.28 wt%). It can therefore be concluded that the detonation 4–5 nm DNPs in the PLLA nanofibrous scaffolds used in our study had a damaging effect on human osteoblast-like MG-63 and Saos-2 cells.

Acknowledgements

This study was supported by the Grant Agency of the Czech Republic (“Center of Excellence”, grant No. P108/12/G108). We gratefully acknowledge Pavla Bauerova and Rayisa Yatskiv (Institute of Physics of the Czech Academy of Sciences) for preparing samples and SEM measurements, and Mr. Robin Healey (Czech Technical University in Prague) for his language revision of the manuscript.

Appendix A. Supplementary data

Supplementary data to this article can be found online at <https://doi.org/10.1016/j.diamond.2019.05.007>.

References

- [1] V.R. Hokmabad, S. Davaran, M. Aghazadeh, E. Alizadeh, R. Salehi, A. Ramazani, A comparison of the effects of silica and hydroxyapatite nanoparticles on poly(ϵ -caprolactone)-poly(ethylene glycol)-poly(ϵ -caprolactone)/chitosan nanofibrous scaffolds for bone tissue engineering, *Tissue Eng. Regen. Med.* 15 (2018) 735–750, <https://doi.org/10.1007/s13770-018-0140-z>.
- [2] K. Novotna, M. Zajdlova, T. Suchy, D. Hadraba, F. Lopot, M. Zaloudkova, T.E.L. Douglas, M. Munzarova, M. Juklickova, D. Stranska, D. Kubies, D. Schaubroeck, S. Wille, L. Balcaen, M. Jarosova, H. Kozak, A. Kromka, Z. Svindrych, V. Lisa, K. Balik, L. Bacakova, Poly(lactide nanofibers with hydroxyapatite as growth substrates for osteoblast-like cells: cells on PLA/HA nanofibers, *J. Biomed. Mater. Res. A* 102 (2014) 3918–3930, <https://doi.org/10.1002/jbm.a.35061>.
- [3] C. Burger, B. Chu, Functional nanofibrous scaffolds for bone reconstruction, *Colloids Surf. B: Biointerfaces* 56 (2007) 134–141, <https://doi.org/10.1016/j.colsurfb.2006.09.023>.
- [4] W. Liu, J. Wei, Y. Chen, P. Huo, Y. Wei, Electrospinning of poly(L-lactide) nanofibers encapsulated with water-soluble fullerenes for bioimaging application, *ACS Appl. Mater. Interfaces* 5 (2013) 680–685, <https://doi.org/10.1021/am400037s>.
- [5] S. Duan, X. Yang, F. Mei, Y. Tang, X. Li, Y. Shi, J. Mao, H. Zhang, Q. Cai, Enhanced osteogenic differentiation of mesenchymal stem cells on poly(L-lactide) nanofibrous scaffolds containing carbon nanomaterials: enhanced osteocompatibility of nanofibrous scaffolds, *J. Biomed. Mater. Res. A* 103 (2015) 1424–1435, <https://doi.org/10.1002/jbm.a.35283>.
- [6] M.A. Brady, A. Renzing, T.E.L. Douglas, Q. Liu, S. Wille, M. Parizek, L. Bacakova, A. Kromka, M. Jarosova, G. Godier, P.H. Warnke, Development of composite poly(lactide-co-glycolide)-nanodiamond scaffolds for bone cell growth, *J. Nanosci. Nanotechnol.* 15 (2015) 1060–1069, <https://doi.org/10.1166/jnn.2015.9745>.
- [7] M. Parizek, T.E. Douglas, A. Kromka, M.A. Brady, A. Renzing, E. Voss, J. Marketa, L. Palatinus, P. Tesarek, P. Ryparova, V. Lisa, A.M. dos Santos, L. Bacakova, Nanofibrous poly(lactide-co-glycolide) membranes loaded with diamond nanoparticles as promising substrates for bone tissue engineering, *Int. J. Nanomedicine* (2012) 1931–1951, <https://doi.org/10.2147/IJN.S26665>.
- [8] M. Mahdavi, N. Mahmoudi, F. Rezaie Anaran, A. Simchi, Electrospinning of nanodiamond-modified polysaccharide nanofibers with physico-mechanical properties close to natural skins, *Mar. Drugs* 14 (2016) 128, <https://doi.org/10.3390/md14070128>.
- [9] Q. Zhang, V.N. Mochalin, I. Neitzel, I.Y. Knoke, J. Han, C.A. Klug, J.G. Zhou, P.I. Lelkes, Y. Gogotsi, Fluorescent PLLA-nanodiamond composites for bone tissue engineering, *Biomaterials* 32 (2011) 87–94, <https://doi.org/10.1016/j.biomaterials.2010.08.090>.
- [10] Z. Xing, T.O. Pedersen, X. Wu, Y. Xue, Y. Sun, A. Finne-Wistrand, F.R. Kloss, T. Waag, A. Krueger, D. Steinmüller-Nethl, K. Mustafa, Biological effects of functionalizing copolymer scaffolds with nanodiamond particles, *Tissue Eng. A* 19 (2013) 1783–1791, <https://doi.org/10.1089/ten.tea.2012.0336>.
- [11] R.G. Stigler, M.M. Schimke, S. Bigus, D. Steinmüller-Nethl, K. Tillmann, G. Lepperding, Pervasion of beta-tricalcium phosphate with nanodiamond particles yields efficient and safe bone replacement material amenable for biofunctionalization and application in large-size osseous defect healing, *Nanomedicine* 16 (2019) 250–257, <https://doi.org/10.1016/j.nano.2018.08.015>.
- [12] L. Bacakova, A. Broz, J. Liskova, L. Stankova, S. Potocky, A. Kromka, The application of nanodiamond in biotechnology and tissue engineering, in: M. Aliofkhaeaei (Ed.), *Diamond and Carbon Composites and Nanocomposites*, Intech, 2016, <https://doi.org/10.5772/63549>.
- [13] L. Grausova, L. Bacakova, A. Kromka, M. Vanecek, B. Rezek, V. Lisa, Molecular markers of adhesion, maturation and immune activation of human osteoblast-like MG 63 cells on nanocrystalline diamond films, *Diam. Relat. Mater.* 18 (2009)

- 258–263, <https://doi.org/10.1016/j.diamond.2008.10.023>.
- [14] S.A. Skoog, G. Kumar, J. Zheng, A.V. Sumant, P.L. Goering, R.J. Narayan, Biological evaluation of ultrananocrystalline and nanocrystalline diamond coatings, *J. Mater. Sci. Mater. Med.* 27 (2016) 187, <https://doi.org/10.1007/s10856-016-5798-y>.
- [15] J. Liskova, O. Babchenko, M. Varga, A. Kromka, D. Hadraba, Z. Svindrych, Z. Burdikova, L. Bacakova, Osteogenic cell differentiation on H-terminated and O-terminated nanocrystalline diamond films, *Int. J. Nanomedicine* (2015) 869, <https://doi.org/10.2147/IJN.S73628>.
- [16] R. Stigler, K. Becker, M. Bruschi, D. Steinmüller-Nethl, R. Gassner, Impact of nanocrystalline diamond enhanced hydrophilicity on cell proliferation on machined and SLA titanium surfaces: an in-vivo study in rodents, *Nanomaterials* 8 (2018) 524, <https://doi.org/10.3390/nano8070524>.
- [17] S. Suliman, Y. Sun, T.O. Pedersen, Y. Xue, J. Nickel, T. Waag, A. Finne-Wistrand, D. Steinmüller-Nethl, A. Krueger, D.E. Costea, K. Mustafa, In vivo host response and degradation of copolymer scaffolds functionalized with nanodiamonds and bone morphogenetic protein 2, *Adv. Healthc. Mater.* 5 (2016) 730–742, <https://doi.org/10.1002/adhm.201500723>.
- [18] M.M. Schimke, R. Stigler, X. Wu, T. Waag, P. Buschmann, J. Kern, G. Untergasser, M. Rasse, D. Steinmüller-Nethl, A. Krueger, G. Lepperding, Biofunctionalization of scaffold material with nano-scaled diamond particles physisorbed with angiogenic factors enhances vessel growth after implantation, *Nanomedicine* 12 (2016) 823–833, <https://doi.org/10.1016/j.nano.2015.11.004>.
- [19] L. Grausova, A. Kromka, Z. Burdikova, A. Eckhardt, B. Rezek, J. Vacik, K. Haenen, V. Lisa, L. Bacakova, Enhanced growth and osteogenic differentiation of human osteoblast-like cells on boron-doped nanocrystalline diamond thin films, *PLoS One* 6 (2011) e20943, <https://doi.org/10.1371/journal.pone.0020943>.
- [20] J. Clover, M. Gowen, Are MG-63 and HOS TE85 human osteosarcoma cell lines representative models of the osteoblastic phenotype? *Bone* 15 (1994) 585–591, [https://doi.org/10.1016/8756-3282\(94\)90305-0](https://doi.org/10.1016/8756-3282(94)90305-0).
- [21] L. Saldaña, F. Bensiamar, A. Boré, N. Vilaboa, In search of representative models of human bone-forming cells for cytocompatibility studies, *Acta Biomater.* 7 (2011) 4210–4221, <https://doi.org/10.1016/j.actbio.2011.07.019>.
- [22] E.M. Czekanska, M.J. Stoddart, R.G. Richards, J.S. Hayes, In search of an osteoblast cell model for in vitro research, *Eur. Cell. Mater.* 24 (2012) 1–17.
- [23] E. Ōsawa, Monodisperse single nanodiamond particulates, *Pure Appl. Chem.* 80 (2008) 1365–1379, <https://doi.org/10.1351/pac200880071365>.
- [24] H. Kozak, A. Artemenko, J. Čermák, V. Švrček, A. Kromka, B. Rezek, Oxidation and reduction of nanodiamond particles in colloidal solutions by laser irradiation or radio-frequency plasma treatment, *Vib. Spectrosc.* 83 (2016) 108–114, <https://doi.org/10.1016/j.vibspec.2016.01.010>.
- [25] S. Stehlik, M. Varga, M. Ledinsky, D. Miliaieva, H. Kozak, V. Skakalova, C. Mangler, T.J. Pennycook, J.C. Meyer, A. Kromka, B. Rezek, High-yield fabrication and properties of 1.4 nm nanodiamonds with narrow size distribution, *Sci. Rep.* 6 (2016) 38419, <https://doi.org/10.1038/srep38419>.
- [26] A. Kromka, J. Čech, H. Kozak, A. Artemenko, T. Ižák, J. Čermák, B. Rezek, M. Černák, Low-temperature hydrogenation of diamond nanoparticles using diffuse coplanar surface barrier discharge at atmospheric pressure: low-temperature hydrogenation of diamond nanoparticles, *Phys. Status Solidi B* 252 (2015) 2602–2607, <https://doi.org/10.1002/pssb.201552232>.
- [27] A. Kromka, O. Babchenko, H. Kozak, K. Hruska, B. Rezek, M. Ledinsky, J. Potmesil, M. Michalka, M. Vanecek, Seeding of polymer substrates for nanocrystalline diamond film growth, *Diam. Relat. Mater.* 18 (2009) 734–739, <https://doi.org/10.1016/j.diamond.2009.01.023>.
- [28] O.A. Williams, O. Douhéret, M. Daenen, K. Haenen, E. Ōsawa, M. Takahashi, Enhanced diamond nucleation on monodispersed nanocrystalline diamond, *Chem. Phys. Lett.* 445 (2007) 255–258, <https://doi.org/10.1016/j.cplett.2007.07.091>.
- [29] C.T. Rueden, J. Schindelin, M.C. Hiner, B.E. DeZonia, A.E. Walter, E.T. Arena, K.W. Eliceiri, ImageJ2: ImageJ for the next generation of scientific image data, *BMC Bioinforma.* 18 (2017), <https://doi.org/10.1186/s12859-017-1934-z>.
- [30] R.C. Gehrau, D.S. D'Astolfo, V. Andreoli, J.L. Bocco, N.P. Koritschoner, Differential expression of the klf6 tumor suppressor gene upon cell damaging treatments in cancer cells, *Mutat. Res. Fundam. Mol. Mech. Mutagen.* 707 (2011) 15–23, <https://doi.org/10.1016/j.mrfmmm.2010.12.002>.
- [31] O.H. Lowry, N.J. Rosebrough, A.L. Farr, R.J. Randall, Protein measurement with the Folin phenol reagent, *J. Biol. Chem.* 193 (1951) 265–275.
- [32] E. Filova, J. Fojt, M. Krysova, H. Moravec, L. Joska, L. Bacakova, The diameter of nanotubes formed on Ti-6Al-4V alloy controls the adhesion and differentiation of Saos-2 cells, *Int. J. Nanomedicine* (2015) 7145, <https://doi.org/10.2147/IJN.S87474>.
- [33] D. Cui, F. Tian, C.S. Ozkan, M. Wang, H. Gao, Effect of single wall carbon nanotubes on human HEK293 cells, *Toxicol. Lett.* 155 (2005) 73–85, <https://doi.org/10.1016/j.toxlet.2004.08.015>.
- [34] V.S. Periasamy, J. Athinarayanan, M.A. Akbarsha, A.A. Alshatwi, Silica nanoparticles induced metabolic stress through EGR1, CCND, and E2F1 genes in human mesenchymal stem cells, *Appl. Biochem. Biotechnol.* 175 (2015) 1181–1192, <https://doi.org/10.1007/s12010-014-1342-z>.
- [35] Y. Liu, W. Li, F. Lao, Y. Liu, L. Wang, R. Bai, Y. Zhao, C. Chen, Intracellular dynamics of cationic and anionic polystyrene nanoparticles without direct interaction with mitotic spindle and chromosomes, *Biomaterials* 32 (2011) 8291–8303, <https://doi.org/10.1016/j.biomaterials.2011.07.037>.
- [36] J.R. Kanwar, G. Mahidhara, K. Roy, S. Sasidharan, S. Krishnakumar, N. Prasad, R. Sehgal, R.K. Kanwar, Fe-bLf nanoformulation targets survivin to kill colon cancer stem cells and maintains absorption of iron, calcium and zinc, *Nanomedicine* 10 (2015) 35–55, <https://doi.org/10.2217/nnm.14.132>.
- [37] K. Stankov, I. Borisev, V. Kojic, L. Rutonjski, G. Bogdanovic, A. Djordjevic, Modification of antioxidative and antiapoptotic genes expression in irradiated K562 cells upon fullereneol C60(OH)24 nanoparticle treatment, *J. Nanosci. Nanotechnol.* 13 (2013) 105–113, <https://doi.org/10.1166/jnn.2013.6847>.
- [38] K.M. Ramkumar, C. Manjula, G. GnanaKumar, M.A. Kanjwal, T.V. Sekar, R. Paulmurugan, P. Rajaguru, Oxidative stress-mediated cytotoxicity and apoptosis induction by TiO2 nanofibers in HeLa cells, *Eur. J. Pharm. Biopharm.* 81 (2012) 324–333, <https://doi.org/10.1016/j.ejpb.2012.02.013>.
- [39] Y. He, Z. Du, S. Ma, Y. Liu, D. Li, H. Huang, S. Jiang, S. Cheng, W. Wu, K. Zhang, X. Zheng, Effects of green-synthesized silver nanoparticles on lung cancer cells in vitro and grown as xenograft tumors in vivo, *Int. J. Nanomedicine* 11 (2016) 1879–1887, <https://doi.org/10.2147/IJN.S103695>.
- [40] K. Chinthalapudi, E.S. Rangarajan, T. Izard, The interaction of talin with the cell membrane is essential for integrin activation and focal adhesion formation, *Proc. Natl. Acad. Sci.* 115 (2018) 10339–10344, <https://doi.org/10.1073/pnas.1806275115>.
- [41] U. Klinge, U. Dietz, N. Fet, B. Klosterhalfen, Characterisation of the cellular infiltrate in the foreign body granuloma of textile meshes with its impact on collagen deposition, *Hernia* 18 (2014) 571–578, <https://doi.org/10.1007/s10029-014-1220-1>.
- [42] R. Takahashi, K. Shimizu, Y. Numabe, Effects of microplasma irradiation on human gingival fibroblasts, *Odontology* 103 (2015) 194–202, <https://doi.org/10.1007/s10266-014-0157-2>.
- [43] A.P. Puzyr, S.V. Tarskikh, G.V. Makarskaya, G.A. Chiganova, I.S. Larionova, P.Y. Detkov, V.S. Bondar, Damaging effect of detonation diamonds on human white and red blood cells in vitro, *Dokl. Biochem. Biophys.* 385 (2002) 201–204.
- [44] Y. Xing, W. Xiong, L. Zhu, E. Ōsawa, S. Hussin, L. Dai, DNA damage in embryonic stem cells caused by nanodiamonds, *ACS Nano*. 5 (2011) 2376–2384. doi:<https://doi.org/10.1021/nn200279k>
- [45] M. Keremidarska, A. Ganeva, D. Mitev, T. Hikov, R. Presker, L. Pramatarova, N. Krasteva, Comparative study of cytotoxicity of detonation nanodiamond particles with an osteosarcoma cell line and primary mesenchymal stem cells, *Biotechnol. Biotechnol. Equip.* 28 (2014) 733–739, <https://doi.org/10.1080/13102818.2014.947704>.
- [46] H. Eidi, M.-O. David, G. Crépeaux, L. Henry, V. Joshi, M.-H. Berger, M. Sennour, J. Cadusseau, R.K. Gherardi, P.A. Curmi, Fluorescent nanodiamonds as a relevant tag for the assessment of alum adjuvant particle biodisposition, *BMC Med.* 13 (2015), <https://doi.org/10.1186/s12916-015-0388-2>.
- [47] A. Brož, L. Bačáková, P. Štenclová, A. Kromka, Š. Potocký, Uptake and intracellular accumulation of diamond nanoparticles – a metabolic and cytotoxic study, *Beilstein J. Nanotechnol.* 8 (2017) 1649–1657, <https://doi.org/10.3762/bjnano.8.165>.
- [48] I. Badea, R. Kaur, Nanodiamonds as novel nanomaterials for biomedical applications: drug delivery and imaging systems, *Int. J. Nanomedicine* (2013) 203, <https://doi.org/10.2147/IJN.S37348>.

A.13

Coating Ti6Al4V implants with nanocrystalline diamond functionalized with BMP-7 promotes extracellular matrix mineralization in vitro and faster osseointegration in vivo



OPEN

Coating Ti6Al4V implants with nanocrystalline diamond functionalized with BMP-7 promotes extracellular matrix mineralization in vitro and faster osseointegration in vivo

Ivana Nemcakova¹, Andrej Litvinec¹, Vaclav Mandys², Stepan Potocky³, Martin Plencner¹, Martina Doubkova¹✉, Ondrej Nanka⁴, Veronika Olejnickova^{1,4}, Barbora Sankova^{1,4}, Martin Bartos⁵, Egor Ukraintsev⁶, Oleg Babčenko⁶, Lucie Bacakova¹, Alexander Kromka³, Bohuslav Rezek⁶ & David Sedmera^{1,4}✉

The present study investigates the effect of an oxidized nanocrystalline diamond (O-NCD) coating functionalized with bone morphogenetic protein 7 (BMP-7) on human osteoblast maturation and extracellular matrix mineralization in vitro and on new bone formation in vivo. The chemical structure and the morphology of the NCD coating and the adhesion, thickness and morphology of the superimposed BMP-7 layer have also been assessed. The material analysis proved synthesis of a conformal diamond coating with a fine nanostructured morphology on the Ti6Al4V samples. The homogeneous nanostructured layer of BMP-7 on the NCD coating created by a physisorption method was confirmed by AFM. The osteogenic maturation of hFOB 1.19 cells in vitro was only slightly enhanced by the O-NCD coating alone without any increase in the mineralization of the matrix. Functionalization of the coating with BMP-7 resulted in more pronounced cell osteogenic maturation and increased extracellular matrix mineralization. Similar results were obtained in vivo from micro-CT and histological analyses of rabbit distal femurs with screws implanted for 4 or 12 weeks. While the O-NCD-coated implants alone promoted greater thickness of newly-formed bone in direct contact with the implant surface than the bare material, a further increase was induced by BMP-7. It can be therefore concluded that O-NCD coating functionalized with BMP-7 is a promising surface modification of metallic bone implants in order to improve their osseointegration.

Metallic alloys are the most widely used materials for the fabrication of load-bearing orthopaedic and dental implants that require outstanding mechanical properties such as excellent ductility, fatigue life and strength^{1–3}. Titanium-based Ti6Al4V alloy possesses significantly lower density and stiffness (elastic modulus), matching the properties of cortical bone much more closely than stainless steel or Co-Cr-based alloys^{2,3}. Moreover, Ti6Al4V has superior biocompatibility, the highest rate of integration with the host bone and the greatest corrosion resistance of these three implant alloys, thanks to the spontaneous formation of an adhesive titanium dioxide layer at its surface with the highest rate of spontaneous recovery after mechanical disruption^{2,4,5}. Although Ti6Al4V is one of the most favourable metallic implant materials, many patients have experienced increasing local pain,

¹Institute of Physiology of the Czech Academy of Sciences, Videnska 1083, 142 20 Prague 4, Czech Republic. ²Department of Pathology, Charles University, Third Faculty of Medicine, Ruska 2411, 100 00 Prague 10, Czech Republic. ³Institute of Physics, Czech Academy of Sciences, Cukrovarnicka 10, 162 00 Prague 6, Czech Republic. ⁴Institute of Anatomy, Charles University, First Faculty of Medicine, U Nemocnice 3, 128 00 Prague 2, Czech Republic. ⁵Institute of Dental Medicine, Charles University, First Faculty of Medicine, U Nemocnice 2, 1280 00 Prague 2, Czech Republic. ⁶Faculty of Electrical Engineering, Czech Technical University in Prague, Technicka 2, 166 27 Prague 6, Czech Republic. ✉email: martina.doubkova@fgu.cas.cz; david.sedmera@fgu.cas.cz

swelling, allergic reactions, and inflammation resulting in implant migration, aseptic loosening, and osteolysis. These reactions increase the need for painful and expensive revision surgeries. Human life expectancy has been increasing, but a recent study has concluded that only about half of hip replacements last for 25 years in patients with osteoarthritis⁶. Many patients nowadays outlive their implant. There is therefore great interest in the innovation and optimization of promising biomaterials such as Ti6Al4V with a view to eliminating factors responsible for implant failure.

The most common causes of implant failure are an accumulation of wear debris (i.e. metallic ions from Ti6Al4V), insufficient implant integration into the host bone (osseointegration), or a bacterial infection⁷. Various types of functional coatings for metallic implants, such as hydroxyapatite-based coatings^{8,9}, ceramic-based coatings^{10,11}, carbon-based coatings, such as diamond-like carbon (DLC)^{12,13} or fullerene coatings^{14,15}, and silver-containing nanocomposite coatings¹⁶ are therefore currently under investigation to address some or all of these issues. Another promising material for coating metallic implants, due to its superior properties, is a nanocrystalline diamond (NCD) coating. The main advantages of an NCD coating over other carbon-based coatings are that NCDs are optically transparent, chemically inert, highly biocompatible, and can easily be functionalized in many ways according to their intended application¹⁷. In addition, NCDs exhibit excellent mechanical hardness as well as high chemical, thermal and wear resistance^{18,19}, which should limit their decomposition or transformation into materials with potential toxicity and accumulation of wear debris near the implant site. A publication by Papo et al. has indeed shown that an NCD coating markedly improved the wear resistance of Ti6Al4V alloy after simulated loading mimicking two years of clinical use²⁰. Moreover, NCD-coated metallic implants should also lower the risk of post-surgical problems associated with a bacterial infection. A considerable number of studies have demonstrated strong antibacterial activity of NCD coatings against various Gram-negative and Gram-positive bacteria, including *Escherichia coli*, *Pseudomonas aeruginosa* and *Staphylococcus aureus*^{21–24}.

In addition, the nanostructured morphology of NCD coatings better imitates the nanoscale architecture of natural bone, and this should promote better osseointegration of an implant into the surrounding bone tissues of a patient. Several studies have shown that NCDs deposited on various substrates, or diamond nanocrystallites added into hydrogels, stimulated osteogenic maturation (evaluated by increased expression of osteogenic markers, e.g., osteocalcin, collagen type I, increased activity of alkaline phosphatase, or increased mineralization of extracellular matrix) of various bone-derived cells in vitro^{25–29}. Usually, however, not all osteogenic markers were elevated but only some of them, depending on the type of cell that was used, or depending on the form of the NCD material that was used. Although these in vitro data are quite promising, in vivo studies evaluating the osseointegration of diamond-coated implants are quite scarce and the results are ambiguous. While Kloss et al. reported enhanced new bone formation promoted by Ti6Al4V implants coated with oxygen terminated NCD coatings³⁰, and Jaatinen et al. reported enhanced new bone formation promoted by Ti implants coated with amorphous diamond coatings³¹, studies by Rupprecht et al. and by Metzler et al. have failed to show a positive effect of NCD coatings on the osseointegration of Ti6Al4V implants in vivo^{32,33}.

Improvements to the early stages of healing after an implant placement are very important because they can greatly enhance the clinical outcome. Implants that are osseointegrated more rapidly can be loaded sooner, and this is increasingly favoured by patients³⁴. A possible way to improve the osteoconductive properties of NCD-coated implants in vivo is by functionalizing NCD coatings with a biomolecule inducing bone formation and regeneration.

Bone morphogenetic protein 7 (BMP-7), also known as osteogenic protein-1, has been recognized as a key modulator of bone and cartilage formation and repair, mainly through the SMAD pathway³⁵. It has been reported that BMP-7 protein not only enhances osteogenic maturation of osteoblasts^{36–38} but also induces osteogenic differentiation of various stem cells^{39–41} and fibroblasts^{42,43} in vitro. Moreover, various animal studies have proved the positive effect of BMP-7-coated implants^{43–45}, or of an administration of BMP-7 into an implant site^{47,48}, or into a wound site without the use of any implant^{49–52} on the regeneration and formation of new bone in vivo. Because of its great osteoinductive effect, BMP-7 protein has been approved by the FDA for clinical application in the healing of fracture non-unions^{53,54}.

The present study set out to assess the benefits of the NCD surface functionalization with BMP-7 protein in vitro and in vivo. The NCD coating deposited on Ti6Al4V alloy plates and screws used for experiments is modified by a plasma oxidation process to create an oxidized NCD (O-NCD) surface. The plasma oxidation process is known to clean a surface from organic residues and to provide a hydrophilic surface with various oxygen-related chemical groups, such as carboxyl and anhydride⁵⁵. The oxidation process is therefore expected to improve both the physisorption of BMP-7 proteins and also the adhesion of human osteoblasts (compared to the hydrogenated surface), as has been observed in our previous studies^{56,57}. The surface functionalization with BMP-7 has a potential to further enhance the osteogenic properties of the material both in vitro and in vivo. We therefore hypothesized that the surface modification of titanium alloy with O-NCD would increase its biocompatibility, manifesting as increased cell adherence, and faster osteogenic cell differentiation, and that these properties would be further enhanced by functionalization with BMP-7. To assess the benefits of this modification, firstly the effect of O-NCD surface with or without BMP-7 coating on phenotypic maturation of osteoblasts and on mineralization of the extracellular matrix is evaluated in vitro. Secondly, the effect of these coatings on osseointegration in vivo is evaluated by micro-CT and histology analyses after implantation into the femurs of New Zealand white rabbits for a period of 4 or 12 weeks. Standard material and morphological analyses of NCD coating and BMP-7 adhesion, thickness and morphology are also included.

Materials and methods

Materials. A conventional Ti implant alloy (Ti6Al4V) was used for the experiments in the form of thin plates (10 × 10 × 3 mm; BEZNOSKA Ltd., Czech Republic) and in the form of self-cutting screws (HA 3.5 × 8 mm; Medin Inc., Czech Republic).

Sample preparation and characterization—nanocrystalline diamond coating. The Ti6Al4V plates and screws were coated with a thin nanocrystalline diamond (NCD) film. The samples were first pre-treated in a suspension of ultra-dispersed detonation nanodiamonds (DND, nominal size of 5 nm; New Metals and Chemicals Corporation Ltd., Japan). The diamond thin film growth was performed in the low-temperature low-pressure linear antenna microwave plasma (LAMWP) chemical vapour deposition (CVD) system (AK 400, Roth & Rau, Germany)⁵⁸ for 60 h at a total gas pressure of 10 Pa, microwave power of 2 × 1.7 kW and a gas mixture of 3.3% CH₄ and 13.3% CO₂ to H₂. The substrate temperature was kept at 450 °C by resistive heating of the substrate holder. The deposition was repeated twice to overcoat the top and the bottom part of the screws. Surface hydrogenation of the sample was carried out in the LAMWP system by microwave hydrogen plasma. The surface of the diamond-coated samples was further modified by an oxidizing process using radio frequency oxygen plasma (100 W, 4 min). The resulting material coating was characterized by standard analytical methods: optical microscopy, scanning electron microscopy (SEM; Maia 3, TESCAN, Czech Republic) and Raman spectroscopy (WITec alpha300 RAS, Germany).

Sample preparation and characterization—BMP-7 functionalization. The Ti6Al4V plates and screws with an NCD coating were sterilized in an autoclave (Tuttnauer Co. Ltd., Israel). A part of the samples coated with oxidized NCD was further functionalized with human bone morphogenetic protein 7 (BMP-7; BioLegend, Cat. No. 595602, USA) to promote phenotypic maturation of osteoblasts in vitro or to promote bone formation and thus to improve the osseointegration of the implants in vivo. The samples were functionalized with BMP-7 by incubating them in a BMP-7 solution with a concentration of 10 µg/mL in phosphate-buffered saline (PBS) for 24 h at room temperature (RT). The samples were subsequently washed in PBS (Sigma-Aldrich, Merck, Germany) and were immediately used for in vitro or in vivo experiments.

In order to study the adsorption of BMP-7 on the diamond surfaces and the interaction of BMP-7 with these coatings, an atomic force microscopy (AFM; Dimension ICON, Bruker, US) analysis was performed. For the AFM analysis, BMP-7 protein was deposited on flat monocrystalline diamond samples with hydrogenated (H-NCD) and oxidized (O-NCD) surfaces that were prepared by the same technology (microwave hydrogen plasma and radio-frequency oxygen plasma) as described above. BMP-7 solution droplets of 30 µL were applied on both samples for 24 h to allow the BMP-7 molecules to adsorb. Then the samples were rinsed with water and were dried by airflow. The thickness of the BMP-7 adsorbed layer was measured by the contact mode (CM) nanoshaving method⁵⁹. Four 2 × 2 µm² images were scanned in CM-AFM. Next, a 5 × 5 µm² overscan was performed in PeakForce Quantitative Nanomechanical mode (PFQNM), which reveals details of the surface morphology and also differences in the adhesion and deformation of the surface layer after adsorption of BMP-7.

In vitro experiments—phenotypic maturation of human osteoblasts hFOB 1.19. The human non-tumour osteoblast cell line (hFOB 1.19; ATCC CRL-11372[™], USA) was used to evaluate the phenotypic maturation of osteoblasts cultured on the investigated materials (Ti6Al4V alloy plates coated with O-NCD films with or without BMP-7 functionalization; unmodified Ti6Al4V plates were used as a reference control material). hFOB 1.19 cells were induced to proliferate when cultured at a permissive temperature of 33.5 °C and were induced to differentiate into mature osteoblasts expressing the normal osteoblast phenotype when cultured at a restrictive temperature of 39.5 °C^{60,61}. The samples, inserted into polystyrene 12-well tissue culture plates (well diameter 21 mm; TPP, Switzerland), were seeded with hFOB 1.19 cells and were cultured in a 1:1 mixture of Ham's F12 medium and Dulbecco's modified Eagle's medium (Gibco, Cat. No. 11039, USA) supplemented with 10% foetal bovine serum (Sebak GmbH, Germany) and geneticin G418 (0.3 mg/mL; Gibco, USA) at 33.5 °C in a humidified air atmosphere containing 5% of CO₂. When the cells reached confluence (3 days after seeding), the temperature was set to 39.5 °C (labelled as day 0 of differentiation) and the cells were cultured for an additional period of 21 days with the medium exchanged every 2–3 days. The metabolic activity of hFOB 1.19 cells cultured on the investigated materials was evaluated on days 0, 3, 10 and 21 of differentiation, while the phenotypic maturation (osteogenic differentiation) of the cells was assessed on days 3, 10 and 21. Three independent samples for each experimental group and time interval were used. The quantitative data were presented as the mean ± S.E.M. (Standard Error of the Mean).

The metabolic activity of the cells (the activity of the mitochondrial enzymes) was assessed by incubation of the samples in a final concentration of 40 µM Resazurin (Sigma-Aldrich, Merck, Germany) in the fresh complete cell culture medium mentioned above. After 1.5 h of incubation at 39.5 °C, the fluorescence of the solution was measured (Ex/Em = 530/590 nm) by a Synergy[™] HT Multi-Mode Microplate reader (BioTek, USA). A solution without cells was used as a blank control.

The activity of alkaline phosphatase (ALP, a marker of early/mid-term osteogenic differentiation) was assessed on days 3, 10 and 21 of differentiation after 10-min incubation of samples in a solution of 1 mg/mL of *p*-nitrophenyl phosphate in a substrate buffer (50 mM glycine, 1 mM MgCl₂, pH 10.5; Sigma-Aldrich, Merck, Germany) at RT. The resulting solution was then mixed with the same volume of 1 M NaOH solution, and the absorbance was measured at 405 nm by a Synergy[™] HT Multi-Mode Microplate reader (BioTek, USA). A solution without cells was used as a blank control. The absorbance of the known concentrations of *p*-nitrophenol diluted in 0.02 M NaOH (9–90 µM; Sigma-Aldrich, Merck, Germany) was measured as a standard.

Gene	Forward primer sequence	Reverse primer sequence	Product length (bp)
BGN	5'-CAG CCC GCC AAC TAG TCA-3'	5'-GGC CAG CAG AGA CAC GAG-3'	93
COL1A1	5'-CAG CCG CTT CAC CTA CAG C-3'	5'-TTT TGT ATT CAA TCA CTG TCT TGC C-3'	83
DCN	5'-GGA GAC TTT AAG AAC CTG AAG AAC C-3'	5'-CGT TCC AAC TTC ACC AAA GG-3'	104
GAPDH	5'-TGC ACC ACC AAC TGC TTA GC-3'	5'-GGC ATG GAC TGT GGT CAT GAG-3'	87
OSX	5'-GGC ACA AAG AAG CCG TAG TC-3'	5'-CAG GTG AAA GGA GCC CAT TA-3'	106
RUNX-2	5'-GCC TTC AAG GTG GTA GCC C-3'	5'-CGT TAC CCG CCA TGA CAG TA-3'	67
SPARC	5'-GTA CAT CGC CCT GGA TGA GT-3'	5'-CGA AGG GGA GGG TTA AAG AG-3'	124

Table 1. Oligonucleotide primers used for qPCR amplification. *BGN* biglycan, *COL1A1* collagen type I, *DCN* decorin, *GAPDH* glyceraldehyde 3-phosphate dehydrogenase, *OSX* osterix, *RUNX-2* runt-related transcription factor 2, *SPARC* osteonectin.

The *extracellular matrix mineralization* (a late marker of osteogenic differentiation) was evaluated on days 10 and 21 of differentiation by Alizarin Red S staining. The cells cultured on the samples were fixed in 4% paraformaldehyde (PFA; Sigma-Aldrich, Merck, Germany) for 15 min at RT. The samples with fixed cells were incubated in 40 mM Alizarin Red S in dH₂O (pH 4.1; Sigma-Aldrich, Merck, Germany) for 20 min at RT with gentle shaking. The unbound dye was washed away by dH₂O (5 times for 10 min with gentle shaking) and the samples were then left to dry and were stored at -20 °C until the quantification was performed. To extract the dye, the samples were incubated in 10% acetic acid for 1 h at RT with gentle shaking. The solution that was obtained, together with the layer of cells (detached by a cell scraper), was transferred to a 1.5 mL tube, was vortexed for 30 s and was heated at 85 °C for 10 min. The tubes were then incubated on ice for 10 min and were subsequently centrifuged at 20,000g for 15 min. The pH of the supernatant was adjusted by 10% NH₄OH (Sigma-Aldrich, Merck, Germany) to 4.2, and the absorbance of the solution was measured at 405 nm by a Synergy™ HT Multi-Mode Microplate reader (BioTek, USA). A solution without cells was used as a blank control.

The *real-time qPCR method* was used to evaluate the expression of other markers of phenotypic maturation of hFOB 1.19 cells cultured on the investigated materials. RNA from the cells was extracted using a Total RNA Purification Plus Micro Kit (Norgen BioTek, USA), according to the manufacturer's instructions. An amount of 300 ng/μL mRNA was used for reverse transcription into cDNA using the ProtoScript First Strand cDNA Synthesis Kit (New England Biolabs, USA) with oligo-dT primers. The reaction ran in a T-Personal Thermocycler (Biometra GmbH, Germany). The relative mRNA expression was quantified using SYBR Green (FastStart Universal SYBR Green Master; Roche Diagnostics GmbH, Switzerland) and primers from Geneti Biotech, as presented in Table 1. The cDNA was amplified in the iCycler iQ™ 5 Multicolor Real-Time PCR detection system (BioRad, USA) in a total reaction volume of 20 μL, under the following conditions: 10 min incubation at 95 °C, followed by 40 cycles of 15 s at 95 °C and 1 min at 60 °C. The data were analysed using the 2^{-ΔΔC_t} method, were normalized against the GAPDH housekeeping gene, and are plotted as mean ± standard deviation (SD).

A *statistical analysis* was performed using SigmaStat (Jandel Corporation, USA). A comparison between the groups was analysed with the ANOVA, Student–Newman–Keuls method. Values of *p* < 0.05 were considered statistically significant.

In vivo experiments on rabbits. The animal experiments were approved by the Animal Care and Use committee of the Institute of Physiology in compliance with the current national legislation. The experiments conformed with all the international and EU ethical standards and also with the ARRIVE guidelines (<https://arriveguidelines.org/arrive-guidelines>).

New Zealand white rabbits were supplied by an accredited supplier (Velaz, Prague, Czech Republic) and were provided with food and water ad libitum. Animals of either sex were used (total N: 44), with a minimum body weight of 3.4 kg. After a habituation period of at least one week, the animals were weighed, and their body weights were recorded. Anaesthesia was initiated by an intramuscular (IM) injection of diazepam (5 mg/kg). The surgery was performed under antibiotic cover of marbofloxacin (5 mg/kg IM). Deep anaesthesia (surgical plane) was induced by ketamine (50 mg/kg, IM) with xylazine (5 mg/kg, IM). After the cessation of reaction to painful stimuli, a dab of antiseptic ointment (Ophtalmo-Septonex) was applied to both eyes to prevent corneal drying, and the limb to be operated on was shaved from ankle to groin. The surgical field was then thoroughly disinfected by povidone iodine and the animal was placed onto an operating table, where the surgical plane of anaesthesia was maintained by continuous administration of 2% halothane (Narcotan) with oxygen applied via a face mask. Pulse and blood oxygen saturation were continuously monitored by a pulse oximeter.

After the field had been covered with sterile wraps, a skin incision was performed in the area of the lateral condyle of the femur, followed by blunt dissection of all the layers up to the bone. After finding and marking the appropriate place on the lateral aspect, a hole 2.7 mm in diameter was drilled by an orthopaedic drill (Acculan 3Ti, B.Braun), followed by the implantation of O-NCD-coated, O-NCD + BMP-7-coated or uncoated control Ti6Al4V screws (HA 3.5 × 8 mm) via a hand screwdriver. To reduce the necessary number of animals (3R), both sides were operated consecutively, i.e., 12 and 4 weeks before sampling, to obtain 2 samples at different time points from each animal. The minimum size for each group was 5 implants for each type of coating and sampling interval. The wound was then closed in layers with a PDS II 4–0 absorbable suture.

After the surgery, the animals received a depot dose of 0.5 mg/kg of non-steroidal anti-inflammatory analgesic meloxicam by a subcutaneous injection (SC), and the suture was smeared with Betadine to prevent infection of the wound. During the recovery period, the animals were monitored continuously until complete awakening. For at least 10 days after surgery, the animals were checked several times a day with emphasis on their general well-being and on wound healing. For a period of 5 days, a combination of an antibiotic (marbofloxacin 5 mg/kg, IM) and an analgesic (meloxicam 0.5 mg/kg, IM) was administered daily. The diet was enriched with fresh vegetables and hay for faster healing. Food and water intake were monitored daily by a veterinarian for the entire duration of the experiment.

At the time of sampling, i.e., 4 or 12 weeks after implantation, the animals were sacrificed by an approved method (rendering them unconscious by a spring-loaded device followed by exsanguination), and the distal femurs containing the implants were extracted. The samples were sawed down to a size that fitted the fixation vials, and were subsequently fixed for 48 h in 4% paraformaldehyde in PBS at 4 °C. After rinsing in PBS, the samples were scanned and evaluated by micro-CT (see 2.6), as in our previous studies^{62,63}. After imaging, the samples were decalcified with a hydrochloric acid solution (Histolab Products, Sweden) and the screws were carefully removed after slicing the decalcified bone in half with a scalpel. The bone samples were then processed for paraffin histology (see below), while the screws were imaged using SEM to confirm the integrity of the coating.

Micro-CT evaluation of the tissue samples. Each specimen was placed in a plastic tube with PBS and was scanned using a SkyScan 1272 micro-CT device (Bruker micro-CT, Kontich, Belgium) with the following scanning parameters: pixel size 10 µm, source voltage 100 kV, source current 100 µA, 0.11 mm Cu filter, frame averaging 3, rotation step 0.2°, rotation 360°. The scanning time was approximately 6 h for each specimen. The flat-field correction was updated before each acquisition. Image data were reconstructed and were processed using NRecon SW (Bruker, Belgium). Standardized cross-section images were acquired using DataViewer (Bruker, Belgium).

Histological analysis of the tissue samples. PFA-fixed, paraffin-embedded tissue samples were cut in series at 10 µm and were stained alternately with Hematoxylin–Eosin and van Gieson/Orcein staining protocol. The stained sections were photographed using an Olympus DP80 CCD camera (Olympus, Tokyo, Japan) fitted on an upright BX51 compound Olympus microscope at different magnifications (2×–20×). The thickness of newly formed bone was measured in the mid-shaft region taking care to exclude any attached trabeculae. Digital images were processed using Adobe Photoshop (background and levels adjustment, Unsharp Mask filtering—always performed on the entire image) and were arranged in plates with the same software.

Results and discussion

Characterization of the NCD layer and BMP-7 adhered on NCD. Raman spectroscopy and surface mapping show uniform coating by NCD with the typical diamond peak and G band in the spectrum (Fig. 1). The SEM image of the coated screw surface along the thread and in the screw tip area exhibits a corrugated morphology conformal to the screw surface finish and fine nanostructures related to the NCD grains in both critical areas.

The BMP-7 morphology, the adhesion map and the thickness profile observed by AFM in PFQNM regime O-NCD and H-NCD surfaces are shown in Fig. 2. The square in the centre corresponds to the area from which the molecules were removed (nanoshaved) by scanning on contact mode AFM. The BMP-7 adsorbed thickness on the O-NCD surface, as determined from the mean heights in the central and outside area, was 1.8 ± 1.3 nm. From the profile across the nanoshaved area, the thickness was also 1.8 ± 1.3 nm. The BMP-7 adsorbed thickness on the H-NCD surface was 1.9 ± 1.2 nm in area and 2.3 ± 1.2 nm from the line profile.

The thickness of the adsorbed BMP-7 was similar on the H-terminated and O-terminated nanocrystalline diamond surfaces. The BMP-7 surface morphology also appeared qualitatively similar, comprised of a uniform conformal coating and a high density of larger (brighter) dots. This is a noteworthy finding, as H-NCD is hydrophobic and O-NCD is hydrophilic. The adsorbed BMP-7 thickness was on average only 2 nm. The three-dimensional structure of BMP-7 exhibits an open boomerang-shaped conformation with dimensions of $13 \times 9 \times 5$ nm³, as deduced from transmission electron microscopy (TEM) measurements and from Small Angle X-ray scattering (SAXS) measurements⁶⁴. Thus, in our case, the BMP-7 molecules must be lying on the diamond surface, forming a uniform primary layer coating, on which the BMP-7 molecules, adsorbed in a more native form, correspond to the observed brighter dots. The relatively small and similar thickness of the BMP-7 primary layer on the hydrogenated and oxidized diamond surfaces may be explained by a tight interaction with the diamond surface dipoles (C-H or C-O) via hydrogen bonding. The BMP-7 could also be collapsed (as observed by comparing the AFM data in air and in solution on other biomolecules⁵⁷). However, the BMP-7 dimensions given above were determined from the TEM in vacuum condition⁶⁴, so this effect can be excluded.

However, the conformation of BMP-7 in the primary layer on H- and O-terminated NCD can differ, as was observed above for adsorbed FBS proteins^{59,65}. This effect may be due to different polarity of the surface dipoles, different protein parts forming hydrogen bonds and/or interacting with the diamond surface via hydrophobic or hydrophilic interactions. This assertion is supported by the PFQNM adhesion data (tip-molecule adhesion forces in the range of 10 nN). There is a uniform background of the adhesion force due to the thin BMP-7 layer, which is lower than on the bare (nanoshaved) diamond in the central area of the adhesion images. The difference in the adhesion force between BMP-7 and bare diamond is greater on H-NCD than on O-NCD. This again hints at a slightly different conformation of the BMP-7 molecules lying on the surface. On both types of surfaces, there are also smaller and larger dark dots in the adhesion map, obviously corresponding to the native form of BMP-7. From the adhesion image, it is evident that these BMP-7 aggregates are larger and more pronounced

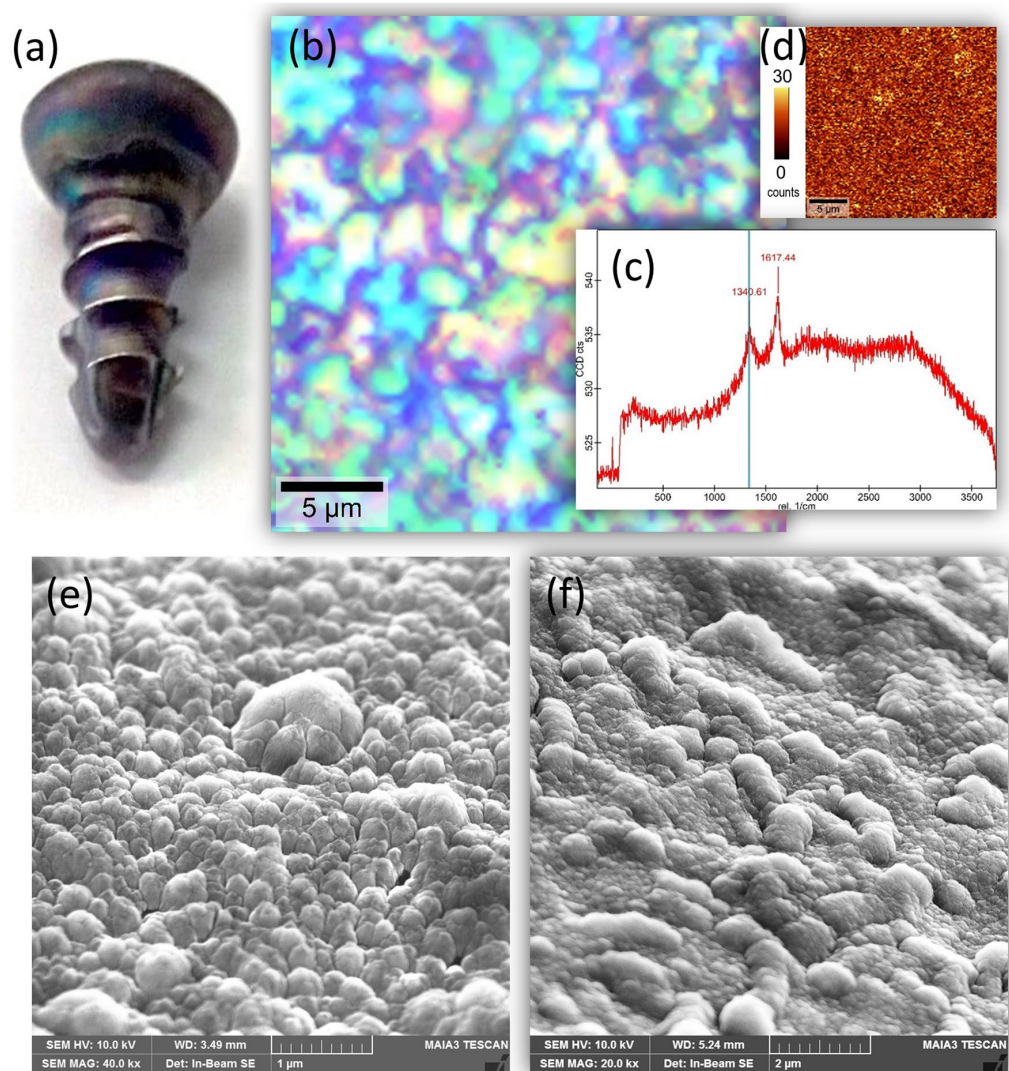


Figure 1. Material and morphological characteristics of the nanocrystalline diamond-coated cortical screws: (a) a photograph of a coated screw, (b) bright-field optical microscope image, (c) Raman spectrum showing characteristic nanocrystalline diamond features, (d) a Raman diamond peak intensity map, (e) SEM image of the coated screw surface along the thread and (f) in the screw tip area.

on H-NCD, while they are fine and more homogeneously distributed on O-NCD. This again suggests that the BMP-7 interaction with H-NCD and O-NCD is different, despite the similar surface morphology and a similar thickness of approximately 2 nm.

Phenotypic maturation of hFOB 1.19 cells in vitro. To investigate the effect of the O-NCD coating and the O-NCD coating functionalized with BMP-7 (O-NCD + BMP-7) on the maturation of human osteoblasts in vitro, confluent hFOB 1.19 cells were cultured for another 21 days at a restrictive temperature of 39.5°, inducing their differentiation into the mature osteoblast phenotype. Figure 3a shows that the values of the metabolic activity (which are usually proportional to the cell numbers) of hFOB 1.19 cells were comparable among all sample groups on days 0 and 3 of differentiation. The cells exhibited the greatest metabolic activity on day 10 of differentiation, with values 2-times higher than on the other evaluated days. Slightly higher metabolic activity of cells cultured on the O-NCD + BMP-7 coating was observed with increasing time of cultivation (from day 10 of differentiation); however, these differences were not proven to be significant (Fig. 3a). The results of metabolic activity at all assessed time intervals did not show any significant differences among the investigated materials.

The evaluation of the activity of alkaline phosphatase (ALP), which is one of the main markers of early/mid-term phenotypic maturation of osteoblasts, showed that on day 3 of differentiation, the activity of ALP in cells

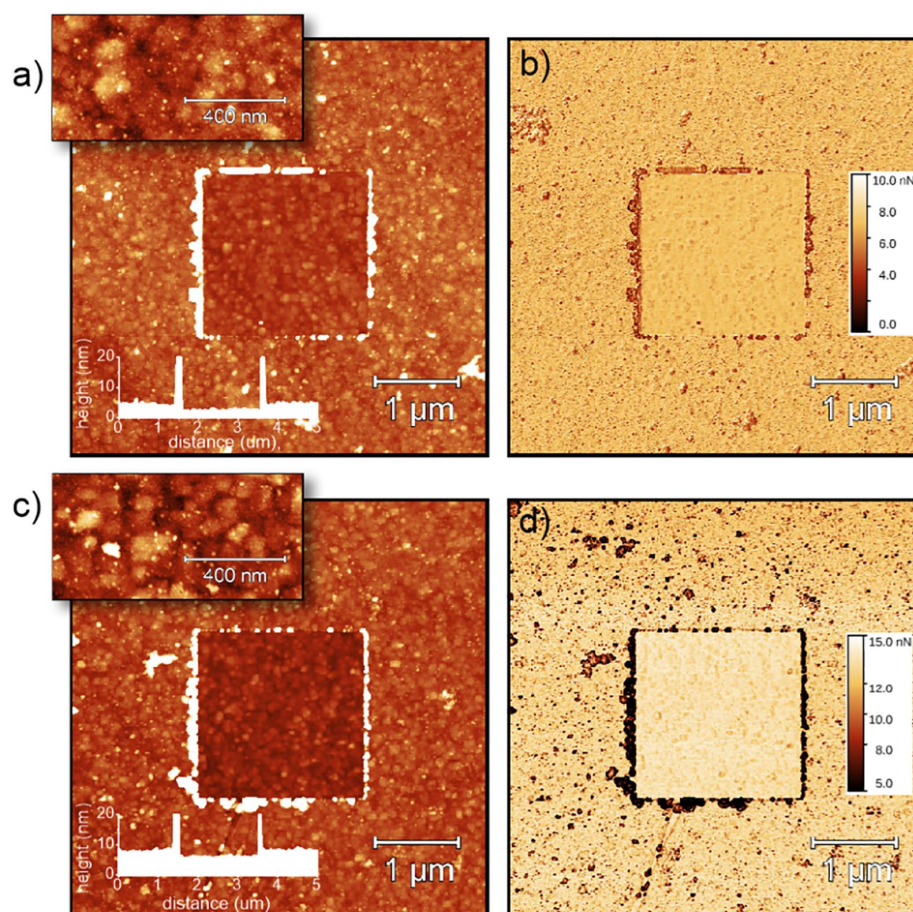


Figure 2. BMP-7 morphology (a,c), adhesion maps (b,d), and thickness profiles (insets) observed by AFM in the PFQNM regime on oxidized (a,b) and hydrogenated (c,d) NCD surfaces. The square in the centre corresponds to the area from which the molecules were removed (nanoshaved) by scanning in contact mode AFM. The Z scale is 20 nm for $5 \times 5 \mu\text{m}^2$ topography images, 10 nm for $0.5 \times 1 \mu\text{m}^2$ topography images (insets) and 10 nN for $5 \times 5 \mu\text{m}^2$ adhesion images.

on both O-NCD-based coatings was lower than in cells on uncoated Ti6Al4V (Fig. 3b), while the gene expression of other early and mid-term markers of osteogenic differentiation, namely RUNX-2, osterix, biglycan and decorin, was usually increased (Fig. 4). However, it should be pointed out that the enzymatic activity cannot be always proportional to the expression of a given enzyme at mRNA and protein level, because enzymes, including ALP, can be present in their immature, pro-enzymatic form. The correlation between the gene expression of ALP, amount of its molecules and its activity in cells on O-NCD-based coatings should be further investigated.

A lower activity of ALP on O-terminated NCD surfaces might also be explained by a certain inhibitory effect of these surfaces on the enzymatic activity. On the one hand, O-NCD surfaces are hydrophilic, and thus they promote the adsorption of cell adhesion-mediating proteins in an appropriate geometric conformation for binding cell adhesion receptors, and by this mechanism, these surfaces support the adhesion, spreading and subsequent proliferation of cells. On the other hand, oxygenated surfaces can also have some adverse effects on cells. It is known that oxygen radicals can inhibit the activity of various enzymes, including ALP. For example, treatment of ALP with oxidizing agents, such as *p*-nitrophenyl phosphate, beta-glycerophosphate or ascorbic acid/ Fe^{2+} , resulted in the inhibition of the enzyme activity, due to generation of oxygen radicals, e.g., $\cdot\text{OH}$ radicals⁶⁶. Other examples are inhibition of ALP by H_2O_2 ⁶⁷ or low activity of serum ALP in patients with Wilson's disease, where the enzyme is inhibited by ROS induced by elevated Cu^{2+} ions⁶⁸. Oxygen-containing radicals might be present on the surface of NCD after oxygen plasma treatment, especially in relatively early culture intervals, when the cultivation substrate is not fully covered with cells and their newly formed extracellular matrix.

It is also known that ALP activity is inversely correlated with the concentration of calcium⁶⁹. Ca^{2+} ions can be attracted to oxygen-containing chemical functional groups on O-NCD surface, which are usually negatively

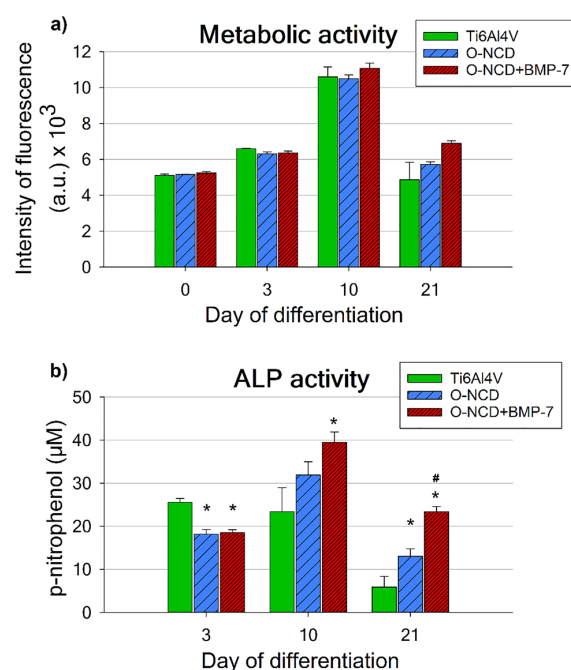


Figure 3. The metabolic activity (a) and the activity of alkaline phosphatase (ALP) (b) of hFOB 1.19 cells cultured on bare Ti6Al4V samples (Ti6Al4V), on Ti6Al4V samples coated with the O-terminated nanocrystalline diamond coating (O-NCD), or on Ti6Al4V samples coated with the O-terminated nanocrystalline diamond coating functionalized with BMP-7 (O-NCD + BMP-7) under differentiation conditions (a restrictive temperature of 39.5 °C) for 3 weeks. Mean \pm S.E.M. * indicates a significant difference from the reference Ti6Al4V, while # shows a significant difference from the O-NCD coating; $p < 0.05$.

charged (-COOH, OH⁻). Last but not least, as every protein, ALP can be adsorbed to the O-NCD surface, which can inhibit its activity. For example, ALP activity was deactivated by adsorption on quartz slides⁷⁰.

Nevertheless, in the following culture intervals (days 10 and 21 of differentiation), the ALP activity of hFOB 1.19 cells cultured on the O-NCD-based coatings increased in comparison with the value on the uncoated Ti6Al4V, especially on O-NCD functionalized with BMP-7. The cells cultured on the O-NCD coating functionalized with BMP-7 revealed the highest ALP activity with significant differences from the reference Ti6Al4V alloy (days 10 and 21) and from the O-NCD coating (day 21). Nevertheless, after 21 days of differentiation, even the O-NCD coating without BMP-7 induced greater ALP activity of the cells than the reference Ti6Al4V. Similarly to the metabolic activity, the ALP activity of the hFOB1.19 cells was also about two times higher on day 10 than on days 3 and 21 (Fig. 3b).

The mineralization of the extracellular matrix, which is a typical marker of late osteogenic differentiation, was assessed by Alizarin Red S staining on days 10 and 21 of differentiation. The extracellular matrix mineralization by hFOB 1.19 cells was about 2 times higher on the O-NCD coatings functionalized with BMP-7 than on the reference Ti6Al4V and on O-NCD without BMP-7 at both evaluated time intervals (Fig. 4a).

The qPCR analysis performed on days 3, 10 and 21 of differentiation revealed that the gene expression of all monitored osteogenic markers (except for OSX) was significantly higher in cells growing on the O-NCD coatings functionalized with BMP-7 than on the other materials (Fig. 4b). The expression of both early osteogenic factors (RUNX-2, OSX), evaluated on day 3 of differentiation, showed a similar trend. The expression of RUNX-2 in cells cultured on O-NCD + BMP-7 was significantly higher than in cells grown on the reference Ti6Al4V and on O-NCD without BMP-7. This is in agreement with the fact that BMP proteins are known to stimulate RUNX-2 expression through the SMAD protein signalling pathway^{34,71}. Moreover, even the O-NCD coating without BMP-7 induced a higher RUNX-2 expression than the reference Ti6Al4V. The expression of OSX, despite following a similar trend to RUNX-2, was not found to be significantly increased due to a big data spread. On day 10 of differentiation, the mid-term osteogenic markers BGN and DCN, which are associated with matrix mineralization *in vitro*^{72,73}, also showed a significantly increased expression in cells cultured on O-NCD + BMP-7 in comparison with other materials. These results correspond with the matrix mineralization results on day 10 assessed by Alizarin Red S staining. The expression of late osteogenic markers, such as COL1A1 and SPARC⁷², measured on day 21 of differentiation, followed the same expression profile, with higher values found on the O-NCD-BMP-7 samples than on the reference Ti6Al4V and on the O-NCD coating without BMP-7 (Fig. 4b).

In summary, the osteogenic maturation of hFOB 1.19 cells *in vitro* was slightly enhanced by the O-NCD coating, which promoted a greater expression of an early osteogenic factor RUNX-2 and greater activity of

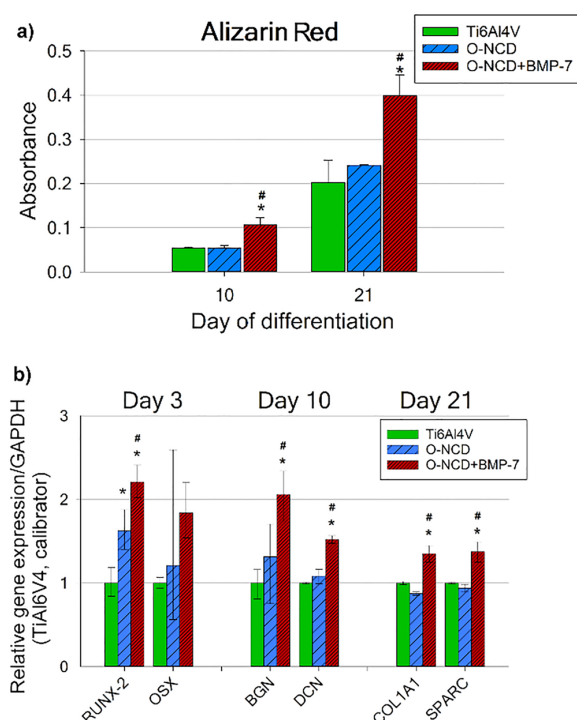


Figure 4. Mineralization of the extracellular matrix, assessed by Alizarin Red S staining, induced by hFOB 1.19 cells (a), and their relative gene expression (b). The cells were cultured on bare Ti6Al4V samples (Ti6Al4V), on Ti6Al4V samples coated with the O-terminated nanocrystalline diamond coating (O-NCD), or on Ti6Al4V samples coated with the O-terminated nanocrystalline diamond coating functionalized with BMP-7 (O-NCD + BMP-7) under differentiation conditions (a restrictive temperature of 39.5 °C) for 3 weeks. Graph (b) compares the gene expression of osteogenic markers RUNX-2 and OSX (osterix; both early markers), BGN and DCN (biglycan and decorin; mid-term markers) and COL1A1 with SPARC (collagen type I and osteonectin; late markers). The relative mRNA expression was quantified by the $2^{-\Delta\Delta C_t}$ method. The data are expressed relative to GAPDH, normalized to gene expression on the reference Ti6Al4V sample (calibrator). Mean \pm S.E.M. (a). Mean \pm SD (b). * indicates a significant difference from the reference Ti6Al4V, while # shows a significant difference from the O-NCD coating; $p < 0.05$.

alkaline phosphatase than the reference uncoated Ti6Al4V alloy. However, O-NCD coating of the Ti6Al4V alloy did not increase matrix mineralization in the case of hFOB 1.19 cells. Our results are in accordance with results reported in other publications, where various NCD coatings (including O-NCD) promoted increased ALP activity in SAOS-2 osteoblastic cells in comparison with a reference polystyrene culture dish^{27,28}. Moreover, other researchers also did not observe increased expression of collagen type I, osteocalcin or osteopontin in SAOS-2 or MG-63 osteoblastic cells cultured on O-NCD samples^{28,74}, whereas neonatal human dermal fibroblasts formed an extracellular matrix with collagen both on O-NCD and on H-NCD⁷⁵. Matrix mineralization or other osteogenic markers investigated in our study were not evaluated in the study by Kalbacova et al.²⁷. In contrast to our results, Liskova et al.²⁸ reported increased matrix mineralization in the case of SAOS-2 cells grown on O-NCD coatings. There are various possible explanations for this discrepancy, e.g., the use of different analysing methods, or more likely the use of different reference controls (the polystyrene culture dish vs. the Ti6Al4V alloy) or different cell lines. Unlike non-tumour osteoblast cell line hFOB 1.19, the SAOS-2 cell line is derived from a malignant bone tumour and has various chromosomal abnormalities and gene mutations^{60,76}, resulting in different cell behaviour in response to the same culture substrate or in response to the same culture conditions, with SAOS-2 cells expressing the most mature osteoblastic phenotype⁷⁷. The differences between non-tumour and tumour-derived osteoblast cell lines have been thoroughly discussed in a recent publication by Nemcakova et al.⁷⁸.

Functionalization of the O-NCD coating with BMP-7 markedly improved the osteogenic maturation of hFOB 1.19 cells in vitro, which was confirmed by the elevation of all osteogenic markers evaluated in the present study. In complete agreement with our results, other studies have also reported improved osteogenic properties of various Ti-based materials with immobilized BMP-7 molecules on their surfaces. Rat primary osteoblasts, human bone marrow mesenchymal stem cells and mouse MC3T3-E1 pre-osteoblasts cultured on these materials showed increased ALP activity, increased osteocalcin and osteopontin expression, as well as increased matrix mineralization in vitro^{38,79,80}.

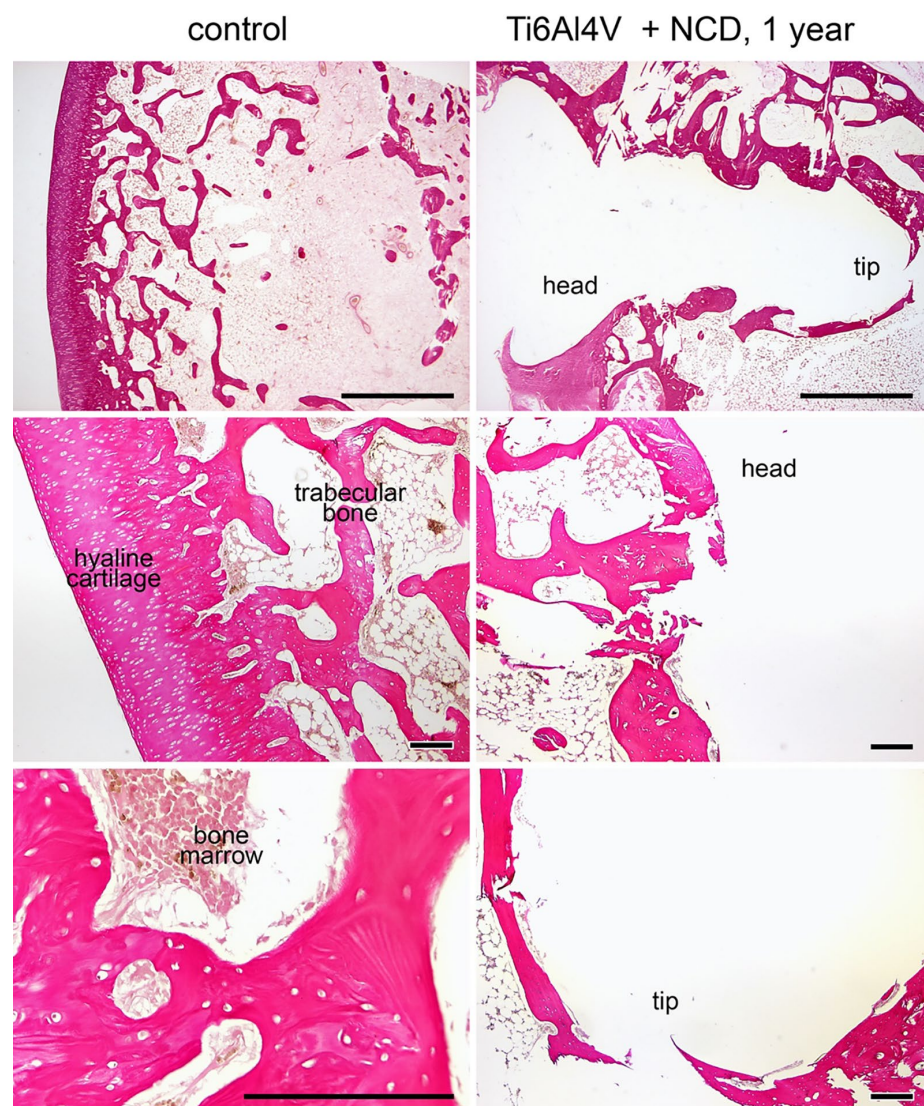


Figure 5. The morphology of distal rabbit femur one year after implantation. Complete embedding of the screw by the bone is visible (top row). The tissue in the contact with the head is partly cartilaginous (middle row), while the tip is covered by newly-formed bone (bottom row). Van Gieson/orcein staining (top row) and hematoxylin–eosin staining, scale bars 1 mm (top row) and 200 μm (remaining panels). Control=unoperated side.

In vivo tissue response to various implant surfaces. The tissue reaction in the vicinity of an implant is a multifactorial and multistep process. Its morphological appearance is closely related to the character, composition and structure of the implant surface and to the duration of implantation^{81,82}. The granulation tissue and the formation of the woven bone around the implant are present soon after implantation – after approximately 3 weeks^{81,83}. Remodelling processes characterized by the formation of the mature lamellar bone surrounding the implant are observed after 4 weeks^{83,84}.

SEM analysis of explanted screws showed over 95% of the surface coating intact (confirmed by element analysis, Ti vs. C, data not shown here), confirming the long-term stability of the NCD coating under in vivo conditions. Our preliminary experiments with a healing period of 6 and 12 months showed excellent osseointegration with a continuous rim formed of trabeculae of lamellar bone (mean thickness 130 μm , range 24–152 μm) in the vicinity of the screw in all groups (Fig. 5) with no differences (both for Ti6Al4V and for stainless steel screws, with and without the O-NCD coating).

Further attention was therefore focused on earlier time points (4 and 12 weeks). Three groups of animals (N = 7 per group) received implants first to the right femur, and 8 weeks later received implants from the same investigated group (either the control Ti6Al4V, O-NCD-coated Ti6Al4V, or O-NCD + BMP-7-coated Ti6Al4V) to the left femur, thus reducing the experimental variation and also the numbers of animals in the experiment. After an additional period of 4 weeks, a non-destructive *ex vivo* whole specimen 2D/3D visualization and analysis was performed by micro-CT. Another advantage of micro-CT 3D visualization is that it may also improve the preparation of subsequent histological sections (i.e., the position and the orientation of the section). The micro-CT results (Fig. 6) showed clear temporal progress in osseointegration. The extent of trabecular bone in contact with the O-NCD-coated implants was clearly and consistently higher than in the bare Ti6Al4V implants. A further increase in the extent of bone formation and in the thickness of the newly-formed bone in direct contact with the implant surface was observed in the O-NCD + BMP-7 implants at both 4-week and 12-week time points.

Serial histological sections (Fig. 7) also confirmed the observation from the micro-CT revealing greater thickness of the newly-formed bone on the O-NCD with a further increase on the O-NCD + BMP-7 surface at both time intervals. There was no foreign body reaction on the surface of the coated implants, and we did not observe any coating detachment with loose parts containing nanodiamonds on or in the bone. Similarly to our observations, good agreement between the micro-CT results and the histology results in the evaluation of the bone-implant contact analysis has also been reported in other studies^{85–87}. The more detailed histology results (Fig. 7) also showed that the mineralization of the connective tissue progressed from the head of the screw towards the tip. The tissue found around the head was histologically hyaline cartilage (from the joint cartilage), with the cavity in the screw head often filled by newly-formed fibrocartilage, which was also formed in the joint capsule that came into contact with the implant. At 4 weeks, the discontinuous rim of the lamellar bone-forming trabeculae and areas of the bone marrow circumscribed by a thin layer of collagen connective tissue was present around the screw. A thin rim of fibrous tissue continuing to the bone marrow covered the tip of the screw. A downward arrangement of osseointegration of this type has also been observed in other publications^{84,88}. At 12 weeks, the continuous rim of the newly-formed lamellar bone was present in most of the implants, including the area of the tip.

We quantified the thickness of newly-formed bone in all three experimental groups by measuring, for consistency, the region of the mid-shaft of the screw (illustrated by green circles in Fig. 7). In all groups, the thickness increased between 4 and 12 weeks (paired t-test, $p < 0.05$, Fig. 8). There was a significant difference between bare metal and coated implants at 4 weeks, while at 12 weeks, the difference was only significant for the O-NCD + BMP-7 group (Fig. 8). At both time points, the layer of the newly-formed bone was significantly thicker in the O-NCD + BMP-7 implants compared to the O-NCD group.

The faster bone formation promoted by the O-NCD coating observed in our study was also reported by Kloss et al. After 4 weeks of implantation in sheep calvarias, O-NCD-coated Ti dental implants showed a thicker layer of mineralized osseous tissue than uncoated Ti implants³⁰. By contrast, two other studies investigating the effect of NCD coatings on the osseointegration of Ti6Al4V implants in domestic pigs or in New Zealand white rabbits failed to show any positive effect of NCD coatings^{32,33}. Moreover, the NCD-coated implants became osseointegrated at a later time point than the uncoated implants³³. This discrepancy with our results can be explained by the use of NCD coatings without the post-deposition oxygen plasma treatment that was applied in our study. The as-deposited NCD diamond coatings are generally hydrogen-terminated. A comparison of the wettability of NCD coatings with various post-deposition treatments showed that both the as-deposited NCD coatings and the hydrogenated NCD coatings were less hydrophilic than the oxygen plasma-treated O-NCD coating^{89,90}. The hydrophilic O-NCD films improved the adsorption of cell-adhesion-mediating proteins, and showed two times higher biological activity and better cell adhesion, proliferation and osteogenic differentiation *in vitro* than the H-NCD films^{28,90}. An oxidized NCD coating should therefore also better promote osseointegration *in vivo* than an as-deposited NCD coating or an additionally hydrogenated NCD coating. Indeed, the study by Kloss et al. confirms this explanation. While the O-NCD-coated implants promoted new bone formation better than the uncoated implants, the H-NCD-coated implants showed even less bone formation than the uncoated implants. Moreover, although the O-NCD-coated implants were overlaid with a thick layer of mineralized osseous tissue, the H-NCD-coated implants were covered with accumulating fibrous tissue³⁰.

The functionalization of O-NCD-coated implants with BMP-7 protein further increased the thickness of the newly-formed bone, as was confirmed by both micro-CT and histological analysis in our study. A recent publication has also shown accelerated new bone formation induced by calcium phosphate + BMP-7-coated Ti implants in goats with osteoporotic-like bones within the first month after implantation⁹¹. Similar results have been reported in some other publications, where BMP-7-modified Ti or Ta implants promoted faster new bone formation in dog jaws or in rabbit femurs, respectively, than the control metallic implants without BMP-7^{44–46}. These results suggest that biological functionalization of bone or dental implants with a strong osteogenic factor such as BMP-7 protein can markedly accelerate the post-surgical healing process. This can be especially important in patients with a hostile bony environment caused by a disease like osteoporosis. However, it is important to mention that the osseointegration process depends on the selected animal model, and this affects the extrapolation of healing dynamics from animal studies to humans. Botticelli et al. have reported that bone healing occurred much faster in smaller mammals such as rabbits than in humans⁹².

Conclusions and further perspectives

Material and morphological analyses have shown the conformal nanocrystalline diamond coating of Ti6Al4V plates and Ti6Al4V screws with a fine nanostructured diamond morphology. AFM confirmed the homogeneous coating and the tight binding of BMP-7 molecules on diamond surfaces. It also revealed the nanostructured morphology of the adsorbed BMP-7 layer, where molecules lie on the surface and form nanoscale aggregates. A

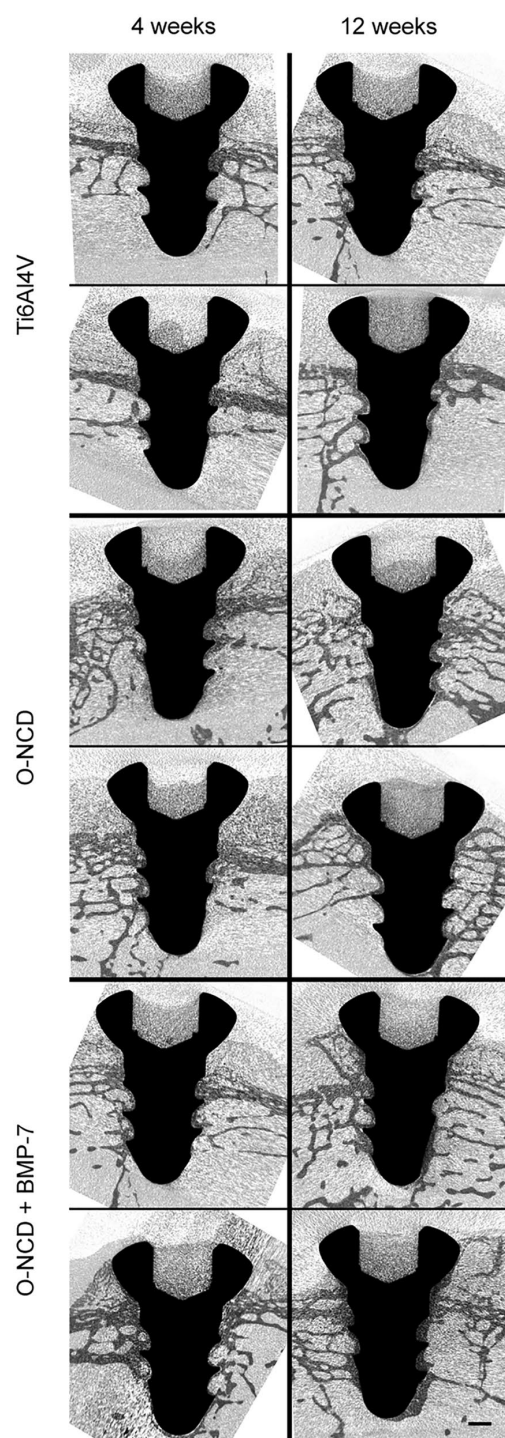


Figure 6. Micro-CT images of implants after 4 and 12 weeks. Two representative cases from each group are shown in longitudinal sections. Increased bone coverage progressing from the screw head towards its tip is evident in all groups. There is clearly more implant coverage in the O-NCD-coated group than in the reference uncoated Ti6Al4V group, and the thickness of the newly-formed bone in contact with the surface of the screw is enhanced in the O-NCD + BMP-7-coated group, especially the tip of the screw. Note also the less mineralized cartilage filling the head of the screw. Scale bar 1 mm.

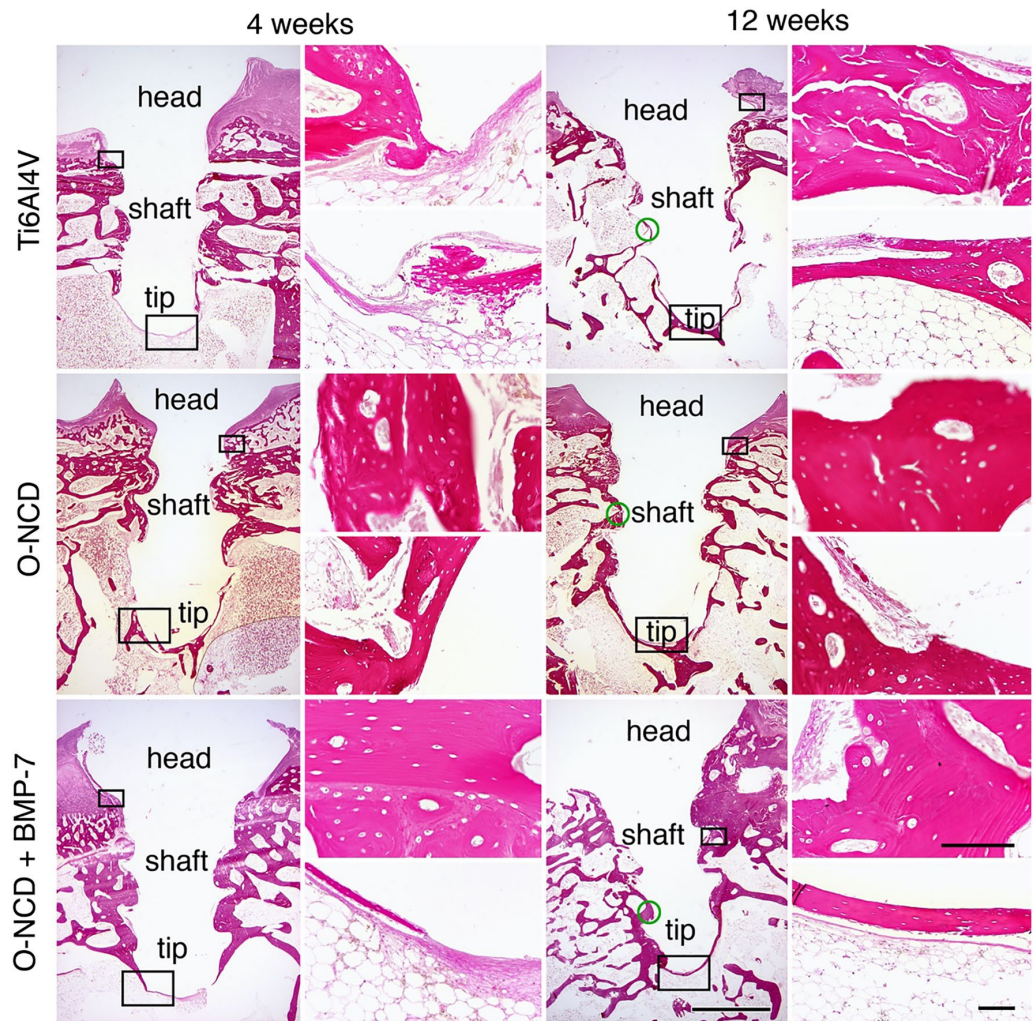


Figure 7. The histology of the implant site 4 and 12 weeks after the procedure. In contrast to bare metal implants, both coatings promoted bone formation at the screw tip at 4 weeks. Increased thickness of the newly-formed bone is evident in the O-NCD-coated group with a further increase in the O-NCD + BMP-7-coated group in both time intervals, confirming the micro-CT data (Fig. 6). The panel on the left shows the whole implant in elastin staining at low magnification, and the panel on the right shows higher power views from the region of the head and the tip (hematoxylin–eosin staining). Empty spaces correspond to fat cells in the bone marrow. Boxes indicate the approximate position of the high-power views taken on the sister sections. Green circles indicate points of measurements for quantification. Scale bars 1 mm (overview images), 100 μ m (high power views).

combination of in vitro and in vivo data has shown (1) no adverse effect of an oxidized nanocrystalline diamond coating with good long-term stability and tolerance and (2) the possibility of functionalizing this O-NCD coating with BMP-7 protein, resulting in a considerable increase in mineralization of the matrix in vitro and significantly faster osseointegration in vivo. Implants coated by nanocrystalline diamond, especially with further functionalization with bioactive molecules, such as BMP-7, can provide significant added value and medical benefits in clinical applications such as orthopaedic or dental implants (1) by promoting faster osseointegration resulting in better bone healing with the possibility of earlier loading, and (2) by limiting allergic reactions to the metal by shielding it from the immune system, which can also be expected (and which could be an interesting topic for further studies).

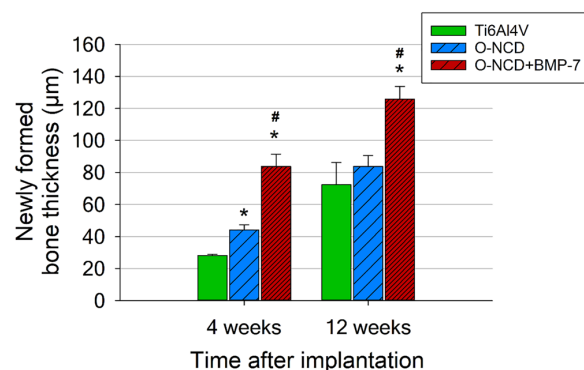


Figure 8. Quantification of newly formed bone at mid-shaft at 4 and 12 weeks after the implantation. Mean \pm S.E.M., * $p < 0.05$ vs. Ti6Al4V, # $p < 0.05$ vs. O-NCD (unpaired two-tailed t-test).

Data availability

The datasets generated during and/or analysed during the current study are available from the corresponding author on reasonable request.

Received: 15 November 2021; Accepted: 18 March 2022

Published online: 28 March 2022

References

- Katti, K. S. Biomaterials in total joint replacement. *Colloids Surf. B Biointerfaces* **39**, 133–142. <https://doi.org/10.1016/j.colsurf.2003.12.002> (2004).
- Geetha, M., Singh, A. K., Asokamani, R. & Gogia, A. K. Ti based biomaterials, the ultimate choice for orthopaedic implants – A review. *Prog. Mater. Sci.* **54**, 397–425. <https://doi.org/10.1016/j.pmatsci.2008.06.004> (2009).
- Navarro, M., Michiardi, A., Castano, O. & Planell, J. A. Biomaterials in orthopaedics. *J. R. Soc. Interface* **5**, 1137–1158. <https://doi.org/10.1098/rsif.2008.0151> (2008).
- Hanawa, T. Metal ion release from metal implants. *Mater. Sci. Eng. C-Mater. Biol. Appl.* **24**, 745–752. <https://doi.org/10.1016/j.msec.2004.08.018> (2004).
- Jinno, T., Goldberg, V. M., Davy, D. & Stevenson, S. Osseointegration of surface-blasted implants made of titanium alloy and cobalt-chromium alloy in a rabbit intramedullary model. *J. Biomed. Mater. Res.* **42**, 20–29. [https://doi.org/10.1002/\(sici\)1097-4636\(199810\)42:1%3c20::aid-jbm4%3e3.0.co;2-q](https://doi.org/10.1002/(sici)1097-4636(199810)42:1%3c20::aid-jbm4%3e3.0.co;2-q) (1998).
- Evans, J. T. *et al.* How long does a hip replacement last? A systematic review and meta-analysis of case series and national registry reports with more than 15 years of follow-up. *Lancet* **393**, 647–654. [https://doi.org/10.1016/S0140-6736\(18\)31665-9](https://doi.org/10.1016/S0140-6736(18)31665-9) (2019).
- Quinn, J., McFadden, R., Chan, C.-W. & Carson, L. Titanium for orthopedic applications: An overview of surface modification to improve biocompatibility and prevent bacterial biofilm formation. *iScience* **23**, 101745. <https://doi.org/10.1016/j.isci.2020.101745> (2020).
- Bral, A. & Mommaerts, M. Y. In vivo biofunctionalization of titanium patient-specific implants with nano hydroxyapatite and other nano calcium phosphate coatings: A systematic review. *J. Cranio-Maxillofac. Surg.* **44**, 400–412. <https://doi.org/10.1016/j.jcms.2015.12.004> (2016).
- Arcos, D. & Vallet-Regi, M. Substituted hydroxyapatite coatings of bone implants. *J. Mater. Chem. B* **8**, 1781–1800. <https://doi.org/10.1039/c9tb02710f> (2020).
- Mohammadi, H., Muhamad, N., Sulong, A. & Ahmadipour, M. Recent advances on biofunctionalization of metallic substrate using ceramic coating: How far are we from clinically stable implant?. *J. Taiwan Inst. Chem. Eng.* **118**, 254–270. <https://doi.org/10.1016/j.jtice.2021.01.013> (2021).
- Doubkova, M., Nemcakova, I., Jirka, I., Brezina, V. & Bacakova, L. Silicalite-1 layers as a biocompatible nano- and micro-structured coating: An in vitro study on MG-63 cells. *Materials* **12**, 3583. <https://doi.org/10.3390/ma12213583> (2019).
- Kopova, I., Kronek, J., Bacakova, L. & Fencel, J. A cytotoxicity and wear analysis of trapeziometacarpal total joint replacement implant consisting of DLC-coated Co-Cr-Mo alloy with the use of titanium gradient interlayer. *Diamond Relat. Mater.* <https://doi.org/10.1016/j.diamond.2019.107456> (2019).
- Orrit-Prat, J. *et al.* Bactericidal silver-doped DLC coatings obtained by pulsed filtered cathodic arc co-deposition. *Surf. Coat. Technol.* <https://doi.org/10.1016/j.surfcoat.2021.126977> (2021).
- Kopova, I., Bacakova, L., Lavrentiev, V. & Vacik, J. Growth and potential damage of human bone-derived cells on fresh and aged fullerene C-60 films. *Int. J. Mol. Sci.* **14**, 9182–9204. <https://doi.org/10.3390/ijms14059182> (2013).
- Kopova, I., Lavrentiev, V., Vacik, J. & Bacakova, L. Growth and potential damage of human bone-derived cells cultured on fresh and aged C60/Ti films. *PLoS ONE* **10**, e0123680. <https://doi.org/10.1371/journal.pone.0123680> (2015).
- Thukkaram, M. *et al.* Investigation of Ag/a-C: H nanocomposite coatings on titanium for orthopedic applications. *ACS Appl. Mater. Interfaces* **12**, 23655–23666. <https://doi.org/10.1021/acsami.9b23237> (2020).
- Szunerits, S., Nebel, C. E. & Hamers, R. J. Surface functionalization and biological applications of CVD diamond. *MRS Bull.* **39**, 517–524. <https://doi.org/10.1557/mrs.2014.99> (2014).
- Bacakova, L. *et al.* Bone cells in cultures on nanocarbon-based materials for potential bone tissue engineering: A review. *Phys. Status Solidi A* **211**, 2688–2702. <https://doi.org/10.1002/pssa.201431402> (2014).
- Erdemir, A. & Martin, J. M. Superior wear resistance of diamond and DLC coatings. *Curr. Opin. Solid State Mater. Sci.* **22**, 243–254. <https://doi.org/10.1016/j.cossms.2018.11.003> (2018).
- Papo, M. J., Catledge, S. A. & Vohra, Y. K. Mechanical wear behavior of nanocrystalline and multilayer diamond coatings on temporomandibular joint implants. *J. Mater. Sci. - Mater. Med.* **15**, 773–777. <https://doi.org/10.1023/B:JMSM.0000032817.05997.d2> (2004).

21. Budil, J. *et al.* Anti-adhesive properties of nanocrystalline diamond films against *Escherichia coli* bacterium: Influence of surface termination and cultivation medium. *Diam. Relat. Mater.* **83**, 87–93. <https://doi.org/10.1016/j.diamond.2018.02.001> (2018).
22. Jakubowski, W., Bartosz, G., Niedzielski, P., Szymanski, W. & Walkowiak, B. Nanocrystalline diamond surface is resistant to bacterial colonization. *Diam. Relat. Mater.* **13**, 1761–1763. <https://doi.org/10.1016/j.diamond.2004.03.003> (2004).
23. Medina, O. *et al.* Bactericide and bacterial anti-adhesive properties of the nanocrystalline diamond surface. *Diam. Relat. Mater.* **22**, 77–81. <https://doi.org/10.1016/j.diamond.2011.12.022> (2012).
24. Rifai, A. *et al.* Engineering the interface: Nanodiamond coating on 3d-printed titanium promotes mammalian cell growth and inhibits *Staphylococcus aureus* colonization. *ACS Appl. Mater. Interfaces.* **11**, 24588–24597. <https://doi.org/10.1021/acsami.9b07064> (2019).
25. Amaral, M. *et al.* Nanocrystalline diamond: In vitro biocompatibility assessment by MG63 and human bone marrow cells cultures. *J. Biomed. Mater. Res. Part A* **87A**, 91–99. <https://doi.org/10.1002/jbm.a.31742> (2008).
26. Ivanova, L. *et al.* Nanocrystalline diamond containing hydrogels and coatings for acceleration of osteogenesis. *Diam. Relat. Mater.* **20**, 165–169. <https://doi.org/10.1016/j.diamond.2010.11.020> (2011).
27. Kalbacova, M., Rezek, B., Baresova, V., Wolf-Brandstetter, C. & Kromka, A. Nanoscale topography of nanocrystalline diamonds promotes differentiation of osteoblasts. *Acta Biomater.* **5**, 3076–3085. <https://doi.org/10.1016/j.actbio.2009.04.020> (2009).
28. Liskova, J. *et al.* Osteogenic cell differentiation on H-terminated and O-terminated nanocrystalline diamond films. *Int. J. Nanomed.* **10**, 869–884. <https://doi.org/10.2147/ijn.s73628> (2015).
29. Steinerova, M. *et al.* Human osteoblast-like SAOS-2 cells on submicron-scale fibers coated with nanocrystalline diamond films. *Mater. Sci. Eng. C-Mater. Biol. Appl.* <https://doi.org/10.1016/j.msec.2020.111792> (2021).
30. Kloss, F. R. *et al.* The role of oxygen termination of nanocrystalline diamond on immobilisation of BMP-2 and subsequent bone formation. *Biomaterials* **29**, 2433–2442. <https://doi.org/10.1016/j.biomaterials.2008.01.036> (2008).
31. Jaatinen, J. J. P. *et al.* Early bone growth on the surface of titanium implants in rat femur is enhanced by an amorphous diamond coating. *Acta Orthop.* **82**, 499–503. <https://doi.org/10.3109/17453674.2011.579522> (2011).
32. Metzler, P. *et al.* Nano-crystalline diamond-coated titanium dental implants - A histomorphometric study in adult domestic pigs. *J. Craniomaxillofac. Surg.* **41**, 532–538. <https://doi.org/10.1016/j.jcms.2012.11.020> (2013).
33. Rupperecht, S. *et al.* The bone-metal interface of defect and press-fit ingrowth of microwave plasma-chemical vapor deposition implants in the rabbit model. *Clin. Oral Implants Res.* **16**, 98–104. <https://doi.org/10.1111/j.1600-0501.2004.01079.x> (2005).
34. Smeets, R. *et al.* Impact of dental implant surface modifications on osseointegration. *Biomed. Res. Int.* **2016**, 6285620. <https://doi.org/10.1155/2016/6285620> (2016).
35. Cecchi, S., Bennet, S. J. & Arora, M. Bone morphogenetic protein-7: Review of signalling and efficacy in fracture healing. *J. Orthopaed. Transl.* **4**, 28–34. <https://doi.org/10.1016/j.jot.2015.08.001> (2015).
36. Maliakal, J. C., Asahina, I., Hauschka, P. V. & Sampath, T. K. Osteogenic protein-1 (BMP-7) inhibits cell proliferation and stimulates the expression of markers characteristic of osteoblast phenotype in rat osteosarcoma (17/2.8) cells. *Growth Factors* **11**, 227–234. <https://doi.org/10.3109/08977199409046920> (1994).
37. Sampath, T. K. *et al.* Recombinant human osteogenic protein-1 (hOP-1) induces new bone formation in vivo with a specific activity comparable with natural bovine osteogenic protein and stimulates osteoblast proliferation and differentiation in vitro. *J. Biol. Chem.* **267**, 20352–20362 (1992).
38. Zhang, F. *et al.* The optimal dose of recombinant human osteogenic protein-1 enhances differentiation of mouse osteoblast-like cells: An in vitro study. *Arch. Oral Biol.* **57**, 460–468. <https://doi.org/10.1016/j.archoralbio.2011.10.008> (2012).
39. Al-Jarsha, M. *et al.* Engineered coatings for titanium implants to present ultralow doses of BMP-7. *ACS Biomater. Sci. Eng.* **4**, 1812–1819. <https://doi.org/10.1021/acsbiomaterials.7b01037> (2018).
40. Lee, H., Min, S. K., Song, Y., Park, Y. H. & Park, J. B. Bone morphogenetic protein-7 upregulates genes associated with osteoblast differentiation, including collagen I, Sp7 and IBSP in gingiva-derived stem cells. *Exp. Ther. Med.* **18**, 2867–2876. <https://doi.org/10.3892/etm.2019.7904> (2019).
41. Sun, H. L. *et al.* Osteogenic differentiation of human amniotic fluid-derived stem cells induced by bone morphogenetic protein-7 and enhanced by nanofibrous scaffolds. *Biomaterials* **31**, 1133–1139. <https://doi.org/10.1016/j.biomaterials.2009.10.030> (2010).
42. Chen, F. G. *et al.* Bone morphogenetic protein 7-transduced human dermal-derived fibroblast cells differentiate into osteoblasts and form bone in vivo. *Connect. Tissue Res.* **59**, 223–232. <https://doi.org/10.1080/03008207.2017.1353085> (2018).
43. Chen, F. G. *et al.* Bone morphogenetic protein 7 enhances the osteogenic differentiation of human dermal-derived CD105(+) fibroblast cells through the Smad and MAPK pathways. *Int. J. Mol. Med.* **43**, 37–46. <https://doi.org/10.3892/ijmm.2018.3938> (2019).
44. Leknes, K. N. *et al.* Alveolar ridge augmentation using implants coated with recombinant human bone morphogenetic protein-7 (rhBMP-7/rhOP-1): Radiographic observations. *J. Clin. Periodontol.* **35**, 914–919. <https://doi.org/10.1111/j.1600-051X.2008.01308.x> (2008).
45. Susin, C. *et al.* Alveolar ridge augmentation using implants coated with recombinant human bone morphogenetic protein-7 (rhBMP-7/rhOP-1): Histological observations. *J. Clin. Periodontol.* **37**, 574–581. <https://doi.org/10.1111/j.1600-051X.2010.01554.x> (2010).
46. Wang, Q. *et al.* Application of combined porous tantalum scaffolds loaded with bone morphogenetic protein 7 to repair of osteochondral defect in rabbits. *Int. Orthop.* **42**, 1437–1448. <https://doi.org/10.1007/s00264-018-3800-7> (2018).
47. Schierano, G. *et al.* Role of rhBMP-7, fibronectin, and type I collagen in dental implant osseointegration process: An initial pilot study on minipig animals. *Materials.* <https://doi.org/10.3390/ma14092185> (2021).
48. Terheyden, H., Jepsen, S., Moller, B., Tucker, M. M. & Rueger, D. C. Sinus floor augmentation with simultaneous placement of dental implants using a combination of deproteinized bone xenografts and recombinant human osteogenic protein-1 - A histometric study in miniature pigs. *Clin. Oral Implants Res.* **10**, 510–521. <https://doi.org/10.1034/j.1600-0501.1999.100609.x> (1999).
49. Cloutier, M. *et al.* Calvarial bone wound healing: A comparison between carbide and diamond drills, Er:YAG and Femtosecond lasers with or without BMP-7. *Oral Surg. Oral Med. Oral Pathol. Endodontology.* **110**, 720–728. <https://doi.org/10.1016/j.tripleo.2010.04.003> (2010).
50. Girard, B. *et al.* Microtomographic analysis of healing of femtosecond laser bone calvarial wounds compared to mechanical instruments in mice with and without application of BMP-7. *Lasers Surg. Med.* **39**, 458–467. <https://doi.org/10.1002/lsm.20493> (2007).
51. Hoellig, M. *et al.* Mesenchymal stem cells from reaming material possess high osteogenic potential and react sensitively to bone morphogenetic protein 7. *J. Appl. Biomater. Funct. Mater.* **15**, E54–E62. <https://doi.org/10.5301/jabfm.5000333> (2017).
52. Westhauser, F. *et al.* Bone formation of human mesenchymal stem cells harvested from reaming debris is stimulated by low-dose bone morphogenetic protein-7 application in vivo. *J. Orthop.* **13**, 404–408. <https://doi.org/10.1016/j.jor.2016.08.002> (2016).
53. Desmyter, S., Goubau, Y., Benahmed, N., De Wever, A. & Verdonk, R. The role of bone morphogenetic protein-7 (osteogenic protein-1 (r)) in the treatment of tibial fracture non-unions - An overview of the use in Belgium. *Acta Orthop. Belg.* **74**, 534–537 (2008).
54. Singh, R., Bleibleh, S., Kanakaris, N. K. & Giannoudis, P. V. Upper limb non-unions treated with BMP-7: Efficacy and clinical results. *Injury-Int. J. Care Injured* **47**, S33–S39. [https://doi.org/10.1016/s0020-1383\(16\)30837-3](https://doi.org/10.1016/s0020-1383(16)30837-3) (2016).
55. Kozak, H. *et al.* Chemical modifications and stability of diamond nanoparticles resolved by infrared spectroscopy and Kelvin force microscopy. *J. Nanopart. Res.* **15**, 1568. <https://doi.org/10.1007/s11051-013-1568-7> (2013).
56. Rezek, B., Michalíková, L., Ukraintsev, E., Kromka, A. & Kalbacova, M. Micro-pattern guided adhesion of osteoblasts on diamond surfaces. *Sensors* **9**, 3549–3562 (2009).

57. Rezek, B. *et al.* Adsorption of fetal bovine serum on H/O-terminated diamond studied by atomic force microscopy. *Diam. Relat. Mater.* **18**, 918–922. <https://doi.org/10.1016/j.diamond.2009.02.009> (2009).
58. Domonkos, M. *et al.* Diamond nucleation and growth on horizontally and vertically aligned Si substrates at low pressure in a linear antenna microwave plasma system. *Diam. Relat. Mater.* **82**, 41–49. <https://doi.org/10.1016/j.diamond.2017.12.018> (2018).
59. Ukraintsev, E., Rezek, B., Kromka, A., Broz, A. & Kalbacova, M. Long-term adsorption of fetal bovine serum on H/O-terminated diamond studied in situ by atomic force microscopy. *Phys. Status Solidi (B)* **246**, 2832–2835. <https://doi.org/10.1002/pssb.200982257> (2009).
60. Harris, S. A., Enger, R. J., Riggs, B. L. & Spelsberg, T. C. Development and characterization of a conditionally immortalized human fetal osteoblastic cell-line. *J. Bone Miner. Res.* **10**, 178–186. <https://doi.org/10.1002/jbmr.5650100203> (1995).
61. Subramaniam, M. *et al.* Further characterization of human fetal osteoblastic hFOB 1.19 and hFOB/ER alpha cells: Bone formation in vivo and karyotype analysis using multicolor fluorescent in situ hybridization. *J. Cell. Biochem.* **87**, 9–15. <https://doi.org/10.1002/jcb.10259> (2002).
62. Bohuslavova, R. *et al.* HIF-1 alpha is required for development of the sympathetic nervous system. *Proc. Natl. Acad. Sci. U.S.A.* **116**, 13414–13423. <https://doi.org/10.1073/pnas.1903510116> (2019).
63. Kubikova, T. *et al.* Comparison of ground sections, paraffin sections and micro-CT imaging of bone from the epiphysis of the porcine femur for morphometric evaluation. *Ann. Anat.-Anat. Anzeiger* **220**, 85–96. <https://doi.org/10.1016/j.aanat.2018.07.004> (2018).
64. Wohl, A. P., Troilo, H., Collins, R. F., Baldock, C. & Sengle, G. Extracellular regulation of bone morphogenetic protein activity by the microfibril component fibrillin-1. *J. Biol. Chem.* **291**, 12732–12746. <https://doi.org/10.1074/jbc.M115.704734> (2016).
65. Kozak, H. *et al.* Infrared absorption spectroscopy of albumin binding with amine-containing plasma polymer coatings on nanoporous diamond surfaces. *Langmuir* **35**, 13844–13852. <https://doi.org/10.1021/acs.langmuir.9b02327> (2019).
66. Ohyashiki, T. *et al.* Oxygen radical-induced inhibition of alkaline phosphatase activity in reconstituted membranes. *Arch. Biochem. Biophys.* **313**(2), 310–317. <https://doi.org/10.1006/abbi.1994.1393> (1994).
67. Lee, D. H. *et al.* Effects of hydrogen peroxide (H₂O₂) on alkaline phosphatase activity and matrix mineralization of odontoblast and osteoblast cell lines. *Cell Biol. Toxicol.* **22**(1), 39–46. <https://doi.org/10.1007/s10565-006-0018-z> (2006).
68. Hoshino, T. *et al.* Low serum alkaline phosphatase activity associated with severe Wilson's disease. Is the breakdown of alkaline phosphatase molecules caused by reactive oxygen species?. *Clin. Chim. Acta* **238**(1), 91–100. [https://doi.org/10.1016/0009-8981\(95\)06073-m](https://doi.org/10.1016/0009-8981(95)06073-m) (1995).
69. Farley, J. R., Hall, S. L., Tanner, M. A. & Wergedal, J. E. Specific activity of skeletal alkaline phosphatase in human osteoblast-line cells regulated by phosphate, phosphate esters, and phosphate analogs and release of alkaline phosphatase activity inversely regulated by calcium. *J. Bone Miner. Res.* **9**(4), 497–508. <https://doi.org/10.1002/jbmr.5650090409> (1994).
70. Ball, V. Activity of alkaline phosphatase adsorbed and grafted on "polydopamine" films. *J. Colloid Interface Sci.* **429**, 1–7. <https://doi.org/10.1016/j.jcis.2014.05.002> (2014).
71. Pimphilai, M., Zhao, Z., Boules, H., Roca, H. & Franceschi, R. T. BMP signaling is required for RUNX2-dependent induction of the osteoblast phenotype. *J. Bone Miner. Res.* **21**, 637–646. <https://doi.org/10.1359/jbmr.060109> (2006).
72. Carvalho, M. S., Cabral, J. M. S., da Silva, C. L. & Vashishth, D. Bone matrix non-collagenous proteins in tissue engineering: Creating new bone by mimicking the extracellular matrix. *Polymers Basel*. <https://doi.org/10.3390/polym13071095> (2021).
73. Kram, V. *et al.* Biglycan in the skeleton. *J. Histochem. Cytochem.* **68**, 747–762. <https://doi.org/10.1369/0022155420937371> (2020).
74. Grausova, L. *et al.* Molecular markers of adhesion, maturation and immune activation of human osteoblast-like MG 63 cells on nanocrystalline diamond films. *Diam. Relat. Mater.* **18**, 258–263. <https://doi.org/10.1016/j.diamond.2008.10.023> (2009).
75. Krátká, M. *et al.* Gamma radiation effects on diamond field-effect biosensors with fibroblasts and extracellular matrix. *Colloids Surf. B* **204**, 111689. <https://doi.org/10.1016/j.colsurfb.2021.111689> (2021).
76. Al-Romaih, K. *et al.* Chromosomal instability in osteosarcoma and its association with centrosome abnormalities. *Cancer Genet. Cytogenet.* **144**, 91–99. [https://doi.org/10.1016/S0165-4608\(02\)00929-9](https://doi.org/10.1016/S0165-4608(02)00929-9) (2003).
77. Pautke, C. *et al.* Characterization of osteosarcoma cell lines MG-63, Saos-2 and U-2 OS in comparison to human osteoblasts. *Anticancer Res.* **24**, 3743–3748 (2004).
78. Nemcakova, I., Jirka, I., Doubkova, M. & Bacakova, L. Heat treatment dependent cytotoxicity of silicalite-1 films deposited on Ti-6Al-4V alloy evaluated by bone-derived cells. *Sci. Rep.* <https://doi.org/10.1038/s41598-020-66228-x> (2020).
79. Chen, S. *et al.* Adenovirus encoding BMP-7 immobilized on titanium surface exhibits local delivery ability and regulates osteoblast differentiation in vitro. *Arch. Oral Biol.* **58**, 1225–1231. <https://doi.org/10.1016/j.archoralbio.2013.03.019> (2013).
80. Zhou, L., Wu, J., Wu, D. & Yu, J. Surface functionalization of titanium with BMP-7/RGD/hyaluronic acid for promoting osteoblast functions. *J. Biomater. Tissue Eng.* **9**, 32–39. <https://doi.org/10.1166/jbt.2019.1938> (2019).
81. Franchi, M. *et al.* Osteogenesis and morphology of the peri-implant bone facing dental implants. *Sci. World J.* **4**, 1083–1095. <https://doi.org/10.1100/tsw.2004.211> (2004).
82. Witek, L. *et al.* Assessing osseointegration of metallic implants with boronized surface treatment. *Med. Oral Patol. Oral Cir. Bucal.* **25**, e311–e317. <https://doi.org/10.4317/medoral.23175> (2020).
83. Soto-Peñaloza, D. *et al.* Effect on osseointegration of two implant macro-designs: A histomorphometric analysis of bicortically installed implants in different topographic sites of rabbit's tibiae. *Med. Oral Patol. Oral Cir. Bucal.* **24**, e502–e510. <https://doi.org/10.4317/medoral.22825> (2019).
84. Karazisis, D. *et al.* The role of well-defined nanotopography of titanium implants on osseointegration: Cellular and molecular events in vivo. *Int. J. Nanomed.* **11**, 1367–1382. <https://doi.org/10.2147/ijn.s101294> (2016).
85. Bissinger, O. *et al.* Comparative 3D micro-CT and 2D histomorphometry analysis of dental implant osseointegration in the maxilla of minipigs. *J. Clin. Periodontol.* **44**, 418–427. <https://doi.org/10.1111/jcpe.12693> (2017).
86. Gabler, C. *et al.* Quantification of osseointegration of plasma-polymer coated titanium alloyed implants by means of micro-computed tomography versus histomorphometry. *Biomed. Res. Int.* **2015**, 103137. <https://doi.org/10.1155/2015/103137> (2015).
87. Schouten, C., Meijer, G. J., van den Beucken, J. J., Spauwen, P. H. & Jansen, J. A. The quantitative assessment of peri-implant bone responses using histomorphometry and micro-computed tomography. *Biomaterials* **30**, 4539–4549. <https://doi.org/10.1016/j.biomaterials.2009.05.017> (2009).
88. Linder, L. Osseointegration of metallic implants. I. Light microscopy in the rabbit. *Acta Orthop. Scand.* **60**, 129–134. <https://doi.org/10.3109/17453678909149239> (1989).
89. Yang, J. H. C. & Teii, K. Mechanism of enhanced wettability of nanocrystalline diamond films by plasma treatment. *Thin Solid Films* **520**, 6566–6570. <https://doi.org/10.1016/j.tsf.2012.06.041> (2012).
90. Grieten, L. *et al.* Real-time study of protein adsorption on thin nanocrystalline diamond. *Phys. Status Solidi (A)* **208**, 2093–2098. <https://doi.org/10.1002/pssa.201100122> (2011).
91. Hunziker, E. B. *et al.* The slow release of BMP-7 at a low dose accelerates dental implant healing in an osteopenic environment. *Eur. Cell Mater.* **41**, 170–183. <https://doi.org/10.22203/eCM.v041a12> (2021).
92. Botticelli, D. & Lang, N. P. Dynamics of osseointegration in various human and animal models - A comparative analysis. *Clin. Oral Implants Res.* **28**, 742–748. <https://doi.org/10.1111/clr.12872> (2017).

Acknowledgements

Kind technical assistance with SEM by Rajisa Jackivova (Institute of Physics) and Jarmila Svotunkova with the *in vivo* protocols (Institute of Physiology) is gratefully appreciated. This study was initially supported by the Czech Health Research Council, Ministry of Health of the Czech Republic (grant No. 15-32497A). Then the work continued with partial support from Operational Programme Research, Development and Education project No. SOLID21-CZ.02.1.01/0.0/0.0/16_019/0000760 (Solid21) and CZ.02.1.01/0.0/0.0/16_019/0000778 (CAAS), which are financed by the European Structural and Investment Funds and the Ministry of Education, Youth and Sports of the Czech Republic. The study was also supported by the Ministry of Education, Youth and Sports of the Czech Republic (Progres Q29/LF1) and by the Grant Agency of the Czech Republic (grant No. 21-06065S). We also acknowledge CzechNanoLab Research Infrastructure supported by MEYS CR (LM2018110), and a project for International Mobility of Researchers at CTU No. CZ.02.2.69/0.0/0.0/16_027/0008465 (O.B.). Mr. Robin Healey (Czech Technical University in Prague) is gratefully acknowledged for his language revision of the manuscript.

Author contributions

L.B., A.K., B.R., D.S.: conception and design of the study. I.N., A.L., V.M., M.B., E.U., O.B.: methodology. I.N., M.P., M.D., M.B., E.U., O.B.: acquisition of data. I.N., M.D., V.M., M.B., E.U., O.B., D.S.: data analysis and interpretation. I.N., M.D.: statistics. I.N., M.D., M.B., E.U., O.B., A.K., B.R., D.S.: visualization. A.L., O.N., V.O., D.S.: *in vivo* experiments, surgery. M.P., M.D., B.S.: assistance in *in vivo* experiments. I.N., M.D., M.B., V.M., B.R.: manuscript preparation. M.P., M.D., L.B., B.R., D.S.: manuscript review and editing. L.B., D.S., A.K., B.R.: funding acquisition. L.B., A.L., A.K., B.R., D.S.: supervision. All authors have contributed to this research, revised it critically, and approved the final version of the manuscript.

Competing interests


The authors declare no competing interests.

Additional information

Correspondence and requests for materials should be addressed to M.D. or D.S.

Reprints and permissions information is available at www.nature.com/reprints.

Publisher's note Springer Nature remains neutral with regard to jurisdictional claims in published maps and institutional affiliations.

 **Open Access** This article is licensed under a Creative Commons Attribution 4.0 International License, which permits use, sharing, adaptation, distribution and reproduction in any medium or format, as long as you give appropriate credit to the original author(s) and the source, provide a link to the Creative Commons licence, and indicate if changes were made. The images or other third party material in this article are included in the article's Creative Commons licence, unless indicated otherwise in a credit line to the material. If material is not included in the article's Creative Commons licence and your intended use is not permitted by statutory regulation or exceeds the permitted use, you will need to obtain permission directly from the copyright holder. To view a copy of this licence, visit <http://creativecommons.org/licenses/by/4.0/>.

© The Author(s) 2022